Search for light CP-odd Higgs bosons with ATLAS and integration of ALTI boards for the ATLAS Liquid Argon calorimeters

---

DISSERTATION

zur Erlangung des akademischen Grades

Doctor rerum naturalium
(Dr. rer. nat.)

vorgelegt

dem Bereich Mathematik und Naturwissenschaften
der Technischen Universität Dresden

von

M. Sc. Tom Kreße

Eingereicht am 4. März 2025.

Verteidigt am 22. August 2025.

Die Dissertation wurde in der Zeit von Januar 2021 bis März 2025
am Institut für Kern- und Teilchenphysik angefertigt.

Eingereicht am 4. März 2025

Verteidigt am 22. August 2025

1. Gutachter: Prof. Dr. Arno Straessner
2. Gutachter: Prof. Dr. Michael G. Strauss

Abstract

Two major topics of modern particle physics are explored in this thesis, namely, physics analysis and the operation and upgrades of particle detectors.
Within the realm of physics analysis, the search for a light CP-odd scalar resonance with a mass of 20 GeV to 110 GeV is presented. The analyzed data comprises an integrated luminosity of 140 fb^{-1}. The data were collected with the ATLAS detector at the Large Hadron Collider (LHC) proton–proton collisions at 13 TeV during LHC Run 2 from 2015-2018. The analysis assumes a resonance that is produced via gluon–gluon fusion and decays into a $\tau^+\tau^-$ pair. Its decay into the fully leptonic final state with exactly one electron, one muon, and the four accompanying neutrinos is analyzed.
No significant excess of events above the background prediction by the Standard Model of particle physics is observed. In a model-independent interpretation, upper limits are set on the production cross-section for a CP-odd Higgs boson that is created via gluon–gluon fusion and decays into a $\tau^+\tau^-$ pair, with the limits ranging from 2.4 pb to 67 pb at 95% confidence level.
In addition, the results are also interpreted within the flavor-aligned two-Higgs-doublet model. An upper limit is given within this model on the absolute value of the up-type quark coupling parameter $|\zeta_\mathrm{u}|$ between 0.074 and 0.47 at 95% confidence level.
In the context of detector operations, this thesis presents the commissioning of the ALTI (ATLAS Local Trigger Interface) boards for the Liquid Argon calorimeter of the ATLAS detector. These boards are responsible for the control and distribution of timing and trigger signals between different parts of the ATLAS detector. They have been installed during the Long Shutdown 2 of the LHC in 2021 and are now in operation for the ongoing Run 3 of the LHC.

Kurzdarstellung

Diese Arbeit befasst sich mit zwei Hauptaspekten der modernen Teilchenphysik: der Datenanalyse und dem Betrieb sowie den Upgrades von Teilchendetektoren.

Im Bereich der Datenanalyse wird die Suche nach einer leichten CP-ungeraden skalaren Resonanz mit einer Masse von 20 GeV bis 110 GeV vorgestellt. Die analysierten Daten umfassen eine integrierte Luminosität von $140\,\mathrm{fb}^{-1}$. Diese wurden mit dem ATLAS-Detektor am Large Hadron Collider (LHC) in Proton-Proton-Kollisionen mit Schwerpunktsenergie von 13 TeV während des zweiten LHC-Betriebslaufs von 2015-2018 aufgenommen. Die Analyse nimmt eine Resonanz an, die durch Gluon-Gluon-Fusion erzeugt wird und in ein $\tau^+\tau^-$-Paar zerfällt, das anschließend in einen vollständig leptonischen Endzustand mit genau einem Elektron, einem Myon und den vier begleitenden Neutrinos zerfällt.

Es wird kein signifikanter Überschuss an Ereignissen oberhalb der Untergrundvorhersage des Standardmodells der Teilchenphysik beobachtet. Im Rahmen einer modellunabhängigen Interpretation werden für den Produktionsquerschnitt eines CP-ungeraden Higgs-Bosons, das durch Gluon-Gluon-Fusion erzeugt wird und in ein $\tau^+\tau^-$-Paar zerfällt, obere Grenzen festgelegt, wobei die ermittelten Grenzen zwischen 2,4 pb und 67 pb mit einem Vertrauensniveau von 95% liegen.

Die Ergebnisse werden auch im Rahmen eines Zwei-Higgs-Dublett-Modells interpretiert, bei dem die Kopplungen anhand des Flavors ausgerichtet sind. Innerhalb dieses Modells wird eine obere Grenze für den absoluten Wert des Up-Typ-Quark-Kopplungsparameters $|\zeta_\mathrm{u}|$ zwischen 0,074 und 0,47 mit einem Vertrauensniveau von 95% gesetzt.

Im Rahmen des Detektorbetriebs wird die Inbetriebnahme der ALTI-Platinen (ATLAS Local Trigger Interface) für das Flüssig-Argon-Kalorimeter des ATLAS-Detektors vorgestellt. Diese Boards sind für die Steuerung und Verteilung von Timing- und Triggersignalen zwischen verschiedenen Teilen des ATLAS-Detektors verantwortlich. Sie wurden während der zweiten längeren Wartungsphase des LHC im Jahr 2021 installiert und sind nun für den aktuellen dritten Betriebslauf des LHC im Einsatz.

Contents

1 Introduction

The discovery of the Higgs boson in 2012 [1, 2] by the ATLAS [3] and CMS [4] collaborations at the Large Hadron Collider (LHC) [5] marked a significant milestone in particle physics, confirming the mechanism of electroweak symmetry breaking as described by the Standard Model of particle physics (SM). Extensive experimental studies [6, 7] have confirmed consistency of the Higgs boson with SM predictions.

While its discovery almost 50 years after being postulated by P. Higgs in 1964 [8] was a great international success, the search for new physics is far from over. There are several fundamental questions that the SM does not address. These include issues pertaining to the nature of dark matter, the hierarchy problem, and the matter–antimatter asymmetry in the universe. Moreover, in other research areas, experimental measurements, like the 2023 Fermilab result [9] for the anomalous magnetic moment of the muon, challenge the predictions of the SM.

It is evident that the SM represents only one puzzle piece in the understanding of the universe, and in order to explain all phenomena requires extensions or a combination with other theories. This necessitates a dual strategy: on the one hand, searching for new particles in unexplored regions of phase space, and on the other, conducting precise examinations of SM parameters. Both approaches are crucial — not only for experimental particle physics but also for theoretical physics — as new findings help refine existing models and develop new ones, which in turn provides new impulses for further experimental investigations. Chapter 2 provides a brief overview of the theoretical concepts, including an introduction to the flavor-aligned two-Higgs-doublet model (2HDM) [10] as a potential extension of the SM. Within this model, the Higgs boson would be part of an extended scalar section, as motivated by several theoretical arguments [11, 12].

Experimental success is based on the interplay of the technical setup of the detector, its operation, data acquisition and processing, reconstruction and identification of physics objects, as well as the analysis of the recorded dataset with all available tools. Chapter 3 presents the ATLAS detector as a prime example of a cutting-edge particle physics experiment, with a particular emphasis on one of its sub-detectors, the liquid argon (LAr) calorimeter. The reconstruction and identification algorithms for the various physics objects is further detailed in Chapter 5.

Detector upgrades are crucial to ensure smooth data taking and incorporate techno-

logical advancements into the experiments. The integration and commissioning of the ATLAS Local Trigger Interface (ALTI) boards for the LAr calorimeter upgrade during the Long Shutdown 2 (LS2) of the LHC is described in Chapter 4. They provide the interface between the LAr system and the Central Trigger Processor (CTP), as well as other subdetectors, for the exchange of timing and trigger signals, which are critical for excellent data-taking. These boards replace the aging components and add a palette of new features for a more stable operation as well as advanced diagnostics and testing opportunities.
Following the description of the theoretical arguments and the experimental setup, Chapter 6 presents the search for a new particle using the Run 2 dataset recorded by the ATLAS detector in proton–proton collisions at $\sqrt{s} = 13\,\text{TeV}$. It focuses on finding a light CP-odd Higgs boson, that is produced via gluon–gluon fusion and then decays into a pair of τ-leptons, which subsequently decay into a fully leptonic final state. This CP-odd Higgs boson is part of the extended scalar sector as predicted by the flavor-aligned 2HDM. It extends the probed mass range of previous searches [13–17] down to previously untested mass ranges as low as $20\,\text{GeV}$. Furthermore, it has the potential of explaining the observed deviation in the anomalous magnetic moment of the muon between experiment and theory [18]. The analysis results contributed to the paper published by *JHEP* in 2024 (see Ref. [19]). This thesis extends the explored mass range and gives a more detailed insight into the analysis implementation and procedures.
This thesis concludes with a brief summary of the obtained results and a discussion of potential future improvements is given in Chapter 7.

2 Theoretical foundation

This chapter provides a brief overview of the physics related to a CP-odd Higgs boson. It begins with an explanation of the SM fundamentals, as the CP-odd Higgs boson is predicted by an extended version of the SM. After discussing the limitations of the SM, the chapter introduces the 2HDM as a common extension of the SM. Finally, it describes the characteristics of the new particle, current theoretical limitations and their implications for its detection.

2.1 The Standard Model of particle physics

The SM [8, 20–30] is a highly successful model in modern high-energy physics. It accounts for all known elementary particles and their interactions. Among the four fundamental forces, the SM precisely describes three: the electromagnetic, weak, and strong interactions. The fourth force, gravity, is negligible at the particle physics scale. Particle interactions are explained through interacting fields, which, when quantized, form a Quantum Field Theory (QFT). The SM integrates QFTs for the various fundamental forces. Furthermore, it includes the Higgs mechanism, which describes how elementary particles acquire their mass.

2.1.1 Phenomenology and particle content

Figure 2.1 presents an overview of the elementary particles in the SM. These particles are organized into two categories based on their spin: fermions, which have half-integer spins, and bosons, which have integer spins. Fermions are further divided into leptons and quarks, each existing in three generations. Within each generation, leptons and quarks can be paired into one ‘up’-type and one ‘down’-type fermion, according to their weak isospin. Fermions across different generations vary only in their mass, while charge and spin remain the came. The term ‘charge’ here encompasses not only the electromagnetic charge (positive or negative) but also the weak isospin and the color charge associated with the strong interaction (red, blue, green).

On the lepton side, the three generations are formed by the electron (e), the muon (μ), and the τ-lepton (τ), each accompanied by their respective neutrino ($\nu_{e,\mu,\tau}$). All leptons participate in the weak interactions. For neutrinos, this is their sole

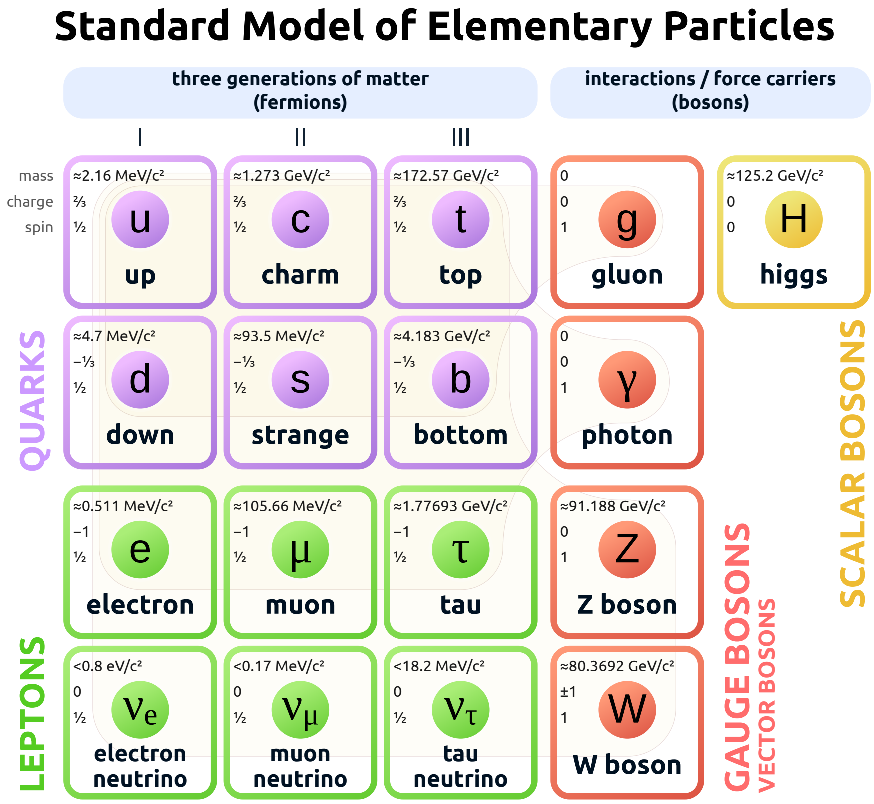

Figure 2.1: The particle content of the SM [31]. Particles are grouped into fermions (left, in purple and green) and bosons (right, in red and yellow). The interactions that particles engage in are determined by the charges they carry. Each interaction involves the exchange of a gauge boson (depicted by the light yellow background). The scalar Higgs boson (far right) represents a massive excitation of the Higgs field.

interaction, as they are electrically neutral and do not have a color charge. Initially, neutrinos were thought to be massless, but the discovery of neutrino oscillations by the SNO experiment in 2001 [32] indicated that they must have mass. To date, only upper limits on their masses have been established, as their masses are extremely small, and neutrinos rarely interact with matter. Electrons, muons, and τ-leptons carry an electric charge of -1, allowing them to also interact via the electromagnetic force. Like neutrinos, they do not possess a color charge and therefore do not take part in the strong interaction.
Unlike leptons, quarks possess a color charge, allowing them to interact via the strong interaction. There are six different quarks, divided into two groups: the three up-type quarks up (u), charm (c), and top (t) with an electric charge of $+2/3$,

and the three down-type quarks down (d), strange (s), and bottom (b) with an electric charge of $-1/3$. Quarks participate in all three fundamental interactions described in the SM. Particles bound by the strong force must be color-neutral. Color neutrality can be achieved by combining a quark with its corresponding anti-quark (e.g., blue and anti-blue) to form *mesons*, or by combining three quarks, each with a different color (red, green, blue), to form *baryons*.
In addition to the fermions already presented, each particle has a corresponding anti-particle. Predicted by the *Dirac equation* [33] for charged massive particles, anti-particles differ from their corresponding fermions only in having opposite charges.
The second big category of elementary particles, the gauge bosons, act as mediators of the fundamental forces. The electromagnetic force is carried by the massless photon (γ). Similarly, the strong force is carried by massless gluons (g), which exist in eight different combinations of color and anti-color charges. This allows them to interact with each other, which does not happen for the neutral photons. The gauge bosons of the weak interaction are formed by the charged W^+ and W^- bosons and the neutral Z boson. They can also interact with one another.
The ranges of the three fundamental forces vary significantly. The electromagnetic force is considered to have an infinite range due to its massless force carrier. Despite the gluons being similarly massless, the strong force has a limited range. As two strongly interacting particles move further apart, the energy between them increases due to the *color confinement* [34], resulting in a short interaction range. Eventually, this energy becomes sufficient to create a quark–antiquark pair. The weak force also has a short range, but for a different reason: the $W^\pm$ and Z bosons that mediate this force are massive. From the concept of the Yukawa potential [35], it follows, that the range of an interaction decreases as the mass of its mediating particle increases. Given the masses of $m_W \approx 80\,\mathrm{GeV}$ and $m_Z \approx 91\,\mathrm{GeV}$, the range of the weak force is approximately $10^{-3}\,\mathrm{fm}$.
The Higgs boson was the final missing particle in the SM until its discovery in 2012 [1, 2]. Unlike other bosons, the Higgs boson does not function as a force carrier. Instead, the related Higgs field is the basis of the mechanism that gives particles their mass. This Higgs mechanism is further detailed in Section 2.1.3.

2.1.2 Electroweak unification

The interactions in the SM are described by gauge groups [36]. The complete gauge group of the SM is $\mathrm{SU}(3)_C \times \mathrm{SU}(2)_L \times \mathrm{U}(1)_Y$. The first part $\mathrm{SU}(3)_C$ part describes the Quantum Chromodynamics (QCD) with the color charge C. The remainder $\mathrm{SU}(2)_L \times \mathrm{U}(1)_Y$ combines the electromagnetic interaction and the weak interaction for left-handed particles (denoted by the L) into the electroweak group with the weak hypercharge Y. The Higgs mechanism spontaneously breaks this symmetry,

resulting in the $\mathrm{U}(1)_Q$ group of the electromagnetic interaction, with the electric charge Q and the photon as the gauge boson, as well as giving mass to the $W^{\pm}$ and Z bosons of the weak interaction.
The Lagrangian of the electroweak part of the SM has the following form:

$$\mathcal{L}_{\mathrm{SU}(2)\times\mathrm{U}(1)} = \mathcal{L}_{\text{gauge}} + \mathcal{L}_f + \mathcal{L}_{\text{Higgs}} + \mathcal{L}_{\text{Yukawa}}. \tag{2.1}$$

The Higgs component $\mathcal{L}_{\text{Higgs}}$ and the Yukawa coupling term $\mathcal{L}_{\text{Yukawa}}$ will be analyzed in Section 2.1.3. Here, first the fermion term $\mathcal{L}_{\text{f}}$ will be explained, followed by a description of the gauge field term $\mathcal{L}_{\text{gauge}}$. The full fermion term is

$$\mathcal{L}_f = \bar{L} i\gamma^\mu \partial_\mu L + \bar{e}_{\mathrm{R}} i\gamma^\mu \partial_\mu e_{\mathrm{R}} + \bar{Q} i\gamma^\mu \partial_\mu Q + \bar{u}_{\mathrm{R}} i\gamma^\mu \partial_\mu u_{\mathrm{R}} + \bar{d}_{\mathrm{R}} i\gamma^\mu \partial_\mu d_{\mathrm{R}},$$

where ∂_μ is the four-gradient, γ^μ are the gamma matrices and the usual summation over the values of the twice-repeated index $\mu = 0, 1, 2, 3$ is implied. It is divided into two parts, because only left-handed particles are affected by the weak interaction. Left-handed fermions are organized into doublets, while right-handed fermions are singlets. The right-handed fermions are represented by e_{R} for leptons, and u_{R} and d_{R} for up- and down-type quarks, respectively. The left-handed lepton part is denoted as $L = (\nu_e, e)^T_{\mathrm{L}}$, and the quark term as $Q = (u, d)^T_{\mathrm{L}}$. These symbols represent sums over all three fermion generations, so for example u_{R} includes right-handed up, charm, and top quarks, and equivalent for the other particles. Here, T represents the weak isospin, which is 0 for singlets and 1/2 for doublets. The third component of the weak isospin T_3 is $+1/2$ for the first particle in a fermion doublet and $-1/2$ for the second particle. Additionally, all fermions have a hypercharge Y, which is related to T_3 and the electromagnetic charge Q through the relation

$$Q = T_3 + Y.$$

The fermion singlets and doublets transform under gauge transformations as

$$\begin{aligned} L \to L' &= e^{i\alpha(x)Y_{\mathrm{L}}} \cdot e^{i\Theta_a(x)T^a} L \\ e_{\mathrm{R}} \to e'_{\mathrm{R}} &= e^{i\alpha(x)Y_{\mathrm{R}}} e_{\mathrm{R}}, \end{aligned}$$

with the weak hypercharges Y_{L} and Y_{R} for the left-handed doublets and right-handed singlets, respectively. The functions $\alpha(x)$ and $\Theta_a(x)$ represent gauge functions, and the two-dimensional matrices T^a are used. They are constructed from the Pauli matrices

$$\sigma^1 = \begin{pmatrix} 0 & 1 \\ 1 & 0 \end{pmatrix}, \ \sigma^2 = \begin{pmatrix} 0 & -i \\ i & 0 \end{pmatrix}, \ \sigma^3 = \begin{pmatrix} 1 & 0 \\ 0 & -1 \end{pmatrix}$$

as

$$T^a = \frac{\sigma^a}{2}.$$

To achieve a Lagrangian that is invariant under the introduced transformations, the covariant derivative D^μ is added:

$$
\begin{aligned}
D^\mu L &= \left(\partial^\mu + i g_W T^a W_a^\mu + i g_Y Y_\mathrm{L} B^\mu\right) L \\
D^\mu e_\mathrm{R} &= \left(\partial^\mu + i g_Y Y_\mathrm{R} B^\mu\right) e_\mathrm{R}.
\end{aligned}
$$

It is constructed with the gauge fields W_a^μ and B^μ from the gauge term of the SM Lagrangian

$$
\mathcal{L}_\mathrm{gauge} = -\frac{1}{4} W_a^{\mu\nu} W_{\mu\nu}^a - \frac{1}{4} B^{\mu\nu} B_{\mu\nu}.
$$

The gauge fields transform according to

$$
\begin{aligned}
W_a^\mu \to W_a^{\mu\prime} &= W_a^\mu - \frac{1}{g_W} \partial^\mu \Theta_a(x) + \epsilon_{abc} \Theta^b(x) W^{c,\mu} \\
B^\mu \to B^{\mu\prime} &= B^\mu - \frac{1}{g_Y} \partial^\mu \alpha(x).
\end{aligned}
$$

The Lagrangian of the Standard Model is then by design invariant under simultaneous transformations of the gauge and fermion fields. Two constants appear in the transformation equations: the weak coupling constant g_W for the coupling strength of the gauge fields W_1^μ, W_2^μ, and W_3^μ of the $\mathrm{SU}(2)_L$ group, and the coupling strength g_Y for interactions involving the fourth gauge field B^μ of the $\mathrm{U}(1)_Y$ group. To obtain the physical mass eigenstates $W^\pm$, Z, and A, the Higgs mechanism, which is explained in the next Section 2.1.3, is required. Through this mechanism, the gauge fields W_a^μ and B^μ mix to form the physical states representing the $W^\pm$ bosons, the Z boson, and the photon A:

$$
W^{\pm,\mu} = \frac{1}{\sqrt{2}} \left(W_1^\mu \mp i W_2^\mu\right) \tag{2.2}
$$

$$
\begin{pmatrix} A^\mu \\ Z^\mu \end{pmatrix} = \begin{pmatrix} \cos\theta_\mathrm{W} & \sin\theta_\mathrm{W} \\ -\sin\theta_\mathrm{W} & \cos\theta_\mathrm{W} \end{pmatrix} \begin{pmatrix} B^\mu \\ W_3^\mu \end{pmatrix}. \tag{2.3}
$$

The occurring *Weinberg angle*[1] θ_W is defined as a combination of the coupling strengths g_W and g_Y

$$
\cos\theta_\mathrm{W} = \frac{g_W}{\sqrt{g_W^2 + g_Y^2}}.
$$

2.1.3 Higgs mechanism in the Standard Model

The Higgs mechanism is an essential part of the SM, as it provides particles with the masses that are observed in nature [36, 37]. The local gauge invariance

[1] It is also known as 'weak mixing angle'.

prevents the inclusion of explicit mass terms in the Lagrangian. Therefore, the gauge invariance needs to be spontaneously broken. The basic concept is that the system's ground state, the vacuum state, does not adhere to the gauge symmetry. This non-compliance enables particles moving through it to obtain mass. To achieve a symmetry that can be spontaneously broken, a scalar spin-0 field Φ is proposed:

$$\Phi = \begin{pmatrix} \phi^+ \\ \phi^0 \end{pmatrix} = \frac{1}{\sqrt{2}} \begin{pmatrix} \phi_1 - i\phi_2 \\ \phi_3 - i\phi_4 \end{pmatrix}.$$

Subsequently, a term $\mathcal{L}_{\text{Higgs}}$ has to be added to the SM Lagrangian for this new field:

$$\mathcal{L}_{\text{Higgs}} = \left(D^\mu \Phi\right)^\dagger \left(D_\mu \Phi\right) - V(\Phi),$$

which contains the effective potential $V(\Phi)$

$$V(\Phi) = \mu^2 \Phi^\dagger \Phi + \lambda \left(\Phi^\dagger \Phi\right)^2. \tag{2.4}$$

The parameter λ denotes the quartic Higgs self-coupling strength, which is always real and positive, whereas the term μ^2 can be either positive or negative. When μ^2

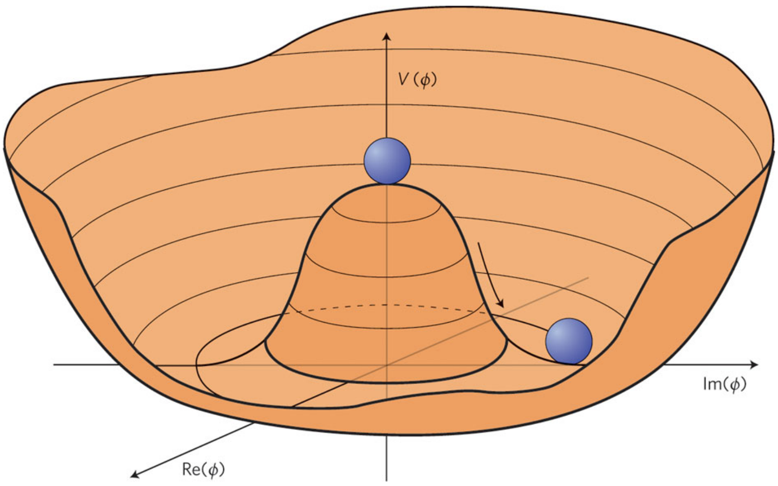

Figure 2.2: Illustration of the Higgs potential in the case that $\mu^2 < 0$ [37]. The rotational U(1) symmetry is broken spontaneously once one of the minimum energy states at the bottom of the potential is chosen.

is positive, the function has a single minimum, placing the ground state at $\Phi = 0$. This scenario does not address the issue of how particles acquire mass, as it simply adds one massive particle to the SM. However, when μ^2 is negative, the potential exhibits an infinite number of degenerate ground states, as illustrated in Figure 2.2. Starting from the local maximum, the system seeks to minimize its energy and

thus settles into one of these ground states. Since they all have the same energy, the symmetry is spontaneously broken.
The ground state can be chosen, without any loss of generality, to be

$$\langle\Phi\rangle = \frac{1}{\sqrt{2}}\begin{pmatrix}0\\v\end{pmatrix},$$

where v is the vacuum expectation value (VEV), that is connected to the parameters λ and μ^2 via $\frac{v^2}{2} = \frac{-\mu^2}{2\lambda}$. This VEV choice spontaneously breaks the electroweak group $\mathrm{SU}(2)_L \times \mathrm{U}(1)_Y$ and results in the electromagnetic subgroup $\mathrm{U}(1)_Q$. In a broken global symmetry, this would furthermore generate three massless *Nambu-Goldstone bosons* [38, 39]. In the here present case of a gauge theory, however, they are absorbed by three of the gauge bosons. To understand this, the Higgs potential is expanded around the minimum:

$$\Phi = \frac{1}{\sqrt{2}}\begin{pmatrix}0\\v + H(x)\end{pmatrix}, \tag{2.5}$$

with the hermitian field $H(x)$ which represents the physical Higgs scalar. The masses of the weak bosons are obtained by analyzing the kinetic term in the Higgs part of the SM Lagrangian:

$$\begin{aligned}(D^\mu\Phi)^\dagger(D_\mu\Phi) &= \frac{v^2}{8}\left[g_W^2((W_\mu^1)^2 + (W_\mu^2)^2) + (g_W W_\mu^3 - g_Y B_\mu)\right] + \dots &(2.6)\\ &\overset{(2.2)}{=} \left(\frac{v g_W}{2}\right)^2 W^{+\mu}W_\mu^- + \frac{1}{2}\left(\frac{v}{2}\right)^2\left(g_W^2 + g_Y^2\right) Z^\mu Z_\mu + 0\cdot A^\mu A_\mu + \dots, &(2.7)\end{aligned}$$

where higher order Higgs terms and mixed terms of Higgs and electroweak content were neglected, as they are not relevant for the mass determination. The boson masses can be read off directly from Equation 2.7:

$$\begin{aligned} m_A &= 0\\ m_W &= \frac{g_W v}{2}\\ m_Z &= \frac{v}{2}\sqrt{g_W^2 + g_Y^2}.\end{aligned}$$

It can be seen that the Higgs mechanism simultaneously provides an explanation why the photon is massless and how the weak bosons acquire their mass.
To obtain the mass of the Higgs boson, the expanded Φ from Equation 2.5 is put into Equation 2.4 of the Higgs potential:

$$m_H = \sqrt{-2\mu^2} = \sqrt{2\lambda}v.$$

While the VEV has been measured in muon lifetime experiments to a value of 246 GeV [40], the parameters λ and μ^2 cannot be predicted by theoretical arguments. Furthermore, the Higgs mechanism is able to provide fermions with their masses. A gauge-invariant term can be formed by combining right- and left-handed fermion components with the scalar Higgs field. This is ingrained in the Yukawa term $\mathcal{L}_{\mathrm{Yukawa}}$ in Equation 2.1. It takes the form

$$\mathcal{L}_{\mathrm{Yukawa}} = f_e \bar{L}\Phi e_{\mathrm{R}} + f_d \bar{Q}\Phi d_{\mathrm{R}} + f_u \bar{Q}\Phi^c u_{\mathrm{R}} + \text{h.c.} \tag{2.8}$$

$$= f_e \frac{v+H}{\sqrt{2}} (\bar{e}_{\mathrm{R}} e_{\mathrm{L}} + \bar{e}_{\mathrm{L}} e_{\mathrm{R}}) + ... \tag{2.9}$$

for the first generation leptons, and equivalent for the other generations. Here, the $f_{e,d,u}$ are the Yukawa couplings for the fermions and $\Phi^c = i\sigma^2\Phi^*$ is the charge conjugate. It can be seen from Equation 2.8 and Equation 2.9 that particles need both a right- and left-handed component to acquire mass through the Higgs mechanism. Hence, neutrinos do not couple to the Higgs field. The masses for the other fermions can be read off from Equation 2.9 as

$$m_e = \frac{f_e v}{\sqrt{2}}$$
$$m_d = \frac{f_d v}{\sqrt{2}}$$
$$m_u = \frac{f_u v}{\sqrt{2}},$$

and equivalent for the second and third generation. Equation 2.8 furthermore contains terms for the interaction between the Higgs boson and fermions.

2.1.4 Symmetry and symmetry violation in the Standard Model

Analyzing symmetries can give interesting insight into the mechanics of the universe. The first example is the parity symmetry, which is obtained when mirroring all spatial coordinates at the origin. The parity operator P is defined as [41]

$$P\Phi(x,y,z) = \Phi(-x,-y,-z). \tag{2.10}$$

Applying Equation 2.10 twice, should restore the initial state:

$$P^2\Phi(x,y,z) = P\Phi(-x,-y,-z) = \Phi(x,y,z). \tag{2.11}$$

It can be read off from Equation 2.11 that the two eigenvalues of the parity operator are $\lambda_P = \pm 1$.

Table 2.1: Behavior of scalars and vectors under the parity transformation for bosons with missing angular momentum. [41].

State	Spin	Parity
Scalar	0	+1
Pseudoscalar	0	−1
Vector (or polar vector)	1	−1
Pseudovector (or axial vector)	1	+1

An intrinsic parity can be assigned to each particle: if $\lambda_P = +1$, the particle has an even parity, and if $\lambda_P = -1$, it has an odd parity. By definition, fermions with spin 1/2 are assigned $\lambda_P = +1$ as intrinsic parity and anti-fermions get $\lambda_P = -1$. The intrinsic parity of bosons depends on their state and spin $\vec{s}$. They are detailed in Table 2.1 for bosons with missing angular momentum $\vec{l}$. In case the $\vec{l}$ is non-zero, only the total angular momentum $\vec{j}$, which is the vector sum of $\vec{s}$ and $\vec{l}$, is conserved and must be considered.
Using the parities of single particles, P_a and P_b, the parity of particle systems can be defined as [41]

$$\lambda^L_{P_a,P_b} = \lambda_{P_a}\lambda_{P_b}\left(-1\right)^L ,$$

where L is the relative angular momentum between the particles. This implies that if the parity of a process is conserved, the parity of the original particle can be determined from its decay products.
The first parity violation in the SM was found in 1957 in an experiment by C. S. Wu [42], who was investigating angles in the β^--decay of cobalt-60 nuclei. The angles exhibited maximal parity violation, demonstrating that only left-handed particles and right-handed anti-particles participate in the weak interaction.
Another type of symmetry that can be considered is charge conjugation. In electromagnetism, the forces remain unchanged when the signs of all electric charges are flipped. The charge conjugation operator C is introduced in particle physics to generalize this concept. It acts as an operator that transforms a particle into its corresponding anti-particle by reversing all of its charges

$$C\left|p\right\rangle = \left|\bar{p}\right\rangle .$$

Just as with the parity operator in Equation 2.11, applying the charge conjugation operator twice returns the system to its original state. Hence, it also has the eigenvalues $\lambda_C = \pm 1$. Charge parity is a multiplicative quantum number that is conserved in strong and electromagnetic interactions. This allows for predictions of

various decays, e.g. it can explain that the neutral pion π^0, which has $\lambda_C = +1$, can only decay into even numbers of photons (most commonly two photons), because photons have $\lambda_C = -1$.
In contrast, the weak interaction does not conserve charge parity. This is evident when examining neutrinos under charge conjugation. When the C operator is applied to a *left*-handed neutrino, it produces a *left*-handed anti-neutrino, which is not observed in the SM.
The previous example suggests how the SM could regain invariance under the two mentioned symmetries by combining them into CP-symmetry, which is the product of the C and P operators. The P operator would convert a left-handed anti-neutrino state into a right-handed anti-neutrino state, in alignment with the SM predictions. It is expected that the SM remains invariant under such CP transformations.
Particle systems can be classified by their quantum numbers, denoted as J^{PC}, where J is the total angular momentum, P is the intrinsic parity, and C is the intrinsic charge parity. Particles are entitled CP-even if the product $C \cdot P = +1$ and CP-odd otherwise. This classification applies only to particles that are eigenstates of the CP operator. For instance, the SM Higgs boson is expected to have both charge parity and parity of $+1$ while having spin 0, denoted as $J^{PC} = 0^{++}$ [43].
The first evidence of CP-violation in the SM was found in 1964 by J. Cronin and V. Fitch when analyzing decays of the neutral kaon system [44]. It is caused by quark mixing effects.
Invariance in the SM can be restored by adding a third parity, the time reversal with operator T to the system. The CPT theorem [45] specifies that the combined transformation of charge parity, parity and time reversal is an exact symmetry at the fundamental level. To date, no process has been observed that violates the combined CPT symmetry.

2.2 Extensions of the Standard Model

The previous section provided a brief overview of the basics of the SM. However, the SM is not perfect and there are various phenomena that it cannot explain. This section will give a few examples of these phenomena and introduce a possible extension of the SM.
One such example, mentioned earlier in this chapter, are the non-zero masses of neutrinos. According to the SM, neutrinos do not interact with the Higgs field and should therefore be massless, which is not observed in the experiments.
Secondly, the SM includes only three of the four fundamental forces in the universe. While gravity is not significant in particle physics at the energy scales currently observable, it becomes relevant as the energy approaches the *Planck scale*. Fur-

thermore, the SM falls short of providing an explanation for dark matter. Whilst its existence has been proven through experiments analyzing rotational curves of galaxies [46] and experiments with gravitational lenses [47], the nature of dark matter remains unclear. The SM does not contain a suitable candidate to explain the additional matter in the universe, and hence extensions of the SM are needed. The focus of this thesis is on yet another observed deviation from the SM: the anomalous magnetic moment of the muon. The *Dirac equation* predicts that spin-$\frac{1}{2}$ particles have a magnetic moment of $g = 2$ on tree level. Small deviations from this value are introduced by including loop corrections from higher-order Feynman diagrams. They are summarized in the *anomalous magnetic moment*

$$a = \frac{g-2}{2},$$

in which g represents the real magnetic moment that can be measured or calculated. Both theory and experiment can provide highly accurate statements about this value for the muon:

$$\begin{aligned} a_\mu^{\text{exp}} &= (116{,}592{,}059 \pm 22) \times 10^{-11} \text{ [9]} \\ a_\mu^{\text{SM}} &= (116{,}591{,}810 \pm 43) \times 10^{-11} \text{ [48].} \end{aligned}$$

Both values differ significantly, showing a deviation slightly above $5\,\sigma$

$$\Delta a_\mu = a_\mu^{\text{exp}} - a_\mu^{\text{SM}} = (249 \pm 48) \times 10^{-11}.$$

While the deviation is significant, it has to be taken with care. In recent years, the theoretical situation became unclear due to contradictory calculations with different methods for the hadronic contributions [49–52]. Until the calculations come to an agreement, the focus should not be on the exact value of $5\,\sigma$. Nevertheless, the apparent discrepancy motivates a careful evaluation and the search for physics beyond the SM. The observed deviation could be explained within a flavor-aligned 2HDM [10], which will be lined out in the next sections.

2.2.1 The two-Higgs-doublet model

The 2HDM [53] provides a mathematically fairly easy extension to the Higgs sector of the SM. It adds a second Higgs doublet alongside the one Higgs doublet from the SM

$$\Phi_1 = \begin{pmatrix} \phi_1^+ \\ \phi_1^0 \end{pmatrix}, \Phi_2 = \begin{pmatrix} \phi_2^0 \\ \phi_2^- \end{pmatrix}.$$

Here, Φ_1 has the positive hypercharge $Y_{\Phi_1} = +1$, and Φ_2 the negative hypercharge $Y_{\Phi_2} = -1$. The Higgs potential $V(\Phi_1, \Phi_2)$ takes on the more complex form

$$\begin{aligned} V(\Phi_1, \Phi_2) = {} & m_{11}^2 \Phi_1^\dagger \Phi_1 + m_{22}^2 \Phi_2^\dagger \Phi_2 - \left(m_{12}^2 \Phi_1^\dagger \Phi_2 + h.c. \right) \\ & + \lambda_1 \left(\Phi_1^\dagger \Phi_1 \right)^2 + \lambda_2 \left(\Phi_2^\dagger \Phi_2 \right)^2 + \lambda_3 \left(\Phi_1^\dagger \Phi_1 \Phi_2^\dagger \Phi_2 \right) - \lambda_4 \left(\Phi_1^\dagger \Phi_2 \right) \left(\Phi_2^\dagger \Phi_1 \right) \\ & + \frac{1}{2} \left[\lambda_5 (\Phi_1^\dagger \Phi_2)^2 + h.c. \right] + \left[\left(\lambda_6 \Phi_1^\dagger \Phi_1 + \lambda_7 \Phi_2^\dagger \Phi_2 \right) \Phi_1^\dagger \Phi_2 + h.c. \right], \end{aligned}$$

where the λ_i are a set of parameters and the m_{kl}^2 are mass terms. CP violation can occur with λ_5 being non-zero and real, if either of m_{12}^2, λ_6 and λ_7 is non-zero.
In the minimum of the Higgs potential, the two Higgs doublets acquire the VEVs v_1 and v_2. The ratio between them is given by

$$\tan \beta = \frac{v_2}{v_1}.$$

It is convenient to rotate the doublets by an angle α to the Higgs basis [54], in order to obtain one doublet with the SM VEV of

$$v = \sqrt{v_1^2 + v_2^2},$$

while the other doublet has a VEV of zero. This second doublet gives rise to the physical CP-odd and neutral Higgs boson A as well as the two charged Higgs bosons $H^\pm$. The two neutral CP-even Higgs bosons h and H arise from mixtures between the two doublets with the mixing angle $(\alpha - \beta)$. The corresponding masses of the Higgs bosons are $m_{h,A,H,H^\pm}$. The lighter h is here identified with the SM Higgs boson.

2.2.2 The flavor-aligned two-Higgs-doublet model

Within this thesis, a special case of the 2HDM is used: the flavor-aligned 2HDM [10]. It aligns the Yukawa couplings between the fermion and Higgs fields according to the flavor. The presence of a second Higgs doublet subsequently introduces two Yukawa matrices. This setup can cause flavor-changing neutral currents (FCNCs) for right-handed fermion fields, which are not observed in nature [40]. The 2HDM addresses this by aligning the two scalar doublets in the flavor space of the Yukawa couplings. As a result, the doublet in the Higgs basis that resembles SM acquires SM-like couplings by design, while the other doublet has Yukawa couplings proportional to these, with the scaling factors $\zeta_{\mathrm{u,d}}$ for up- and down-type quarks and ζ_{l} for charged

Table 2.2: Yukawa parameters ζ_{f} in the usual model types of the general aligned 2HDM [10].

Model	ζ_{u}	ζ_{d}	ζ_{l}
Type I	$\cot\beta$	$\cot\beta$	$\cot\beta$
Type II	$\cot\beta$	$-\tan\beta$	$-\tan\beta$
Type X	$\cot\beta$	$\cot\beta$	$-\tan\beta$
Type Y	$\cot\beta$	$-\tan\beta$	$\cot\beta$

leptons. The Yukawa Lagrangian of the Higgs mass eigenstates takes on the form

$$\begin{aligned}\mathcal{L} \;&=\; -\frac{\sqrt{2}}{v}H^{\pm}\Big(\bar{u}\left[\zeta_d V_{\mathrm{CKM}} M_d P_{\mathrm{R}} - \zeta_u M_u V_{\mathrm{CKM}} P_{\mathrm{L}}\right] d + \zeta_l \bar{\nu} M_l V_{\mathrm{CKM}} P_{\mathrm{L}} l\Big) \\ &\quad - \sum_{S=h,H,A}\sum_{f=u,d,l} S\bar{f} y_f^S P_{\mathrm{R}} f + \mathrm{h.c.},\end{aligned} \tag{2.12}$$

with $P_{\mathrm{R,L}} = \frac{1}{2}(1 \pm \gamma_5)$ and the Cabbibo–Kobayashi–Maskawa (CKM) matrix V_{CKM}. The diagonal 3×3 mass matrices, M_f, enter the Yukawa coupling matrices defined as:

$$y_f^S = \frac{Y_f^S}{v} M_f \tag{2.13}$$

with

$$\begin{aligned} Y_f^h &= \sin(\beta - \alpha) + \cos(\beta - \alpha)\zeta_f, \\ Y_f^H &= \cos(\beta - \alpha) - \sin(\beta - \alpha)\zeta_f, \\ Y_{d,l}^A &= i\zeta_{d,l}, \\ Y_u^A &= -i\zeta_u. \end{aligned} \tag{2.14}$$

The flavor-aligned 2HDM includes the four standard 2HDM models, named Type I, II, X, and Y. In these models, tree-level FCNCs are avoided by following the Paschos–Glashow–Weinberg theorem [55, 56] and by imposing an additional Z_2 symmetry [57]. In Type I, all fermions are coupling to Φ_1. In Type II, down-type quarks and charged leptons couple to Φ_1 and up-type quarks to Φ_2. In Type X, charged leptons couple to Φ_1 and all quarks couple to Φ_2, while in Type Y, up-type quarks couple to Φ_1 and charged leptons and down-type quarks couple to Φ_2. The connections of the ζ_f parameters and the couplings of the Type I, II, X and Y models are summarized in Table 2.2.
All of these usual models have trouble explaining the deviation in a_μ between

theory and experiment for different reasons. Following the analysis in Ref. [58], all important contributions to a_μ scale with either $|\zeta_\mathrm{l}|$, ζ_l^2 or $-\zeta_\mathrm{l}\zeta_\mathrm{u}$. To achieve a significant size of the contributions, the coupling parameter values need to be close to their maximum not yet excluded value. This is around $|\zeta_\mathrm{l}| \approx 50$ and $|\zeta_\mathrm{u}| \approx 0.5$. With this information, the types II and X are directly disfavored, as they cannot be simultaneously large ($\zeta_\mathrm{u} = \cot\beta = \frac{1}{\tan\beta} = -\frac{1}{\zeta_\mathrm{l}}$). Only a tiny parameter space in the type X still has the potential to explain the deviation [18]. In the type Y, the product $|\zeta_\mathrm{u}\zeta_\mathrm{d}| = \cot\beta\tan\beta = 1$ can never be small, which is constraining the parameters heavily by data from $b \to s\gamma$ measurements [59]. While this product could be small within the type I model, this would imply a simultaneously small ζ_l, which then could not create a large enough contribution to a_μ to explain its deviation.
As none of the usual models can explain the observed deviation in a_μ, the general flavor-aligned 2HDM with its independent coupling strengths is needed [18].

2.2.3 The CP-odd Higgs boson in the general flavor-aligned 2HDM

The possible contributions to a_μ within the flavor-aligned 2HDM are calculated in detail in Ref. [18] and shown in Figure 2.3(a). For each point, the maximal possible values for ζ_l and ζ_u are used. Significant contributions are only possible for A boson masses below the mass of the SM Higgs boson in the range of 5 to 105 GeV. Within this range, a big part of the deviation in a_μ between theory and experiments could be explained. Hence, a direct search for the A boson is an excellent probe of this model.
The masses of the other additional Higgs bosons H and $H^\pm$ have only a minor influence on the contributions. Particularly important for the contributions of the additional A boson to a_μ are fermionic two-loop processes of the Barr–Zee type [63], which involve τ-lepton and top-quark loops that couple to the intermediate CP-odd Higgs boson and the external photon [62, 64–67]. The corresponding Feynman diagram is shown in Figure 2.3(b). While the coupling of the A boson to leptons and up-type quarks should be maximized, the coupling to down-type quarks can be set to zero, because it has a negligible effect on a_μ.
From these coupling parameter values, the production and decay modes of the A boson for a search at the LHC can be derived. The production of a CP-odd Higgs boson can happen via gluon–gluon fusion and a quark loop, similar to the SM Higgs boson. As the coupling to up-type quarks is enhanced and the coupling to down-type quarks is insignificant, the production mode is assumed to be exclusively via top-quark loops.
On the decay side, the large couplings to leptons are dominating. With the vanishing

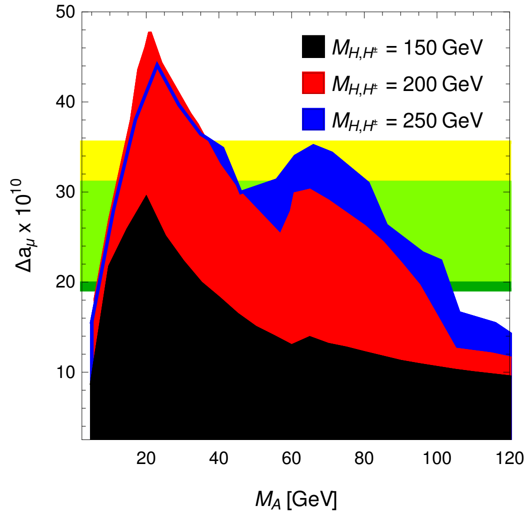

(a)

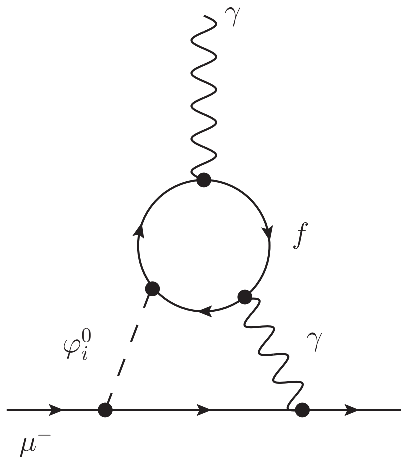

(b)

Figure 2.3: Maximal possible contribution to a_μ within the flavor-aligned 2HDM (a) for different masses of the heavy Higgs bosons H and $H^\pm$ (shown in black, red and blue) in dependence of the mass of the CP-odd A boson [18]. The yellow band shows the $1\,\sigma$ band around the Brookhaven National Laboratory (BNL) measured value [60], the green band the experimental world average from 2021 [61] and the light green band the overlap between the two regions. The main contribution comes from fermionic two-loop Feynman diagrams of the Barr–Zee type (b) with τ-lepton and top-quark loops [62]. The Higgs boson is here denoted with φ_i^0.

coupling to down-type quarks and the large lepton couplings, the decay is purely into pairs of leptons. Due to the much larger mass of the τ-lepton compared to the other leptons, these will essentially always be τ-lepton pairs. Figure 2.4 shows the Feynman diagram for this process. It also highlights how the coupling parameter ζ_u enters the production rate of A bosons, which gives a handle to measure this parameter.

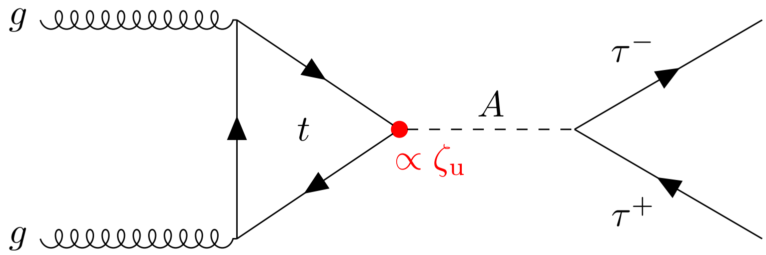

Figure 2.4: Leading-order Feynman diagram of the process $gg \to A \to \tau^+\tau^-$ within the flavor-aligned 2HDM with enhanced A boson couplings to leptons and up-type quarks, and suppressed couplings to down-type quarks. The red vertex represents the coupling of up-type quarks to the A boson and scales with ζ_u.

2.2.4 Parameter constraints

Although large values for ζ_l and ζ_u are ideal for explaining the deviation in a_μ, these parameters are limited by various experimental constraints. This section provides a brief overview of the relevant constraints for this analysis, following the detailed explanations from Ref. [58]. Since the flavor-aligned 2HDM is an extension of the SM, it must be consistent with existing measurements. This is particularly important for new processes that have the same initial and final states as those already present in the SM. When adding new processes, their contributions must remain within the uncertainty bands of the existing measurements to maintain consistency.

The first parameter to examine is the lepton coupling parameter ζ_l, or more

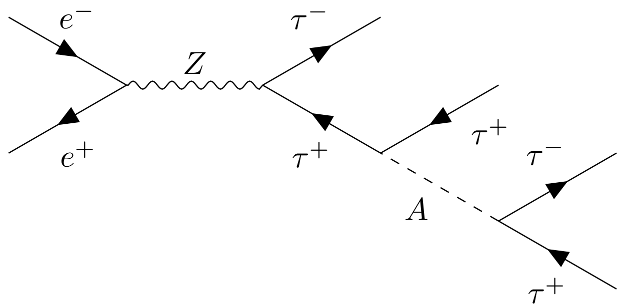

Figure 2.5: Feynman diagram for the Large Electron–Position Collider (LEP) process $ee \to \tau\tau(A) \to \tau\tau(\tau\tau)$

specifically $|\zeta_l|$ as the sign in front of the parameter does not matter too much. In higher mass regions of the A boson, the upper limits on ζ_l are derived from τ-lepton decays in the mode $\tau \to \mu\nu_\tau\bar{\nu}_\mu$ and from leptonic Z boson decays. Additional

diagrams from the 2HDM include exchanges or loop contributions involving A or $H^{\pm}$. If ζ_l is too large, it would overly enhance these contributions, leading to inconsistencies with observed measurements [58].
For lower masses of m_A, particularly in the range from 5 to 20 GeV, the process $ee \to \tau\tau(A) \to \tau\tau(\tau\tau)$ takes the leading role for determining the upper limit on $|\zeta_l|$. This process was studied by the DELPHI collaboration at LEP [68]. In this

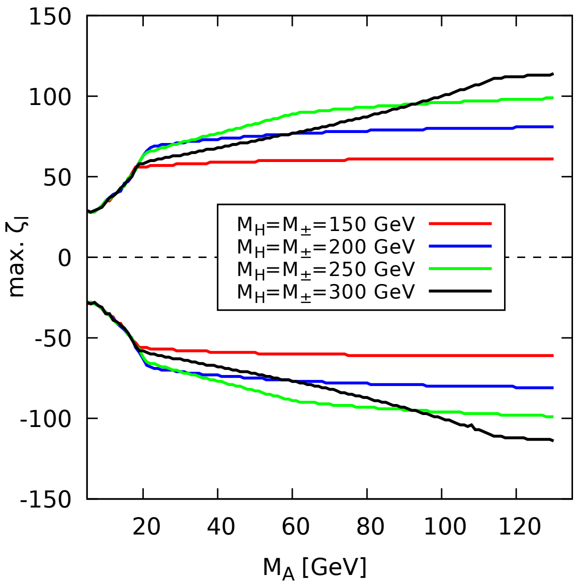

Figure 2.6: Experimental constraints on the lepton Yukawa coupling parameter ζ_l as a function of the CP-odd Higgs boson mass [58]. The constraints are determined from τ-lepton and Z boson decays and calculated for different masses of the heavy Higgs bosons H and $H^{\pm}$ as indicated.

setup, an electron–positron pair collides and annihilates into a Z boson, which then decays into two τ-leptons. One of these τ-leptons creates an A boson in resonance, which subsequently decays into another pair of τ-leptons, resulting in a final state with four τ-leptons. Figure 2.5 shows the Feynman diagram of this process. The combined constraints on $|\zeta_l|$ for various masses of the heavy Higgs bosons are depicted in Figure 2.6. Generally, the upper limit ranges between $|\zeta_l| < 40$ and $|\zeta_l| < 100$, with a sharp decrease for m_A below 20 GeV.
After examining the limits for the lepton coupling, the coupling to up-type quarks is scrutinized. For the here relevant scenario where $m_A < m_h$ and ζ_l is large, constraints on this parameter come from both B-physics and LHC collider experiments. In B-physics, the main constraints arise from the two processes $b \to s\gamma$ and $B_s \to \mu^+\mu^-$. The Feynman diagrams for these processes are shown in Figure 2.7.

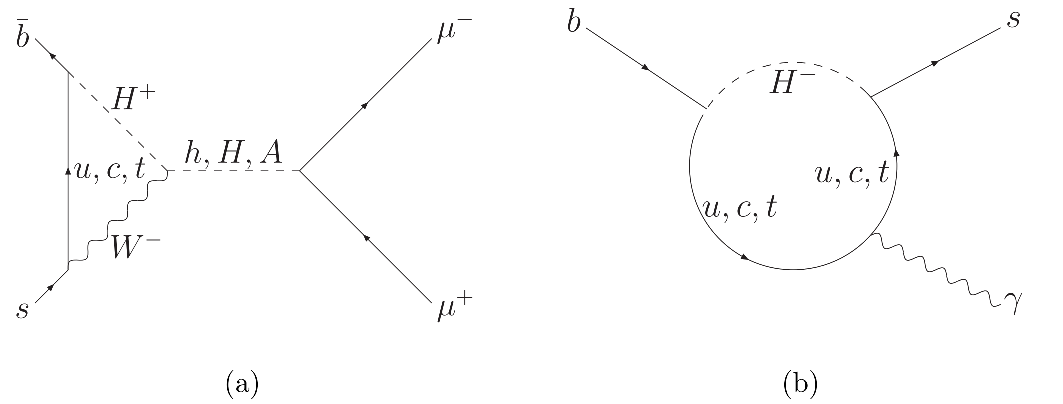

Figure 2.7: Feynman diagrams for the processes (a) $B_s \to \mu^+\mu^-$ and (b) $b \to s\gamma$. Both processes are dependent on the Yukawa couplings for up- and down-type quarks as well as leptons [58].

These diagrams show that the relevant processes depend on all Yukawa parameters ζ_f as well as the masses of the Higgs bosons m_A and $m_{H^\pm}$. Individually, these processes would allow very large values of $\zeta_\mathrm{u} \gg 1$ by fine-tuning the couplings ζ_d and ζ_u. However, when combining the results from both processes, a general upper limit of $\zeta_\mathrm{u} < 0.3$ to $\zeta_\mathrm{u} < 0.6$ is obtained, depending mostly on m_A, and slightly on $m_{H^\pm}$ and ζ_l [58]. The calculated limits for each value of m_A and different values of m_H and $m_{H^\pm}$ are shown as solid lines in Figure 2.8.
The plots also show the limits from LHC Higgs physics, which are obtained through several processes. For masses m_A greater than the mass of the Z boson, the process $pp \to A \to \tau\tau$ imposes a general upper limit of approximately $\zeta_\mathrm{u} < 0.2$ [69], as the production of neutral Higgs bosons via top-quark loop depends directly on ζ_u and final states with two τ-leptons are well measured.
For lower m_A, the limits are determined from the process $pp \to H \to \tau\tau$, which was previously investigated by CMS in Ref. [69]. These limits are derived from the fact that the production rate of heavy neutral Higgs bosons depends on ζ_u, and precise measurements have been carried out for the final state of two τ-leptons. In Figure 2.8, the contribution of the LHC data to the overall constraints on ζ_u is shown with dashed lines.
The spikes in some plots occur because, in cases where $m_A < m_Z$ and $m_A < \frac{m_H}{2}$, the heavy Higgs boson H can decay into a pair of CP-odd Higgs bosons: $H \to AA$. This slightly reduces the constraints on ζ_u from the production side. The drop in the limits below half of the SM Higgs mass $m_A < \frac{m_h}{2}$ is due to perturbativity restricting the triple Higgs coupling [58].

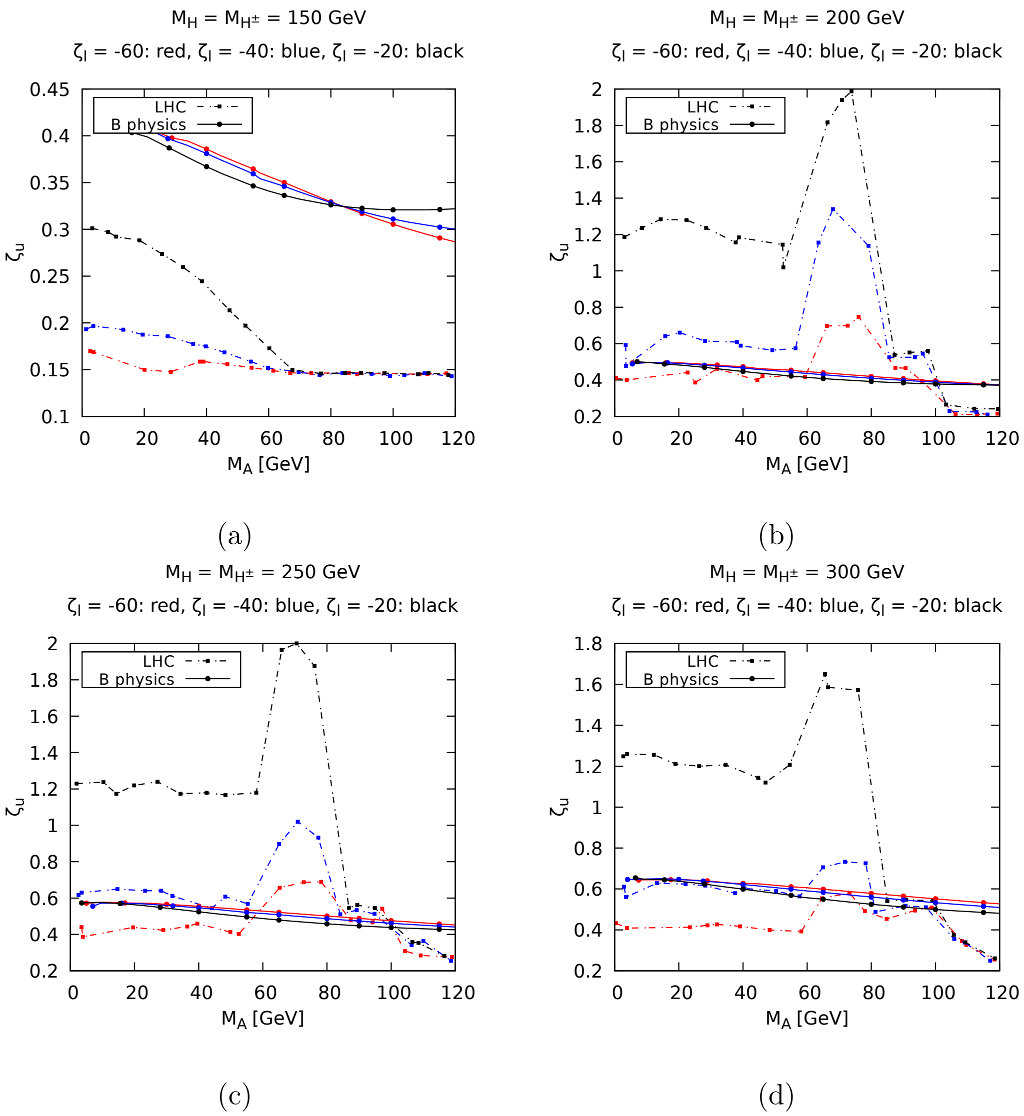

Figure 2.8: Maximum allowed values for the up-type quark coupling parameter ζ_u, in dependence of the CP-odd Higgs boson mass for the masses of the heavy Higgs boson of (a) 150 GeV, (b) 200 GeV, (c) 250 GeV and (d) 300 GeV [58]. The solid lines represent the limits obtained from B-physics, and the dashed lines give the constraints gathered from LHC collider experiments. They were both calculated for different values of the lepton Yukawa parameter ζ_l, shown in red, blue and black, as indicated.

3 The ATLAS experiment at the LHC

The ATLAS detector is one of the two large multi-purpose detectors at the LHC. The LHC is introduced in Section 3.1, followed by a description of the parts of the ATLAS detector in Section 3.2, with its trigger system being described in Section 3.3. The last part of this chapter explains the details of data-taking (Section 3.4), Monte Carlo (MC) simulation (Section 3.5) and the simulation of the detector response (Section 3.6).

3.1 The Large Hadron Collider

The LHC is a two-ring particle accelerator and collider located at CERN in Geneva. It reuses the 26.7 km long tunnel that hosted the LEP [70] until 2000. In the two rings, proton or ion beams can be accelerated in opposite directions. To keep the charged particle beams on track, a total of 1232 superconducting dipole magnets is used. They are cooled down to 1.9 K with superfluid helium which enables the creation of magnetic fields of up to 8.3 T strength. In addition to this, quadrupole and higher order multi-pole magnets are used to focus the particle beams and to counter dispersion.

The LHC is designed to deliver an energy of 7 TeV for each proton beam. As of 2024, the maximum center-of-mass energy reached is $\sqrt{s} = 13.6\,\text{TeV}$ in 2022. For this thesis, the center-of-mass energy used is $\sqrt{s} = 13\,\text{TeV}$. To reach these high energies, a series of smaller accelerators is put in place before the particles enter the LHC. The proton beams are created in a linear accelerator (LINAC2 for Run 2 and LINAC4 for Run 3). They are then accelerated up to an energy of 450 GeV in the following injector chain consisting of Proton Synchrotron Booster (BOOSTER), Proton Synchrotron (PS) and Super Proton Synchrotron (SPS). The synchrotron principle with radio frequency cavities is used for the acceleration. A schematic overview of the CERN accelerator complex is shown in Figure 3.1.

Each beam contains the protons packed in up to 3564 bunches. The bunches from the two beams are brought to collision at 4 interaction points (IPs). At each of the IPs, detectors are located to measure and analyze the particle collisions. The two general-purpose detectors ATLAS [3] and CMS [4] are placed at IPs on opposite sides of the LHC ring. The remaining two IPs are filled with the ALICE [71] and LHCb [72] detectors. The former is specialized in analyzing ion beam collisions while the latter is designed to study B-physics.

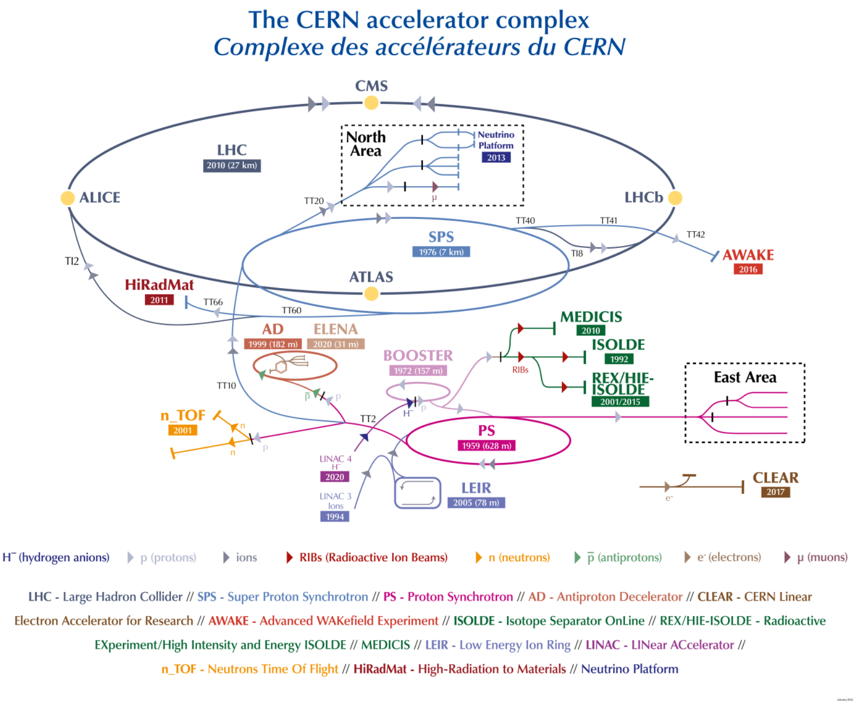

Figure 3.1: The CERN accelerator complex in 2022. In the injection chain for the LHC during Run 2 operation the accelerators LINAC2 (now replaced by LINAC4 for Run 3), BOOSTER, PS, and SPS were used [73].

A very important quantity for running a particle collider is the machine luminosity L. It directly influences the mean number of events N_{events} that are generated every second:

$$N_{\text{events}} = L \cdot \sigma_{\text{event}},$$

with σ_{event} being the cross-section of the process under study. The machine luminosity only depends on a number of beam parameters:

$$L = \frac{N_b^2 n_b f_{\text{rev}} \gamma_r}{4\pi \epsilon_n \beta *} F.$$

The relevant parameters are the number of particles per bunch N_b, the number of bunches per beam n_b, the revolution frequency f_{rev}, the relativistic gamma factor γ_r, the normalized transverse beam emittance ϵ_n, the beta function at the collision point $\beta *$, and the geometric luminosity reduction factor F which depends on the crossing angle between the two beams. Each beam consists of around 2500 proton bunches [5] filled with approximately 1.2×10^{11} protons [74] each (in LHC Run 2).

3.2 The ATLAS detector

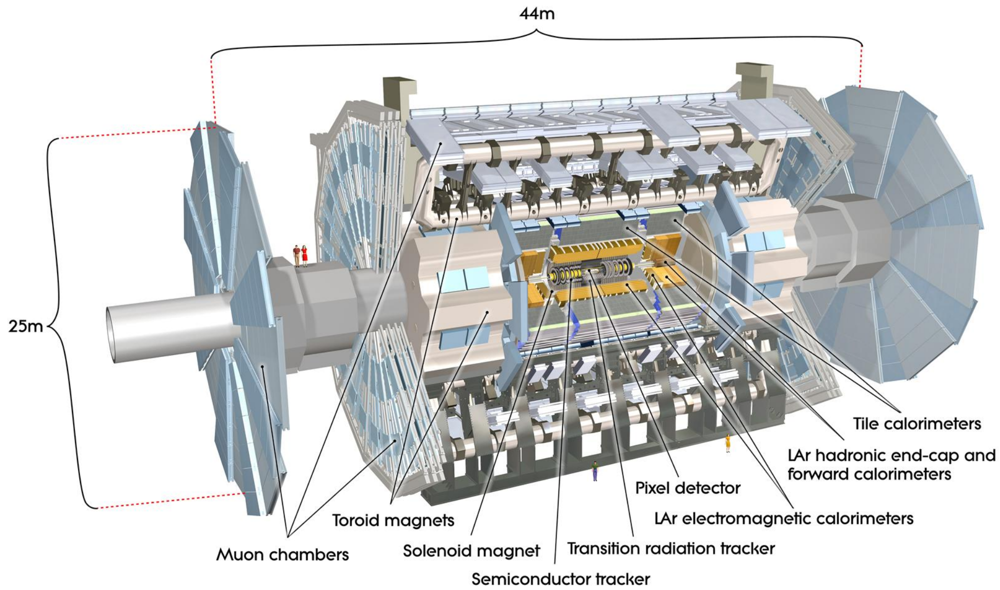

Figure 3.2: Cutaway view of the entire ATLAS detector [3].

The ATLAS detector is one of the two large multi-purpose experiments at the LHC. It has the shape of a huge cylinder with a length of 44 m and a diameter of 25 m with an overall weight of around 7000 t. The ATLAS detector is a high-tech tool used to probe the universe for new physics and provide precision measurements of the SM predictions. Its outstanding achievement is the discovery of the Higgs boson in 2012 [1]. To achieve performance at such a high standard, multiple layers of different sub-detectors are arranged around the IP in the middle of the cylinder. These can be seen in Figure 3.2 and will be explained further in the following sections.

3.2.1 The ATLAS coordinate system

As a first step towards understanding the ATLAS detector, its coordinate system has to be explained. The nominal IP forms the origin of a right-handed Cartesian

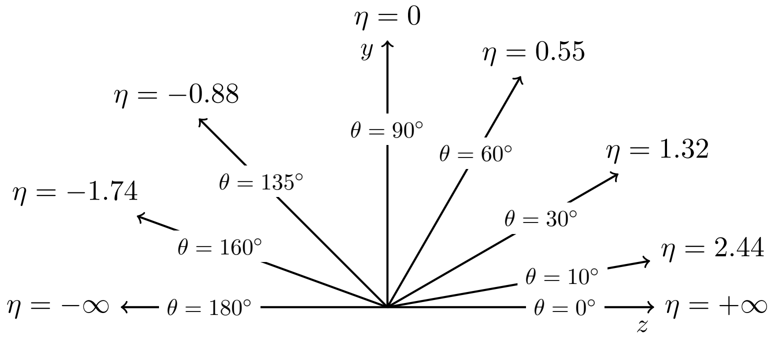

Figure 3.3: Illustration of the dependency of the pseudorapidity η on the polar angle θ.

coordinate system. The direction of the beam line forms the z-axis, while the positive x-axis points towards the center of the LHC and the positive y-axis points upwards.
Of particular importance is the x-y-plane because it is transverse to the beam axis. Only in this plane momentum conservation can be applied, because the exact momenta of the colliding partons inside the protons along the beam line are a priori unknown. Therefore, it is useful to define transverse components for vectors, e.g. the transverse momentum

$$p_{\mathrm{T}} = \sqrt{p_x^2 + p_y^2}.$$

For multiple applications, spherical coordinates (r, θ, ϕ) are used with the radius $r = \sqrt{x^2 + y^2 + z^2}$. Here, the polar angle θ is the angle from the beam axis ($\cos\theta = \frac{z}{r}$), while the azimuthal angle ϕ is measured around the z-axis ($\tan\phi = \frac{y}{x}$). However, in most cases, the polar angle θ is replaced by the pseudorapidity η, which is defined by:

$$\eta = \frac{1}{2}\ln\frac{|\boldsymbol{p}| + p_z}{|\boldsymbol{p}| - p_z} = -\ln\tan\frac{\theta}{2}$$

with the absolute value of the three-momentum $|\boldsymbol{p}|$. In the case of massless particles or particles with negligible mass, the momentum can be approximated by $|\boldsymbol{p}| \approx E$. Hence, for highly relativistic particles, the pseudorapidity approaches the rapidity $y = \frac{1}{2}\ln\frac{E+p_z}{E-p_z}$. Choosing η over θ has two main advantages: firstly, particle colliders produce particles in roughly constant amounts as a function of η. The second advantage is that differences in η of two particles $\Delta\eta = \eta_2 - \eta_1$ are Lorentz-invariant under boosts along the z-axis. Consequently, measures in $\Delta\eta$ are invariant under the different energy fractions of the colliding partons in the proton–proton scattering. A visualization of the relation between the pseudorapidity and the polar angle can

be seen in Figure 3.3 [3].
Using the pseudorapidity, the angular difference between two locations in the ATLAS detector can be defined [3]:

$$\Delta R = \sqrt{(\Delta\phi)^2 + (\Delta\eta)^2} = \sqrt{(\phi_1 - \phi_2)^2 + (\eta_1 - \eta_2)^2}.$$

3.2.2 Inner Detector

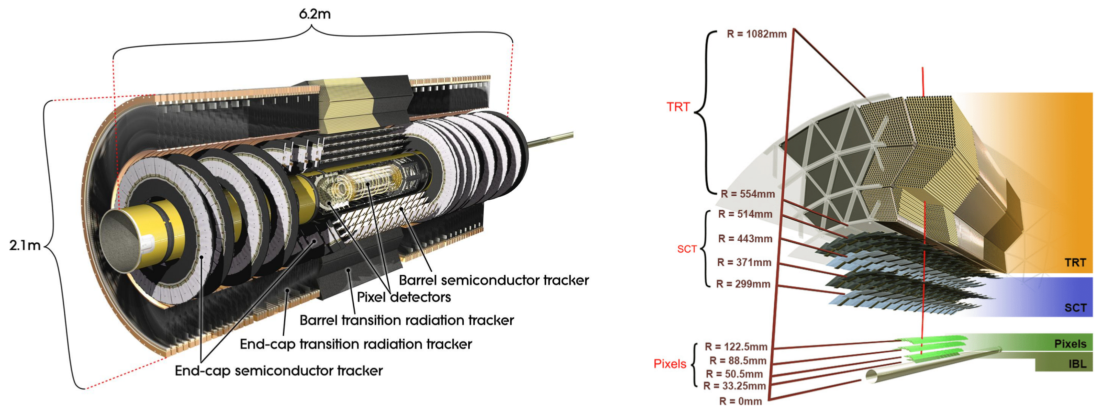

(a) (b)

Figure 3.4: Cutaway view of the ATLAS inner detector showing the overall dimension and sub-detector placement (a) and the transverse plane in the barrel region (b) [3, 75].

The detector system closest to the IP is the Inner Detector (ID) [76, 77]. Its purpose is to precisely measure the trajectories of electrically-charged particles emerging from the proton–proton collisions. It operates in a range of $|\eta| < 2.5$ and consists of three sub-detectors, which are displayed in Figure 3.4: pixel detectors, Semiconductor Trackers (SCTs) and Transition Radiation Trackers (TRTs). Each of them is segmented into a cylindrical part for the barrel region and disks for the end-caps (high η regions, i.e. angles close to the beam axis). In total, the ID measures 6.2 m in length and 2.1 m in diameter. A homogeneous magnetic field along the z-axis of 2 T strength, produced by the central solenoid, encloses the ID. It bends the flight path of charged particles due to the Lorentz force, which can be used to calculate the electrical charge sign and the momentum of particles. Additionally, the ID is used to map particle tracks to decay vertices, which is important to understand particle decays [3].

The pixel detector

To precisely measure the particle's tracks, it is crucial to have a high detection granularity close to the IP. The pixel detector [78, 79] delivers that with 1744 identical pixel sensors with 47,232 pixels each. They are arranged in three layers and amount to a total of about 80 million readout channels. The pixels are silicon-based semiconductor sensors which are doped and operated under a bias voltage of up to $V_{\text{bias}} \approx -600\,\text{V}$ to create a depletion region between the doped sides. Charged particles passing through the pixels create electron–hole pairs which are drained by the electrodes and produce a current that is read out. The pixel layers in the barrel region are concentric cylinders around the beam axis with a resolution of $10\,\mu\text{m}$ in $(r-\phi)$ and $115\,\mu\text{m}$ in z. The end-caps consist of 3 layers of disks with $10\,\mu\text{m}$ resolution in $(r-\phi)$ and $115\,\mu\text{m}$ in r [3].
A fourth layer, the Insertable B-Layer (IBL), was added during the LS2 in 2013/14 alongside the new and thinner beam pipe. It incorporates two different sensor designs: planar sensors, similar to the already existing layers, and new 3D design sensors. Overall, the IBL adds about 12 million readout channels to the pixel detector. It provides improved track reconstruction efficiency, which gives rise to significantly improved vertex reconstruction and b-tagging performance while also providing better radiation robustness [80].

The Semiconductor Tracker

Adjacent to the pixel detector is the SCT, which is similarly using doped silicon as active material [81, 82]. It comprises 4088 modules in four double layers of silicon micro-strips in the barrel region and nine disk layers in each end-cap. This amounts to a total of about 6.3 million readout channels. The average strip pitch is $80\,\mu\text{m}$ in both regions, resulting in a resolution of $17\,\mu\text{m}$ in $(r-\phi)$ and $580\,\mu\text{m}$ in z (r) for the barrel (end-cap) region. With a coverage of $|\eta| < 2.5$, it covers the same pseudorapidity region as the pixel detector [3].

The Transition Radiation Tracker

The outermost part of the ID is formed by the TRT [83]. It comprises around 300,000 straw tubes with a diameter of 4 mm containing a $31\,\mu\text{m}$ thick gold-plated tungsten wire. The tubes are arranged in 73 (160) straw planes for the barrel (end-cap) region with a coverage of $|\eta| < 2.0$. In the barrel the straws are 144 cm long and oriented parallel to the beam axis, while the end-cap straws are only 37 cm long and aligned perpendicular to the beam axis. The TRT can only measure $r-\phi$ information, for which its resolution is $130\,\mu\text{m}$.

The tubes are filled with a gas mixture (70 % Xe, 27 % CO_2 and 3 % O_2) and are operated with an electric potential of around -1.5 kV. After leaks were discovered at the end of Run 1, the xenon in the gas mixture in areas with high gas leakage was replaced by argon [84]. Charged particles crossing the straws ionize the gas along the particle trajectory. The resulting electrons drift towards the anode wire, creating a signal which is amplified and read out.
Furthermore, the TRT provides excellent particle identification. The gaps between the straws are filled with polymer fibers and foils of varying refraction indices. When charged particles pass through the interface of the polymer, they emit transition radiation (TR) in form of low-energy photons. These are detected as well, producing an increased signal yield compared to the original particle. As the TR is dependent on the γ-factor, the amount of produced TR varies significantly between relativistic electrons[1] and pions of the same momentum. Hence, additional electron identification can be provided by a high number of TRT hits [3].

3.2.3 The calorimeter system

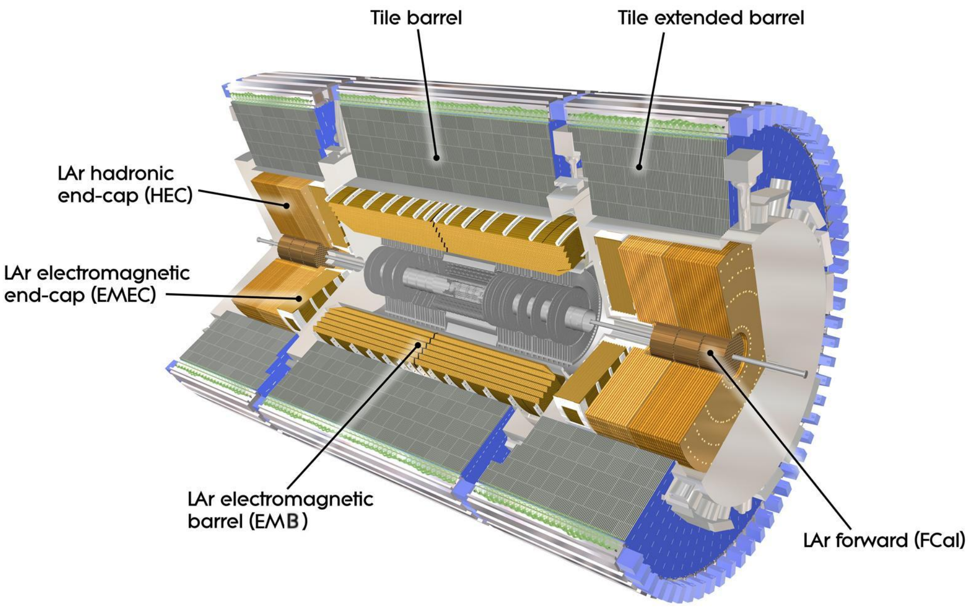

Figure 3.5: Cutaway view of the ATLAS calorimeter system [3].

The calorimeter system encloses the solenoid magnet that surround the ID. Its main purpose is to precisely measure the energies of the particles from the collisions.

[1] Throughout this thesis, the term 'electron' is used to refer to both electrons and positrons

Additionally, the punch-through of particles other than muon to the Muon Spectrometer (MS) is reduced and shapes of particle showers are measured. This can all be achieved by completely absorbing the particles and determining the energy deposited in the active detector material. The calorimeter system is separated into two parts, the Electromagnetic Calorimeter (ECAL) which is optimized to absorb electromagnetically interacting particles and the Hadronic Calorimeter (HCAL) which is the counterpart for hadronically interacting particles. In addition, the Forward Calorimeters (FCals) are placed on both sides of the detector close to the beam line to enable jet measurements in forward regions up to $|\eta| < 4.9$. A schematic overview of the calorimeters is given in Figure 3.5 and the parts will be described in more detail in the following [3].

LAr calorimeters

The inner part of the calorimeter system is formed by the liquid argon (LAr) electromagnetic (EM) calorimeters [85]. The LAr EM calorimeters are sampling

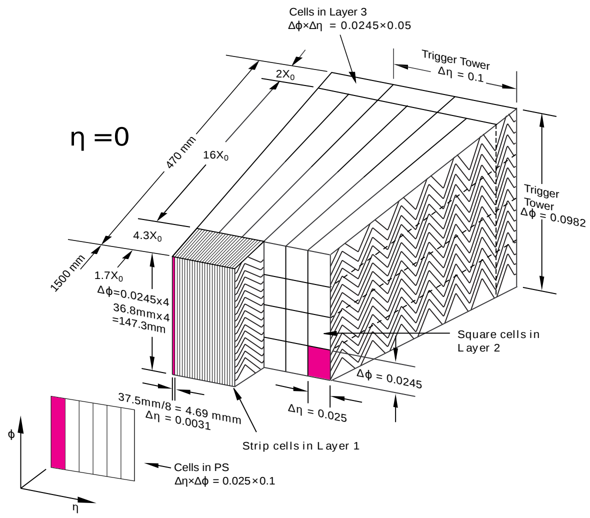

(a)

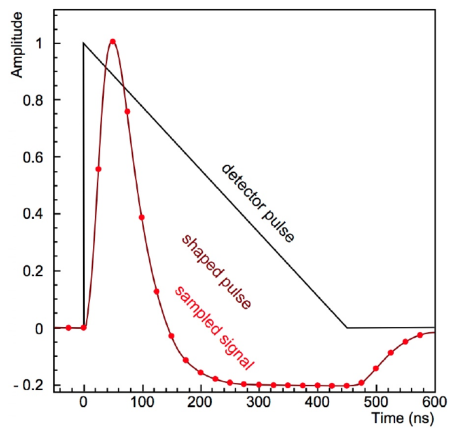

(b)

Figure 3.6: Sketch of a LAr barrel module (a) and the LAr pulse shape (b). The detector pulse (black line) and shaped pulse (red line) are shown together with the sampled signal (red points along the shaped pulse) [85].

calorimeters that use lead plates as absorber material and LAr as active detector material in the interjacent gaps. LAr was chosen as the active material thanks to its radiation hardness and linear response. The lead plates are supplemented by stainless-steel sheets for stability. The LAr EM calorimeters are split into the Electromagnetic Barrel (EMB) and the Electromagnetic End-Caps (EMECs) that cover a range of $|\eta| < 1.52$ and $1.375 < |\eta| < 3.2$, respectively. The overlap is intended to guarantee a smooth transition. The EMB consists of two wheels with 16 modules each and the EMEC is formed of eight wedges per end-cap. Both are segmented into three longitudinal layers with an accordion geometry that allows for perfect azimuthal coverage with an exception being the 6 mm gap at $z = 0$ for technical reasons. A sketch of an EMB module showing the accordion structure is displayed in Figure 3.6(a). In addition, a presampler (PS) is set up as a fourth layer in $|\eta| < 1.8$ to measure the energy loss upstream of the calorimeter. The main fraction of energy from the EM shower is deposited in the largest middle layer with shower tails expanding into the back layer. In combination, the layers have more than 22 interactions lengths for electromagnetic showers, while they have only 1.5 nuclear radiation lengths, hence they are capable of stopping almost all electromagnetically interacting particles while being almost transparent for hadronically interacting particles. Overall, the LAr EM calorimeters amount to 173,312 readout channels, which are listed in detail and with the corresponding granularity in Table 3.1 [3].

In the end-caps, two more calorimeters are placed using the LAr technology but featuring different designs. The hadronic end-cap calorimeter (HEC) uses copper as absorber material arranged in a sandwich structure over four layers and covers $1.5 < |\eta| < 3.2$. A design with two wheels per end-cap was chosen of which each holds 32 wedge shaped modules, providing 5632 channels in total.

In the forward region of $3.1 < |\eta| < 4.9$, the FCal serves as both an EM and hadronic calorimeter. It uses a design with cylindrical electrodes parallel to the beam line arranged in an absorber matrix. Tungsten is chosen for the second and third layer of the FCal in order to cope with the high particle flux in the forward region. However, tungsten produces too narrow EM showers, hence copper is used for the first layer. The FCal consists of a total of 3524 readout channels in three modules per end-cap and provides approximately 10 nuclear interaction lengths [3].

Electrons and photons entering the EM calorimeter lose energy through interaction with the absorber via bremsstrahlung or electron–positron pair production, respectively. The emerging particles interact in the same way, and thus an EM shower is formed. The LAr in the gaps is ionized by the charged shower particles, creating ions and electrons. These drift towards the electrodes due to the high electric field created by around 2 kV high voltage. There, the charges are collected by the copper readout electrodes. The resulting signal is amplified and shaped by the Front-end boards (FEBs) which can operate in three gain levels. It is then sampled at 40 MHz and stored in memory until a trigger decision was made. For triggered events, the optimal gain (low, medium or high) is chosen and the four samples around the pulse peak are digitized. The signal amplitude is determined by using optimal filtering to compute the deposited energy, cell time and quality

with respect to the ideal pulse shape. In order to achieve so, several daily and weekly calibration runs are used to determine calibration constants. For these, a well known calibration signal is injected and the electronics response is evaluated. This procedure allows the extraction of noise levels, electronics gain and pedestal shifts. Furthermore, the optimal filtering coefficients (OFCs) can be determined by measuring the calibration pulse shape and transforming it into the physics pulse shape. The pulse shape of the detector pulse and the shaped pulse together with the sampled signal can be seen in Figure 3.6(b). The shaped pulse is bi-polar with an integral of zero over the full pulse. This is used to correct the amplitude for contributions from in-time and out-of-time pile-up. Precise timing of the readout electronics is very important to ensure excellent energy resolution and veto cosmic and beam-induced backgrounds. To ensure this, a fine adjustment of the FEBs is carried out using beam splashes and early collision data. Additionally, the LAr has to be constantly monitored to ensure a uniform response. Impurities like O_2 molecules and temperature changes can lead to a change in the drift time and a degradation of the signal measurement. Hence, 508 temperature probes and 30 purity probes are installed to control these important parameters.
The relative energy resolution of the LAr calorimeter is parametrized as:

$$\frac{\sigma(E)}{E} = \frac{a}{\sqrt{E}} \oplus \frac{b}{E} \oplus c, \tag{3.1}$$

where a is the stochastic term related to shower fluctuations, b the electronic noise term and c the noise term. The first two terms are mostly relevant at lower energies with a being in the order of $10\,\% \cdot \sqrt{\mathrm{GeV}}$ and $b \approx$200–400 MeV [85]. For very high energies, the constant term, which has an approximate size of 0.5–0.7 % [86], becomes the dominant contribution [3].

Tile calorimeter

The Tile calorimeter [87] follows outside the LAr calorimeters and is designed to measure hadronic showers. It similarly is a sampling calorimeter but uses plastic scintillator tiles as the active material and steel as absorber. The tiles are arranged in three layers in the radial direction and cover 9.7 hadronic interaction lengths. The Tile calorimeter spans over the range of $|\eta| < 1.7$ and has a total of 9852 readout channels. When a hadronic shower emerges in the Tile Calorimeter, the particles interact with the scintillators, causing them to emit relaxation light. Wave length shifting fibers are used to guide these photons towards the photomultiplier tubes (PMTs) which read out the signal [3].

	Barrel		**End-cap**	
EM calorimeter				
Number of layers and $\|\eta\|$ coverage				
Presampler	1	$\|\eta\| < 1.52$	1	$1.5 < \|\eta\| < 1.8$
Calorimeter	3	$\|\eta\| < 1.35$	2	$1.375 < \|\eta\| < 1.5$
	2	$1.35 < \|\eta\| < 1.475$	3	$1.5 < \|\eta\| < 2.5$
			2	$2.5 < \|\eta\| < 3.2$
Granularity $\Delta\eta \times \Delta\phi$ versus $\|\eta\|$				
Presampler	0.025×0.1	$\|\eta\| < 1.52$	0.025×0.1	$1.5 < \|\eta\| < 1.8$
Calorimeter 1st layer	$0.025/8 \times 0.1$	$\|\eta\| < 1.40$	0.050×0.1	$1.375 < \|\eta\| < 1.425$
	0.025×0.025	$1.40 < \|\eta\| < 1.475$	0.025×0.1	$1.425 < \|\eta\| < 1.5$
			$0.025/8 \times 0.1$	$1.5 < \|\eta\| < 1.8$
			$0.025/6 \times 0.1$	$1.8 < \|\eta\| < 2.0$
			$0.025/4 \times 0.1$	$2.0 < \|\eta\| < 2.4$
			0.025×0.1	$2.4 < \|\eta\| < 2.5$
			0.1×0.1	$2.5 < \|\eta\| < 3.2$
Calorimeter 2nd layer	0.025×0.025	$\|\eta\| < 1.40$	0.050×0.025	$1.375 < \|\eta\| < 1.425$
	0.075×0.025	$1.40 < \|\eta\| < 1.475$	0.025×0.025	$1.425 < \|\eta\| < 2.5$
			0.1×0.1	$2.5 < \|\eta\| < 3.2$
Calorimeter 3rd layer	0.050×0.025	$\|\eta\| < 1.35$	0.050×0.025	$1.5 < \|\eta\| < 2.5$
Number of readout channels				
Presampler	7808		1536 (both sides)	
Calorimeter	101760		62208 (both sides)	
LAr hadronic end-cap				
$\|\eta\|$ coverage			$1.5 < \|\eta\| < 3.2$	
Number of layers			4	
Granularity $\Delta\eta \times \Delta\phi$			0.1×0.1	$1.5 < \|\eta\| < 2.5$
			0.2×0.2	$2.5 < \|\eta\| < 3.2$
Readout channels			5632 (both sides)	
LAr forward calorimeter				
$\|\eta\|$ coverage			$3.1 < \|\eta\| < 4.9$	
Number of layers			3	
Granularity $\Delta x \times \Delta y$(cm)			FCal1: 3.0×2.6	$3.15 < \|\eta\| < 4.30$
			FCal1: $\sim$ four times finer	$3.10 < \|\eta\| < 3.15$,
				$4.30 < \|\eta\| < 4.83$
			FCal2: 33×43	$3.24 < \|\eta\| < 4.50$
			FCal2: $\sim$ four times finer	$3.20 < \|\eta\| < 3.24$,
				$4.50 < \|\eta\| < 4.81$
			FCal3: 5.4×4.7	$3.32 < \|\eta\| < 4.60$
			FCal3: $\sim$ four times finer	$3.29 < \|\eta\| < 3.32$
				$4.60 < \|\eta\| < 4.75$
Readout channels			3524 (both sides)	

Table 3.1: Segmentation of the LAr calorimeter [3].

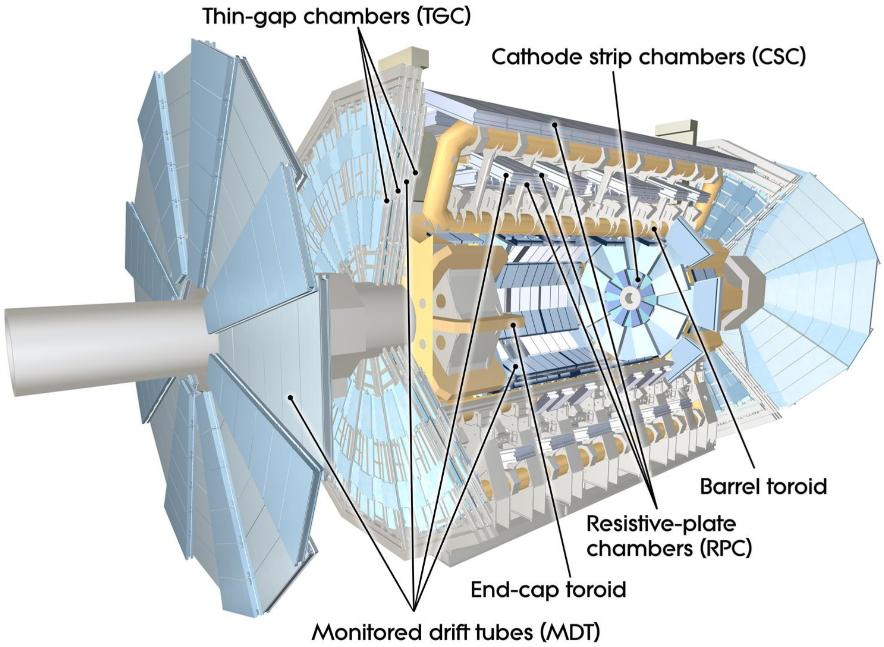

Figure 3.7: Cutaway view of the ATLAS muon system [3].

3.2.4 The muon system

At LHC energies, most muons are minimal ionizing particles, so only those with energies below around 5 GeV are stopped in the calorimeters. As most other particles deposit all their energy in the calorimeters, the outer part of the ATLAS detector is formed by the MS [88] which is dedicated to measure tracks and momenta of muons. The measurements are based on magnetic deflection of the charged muons in the magnetic field produced by the superconducting toroid magnet system. It consists of a large barrel toroid operating in the range $|\eta| < 1.4$ and two smaller end-cap magnets for $1.6 < |\eta| < 2.7$. For the intermediate region, a combination of the magnetic fields of both magnets is providing the deflection. The magnetic fields locally reach strengths of up to 3.5 T and provide a bending power of 1.5 to 5.5 T m (1 to 7.5 T m) by the barrel (end-cap) toroid. An overview of the MS with the four different detector types used is given in Figure 3.7 [3].
Monitored Drift Tubes (MDTs) are found throughout the whole detector where they provide precision measurements of the track coordinates. They are gas-filled aluminum cylindrical drift chambers operating with Ar/CO_2 gas (93 %/7 %) at 3 bar. The gas is ionized by passing muons and the resulting electrons are collected at a central tungsten-rhenium wire which is at a potential of 3080 V. The MDTs are arranged in three to eight layers of drift tubes in a range $|\eta| < 2.7$ ($|\eta| < 2.0$ for the innermost end-cap layer) with an average resolution of 80 µm per tube (or

35 µm per chamber).
In the forward region of $2.0 < |\eta| < 2.7$, the MDTs are supplemented by Cathode Strip Chambers (CSCs) to handle the increased particle flux. They are multi-wire proportional chambers with the same physics principle as the MDTs, but the cathode planes are arranged orthogonally to the anode wires. This allows to measure both η and ϕ from the induced-charge distributions. The gas mixture is Ar/CO_2 as well with a (80/20) proportion. By the CSC design, a faster readout and a tracking precision of 40 µm (5 mm) in the bending (transverse) plane can be reached.
Since highly energetic muons are often found in interesting proton–proton collisions, they are good candidates to trigger on. For this task, the MDTs and CSCs are too slow, so they are supported by the faster Resistive-Plate Chambers (RPCs) and Thin-Gap Chambers (TGCs). Their intrinsic time resolutions are 1.5 ns and 4 ns, respectively. In the barrel region of $|\eta| < 1.05$, RPCs are used. They are gaseous parallel electrode-plate detectors. Two resistive plates are inserted between the electrode plates and kept at a distance of 2 mm by spacers. The gas (a mixture of $C_2H_2F_4$, Iso-C_4H_10 and SF_6) gets ionized by traversing muons. A high electric field of $4.9\,\mathrm{kV\,mm^{-1}}$ enhances the signal by creating avalanches.
For the end-cap region of $1.05 < |\eta| < 2.4$, TGCs are implemented for triggering. TGCs are multi-wire proportional chambers with the specialty of a smaller wire-to-cathode distance (1.4 mm) compared to the wire-to-wire distance (1.8 mm). The small distance paired with a high voltage of 2900 V allows for a fast readout. To prevent the occurrence of streamers, a highly quenching gas mixture (CO_2 and n-C_5H_12) is used [3].

3.2.5 ATLAS forward detectors

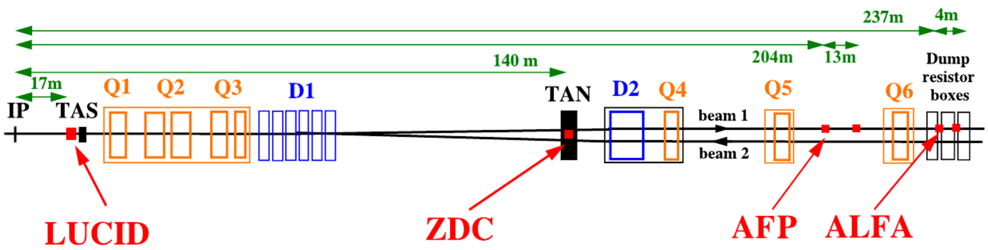

Figure 3.8: Placement of the ATLAS forward detectors along the beam-line around the ATLAS IP. The figure is taken from Ref. [89], where the original illustration from Ref. [3] was complemented by including the AFP (ATLAS Forward Proton) detectors [90].

In addition to the main detector, four specialized devices are placed in both directions of the beam pipe: LUCID-2 (LUminosity Cherenkov Integrating Detector) [91], the ZDC (Zero Degree Calorimeters) [92], the AFP detector [90] and the ALFA (Absolute Luminosity For ATLAS) detector [93]. The overview of the placement of these detectors with respect to the IP is displayed in Figure 3.8.
The closest forward detector is LUCID-2 which is placed inside the ATLAS detector between the middle and outer MS wheel. It consists of PMTs which use Cherenkov radiation from inelastic proton–proton scattering to provide a luminosity measurement for ATLAS. It is used to both measure the integrated luminosity and provide monitoring of the instantaneous luminosity.
The ZDC detectors are mostly used during heavy-ion runs where they validated the centrality of the ion collisions and supply minimum-bias trigger capabilities. This is achieved by detecting forward neutrons with $|\eta| > 8.3$. The detectors located the furthest away from the IP are AFP and ALFA. They both feature a Roman pot design and intent to measure elastic and diffractive proton scattering. This data is used to determine the total proton–proton cross-section, and hence, the absolute luminosity. Furthermore, the scattering data can be used in various searches for exotic particles [3].

3.3 Trigger system of the ATLAS detector

Protons collide in the LHC with a rate of 40 MHz. Given that the information of one particle collision produces around 1.3 MB of data in the ATLAS detector, this amounts to approximately 50 TB of data generated every second. This is far too much to be handled by any data center to process or store. Hence, a two level trigger system [95] is used to filter for events containing interesting physics processes. The whole trigger chain and data flow is sketched in Figure 3.9.
The first trigger stage is the level-1 (L1) trigger, which is fully hardware based and is capable to reduce the event rate to 100 kHz. It uses fast detector components to select events with large missing transverse energy and particles with high momenta. From the muon spectrometer, information from the RPCs and TGCs are utilized for the Level-1 Muon (L1Muon) trigger sub-system. The Level-1 Calorimeter (L1Calo) trigger decisions are based on reduced-granularity calorimeter inputs. In addition, the Level-1 Topological Processor (L1Topo) trigger searches for specific topological structures with the input from the other triggers. The information from the L1 triggers is passed on to the CTP which makes the final L1 decision. If an event is decided to be interesting, the entire detector is read out. When this happens, the front-end (FE) electronics send the data to Readout Drivers (RODs) where an initial formatting is carried out. Afterwards, the data is stored temporarily in Readout Systems (ROSes). Furthermore, the L1 trigger forms regions of interest

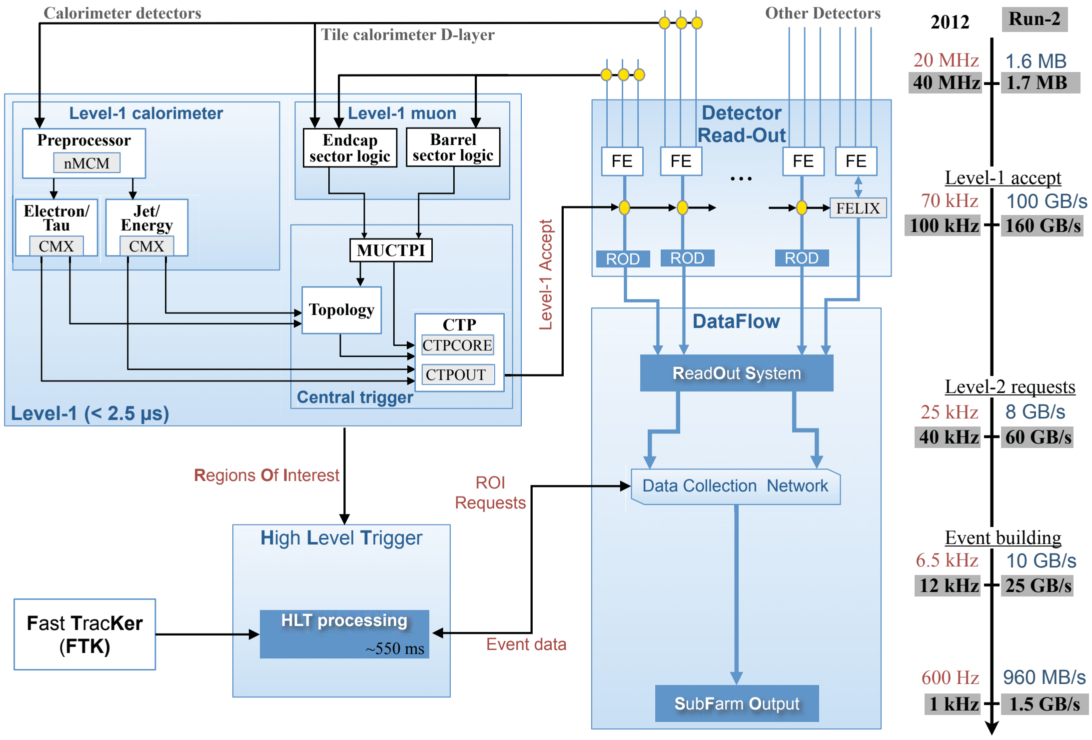

Figure 3.9: Schematic layout of the Run 2 ATLAS trigger and data acquisition system [94].

(RoI's), which are regions in η and ϕ with interesting features to aid later trigger stages.

The second stage of the trigger is the software-based High Level Trigger (HLT), which has a latency of 40 ms. Thus, it can build on the full detector granularity in the RoI and use a reconstruction similar to the offline algorithms. These algorithms reconstruct physics objects like electrons or muons and apply various kinematic cuts and identification algorithms. A number of HLT decisions are combined consecutively to form a trigger chain based on certain kinetic and topological cuts on physics objects. Since these calculations are more computationally extensive than the ones of the L1 trigger, they are carried out in parallel in a computing farm in a service cavern next to the detector. Events that are accepted by one of the HLT trigger chains are written out to the permanent storage. After the HLT trigger stage, the read-out rate is reduced to around 1 kHz.

The trigger menu is a complex structure where over 2000 triggers are grouped into several streams for different usages. Each of the individual trigger items consists of a L1 seed and an HLT trigger. The composition of the trigger menu is optimized for different luminosity stages to maximize the physics output dependent on the available bandwidth and computing capacities. Even though the trigger system is capable of significantly reducing the trigger rate, this is not always enough. Some triggers have very low thresholds, for example to gather low-momentum muons, and hence produce a very high rate. To handle these rates, a prescale can be applied to these trigger items, resembling a probability that an accepted event is written out. Since the readout speed of the detector is limited and the collision rates are very high, multiple collisions are recorded during one read-out cycle of the detector. This effect of overlapping events is called *pile-up*, which comes in two types: Firstly, it can happen that multiple protons collide in the same bunch crossing due to the high number of protons per bunch. This is called *in-time* pile-up. On the other hand, *out-of-time* pile-up describes the effect of overlap of several collisions from different bunch crossings which happens if the detector signal read-out time is longer than the 25 ns between two bunches crossings. For analyses, both pile-up sources are parametrized by the mean number of interactions per bunch crossing $\langle\mu\rangle$.

3.4 Data taking at ATLAS

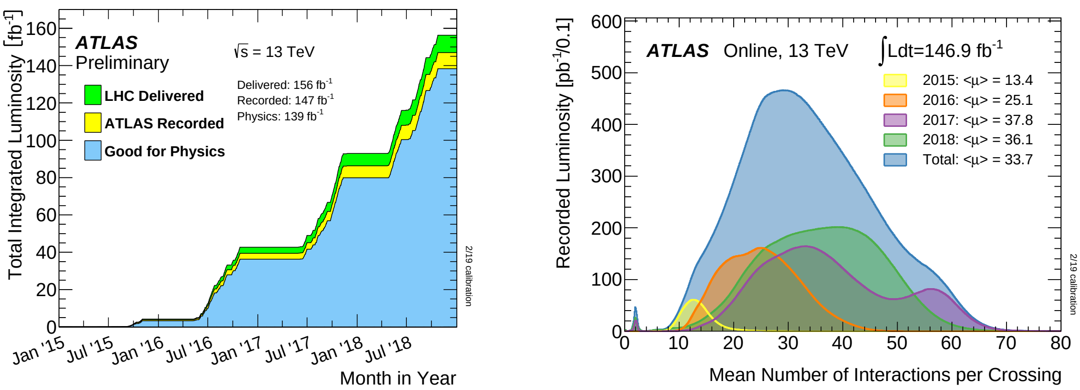

(a) (b)

Figure 3.10: Cumulative integrated luminosity (a) and measured pile-up (b) during Run 2 data-taking from 2015 to 2018 [96].

The LHC delivered a total integrated luminosity of 156 fb^{-1} during Run 2. Of these, the ATLAS detector recorded 149 fb^{-1}, which corresponds to a data-taking efficiency of 95 %. The evolution of the integrated luminosity during Run 2 is displayed in Figure 3.10(a). After applying data quality selections, the total integrated luminosity available for physics analyses is 140 fb^{-1} with an associated uncertainty of 0.83 % [97]. The luminosity measurements have been primarily

carried out by the LUCID-2 detector, with supplementary information taken from the calorimeter systems. Over the four years, the mean number of interactions per bunch crossing varied between around 10 and 70, with the average over all data-taking periods being $\langle\mu\rangle = 33.7$. Figure 3.10(b) shows the distributions for the different data-taking years.
For data-taking, the fundamental time granularity unit is the luminosity block (LB) [98]. It represents an interval of time (approximately one minute) for which the detector conditions stay the same and the luminosity can be assumed to be constant. Changes in the detector configuration cause the start of a new LB. An ATLAS run (identified by a unique six digit *run number*) consists of multiple LBs and covers a time period from before the beam injection to the beam dump, which typically lasts 12-15 h. During this time, the status of the proton beam, the LHC and the detector is monitored closely. A quality assessment of all systems is conducted with the goal to produce a list of LBs that are good for physics analyses, called the Good Runs List (GRL) [99].

3.5 Monte Carlo event simulation

In the analysis of particle collision data, their simulations play a crucial role. On one hand, the background behavior can be studied, and on the other hand new processes and their signatures can be checked. MC generators are used for the task of simulating the required events.
The simulation of events happens in multiple stages which are conducted using the Athena software framework [101–103]. In the first step, matrix element (ME) MC generators are used to generate the hard-scatter collision process. This comes with the production of initial and final state radiation according to the ME calculations. The partons produced in the hard-scattering event are then undergoing hadronization and radiative corrections. As a result, cone-like hadronic particle showers, called jets, are produced. This hadronization and showering of the partons is carried out by parton shower (PS) MC generators. There are multiple-purpose MC generators, like Pythia [104] or Sherpa [105], which are designed to deal with both the ME and PS calculations. In other cases, the ME and PS are calculated by different generators and are subsequently combined by a ME+PS matching algorithm. In this thesis it is the case for the Higgs and top-quark simulations, where Powheg-Box [106] is used for the ME and interfaced with Pythia for the PS. Usually, the MC generators simulate collisions at a fixed perturbative theory order and model the parton content of the hadrons with external parton density function (PDF) sets. These PDFs cannot be easily derived from the underlying QCD theory, and are therefore obtained from measurements.
For a complete modeling of collision events, softer interactions have to be added to

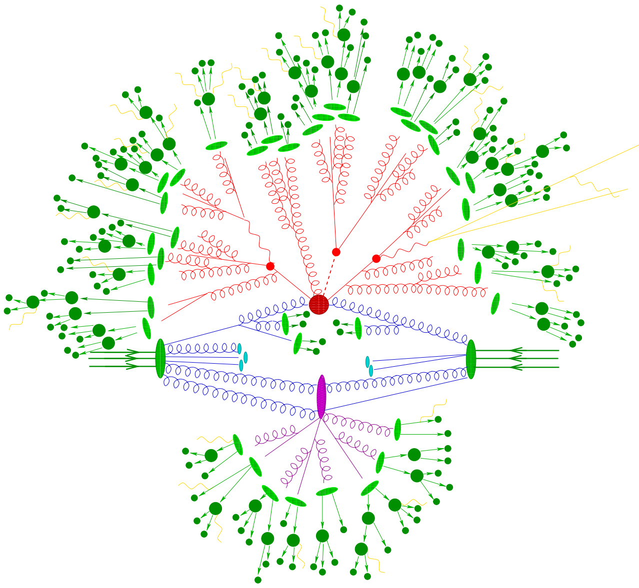

Figure 3.11: Schematic representation of a $t\bar{t}H$ event as produced by an event generator. The hard interaction (big red dot) produces the three particles t, $\bar{t}$ and H, which decay further (small red dots). Additionally, hard QCD radiation is created (red) and a secondary interaction happens (purple oval), before the final-state particles hadronize (light green ovals) and the hadrons decay (dark green dots). During each stage, photon radiation can occur (yellow) [100].

the hard-scattering process. These arise from multi parton interactions (MPIs), initial state radiation (ISR) and final state radiation (FSR). They describe additional lower energy hard-scatter events and radiation in the same collision event. This so-called underlying event is likewise generated by MC generators. As the underlying QCD interactions are difficult to describe with perturbative calculations, the generators utilize an effective description of the underlying event and the low-energy PS, which can be tuned with a set of free parameters. These parameters include the momentum cutoff for parton decays or the factorization and renormalization scale. The optimal values for these parameters are obtained from comparison to data. An example for a commonly used parameter set is the *A14 tune* [107] for the Pythia 8 shower generator. Figure 3.11 gives an illustration of a hard-scatter event together with the underlying event and additional radiation as well as the PSs.

3.6 Detector simulation

After generating the hard-scatter and underlying events, the interactions with the detector and its response need to be simulated. For this, a model of the entire detector, including the support structure, active and passive detector material and magnetic fields, need to be known precisely and fed into the simulation. The GEANT4 framework [103, 108] is used to simulate the particle interactions with detector material and the signal generation. The full detector response simulation is very complex and therefore computationally expensive. Unfortunately, many studies within physics analyses require large numbers of simulated events in order to achieve acceptable statistics. The time to reach the required precision would be limited by the simulation time of the detector response. To circumvent this problem, the ATLFAST-II simulation [109] has been developed. It similarly utilizes GEANT4 for the simulation of the ID and MS but exchanges its calorimeter simulation by the ATLAS fast calorimeter simulation FASTCALOSIM [109]. It uses a parametric approach which cuts down the computing time by around one order of magnitude while maintaining a good agreement with the results from the full GEANT4 simulation.

As the next step, the simulated events undergo the same trigger selections, reconstruction and calibration as the recorded data. One advantage of the MC simulation is that the original event information can be stored as *truth level information*.

To model the pile-up from the same or neighboring bunch crossings as it is occurring in data, the hard-scatter events are overlaid by a separately simulated set of minimum-bias events. These are generated with PYTHIA 8, using the NNPDF2.3LO PDF set with the A3 tune [110]. In order to match the MC simulation as closely as possible to the recorded data, the pile-up overlay is adjusted to the ATLAS detector run conditions. As these run conditions changed over the course of Run 2, the MC simulations are split into three campaigns, each matching the run conditions of a different data-taking period [111]. The campaign MC16a matches the run conditions and pile-up during the 2015-2016 data-taking period, MC16d similarly the conditions of the 2017 data-taking and MC16e the conditions of the 2018 data-taking. In the latter case, the expected conditions have been extrapolated from the previous periods because the event generation mostly finished before the end of the 2018 data-taking. In order to reduce any potential residual mismatch in the generated and measured pile-up, a pile-up reweighting procedure is applied, which corrects the simulated events with a scale factor.

MC event samples are assigned a six digit dataset identifier (DSID) number, similar to the run number for data samples. These DSIDs are unique for each physics process sample.

4 Integration of the ALTI boards for the LAr detector

Several upgrades have been made to the ATLAS detector during the LS2 from 2019 to 2022 in order to make the detector ready for the challenges of the LHC Run 3. One of the upgrades was the installation of the ALTI boards [112] for all the subdetectors. They deal with the communication between subdetectors and from the subdetectors to the CTP for the crucial trigger, timing and control (TTC) signals. This chapter explains the integration and commissioning of the ALTI boards for the LAr detector, in which the author was strongly involved.

4.1 Preparation for Run 3

In Run 3, an increase in the instantaneous luminosity by a factor of two with respect to Run 2 conditions is expected. To manage these increasingly demanding conditions, the LAr detector requires multiple upgrades. The integration of the ALTI boards was necessary, because the legacy system, containing of the four modules ATLAS Local Trigger Processor (LTP), ATLAS Local Trigger Processor Interface (LTPi), TTC VMEbus interface (TTCvi) and TTC encoder/transmitter (TTCex), were showing aging effects and the supply of spares was running too low. The ALTI encompasses the functionalities of the four aforementioned modules into one board, which makes the system more robust. It furthermore allows a modular running, which greatly improves the opportunities for commissioning, testing and validation of the LAr detector.
The major update to the LAr detector during the LS2 is the Phase-1 upgrade [113]. It incorporates the integration of a new Digital Trigger (DT) path which was implemented to replace the old analog trigger, significantly enhancing the trigger performance. The new trigger exhibits up to ten times finer granularity, leading to improved trigger energy resolution and greater efficiency in selecting physics objects, which enables the ATLAS detector to cope with the increased luminosities of Run 3. This improvement required the installation of new electronics on both the FE and off-detector sides. The commissioning of the DT benefited significantly from the newly added ALTI functionalities.

4.2 The ALTI board

The ALTI [112] is a new module of the TTC system of the ATLAS detector designed for the operation during Run 3. It is a custom-made 6U VME64x module consisting of two printed circuit boards (motherboard [114] and mezzanine [115]) that occupy two slots in the VME64x crate. This field programmable gate array (FPGA) based system employs the Xilinx 7-Series FPGA chip from the Artix family. The module interfaces with other modules in the same crate via a shared Versa Module Eurocard (VME) back plane. The control software for the ALTI runs on a single board computer (SBC) with an Intel Central Processing Unit (CPU), positioned in the first slot of the same crate and operating on the scientific Linux operating system. A photo of the ALTI board is shown in Figure 4.1.

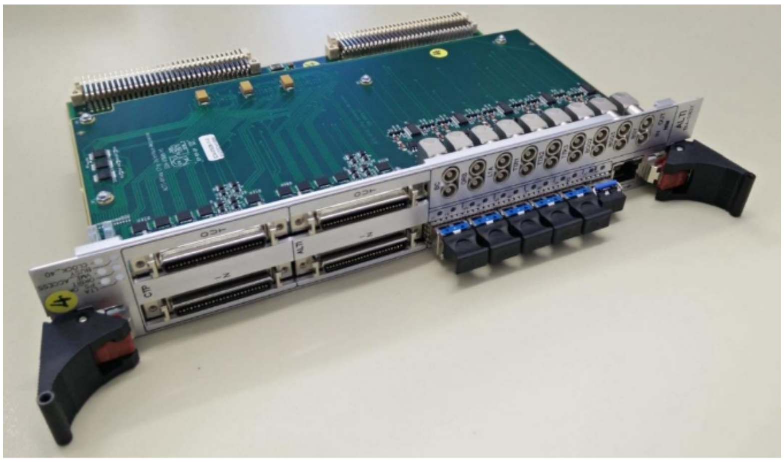

Figure 4.1: Photo of the ALTI board [112].

The ALTI serves as the interface between the CTP and a subdetector TTC partition. It generates an optical TTC stream based on signals received from the CTP, which is then distributed to the subdetector FE electronics via an intermediate Front-End Link eXchange (FELIX). Additionally, the ALTI can function as a TTC signal generator or pass signals received from the CTP module to other daisy-chained TTC partitions. The generated TTC signals are playing an important role in taking calibrations. The overview over all distributed signals is given in Table 4.1. From this table it can be seen, that the ALTI has a very important role in the communication between the CTP and the subdetectors. It provides the clock signals for the FE electronics, transmits information about which events were triggered, and propagates to the CTP when subdetectors are busy due to filled readout buffers.
The ALTI can operate in three different modes. Firstly, it can be the *Master*, which means it is generating all signals by itself, according to a predefined pattern.

Table 4.1: Signals distributed by the ALTI module. The direction indicates, if the signal is distributed from the CTP to the subdetector FE electronics (downstream) or from the subdetector FE electronics to the CTP (upstream).

Signal	Direction	Explanation
BC	downstream	40 MHz bunch crossing clock of the LHC
ORB	downstream	LHC orbit clock (11.2 kHz) with a length of 40 BC, used as bunch counter reset (BCR)
L1A	downstream	Level-1 trigger accept
TTR [1...3]	downstream	locally generated test triggers
BGO [0...3]	downstream	B-Go commands used to trigger B-channel TTC commands, such as the event counter reset (ECR)
TTYP [0...7]	downstream	8-bit trigger-type identification word associated to each L1A
BUSY	upstream	signal sent by subdetectors to stop the generation of L1A due to filling up readout buffers
CALREQ [0...2]	upstream	3-bit word sent by the subdetectors to request calibration triggers

The other two modes are *Slave* modes, where the ALTI transmits all the signals received from either the CTP or from another ALTI.
With respect to the previously used legacy system, a number of new functionalities have been added by integrating the ALTI. The monitoring has been largely improved by adding the possibility to monitor the phases of the input signals and taking snapshots of incoming TTC signals, which can then be stored in memory. Additionally, the optical TTC stream analyzer is added, allowing to decode and save commands and triggers sent on the TTC stream. Furthermore, the pattern generation functionalities have been expanded, being now able to provide longer patterns than with the LTP. Another improvement is the 'miniCTP' feature, which adds CTP-like functions, random triggers with pseudo-random prescaling or simple and complex deadtime generation. Finally, the ALTI includes a jitter cleaner option for the TTC output and an option to set the TTC fine delay for adjusting the subdetector bunch crossing (BC) timing.

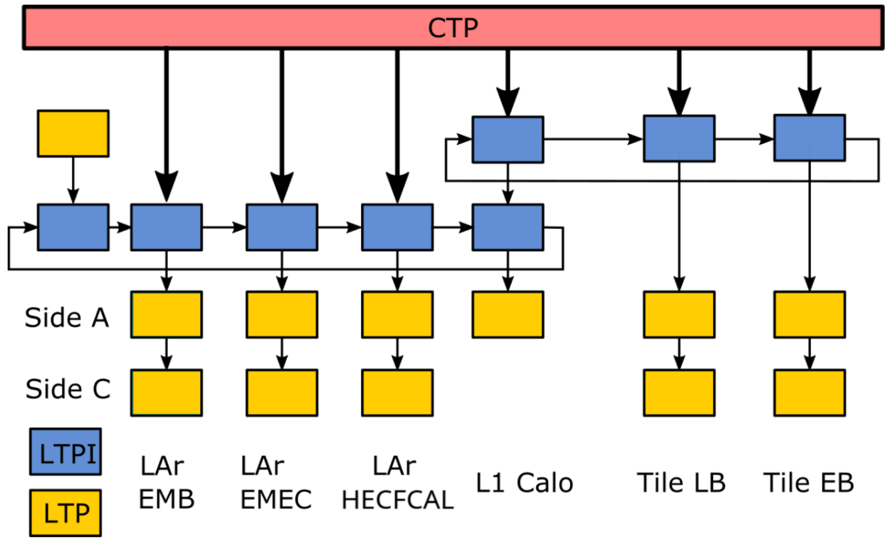

(a)

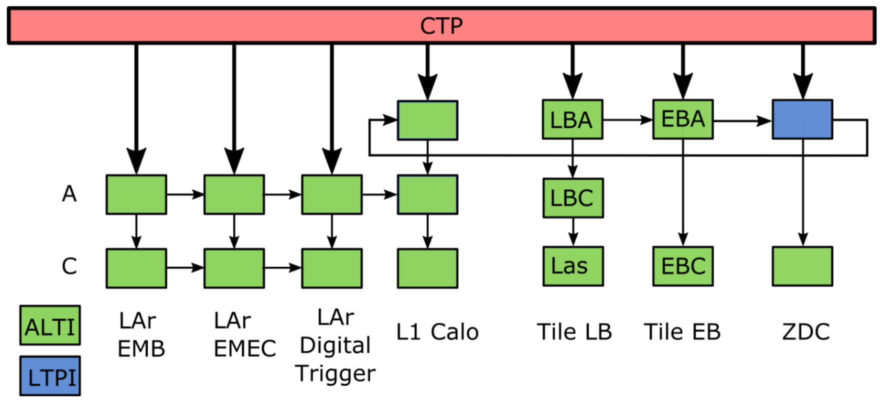

(b)

Figure 4.2: TTC setup of the calorimeters in (a) Run 2 and (b) Run 3. The setup for Run 2 consisted only of LTP and LTPi modules. These have mostly been exchanged with ALTIs during LS2. Only the connections between Tile and L1Calo, and to ZDC, are still handled via an LTPi. One major advantage for LAr of the new setup is that it allows the parallel independent usage of A-side and C-side due to the new horizontal connections, which opens additional opportunities for testing and validation [116].

4.3 Integration of the ALTI for LAr

During Run 2, the LAr system used both LTP and LTPi modules for its TTC management, as is shown in Figure 4.2(a) on the left side. These have all been replaced with six ALTI boards during LS2 for the TTC partitions EMB A-side (EMBA), EMB C-side (EMBC), EMEC A-side (EMECA), EMEC C-side (EMECC), DT A-side (DTA) and DT C-side (DTC). The new setup is visualized in Figure 4.2(b) and a photograph of the EMB ALTIs is shown in Figure 4.3. It can be seen that the LAr system and the relevant connection to L1Calo have fully switched to ALTI modules. Only one LTPi remains in the system, managing the signal exchange between L1Calo and the Tile calorimeter. Several advantages arise from the new setup for the LAr system. The number of modules is reduced significantly, which lessens the risk of failures. A great advantage of the new structure is that modular parallel running is now possible. This is enabled through the new horizontal connections and the characteristic of the ALTI, that each board can run in *Master* mode. Now it is for example possible to run the C-side in parallel to the A-side to perform two independent tests in parallel. It is also possible to run every single TTC partition on its own, which was not doable beforehand. This change greatly

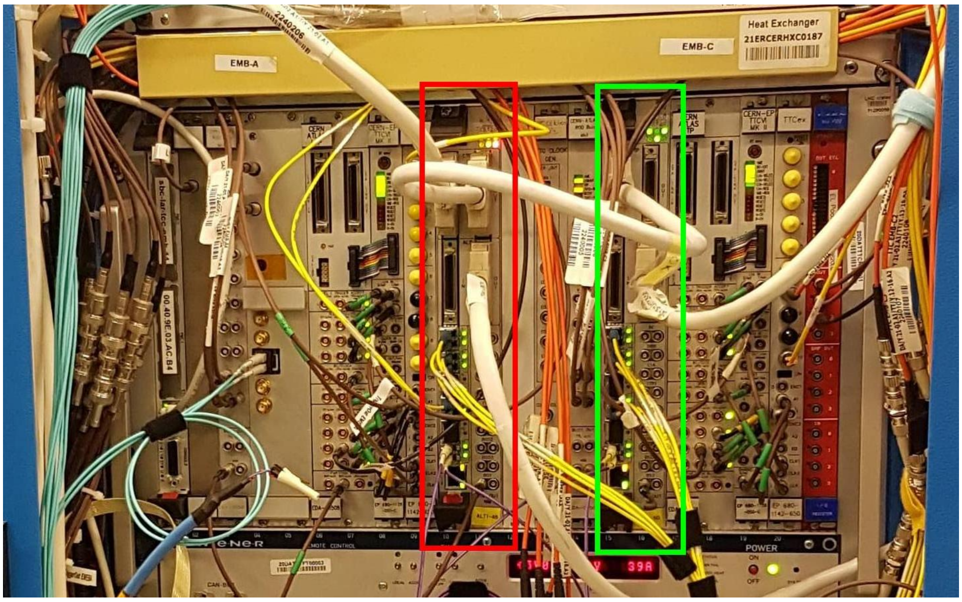

Figure 4.3: The VME TTC crate of the EMB. The ALTI boards are highlighted with the red rectangle for the EMBA ALTI and the green rectangle for the EMBC ALTI. On the left and right sides of the rectangles, respectively, the four legacy modules LTP, LTPi, TTCvi and TTCex can be seen, which have been decommissioned.

enhances the validation, testing and commissioning opportunities.
Another change in the TTC setup for Run 3 is that the HEC and FCal partitions are now handled by the EMEC ALTIs, which frees up capacities to use two ALTIs for the new DT system.
After physically inserting the new boards and cabling the connections, several tasks had to be done to re-establish the previous functionalities and make use of the new features of the ALTI. The author of this thesis was strongly involved in the LAr ALTI team, consisting of a postdoctoral supervisor, an early-career postdoctoral researcher and the author. The shared tasks were integrating the ALTI hardware and connection description into the software suite, recreating the various TTC partitions there, tuning the timing delay of the Level-1 Accept (L1A) signal after a pulse and restoring the calibration environment. For taking a calibration, the predefined pattern needed to be matched to the latency between the pulse injection command and the pulsing response to make sure the timing window captures the full pulse.
The author's main contributions to the remaining tasks will be explained in the four following sections. More details about the contributions are given in the appendix.

4.3.1 A pattern generator for the ALTI

The signal sequence pattern is an integral part of the operation in the ALTI `Master` mode. It defines the sequence in which the various signals are sent. A pattern generator script has been set up to dynamically create these patterns for different use cases. All patterns have to include the orbit signal to inform the electronics that the new cycle around the LHC ring has started, which triggers the reset of the BC counter.
Different common use cases are pedestal runs (i.e. runs without pulses) and calibration runs with pulses. For both cases, the frequency of the events (represented by the L1A signal) can be defined. An example pattern generated with pulsing for a calibration run is given in Figure 4.4.
The patterns generated with the pattern generator script have been in use for multiple years during Run 3 for daily calibration runs and continuous testing activities.

4.3.2 Online panel for board monitoring

To exploit the new monitoring features of the ALTI, an online monitoring panel has been developed with Java. It is shown in Figure 4.5 and gives information about the current run. The information includes the TTC structure in use (i.e. which parts of LAr are activated), the pattern generator in use, and detailed information about the status of the ALTIs. This ALTI monitoring information is streamed from

```
#-----------------------
# Rate = 400Hz
# Number L1A = 1
# Pulsing = yes
#-----------------------
#                      M
#                      u
#                      l
#                      t
#                      i
#                      p
#                      l
#   CCC                i
#  BRRR     T BBBB TTT  c
#O UEEE     T GGGG TTTL i
#R SQQQ     Y OOOO RRR1 t
#B Y210     P 3210 321A y
-----------------------
 1 0000 0x00 0000 0000 40       # orbit signal
 0 0000 0x00 0000 0000 60
 0 0000 0x00 0100 0000 1        # BGO2 command representing pulse
 0 0000 0x00 0000 0000 147
 0 0000 0x02 0000 0001 1        # Level-1 accept with trigger type 0x02
 0 0000 0x02 0000 0000 4        # Trigger type 0x02 continuing for 4 BC
 0 0000 0x00 0000 0000 3311
 1 0000 0x00 0000 0000 40
```

Figure 4.4: Example signal sequence pattern for the ALTI. The various signals sent on each BC are listed. Consecutive BCs with the same signals are compresses into one line with given multiplicity. This example starts with an orbit signal over 40 BC (red), which is followed by 60 BC without any signals. Then a BGO2 signal is sent (magenta), which communicates to the calibration board to issue a calibration pulse. After a delay of 147 BC, the L1A signal is sent with the trigger type 0x02 (green), which is continued for another 4 BC (orange). No signal is sent for the remaining 3311 BC of the orbit. Afterwards, the next orbit signal is issued.

the partition information service and consists of the settings, current counter values and rates, as well as the BUSY state of the system. The user can also interactively generate a new signal sequence pattern with settings as desired.
The online monitoring panel has been in use throughout Run 3 and is providing useful real-time information about the state of the LAr TTC system.

4.3.3 Standalone pulsing with the ALTI

In some situations, it is required to send calibration pulses, when included in a combined run (ATLAS run or standalone together with L1Calo). Example

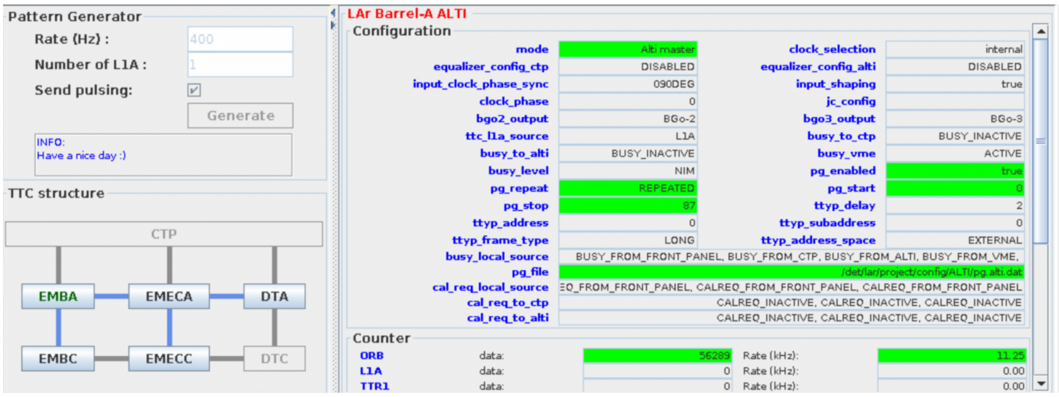

Figure 4.5: TTC panel for the LAr partitions. The upper left side shows the currently used signal pattern specification and lets the user generate new pattern with the script explained in Section 4.3.1. The lower left side shows the active parts of the LAr system during the current run, highlighting the master ALTI in green. It is also visible if it is an ATLAS run (CTP enabled) or a standalone run (CTP disabled). On the right side, more information about the selected ALTI is displayed, including settings used, as well as counter values, rates and information about the BUSY state.

use cases are connectivity checks for single channels or producing test pulses for L1Calo to trigger on, which is particularly useful to emulate beam splashes[1]. In these cases, the ALTI boards will be in *Slave* mode and cannot use the pattern generator (which is only activated in *Master* mode). Therefore, another method is required for pulsing, which can be done using low-level C++ commands to directly communicate to the ALTI.

Scripts have been developed within the standalone pulsing package to allow the user to send the pulsing commands to the desired detector region, in a defined frequency and for the requested time. Wrapper scripts using PYTHON have also been set up in order to facilitate the user experience and automate the FEB setup needed for pulsing.

The standalone pulsing package has been heavily used to validate the real-time path for the newly installed DT system as well as the mapping between the DT and L1Calo. On the legacy trigger side, it was used to ensure the connectivity

[1]Beam splashes are usually the first proton events that happen after a maintenance period of the LHC. The proton beam is stopped by a closed collimator just before the detector, resulting in a large shower of particles that hit most detector channels. They are important to check the timing of the detector and usually provide the first data after upgrades of detector parts. Since these are singular events, it is particularly important that the trigger does not miss them, and hence the emulation of the beam splashes to verify that is important.

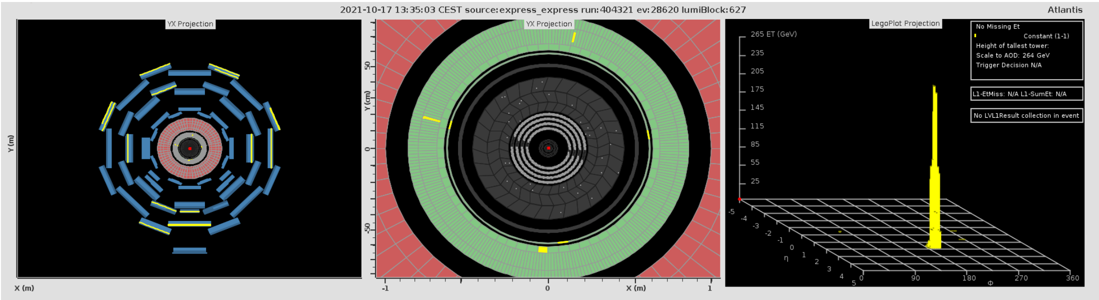

Figure 4.6: Event display of an emulated beam splash, created with the ATLANTIS visualization software [117]. Energy deposits are highlighted in yellow. The left panel gives the overview of the whole ATLAS detector in the x-y-plane, showing energy deposits from noise in the muon systems (blue). The middle panel shows the EM calorimeter (green) in the x-y-plane, with the pulse responsible for triggering the emulated beam splash shown in yellow on the left side. The right panel visualizes the deposited energy in the η-ϕ-plane.

of all legacy trigger channels at the end of LS2, after many components of the system had been exchanged for Run 3. It is also used to emulate beam splashes during the end of each LHC maintenance period in order to make sure the system is ready to receive the real beam splashes. An example from October 2021 is shown in Figure 4.6, where a pulse was injected with the pulsing scripts and successfully triggered on by L1Calo. Furthermore, the pulsing scripts are used any time L1Calo has changes in the trigger configuration and needs to validate them.

4.3.4 ALTI integration at EMF

The Electronics Maintenance Facility (EMF) is the test facility for the LAr system. It is located in a building separated from the main ATLAS detector and holds a test setup for all component of the LAr system. Consequently, it also had to be upgraded to use ALTI modules for the TTC distribution, instead of the old LTP based system. Therefore, two ALTI boards have been installed at the EMF and were integrated into the system. Similar to the integration on the main detector, they had to be cabled first, and afterwards the setup has been defined in configuration files for various running modes. A monitoring panel equivalent to the one described in Section 4.3.2 has been created.
The test setup at the EMF has been equipped with ALTI boards towards the end of the LS2 in 2021 and assisted with countless testing and validation steps of new hardware and software since then.

4.4 Run 3 operation with the ALTI

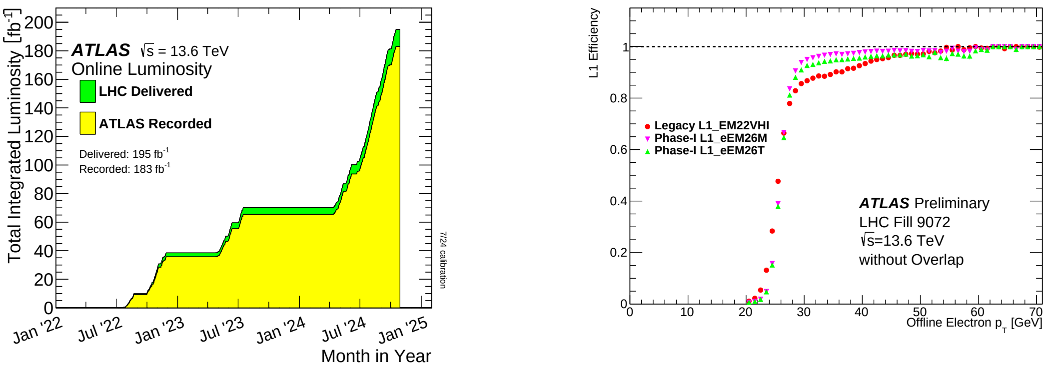

(a) (b)

Figure 4.7: Two plots are given for the operation during Run 3 with the upgraded system: (a) shows the cumulative luminosity delivered to (green) and recorded by the ATLAS detector (yellow) during stable beams for *pp* collisions at a center-of mass energy of 13.6 TeV in 2022-2024 [118]. (b) shows the comparison of L1Calo single-electron trigger efficiencies between the legacy system (red) and the new Phase-1 system (green and magenta), which is fed with inputs from the new LAr DT system [119]. The steeper turn-on curve shows the improved trigger performance of the new system.

The LAr system has been running stably with the new ALTI setup for the TTC handling since the beginning of LHC Run 3. Figure 4.7(a) shows the luminosity recorded in ATLAS since the ALTI installation.
More importantly, the new DT system was installed and commissioned prior to and in the early stages of Run 3. During this process, the new testing opportunities due parallelizing the running of A-side and C-side of the LAr system with the new ALTI features, helped greatly with the commissioning process. As of 2024, the DT system provides the main L1 trigger for EM objects. A comparison of the single-electron trigger efficiencies of the legacy and the upgraded system is shown in Figure 4.7(b). The much steeper turn-on curve of the new trigger shows its improved capabilities. Due to the better background rejection, ATLAS is able to reduce the L1 trigger rate and cope with the higher pile-up environment of Run 3. LAr will continue to run with the ALTI modules until the end of Run 3, which is foreseen in 2026.

5 Physics object identification and reconstruction

During the proton–proton collisions at the LHC, a variety of particles are produced. However, most of these particles are unstable and rapidly decay into more stable ones. Some of the particles also undergo hadronization, resulting in the creation of large particle showers. At the end of these processes, the final stable particles reach the detector, interact with it, and mostly get absorbed. Advanced algorithms are employed to reconstruct the energy and trajectories of the decay particles from the signatures they leave in different detector parts. A precise reconstruction and identification of these particles plays a crucial role in physics analyses.
This chapter details the process of reconstructing and identifying physics objects in the ATLAS experiment, starting with basic structures like tracks and clusters, which are then merged to form higher-level objects such as electrons, muons, and hadronic jets.

5.1 Low-level physics objects

The raw detector data provides detailed information about the energy deposits in the calorimeter systems as well as the position of particle hits in the ID and MS. These data are used to calculate and reconstruct low-level objects. These low-level objects include vertices, tracks and calorimeter clusters. They are later used as the basis to derive higher-level objects, like electron or muon candidates.

5.1.1 Track reconstruction

Tracks of charged particles are formed from hits in the ID [120]. In a first step, hits in each layer of the pixel and SCT detector are clustered. From these, track seeds are formed, consisting of three clusters each. Cuts on the impact parameter and on the momentum of the track seeds are implemented in order to increase the purity and reduce solely combinatorial tracks. With the help of a combinatorial Kalman filter [121], track candidates are built from the track seeds as well as residual clusters in the remaining pixel and SCT layers. It also propagates the track out from the seed towards the TRT. Next, the candidate tracks undergo an ambiguity-solving stage, where each track is assigned a goodness score. It is based on the quality of the trajectory fit and the presence of holes (i.e. expected but missing clusters) along the track path. This score helps to resolve cases where tracks share common clusters, favoring those with higher scores. Additionally, a neural network is employed to aid the ambiguity solver and identify merged cluster created by multiple particles' tracks. This increases the track reconstruction efficiency for dense track environments. As a last stage, for all remaining tracks fulfilling the quality requirements, a high-resolution fit is performed. Tracks passing this stage are added to the final track collection. Physical quantities such as momentum and charge of the particle associated with the track are calculated based on the curvature of the fitted track within the magnetic field of the ID.

5.1.2 Primary vertex reconstruction

Reconstructing interaction vertices is essential for distinguishing objects produced in different interactions. The space points where inelastic proton–proton collisions take place are defined as primary vertices. In the ATLAS experiment, the vertex reconstruction is happening in two stages [122]. The first vertex finding stage determines the position of the vertex. Reconstructed tracks satisfying the quality criteria of the vertex reconstruction algorithm are associated to vertex candidates. The transverse coordinates of the vertex seed are set to the center of the beam spot. Its z-coordinate is derived from the distribution of the closest points of approach of the tracks to the beam spot. In the second vertex fitting stage, the exact position of the vertex is obtained through an iterative fitting algorithm. Each iteration weighs less compatible tracks down and recomputes the vertex position. After this step, tracks that are incompatible with the new vertex are removed and become available for other vertices. This procedure repeats until the vertex position converges. With the remaining tracks, more vertices are formed until no more tracks are left, or no more vertices can be found in the leftover tracks. The primary vertex with the highest sum of squared transverse contributing track momenta $\sum p_{\mathrm{T}}^2$ is considered the primary hard-scatter vertex and will be used in the analysis.

5.1.3 Calorimeter clusters

Once particles have passed through the ID, they arrive at the calorimeter. Upon colliding with the detector material, a cascade of secondary particles is produced, generating signals in the active components of the detector. The deposited energies in the calorimeter cells are measured and combined into clusters [123]. As a first step, cluster seeds are identified by finding cells with a significant signal-to-noise ratio. The threshold for this cell signal significance in the first step is

$$\left|\varsigma_{\text{cell}}^{\text{EM}}\right| = \left|\frac{E_{\text{cell}}^{\text{EM}}}{\sigma_{\text{noise,cell}}^{\text{EM}}}\right| > 4,$$

with the deposited cell energy $E_{\text{cell}}^{\text{EM}}$ and the expected period-specific noise $\sigma_{\text{noise,cell}}^{\text{EM}}$. Each seed cell forms the starting point of a proto-cluster. Starting with the highest cell signal significance cluster, neighboring cells from the same or adjacent layers are merged into the proto-cluster when they pass the significance criterion $\left|\varsigma_{\text{cell}}^{\text{EM}}\right| > 2$. A cluster splitting algorithm is deployed for cases where large clusters have multiple local maxima. These clusters can be separated to improve the resolution of overlapping particle showers and support shower substructure analysis. The resulting collection of clusters is utilized in the reconstruction of calorimeter showers, produced by both electromagnetically and hadronically interacting particles.

5.2 High-level physics objects

The information from the low-level objects is used to reconstruct high-level objects like electrons or muons. This process usually happens in two steps. The first stage identifies candidates from the low-level objects. These are then fed in the second stage through identification algorithms, which separate signatures of real particles from those arising due to misreconstruction of signatures from different origins. The algorithms also define a set of *working points*, which correspond to a selection of objects with a specific truth efficiency that is estimated from MC simulations. Tighter working points have the benefit of an increased purity, but come with the drawback of decreased statistics. After the objects are reconstructed, they need to undergo an energy calibration, which scales the reconstructed energies to the expected ones from data measurements and MC simulations.

5.2.1 Electrons

As electrons move through the detector, they leave two main signatures: tracks in the ID and energy clusters in the ECAL. These come both from the electron itself as well as from secondary particles from bremsstrahlung and electron–positron pair production. The combination of the two signatures starts by forming seeds for geometrically matching ECAL clusters to ID seeds [124]. To address the energy loss from bremsstrahlung, tracks are refitted using an electron hypothesis that accounts for bremsstrahlung, provided there are enough hits in the ID. The algorithm then proceeds to form superclusters in the calorimeter by identifying and merging clusters caused by bremsstrahlung near the seed cluster. Electron candidates

are created by refitting the ID tracks to these superclusters. Additionally, an multivariate algorithm (MVA) is used to optimize the energy resolution of the electron candidates. Further corrections to the resolution and energy scale are taken from $Z \to ee$ measurements.
With the help of a likelihood (LH) discriminant, electron candidates are identified as prompt electrons. Its LH score is constructed using various quantities measured in the ID and the ECAL. The probability density functions (pdfs) of these quantities are measured in data from $J/\psi \to ee$ and $Z \to ee$ events. As a result of the identification process, the working points *Loose*, *Medium* and *Tight* are defined by cutting on the LH score and on track parameters. The working points correspond to an average signal efficiency of 93 %, 88 % and 80 %, respectively.
Prompt electrons can be differentiated from electrons created from background processes, like hadrons misidentified as leptons or semileptonic decays of heavy quarks, by measuring the activity in the vicinity of the electron. Two classes of isolation variables can be defined, quantifying the tracks of nearby particles and close-by energy deposits in the calorimeter. Both measure the energy or momentum as a ratio to the electron p_{T} in a cone (of variable size in the ID) around the electron. The isolation working points *Loose* and *Tight* are set up based on the selection signal efficiency.

5.2.2 Muons

Muons are minimum-ionizing particles in the energy regime of the LHC, hence can usually not be stopped within the detector. They are reconstructed by first reconstructing ID tracks as well as MS tracks independently and then combining them to create muon candidates [125]. For the ID tracks, the method described in Section 5.1.1 is applied, while the MS tracks are reconstructed with a different algorithm that will be outlined here.
Firstly, short straight-line local track segments are identified in individual MS stations. These segments are then combined into preliminary track candidates by a combinatorial fitting algorithm, taking into account an approximation for the muon trajectory bending in the magnetic field and a pointing constraint towards the IP. After adding previously not considered hits along the trajectory and removing outliers, a global χ^2 fit is performed to gain the muon trajectory. In the case of multiple tracks sharing the same hits, the track with the lower quality is removed to avoid double counting.
The global muon candidates are created by combining the tracks from the ID and MS, using five different strategies that lead to the following muon types: combined muon (CB), inside-out combined muon (IO), muon spectrometer extrapolated muon (ME), segment-tagged muon (ST) and calorimeter-tagged muon (CT). Both the CB

and the IO strategy match MS tracks to ID tracks by performing a combined track fit. While the CB strategy starts from the MS and interpolates the track towards the ID, the opposite direction is used in the IO strategy. If no ID track can be found for an MS track, the MS track can still be extrapolated to the beamline to form an ME muon. An ST muon is identified by matching an ID track tightly to at least one reconstructed MS segment. Finally, the CT strategy combines ID tracks with calorimeter entries that are consistent with a low-ionizing particle. Overlaps between the different muon types are resolved, prioritizing CB muons, followed by IO, ST, CT and lastly ME muons.

A muon identification is performed to suppress muons from QCD background and increase the purity of prompt muons. It uses criteria on the number of hits in the different parts of the ID and MS, as well as on the track fit quality and the muon type. The three standard working points *Loose*, *Medium* and *Tight* are defined based on signal efficiencies. The efficiencies for these working points vary with the muon's p_T. For muons with $20\,\mathrm{GeV} < p_\mathrm{T}^{\mu} < 100\,\mathrm{GeV}$, the corresponding efficiencies are $99\,\%$, $97\,\%$ and $93\,\%$, respectively. Additional working points exist for low-p_T and high-p_T muons.

Prompt muons can be discriminated from muons originating from hadronic sources by studying the hadronic activity around the muon. The isolation is defined as the amount energy in a cone around the muon, divided by the muon p_T. It is measured independently as track-based isolation in the ID and calorimeter-based isolation in the calorimeter. The two methods are combined to define the variable cone size isolation working points *Loose* and *Tight*, based on the signal efficiency of the selection.

Scale factors and their corresponding uncertainties are determined from $J/\psi \to \mu\mu$ and $Z \to \mu\mu$ measurements using a tag-and-probe method.

5.2.3 Jets

The cone-shaped clusters created by particle showers from interactions with the absorber material in the calorimeters are called *Jets*. Jets are reconstructed from particle-flow objects [126]. The reconstruction is using the anti-k_t algorithm [127] with a radius parameter of $R = 0.4$. It clusters energy deposits in the calorimeter to form jets. Tracks in the ID are taken into account by replacing the energy deposits in the calorimeter originating from primary vertex tracks with the track momenta. The jet energy scale (JES) is calibrated at particle level through MC simulation and further refined with in-situ methods [128]. Differences in the jet energy resolution (JER) between data and MC simulation are treated with a p_T smearing on the simulated jets. Cleaning criteria are applied to remove jets originating from non-collision backgrounds or calorimeter noise [129]. A specialized jet vertex tagger (JVT) algorithm [130] is used to exclude jets within $|\eta| < 2.5$ that are not associated with the primary vertex of the hard-scatter event. Likewise, a dedicated algorithm is applied in the forward region to remove such jets from additional softer proton–proton collisions [131].

5.2.4 *b*-tagged jets

Jets can be classified as *b-jets* identifying them as jets coming from b-hadrons [132]. This can be especially useful for cases where the signal process contains a bottom quark or a background that includes bottom quarks needs to be suppressed. Energetic b-hadrons can travel a significant distance from the hard-scatter vertex due to their lifetime in the picoseconds range, forming a displaced vertex a few millimeters away from the collision point. This is exploited to tag jets originating from b-hadron decays with a two-stage approach. As a first step, a series of low-level algorithms reconstruct the characteristic features of b-jets. The algorithms use both the large impact parameters of tracks from the b-hadron decays and displaced vertices in the process. In the second stage, deep-learning classifiers based on neural networks (NNs) are trained with the results from the low-level algorithms and kinematic properties of the jets. In this analysis, the DL1r tagger is used, providing the working points for b-tagging efficiencies of 85 %, 77 %, 70 % and 60 %, as determined in simulated $t\bar{t}$ events.

5.2.5 Efficiency corrections

All the reconstruction and identification techniques discussed in the previous sections have specific efficiencies. Even though an effort is made to minimize the difference between collision data and MC simulation, typically a small residual efficiency difference remains. Event-wise scale factors are applied to simulations in order to match them to the recorded data. They are calculated as the ratio of the efficiencies ϵ in data and MC simulation:

$$\mathrm{SF} = \frac{\epsilon_{\mathrm{data}}}{\epsilon_{\mathrm{MC}}}.$$

The scale factors for electron reconstruction, identification, isolation and trigger were determined from $J/\psi \to ee$ and $Z \to ee$ events [124, 133]. Muon scale factors from identification, isolation and trigger were derived in $J/\psi \to \mu\mu$ and $Z \to \mu\mu$ events [125, 134]. The JVT and forward-jet vertex tagger (FJVT) efficiencies were determined using $Z \to \mu\mu) +$ jets as well as semileptonic $t\bar{t}$ events [135]. The efficiencies of the b-tagging were measured in $t\bar{t}$ events [136].

5.2.6 Missing transverse energy

The incoming protons of hard-scatter collisions in the ATLAS detector ideally have no momentum in the transverse plane of the detector. As a consequence, the sum of the 2-dimensional transverse momentum vectors ($\vec{p}_{\mathrm{T}} = (p_x, p_y)$) of all objects produced in the collision should be zero. This enables the use of momentum conservation to reconstruct missing energy and momentum from particles that leave the detector without interacting with any detector material, like neutrinos and potential beyond-SM particles.
The missing transverse momentum $\vec{p}_{\mathrm{T}}^{\mathrm{miss}}$ (with magnitude $E_{\mathrm{T}}^{\mathrm{miss}}$) is determined with an algorithm that calculates its direction and magnitude from various physics objects [137]:

$$\vec{p}_{\mathrm{T}}^{\mathrm{miss}} = \underbrace{- \sum_{\substack{\text{selected}\\\text{electrons}}} \vec{p}_{\mathrm{T}}^{e} - \sum_{\substack{\text{accepted}\\\text{photons}}} \vec{p}_{\mathrm{T}}^{\gamma} - \sum_{\substack{\text{accepted}\\\tau-\text{leptons}}} \vec{p}_{\mathrm{T}}^{\tau} - \sum_{\substack{\text{selected}\\\text{muons}}} \vec{p}_{\mathrm{T}}^{\mu} - \sum_{\substack{\text{accepted}\\\text{jets}}} \vec{p}_{\mathrm{T}}^{\mathrm{jet}}}_{\text{hard term}} \underbrace{- \sum_{\substack{\text{unused}\\\text{tracks}}} \vec{p}_{\mathrm{T}}^{\mathrm{track}}}_{\text{soft term}} .$$

It takes into account hard terms, referring to reconstructed physics objects, and a soft term, which aims to cover remaining ID tracks from the hard-scatter event that are not yet used by any of the physics objects in the hard term. An overlap removal procedure is applied to make sure that there is no double-counting of energy deposits in the detector.

5.2.7 Missing Mass Calculator

The reconstruction of decays of resonances into pairs of τ-leptons is challenging because of the neutrinos in the final state. They carry away an unknown fraction of the momentum, making it difficult to determine the properties, like the mass, of the mother particle. The Missing Mass Calculator (MMC) technique is a likelihood-based approach to estimate the mass of a resonance decaying into a τ-lepton pair by studying the visible decay product kinematics. It uses $Z/\gamma \to \tau\tau$ events with τ-lepton momenta from 10 GeV to 100 GeV, however, the method does not depend on the source of the τ-leptons when neglecting the τ-lepton polarization. The detailed description of the algorithm is given in Ref. [138] and briefly outlined here.

The assumption made by the MMC is that only neutrinos from the two τ-lepton decays contribute to the missing transverse momentum. Consequently, this leaves six to eight unknown quantities in the two τ-lepton decays: six from the three entries of the momentum vectors of the two τ-lepton neutrinos ($\vec{p}_{\mathrm{miss},1}, \vec{p}_{\mathrm{miss},2}$) and, for the case of leptonic τ-lepton decays, the invariant mass of the two-neutrino-system of each τ-lepton decay ($m_{\mathrm{miss},1}, m_{\mathrm{miss},2}$). On the other hand, there are only four

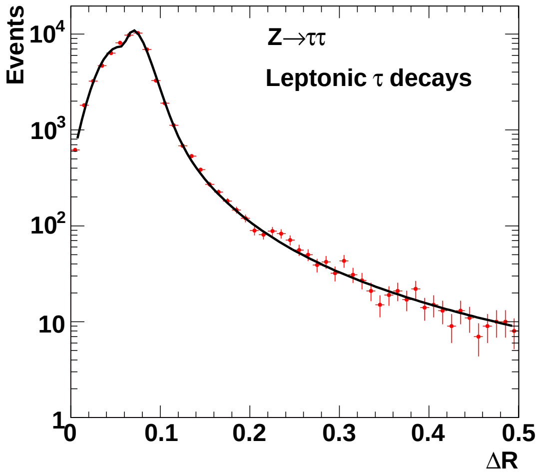

Figure 5.1: Example pdf $\mathcal{P}(\Delta R, p_{\mathrm{T}}^{\tau})$ for a particular value of the original τ-lepton transverse momentum p_{T}^{τ}. The solid line represents the fit functions using a linear combination of Gaussian and Landau functions. [138]

equations relating these unknown quantities: the equations for the invariant masses of the τ-leptons and the equations for the x and y components of $\vec{p}_{\mathrm{T}}^{\mathrm{miss}}$. Hence, it is impossible to find an exact solution, as the number of unknown quantities exceeds the number of constraints. However, not all solutions to these equations are similarly likely and adding further information about τ-lepton decay kinematics can be used to distinguish more probable from improbable solutions. This additional information comes for examples from the expected angular distance

$$\Delta R = \sqrt{(\eta_{\mathrm{vis}} - \eta_{\mathrm{miss}})^2 + (\phi_{\mathrm{vis}} - \phi_{\mathrm{miss}})^2} \tag{5.1}$$

between visible parts (*vis*) of the τ-lepton decay and the neutrinos (*miss*). For each original τ-lepton momentum p_{T}^{τ}, a pdf $\mathcal{P}(\Delta R, p_{\mathrm{T}}^{\tau})$ can be determined. One example pdf is displayed in Figure 5.1.
A solution can be found for the four equations connecting the unknown quantities for any point in the parameter space $(\phi_{\mathrm{miss},1}, \phi_{\mathrm{miss},2}, m_{\mathrm{miss},1}, m_{\mathrm{miss},2})$. At the same time, Equation 5.1 can be used to calculate ΔR for each parameter space point. A probability for this given decay topology can be estimated by utilizing pdfs like the one in Figure 5.1. These pdfs $\mathcal{P}(\Delta R, p_{\mathrm{T}}^{\tau})$ are retrieved from simulated $Z/\gamma^* \to \tau\tau$ events. After applying this process for both τ-leptons, the results are combined into the logarithmic event probability (i.e. likelihood)

$$\mathcal{L} = -\log(\mathcal{P}(\Delta R_1, p_{\mathrm{T}}^{\tau_1}) \times \mathcal{P}(\Delta R_2, p_{\mathrm{T}}^{\tau_2})).$$

These obtained event probabilities are used to weight the invariant mass of the ditau system $m_{\tau\tau}$ for all parameter space points of $(\phi_{\text{miss},1}, \phi_{\text{miss},2}, m_{\text{miss},1}, m_{\text{miss},2})$. Then, a distribution of the weighted $m_{\tau\tau}$ is created. The most probable mass in this distribution is taken as the best estimate for $m_{\tau\tau}$ and called m_{MMC}.
The most probable value of this distribution is used as the final estimator for $m_{\tau\tau}$ and will hereinafter be referred to as m_{MMC}. The measured m_{MMC} distributions for leptonic $A \to \tau\tau$ and $Z \to \tau\tau$ decays are displayed in Figure 5.2. It is shown that despite the unknown neutrino momenta, the masses of the original particles can be reconstructed well. The resolution is better for low-mass points, i.e. far away from the influence of the mass-dependent and the $\Delta R_{\ell\ell}$ cuts (see Section 6.2). The resolution of the $Z \to \tau\tau$ process is similar (mean = 84.0 GeV, $1\,\sigma$ = 12.5 GeV) to the one reported in the SM $H \to \tau\tau$ measurement [139].

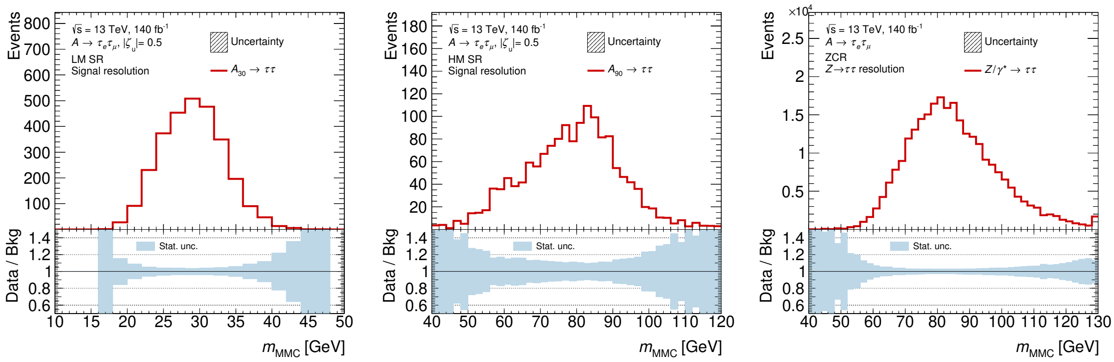

(a) (b) (c)

Figure 5.2: Measured m_{MMC} distributions for $A \to \tau\tau$ events with (a) $m_A = 30$ GeV in the low-mass signal region (LMSR) and (b) $m_A = 90$ GeV in the high-mass signal region (HMSR) as well as (c) for $Z \to \tau\tau$ events in the $Z \to \tau\tau$ control region (ZCR).

6 Search for a light CP-odd Higgs boson

In the main part of this thesis, the search for a light CP-odd Higgs boson decaying into a pair of τ-leptons is presented. The focus is set on the leptonic decay channels of the τ-leptons despite their smaller branching ratios because they allow exploiting the lower lepton p_{T} trigger thresholds. The analysis described in this thesis forms a major part of the results published in Ref. [19]. It is giving further insight into the methods used and provides additional studies compared to the published paper. Additionally, the mass range of the probed A boson values is expanded to 110 GeV, while the previously published results only cover the region up to 90 GeV.

This thesis also builds up and expands on results from various bachelor's (see Refs. [140, 141]) and master's theses (see Refs. [142–147]), which were mostly advised by the author of this thesis.

A key part of the analysis design is to select events based on certain selection criteria to reduce background from SM processes and maximize the signal sensitivity. In this analysis, the main signal features that are used for this are the angles of the τ-lepton decay products and the reconstructed mass of the CP-odd Higgs boson. Before applying these cuts, the expected background needs to be understood. It is modeled using MC simulation and data-driven methods. This required to set up a selection of control and validation regions to derive, study and validate the modeling. Afterwards, the statistical and systematic uncertainties are analyzed, and a fit is carried out using a profile likelihood method [148].

The author of this thesis had major contributions to all analysis parts, starting from the analysis setup, going through background estimation, uncertainty calculation and statistical analysis to the interpretation of the results.[1]

6.1 Higgs signal samples

The signal process for this analysis is the gluon–gluon fusion production of an A boson that decays in to a pair of τ-leptons: $gg \to A \to \tau\tau$. It was simulated with the Pythia 8.2 [104] generator using leading order (LO) MEs for the signal

[1] Details about the contributions are given in the appendix.

mass range from 20 GeV to 110 GeV in steps of 10 GeV. Additionally, samples for 25 GeV, 75 GeV, 85 GeV, 95 GeV and 105 GeV are produced. The simulation parameters for Pythia were set according to the A14 tune using the PDF set NNPDF2.3lo. The truth-level distribution for the mass hypotheses $m_A = 40$ GeV and $m_A = 90$ GeV are displayed in Figure 6.1. To avoid generating lots of events that would be disregarded by the trigger later, the generator-level lepton p_{T} filter *lep15lep6* was applied, requiring the leading lepton to have $p_{\mathrm{T}}^{\mathrm{leadlep}} > 15$ GeV and the subleading lepton to have $p_{\mathrm{T}}^{\mathrm{subleadlep}} > 6$ GeV. The effects of this filter are visible in the electron and muon p_{T} distributions in form of the double-peak structure. The $\Delta R_{\ell\ell}$ distribution for the 40 GeV mass point in Figure 6.1(c) shows that for the lower mass points a topology where the two leptons are closer together is preferred. The signal production cross-sections have been calculated at next-to-next-to-next-to-leading order (N^{3}LO) with `ggHiggs` [149–160] version 4.0. The PDF set PDF4LHC15_nnlo was used with the value $\alpha_s = 0.118$ (at m_Z) for the strong coupling, the coupling parameter of the A boson to up-type quarks has been set to $\cot\beta = \zeta_{\mathrm{u}} = 1$, the top-quark mass used is 172.5 GeV and the factorization and renormalization scales are set to $\frac{\mu_{\mathrm{F,R}}}{m_A} = 1.0$. The obtained cross-section values are listed in Table 6.1. The list of all MC signal samples is provided in Section B.2.2.

Table 6.1: N^{3}LO prediction of the production cross-section for A bosons, $\sigma(pp \to A + X)$, via gluon–gluon fusion in the mass range from 20 GeV to 110 GeV. The values were calculated with `ggHiggs` [149–160] version 4.0. The fermionic coupling strength parameter of the A boson to up-type quarks was set to $\cot\beta = \zeta_{\mathrm{u}} = \zeta_\ell = 1$. The relevant uncertainties are given in Table 6.6.

m_A [GeV]	20	25	30	40	50	60	70	75
$\sigma(pp \to A + X)$ [pb]	1854	1394	1090	722	514	385	299	266

m_A [GeV]	80	85	90	95	100	105	110
$\sigma(pp \to A + X)$ [pb]	239	215	195	178	162	149	137

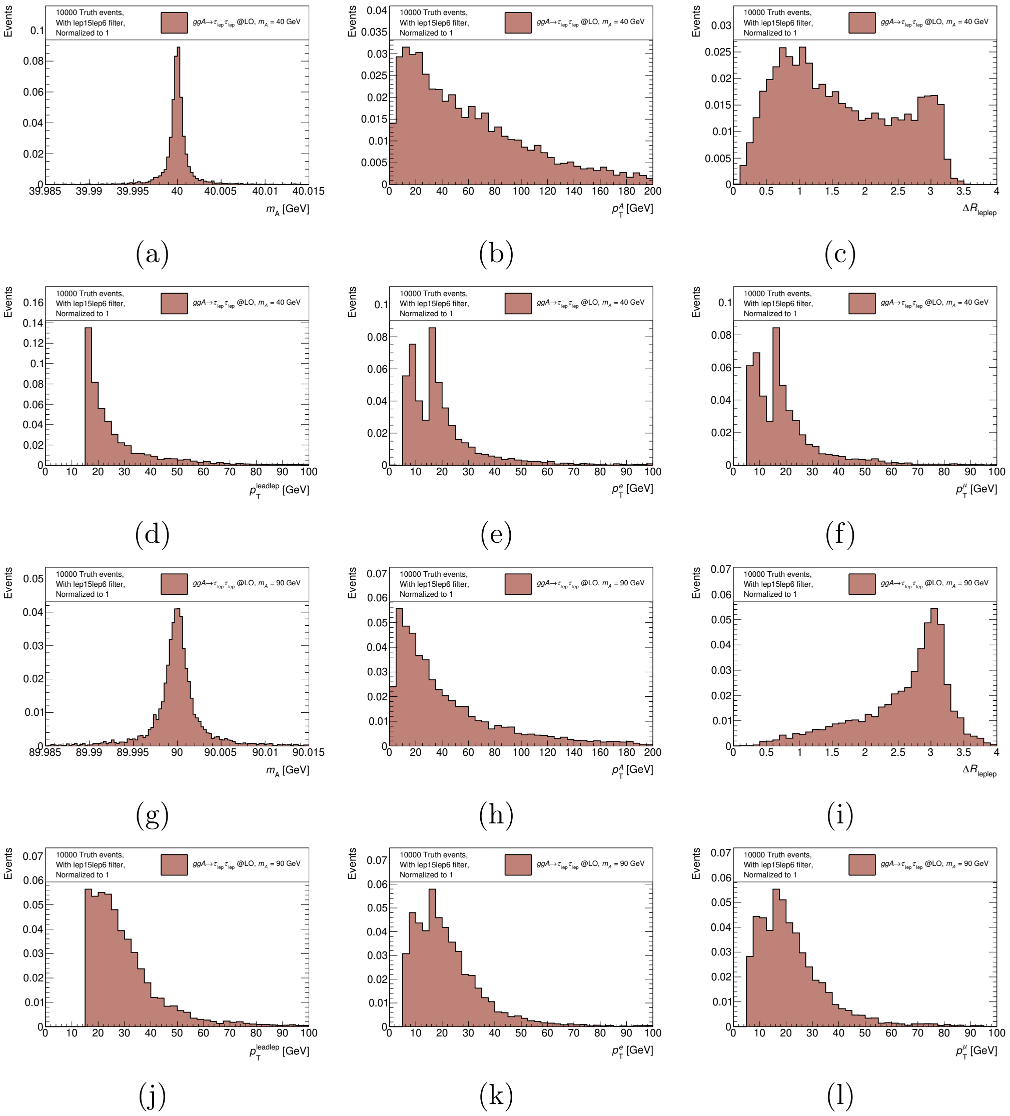

Figure 6.1: Truth-level variable distribution of A bosons produced in gluon–gluon fusion with PYTHIA 8.2 at LO MEs. The generator-level lepton p_{T} filter *lep15lep6* was applied, requiring the leading lepton to have $p_{\mathrm{T}} > 15\,\mathrm{GeV}$ and the subleading lepton to have $p_{\mathrm{T}} > 6\,\mathrm{GeV}$. The figures (a) to (f) show the distributions from an A boson with the mass $m_A = 40\,\mathrm{GeV}$ while for (g) to (l) the mass is $m_A = 90\,\mathrm{GeV}$. The mass distributions of the A bosons are shown in (a) and (g) with their transverse momenta displayed in (b) and (h). Figures (c) and (i) give the angular distance between the two leptons. The p_{T} distributions are shown in (d) and (j) for the leading lepton, in (e) and (k) for the electron and in (f) and (l) for the muon.

6.2 Event selection

In the quest to discover light CP-odd Higgs bosons, the production cross-section of the hypothetical Higgs signal is typically much smaller than that of the various SM background processes. This necessitates a specialized selection process to maximize signal contribution while minimizing background contamination. The *signal region* (SR) describes the selected phase space which has the best signal sensitivity. By modifying the selection criteria, additional phase space regions can be defined that are rich in specific SM backgrounds but have low signal contamination. These background-enriched regions are used for the most important backgrounds to validate the modeling or assist in the background estimation within the SR. Regions used for the former purpose are called *validation regions* (VRs), while those aiding in background estimation are called *control regions* (CRs). This section provides an overview of the baseline selection and the definitions of the various regions. Two SRs are set up: the low-mass signal region (LMSR) for the lower mass hypotheses and the high-mass signal region (HMSR) for the higher ones. The two main MC backgrounds are controlled using the $Z \to \tau\tau$ control region (ZCR) for $Z \to \tau\tau$ events and the Top control region (TCR) for top-quark events. The data-driven background from fake- and non-prompt leptons is estimated and validated in the fake-lepton validation region (FVR) as well as in the low-mass same-sign validation region (LMSSVR) and high-mass same-sign validation region (HMSSVR). The selection criteria for all regions are summarized in Table 6.2 and explained in more detail in the following sections.

6.2.1 Baseline selection

The first selection step of the recorded data is vetoing events that fail common data quality criteria. Events are only accepted if their corresponding luminosity block (LB) is found in the centrally provided Good Runs List (GRL) [98, 99]. These are built for each data-taking period and listed in Section B.2.1. Additional vetoes are installed for events that were recorded in a period when parts of the detector were not fully operational or when the event contains signals from non-collision backgrounds. These can originate from cosmic rays, calorimeter cell noise or beam-induced background [129]. After applying these event quality criteria, a set of loose requirements are required with the goal to preselect suitable candidates for τ-lepton pairs coming from an A boson decay.

The event needs to contain at least one electron and one muon which shall fire the trigger as described in the following Section 6.2.2. Leptons are required to fulfill *Loose* identification and *Loose* isolation criteria. A requirement on the transverse momentum of the leptons is set to $p_{\mathrm{T}} > 7\,\mathrm{GeV}$. Muons need to lie within $|\eta| < 2.7$ while electrons need to have $|\eta| < 2.47$. Additionally, events with electrons in

Table 6.2: Overview of the selection criteria for all analysis regions. In the nominal regions and for the results of the analysis, *Medium* identification and *Tight* isolation criteria are used [124, 125]. Additionally, *Loose* criteria are used in the fake-lepton background estimation.

	SR		TCR	ZCR	FVR	SS VR	
	Low-mass	High-mass				Low-mass	High-mass
$\lvert\eta_e\rvert$	$[0, 1.37] \cup [1.52, 2.47]$						
$\lvert\eta_\mu\rvert$	$[0, 2.7]$						
$\lvert\eta_{\text{jet}}\rvert$	$[0, 4.5]$						
p_{T}^{ℓ}	$> 10\,\text{GeV}$						
$p_{\text{T}}^{\text{jet}}$	$> 20\,\text{GeV}$						
$E_{\text{T}}^{\text{miss}}$	$> 50\,\text{GeV}$	$> 30\,\text{GeV}$	$> 30\,\text{GeV}$	–	–	$> 50\,\text{GeV}$	$> 30\,\text{GeV}$
$m_{\text{T}}^{\text{tot}}$	$< 45\,\text{GeV}$	$< 65\,\text{GeV}$	$< 65\,\text{GeV}$	$< 65\,\text{GeV}$	$< 65\,\text{GeV}$	$< 45\,\text{GeV}$	$< 65\,\text{GeV}$
$\Delta R_{\ell\ell}$	< 0.7	< 1.0	< 1.0	> 1.4	> 1.4	< 0.7	< 1.0
m_{MMC}	$> 0\,\text{GeV}$	$> 35\,\text{GeV}$& $< 130\,\text{GeV}$	$> 0\,\text{GeV}$	$> 0\,\text{GeV}$	$> 0\,\text{GeV}$	$> 0\,\text{GeV}$	$> 35\,\text{GeV}$& $< 130\,\text{GeV}$
$q_e \cdot q_\mu$	-1	-1	-1	-1	1	1	1
$n_{b\text{-jets}}$	0	0	≥ 2	0	0	0	0

the crack region $1.37 < |\eta| < 1.52$ are disregarded. Furthermore, all events that contain electrons or muons, which are flagged as 'bad' by the cleaning algorithms, are removed.
Jets are required to have a p_{T} of at least 20 GeV and have to lie within the range $|\eta| < 4.5$. Jets within $|\eta| < 2.5$ are b-tagged as described in Section 5.2.4.
To prevent the case that tracks or energy deposits in the detector are used for more than one physical object, an overlap removal procedure is put in place. It is designed to give priority to objects with a higher signal purity while maintaining events with the final state produced by the signal process. For this analysis, it means that muons are favored over electrons and leptons are favored over jets. An overview of the overlap removal procedure is given in Table 6.3.

After all the above-mentioned lepton requirements, events with more than one electron or more than one muon are vetoed because no additional leptons are expected in the decay of the A boson.
Whilst commonly used for ATLAS analyses, no impact parameter cuts are applied to the leptons here. This is due to the leptons coming from τ-leptons and not directly from the primary vertex. A study has been performed to check the influence of the standard impact parameter cuts ($|\sigma(d_0)/d_0| < 5$ and $|z_0 \cdot \sin\theta| < 0.5$ for electrons

Table 6.3: Overview of the performed overlap removal. If one of the objects in the first column is within a cone of ΔR around the object in the second column, it is removed. The overlap removal between electrons and muons is carried out first.

Object removed	Object kept	Angular separation ΔR
electron	muon	0.2
jet	electron	0.4
jet	muon	0.4

and $|\sigma(d_0)/d_0| < 3$ and $|z_0 \cdot \sin\theta| < 0.5$ for muons). The electron cuts reduce the signal yield by $10-15\,\%$ while maintaining a similar signal-to-background ratio. For the muon cuts the reduction is of the order of $30\,\%$ and the signal-to-background ratio is worsened as well.
Tables summarizing all the selection criteria and specifying the tool settings can be found in Section B.1.

6.2.2 Trigger

Events are required to be accepted by any of the electron–muon triggers that were active during the data-taking periods. It has been chosen to use these triggers with two different lepton flavors in order to highly suppress the background from Z boson decays to electron or muon pairs: $Z/\gamma^* \to ee$ and $Z/\gamma^* \to \mu\mu$.
There are three different triggers that cover the signatures of this analysis. In the following, the triggers are referred to as `e7mu24`, `e17mu14` and `e26mu8`, where the given numbers refer to the online p_{T} thresholds for the electron and the muon. The list of considered triggers is given in Table 6.4, together with the full specifications on HLT level. The leptons firing the trigger have to be matched to the two leptons with the highest p_{T} in the event. The matching is performed using a ΔR cone between the lepton and the trigger signature with the thresholds $\Delta R < 0.07$ for electrons and $\Delta R < 0.1$ for muons. Single-lepton triggers have been analyzed and were found not to improve the sensitivity of this search, hence they are not used. More details on the investigations on single-lepton triggers can be found in Section B.5.
Due to trigger efficiency turn-on effects and the necessary trigger efficiency simulations, not all triggered events are good for physics analyses. In general, the trigger efficiencies are provided starting from 1 GeV above the online p_{T} threshold. In the two cases of the very low-p_{T}, this criterion is extended slightly, so that for both

Table 6.4: Overview of the utilized HLT triggers. The term 'nod0' specifies that no d_0 information (information about the distance between particle track and hard-scattering vertex in the x-y plane) is used. The term 'noL1' shows that the object reconstruction happens without L1 seed. The term 'L1EM20VHI' ('L1EM22VHI') contains the information that hadronic core isolation ('H') and electromagnetic isolation ('I') are applied, the p_{T} is above 20 GeV (22 GeV) and the p_{T} threshold varies with η to incorporate energy loss ('V').

Data-taking year	Short name	ATLAS trigger name
2015	`e7mu24`	`HLT_e7_lhmedium_mu24`
	`e17mu14`	`HLT_e17_lhloose_mu14`
	`e26mu8`	`HLT_e24_lhmedium_nod0_L1EM20VHI_mu8noL1`
2016	`e7mu24`	`HLT_e7_lhmedium_nod0_mu24`
	`e17mu14`	`HLT_e17_lhloose_nod0_mu14`
	`e26mu8`	`HLT_e26_lhmedium_nod0_L1EM22VHI_mu8noL1`
$2017-18$	`e7mu24`	`HLT_e7_lhmedium_nod0_mu24`
	`e17mu14`	`HLT_e17_lhloose_nod0_mu14`
	`e26mu8`	`HLT_e26_lhmedium_nod0_mu8noL1`

the electron and the muon the lower p_{T} cut is set to $p_{\mathrm{T}}^{\ell} > 10\,\mathrm{GeV}$. Furthermore, the electron p_{T} cut for the `e26mu8` is kept at $p_{\mathrm{T}}^{e} > 27\,\mathrm{GeV}$ for all data-taking years. Whilst it would have been possible to lower it for the 2015 data by 2 GeV, it was decided to keep it at the same level for simplicity reasons and because the extra amount of events would be negligible. The three are combined by always using the central `e17mu14` trigger and combining it on both sides with one of the other two triggers as illustrated in Figure 6.2. The separation between the two side triggers is chosen diagonally such that efficiency can be recovered both for high-p_{T} electrons and muons similarly.

6.2.3 Common selection for all regions

All nominal regions require both the electron and the muon to pass *Medium* identification and *Tight* isolation criteria. This helps to select prompt leptons and reduces the contamination of leptons from other sources, like misidentification from jets or heavy flavor decays. Furthermore, events for which the MMC algorithm

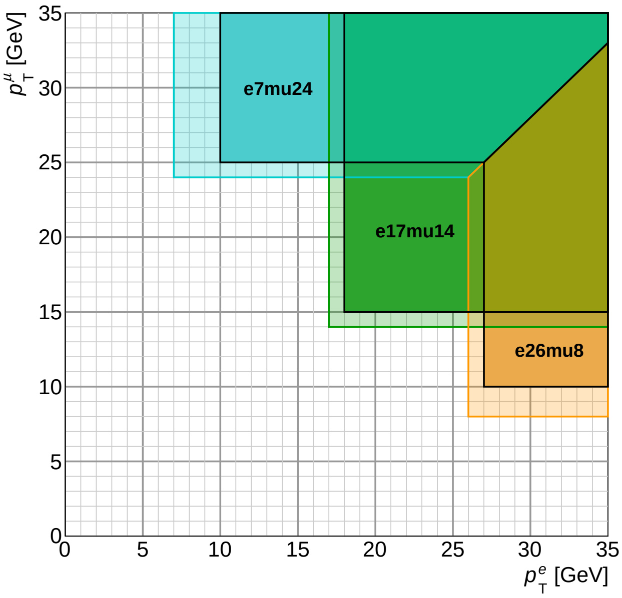

Figure 6.2: Schematic illustration of the electron–muon trigger p_{T} ranges. The `e7mu24` and `e26mu8` triggers are strictly separated by p_{T} selection criteria, i.e. a maximum of two triggers are used in the analysis simultaneously. In the transparent regions, the triggers are active but are excluded in the analysis to avoid the p_{T} intervals close to the trigger turn-on regions.

does not converge (resulting in negative algorithm output values) are vetoed. After tuning the parameters, this only happens to less than 3 % of events (for signals and most backgrounds less than 0.5 % of events), but they are nevertheless rejected to ensure all selected events are well understood.

6.2.4 Signal region definitions

The definition of the SR depends on the probed mass of the A boson: the mass points from 20 to 75 GeV are evaluated in the LMSR while the masses from 75 to 110 GeV are evaluated in the HMSR. The 75 GeV mass hypothesis is chosen as the cutoff value because of a similar expected sensitivity in the two SRs. It is evaluated in both of them in order to be able to extrapolate the obtained results both towards lower and higher masses. A common requirement for both SRs is that the leptons must have an opposite charge. This arises from the electrical neutrality of the A boson. Furthermore, the number of b-tagged jets, $n_{b\text{-jets}}$, has to be zero. This ensures that the background from top quarks is reduced significantly.

The SRs have individual selection criteria on three main variables: $E_{\mathrm{T}}^{\mathrm{miss}}$, the angular distance between the electron and the muon $\Delta R_{\ell\ell}$, and the total transverse mass defined as

$$m_{\mathrm{T}}^{\mathrm{tot}} = \sqrt{(p_{\mathrm{T}}^{e} + p_{\mathrm{T}}^{\mu} + E_{\mathrm{T}}^{\mathrm{miss}})^2 - (\vec{p}_{\mathrm{T}}^{\,e} + \vec{p}_{\mathrm{T}}^{\,\mu} + \vec{p}_{\mathrm{T}}^{\,\mathrm{miss}})^2}.$$

A large $E_{\mathrm{T}}^{\mathrm{miss}}$ is preferred because of the four neutrinos in the final state of the signal process. Selecting only events with small $\Delta R_{\ell\ell}$, i.e. requiring the charged leptons to be emitted at small angles, helps to greatly reduce the $Z \to \tau\tau$ background. It is motivated by the spin, mass and CP properties of the A boson signal. A study showing the different $\Delta R_{\ell\ell}$ distributions of the signal process and the $Z \to \tau\tau$ background is given in Section B.7. The requirement on $m_{\mathrm{T}}^{\mathrm{tot}}$ removes background from processes with larger produced masses compared to the signal process. This primarily eliminates events from diboson and top-quark processes, but also helps with cutting down events from SM Higgs and $Z \to \tau\tau$ decays.

High-mass signal region

The HMSR uses the selection cut values $E_{\mathrm{T}}^{\mathrm{miss}} > 30\,\mathrm{GeV}$, $\Delta R_{\ell\ell} < 1.0$ and $m_{\mathrm{T}}^{\mathrm{tot}} < 65\,\mathrm{GeV}$. In addition to that, a cut window for m_{MMC} is introduced: $35\,\mathrm{GeV} < m_{\mathrm{MMC}} < 130\,\mathrm{GeV}$. This helps to cut out areas with no expected signal, while reducing the overall fake-lepton background and its corresponding large uncertainties.

Low-mass signal region

The LMSR sets tighter cuts on the three former variables because the signal distribution is further away from the relevant backgrounds and a better signal-to-background ratio can be achieved like this. The selection used is $E_{\mathrm{T}}^{\mathrm{miss}} > 50\,\mathrm{GeV}$, $\Delta R_{\ell\ell} < 0.7$ and $m_{\mathrm{T}}^{\mathrm{tot}} < 45\,\mathrm{GeV}$.

Kinematic implications of the cuts

The combination of these selection criteria also has the effect of favoring A bosons with a sizable transverse momentum. Depending on the mass hypothesis, the corresponding distribution of the transverse momentum of the ditau system starts between 100 and 200 GeV as can be seen in Figure 6.3. For reasons of transverse momentum conservation, hadronic jets are emitted in the opposite direction. As a consequence, the process '$pp \to A + \text{jets}$' is preferred for this topology (which is only considering gluon–gluon fusion as suggested by the flavor-aligned 2HDM).

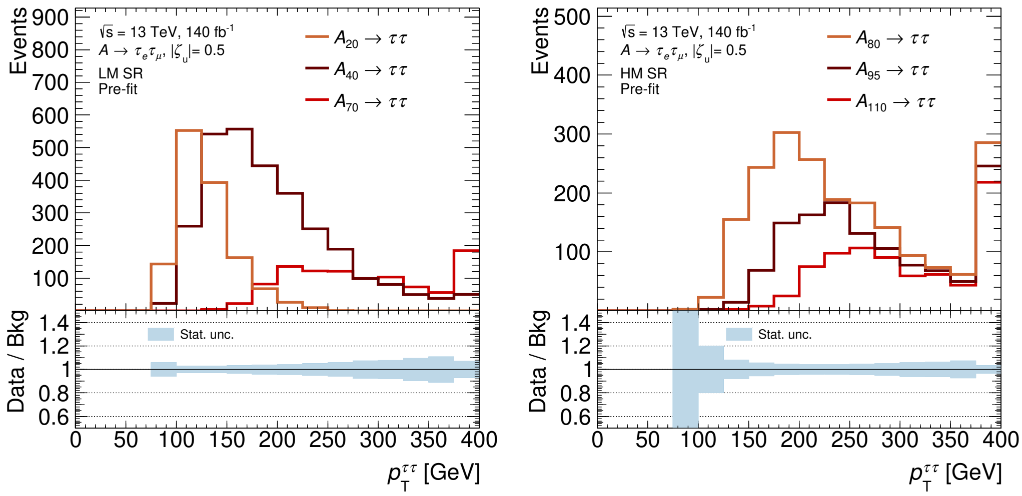

(a) (b)

Figure 6.3: Signal distributions of the p_{T} of the reconstructed ditau system in (a) the LMSR and (b) the HMSR.

6.2.5 Control and validation region definitions

Two CRs and three VRs are set up to assist with the background modeling in the SRs. The former cover the two largest backgrounds that are modeled by MC simulation while the three latter are used in the data-driven fake-lepton estimation.

$Z \to \tau\tau$ control region

The main background of this analysis is originating from $Z \to \tau\tau$ decays. They have a very similar decay topology as the signal process and are therefore hard to separate from each other. The goal for the ZCR is to have an abundance of $Z \to \tau\tau$ decays, being orthogonal to the SR and having a low contamination of signal events, while at the same time being kinematically close to the SR. This is realized by choosing similar selection criteria as for the SR, but only accepting events with $\Delta R_{\ell\ell} > 1.4$. Requiring this and at the same time dropping the $E_{\mathrm{T}}^{\mathrm{miss}}$ criterion is helping with gaining a large $Z \to \tau\tau$ sample with low signal contamination of under $3\,\%$ because the leptons in the Z boson decay are well separated.

Top control region

The TCR is used to control the background from processes that involve top quarks, which are responsible for one of the largest backgrounds in this analysis. The selection criteria are almost identical to that of the HMSR, except that at least two b-tagged jets are required in each event. This ensures a high abundance of top-quark processes while keeping the signal contamination below 1 %. It was also tested to require $n_{b-\mathrm{jets}} \geq 1$, but this resulted in a still too large signal contamination.

Fake-lepton validation region

The FVR is constructed to perform the data-driven fake-lepton estimation in a phase space enriched in non-prompt leptons. It uses the same cuts as the ZCR, except for requiring the two leptons to have the same charge. As SM processes usually do not produce two leptons with different flavor and the same charge, this gives a very pure sample of non-prompt leptons. After the estimation, the obtained fake-lepton background can be validated. Furthermore, this region is utilized to extract systematic uncertainties on the fake-lepton background and the estimation method.

High-mass same-sign validation region

The HMSSVR is a copy of the HMSR with the only exception of the charge cut, as it requires the two leptons to have the same charge. Consequently, it contains mostly non-prompt leptons, similarly to the FVR but being kinematically closer to the HMSR. It is used in the validation of the fake-lepton background estimation and determination of its systematic uncertainties.

Low-mass same-sign validation region

The LMSSVR is a copy of the LMSR with the only exception of the charge cut, as it requires the two leptons to have the same charge. As the previous two explained regions, it contains mostly non-prompt leptons, but it is suffering from worse statistics. For that reason, it is only used in studies for the fake-lepton estimation.

6.3 Background estimation

Backgrounds generated by SM processes are a significant part of the event yields within the SR. Therefore, it is essential to identify these contributing processes and develop methods to estimate and validate them accurately. Except for fake-lepton backgrounds, all backgrounds are estimated using MC simulation. The major backgrounds stem from decays of Z and W bosons as well as top quarks. Due to the complexity of simulating quark and gluon hadronization, backgrounds where one or more QCD jets are misidentified as leptons require a data-driven estimation. These backgrounds from fake or non-prompt leptons, as well as leptons with a misidentified charge will hereinafter be collectively referred to as 'fake-lepton background'. This section provides an overview of the simulated SM processes and the data-driven methods used, with a particular focus on validating the background estimation.

6.3.1 Monte Carlo simulated backgrounds

The backgrounds estimated from MC simulation in this analysis are all modeled differently. The processes include those with vector bosons (both diboson and V+jets, with $V = W, Z$), top quarks (produced as $t\bar{t}$ pairs, as single-top in s- or t-channel, or in association with a W boson: tW), and SM Higgs bosons.
The production processes of V+jets were simulated with the Sherpa 2.2.1 [105] generator with next-to-leading order (NLO) MEs for up to two partons, and LO MEs for up to four partons, calculated with the OpenLoops [161–163] and Comix [164] libraries. They were matched with the Sherpa PS[165] applying the MEPS@NLO prescription [166–169], thereby using the set of tuned parameters as developed by the Sherpa authors. The NNPDF3.0nnlo PDFs set [170] was used and the samples were normalized to a next-to-next-to-leading order (NNLO) prediction [171].
Samples for the diboson final states VV were simulated with the Sherpa 2.2.1 or 2.2.2 generator depending on the process, including off-shell effects and SM Higgs boson contributions, where appropriate. Fully leptonic final states and semileptonic final states, where one boson decays leptonically and the other hadronically, were generated using NLO accuracy MEs in QCD for up to one additional parton and LO accuracy for up to three additional emitted partons. Samples for the loop-induced processes $gg \to VV$ were generated using LO-accurate MEs for up to one additional emitted parton for both fully leptonic and semileptonic final states. The ME calculations were matched and merged with the Sherpa PS based on Catani–Seymour dipole factorization applying the MEPS@NLO prescription. The virtual QCD corrections were provided by the OpenLoops library. The NNPDF3.0nnlo PDFs set was used, along with the dedicated set of tuned PS parameters as developed by the Sherpa authors.
All top-quark processes were modeled using the PowhegBox v2 [172–175] generator at NLO with the NNPDF3.0nlo PDF set. The single-top t-channel production used the four-flavor scheme while the s-channel and tW single-top events used

the five-flavor scheme. For the $t\bar{t}$ process, the resummation damping factor h_{damp}, that controls the matching of the POWHEG MEs to the PS and hence effectively regulates the high-p_{T} radiation against which the $t\bar{t}$ system recoils, was set to $1.5\,m_t$ [176]. The diagram removal scheme [177] was used for the tW sample to remove interferences and overlap with the $t\bar{t}$ production. For all processes, the events were interfaced with PYTHIA 8.230 [104] to model the PS, hadronization, and the underlying event, thereby setting the parameters according to the A14 tune [107] and using the NNPDF2.3LO set of PDFs [178]. The decays of bottom and charm hadrons were performed by EVTGEN 1.6.0 [179].
The last background considered is from SM Higgs bosons. Its production processes were all simulated using POWHEGBOX V2 [180, 181], which was consequently interfaced with PYTHIA 8 for non-perturbative effects and parton showering. The PDF set PDF4LHC15NLO [182] was used together with the AZNLO tune [183] of PYTHIA 8. The SM Higgs boson production via gluon–gluon fusion was simulated at NNLO accuracy in QCD while the vector-boson fusion production used NLO accuracy. The POWHEG prediction achieves NLO for the Vh production accompanied by a single jet. The loop-induced $gg \to Zh$ process was independently generated at LO. The normalization of all SM Higgs boson samples incorporates the decay branching ratios calculated with HDECAY [184–186] and PROPHECY4F [187–189]. The MC prediction for SM Higgs boson production through gluon–gluon fusion was normalized to match the cross-section calculated to N^{3}LO in QCD with NLO electroweak (EW) corrections [156, 157, 159, 190–197], while that for production through vector-boson fusion was matched to the cross-section calculated to approximate-NNLO in QCD with NLO EW corrections [198–200]. The MC predictions for $q\bar{q}/qg \to Vh$ and $gg \to Zh$ were normalized to the cross-sections calculated up to NNLO in QCD using NLO EW corrections or to NLO with next-to-leading-logarithm accuracy in QCD, respectively [201–207].
The complete list of all SM background samples and their production settings is given in Section B.2.2.

6.3.2 Higher order corrections to the $t\bar{t}$ MC background

Previous studies have seen improved agreement between data and prediction in $t\bar{t}$ events, particularly for the top-quark p_{T} distribution, when comparing with NNLO calculations [208]. Top-quark pair differential calculations, carried out at NNLO QCD accuracy and including EW corrections, became available through Ref. [209]. Hence, a small improvement to the modeling is incorporated by correcting all $t\bar{t}$ samples to match their top quark p_{T} distribution to that predicted at NNLO in QCD and NLO EW accuracy.
The distributions of the applied weights are shown in Figure 6.4 for the TCR, LMSR and HMSR. The weights are similar across the three regions and the overall

changes in the event yields from $t\bar{t}$ are less than 0.5 %. This is expected as this reweighting is nominally not touching the overall normalization (but small changes can still occur due to the specific phase space selection). The changes of the reweighting on the leading lepton p_{T} in the TCR are displayed in Figure 6.5. It is the variable most sensitive to the reweighting. Before applying the corrections, there is a visible slope in the data-to-background ratio. With the reweighting, this slope is corrected and almost entirely disappears.

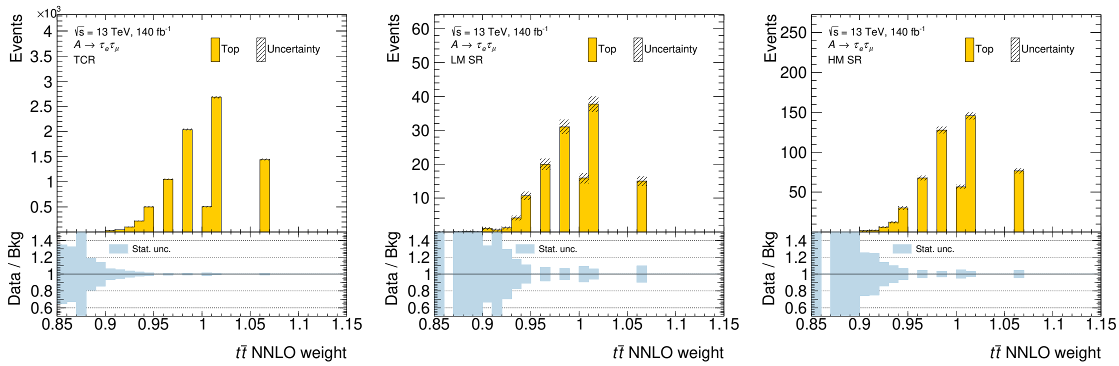

(a) (b) (c)

Figure 6.4: Distribution of the $t\bar{t}$ reweighting weights in (a) the TCR, (b) the LMSR and (c) the HMSR.

6.3.3 Data-driven modeling of the fake-lepton background

The collision data contains events, in which one or both final-state particles were mistakenly reconstructed as prompt leptons, while the actual source of these leptons are hadronic jets, decays of heavy quarks or photon conversions. MC simulations cannot reliably simulate these backgrounds, hence data-driven approaches are commonly used. One such approach is the matrix method [210], which is particularly beneficial in scenarios where events with either zero, one, or two fake leptons are expected.

The basic idea is to use the efficiencies of fake and real leptons meeting the *Tight* criteria (*Medium* identification and *Tight* isolation), to estimate the amount of fake-lepton events from the number of events with *Tight* and *Non-tight* leptons of a *Baseline* selection (*Loose* identification and *Loose* isolation). The efficiencies for fake leptons, $\varepsilon^{\ell}_{\text{fake}}$, and for real leptons, $\varepsilon^{\ell}_{\text{real}}$, are calculated as the rate of events with *Tight* leptons to the events of the *Baseline* selection. The numbers of events with *Tight* and *Non-tight* leptons is connected to the numbers of fake and real

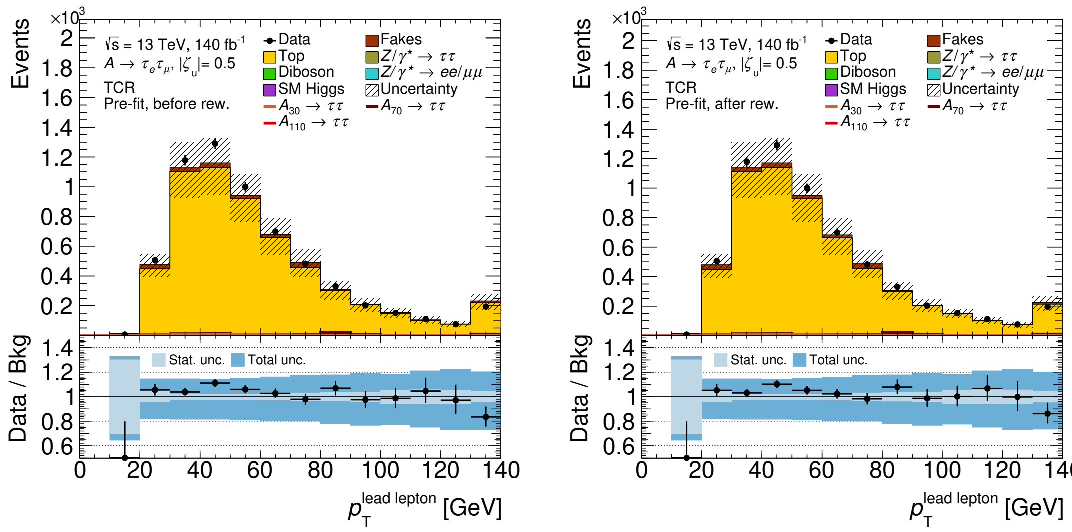

(a) (b)

Figure 6.5: Distribution of the leading lepton p_T in the TCR (a) before the $t\bar{t}$ reweighting and (b) after the $t\bar{t}$ reweighting. The slight slope that was observed in the ratio plot before the reweighting (a) almost vanishes after the reweighting (b).

Baseline leptons by the equation

$$\mathbf{N}^{\mathrm{T}} = \begin{pmatrix} N^{\mathrm{TT}}_{\mathrm{XX}} \\ N^{\mathrm{T\overline{T}}}_{\mathrm{XX}} \\ N^{\mathrm{\overline{T}T}}_{\mathrm{XX}} \\ N^{\mathrm{\overline{T}\overline{T}}}_{\mathrm{XX}} \end{pmatrix} = \begin{pmatrix} \varepsilon^e_{\mathrm{real}}\varepsilon^\mu_{\mathrm{real}} & \varepsilon^e_{\mathrm{real}}\varepsilon^\mu_{\mathrm{fake}} & \varepsilon^e_{\mathrm{fake}}\varepsilon^\mu_{\mathrm{real}} & \varepsilon^e_{\mathrm{fake}}\varepsilon^\mu_{\mathrm{fake}} \\ \varepsilon^e_{\mathrm{real}}\bar{\varepsilon}^\mu_{\mathrm{real}} & \varepsilon^e_{\mathrm{real}}\bar{\varepsilon}^\mu_{\mathrm{fake}} & \varepsilon^e_{\mathrm{fake}}\bar{\varepsilon}^\mu_{\mathrm{real}} & \varepsilon^e_{\mathrm{fake}}\bar{\varepsilon}^\mu_{\mathrm{fake}} \\ \bar{\varepsilon}^e_{\mathrm{real}}\varepsilon^\mu_{\mathrm{real}} & \bar{\varepsilon}^e_{\mathrm{real}}\varepsilon^\mu_{\mathrm{fake}} & \bar{\varepsilon}^e_{\mathrm{fake}}\varepsilon^\mu_{\mathrm{real}} & \bar{\varepsilon}^e_{\mathrm{fake}}\varepsilon^\mu_{\mathrm{fake}} \\ \bar{\varepsilon}^e_{\mathrm{real}}\bar{\varepsilon}^\mu_{\mathrm{real}} & \bar{\varepsilon}^e_{\mathrm{real}}\bar{\varepsilon}^\mu_{\mathrm{fake}} & \bar{\varepsilon}^e_{\mathrm{fake}}\bar{\varepsilon}^\mu_{\mathrm{real}} & \bar{\varepsilon}^e_{\mathrm{fake}}\bar{\varepsilon}^\mu_{\mathrm{fake}} \end{pmatrix} \cdot \begin{pmatrix} N^{\mathrm{BB}}_{\mathrm{RR}} \\ N^{\mathrm{BB}}_{\mathrm{RF}} \\ N^{\mathrm{BB}}_{\mathrm{FR}} \\ N^{\mathrm{BB}}_{\mathrm{FF}} \end{pmatrix} = \mathbf{M} \cdot \mathbf{N}^{\mathrm{R}}, \tag{6.1}$$

where $\bar{\varepsilon}^\ell_{\mathrm{real/fake}} = 1 - \varepsilon^\ell_{\mathrm{real/fake}}$.

The indices of the event yields N should be interpreted as follows. The upper indices represent the tightness of the leptons: T indicates a *Tight* lepton, $\overline{\mathrm{T}}$ indicates a *Non-tight* lepton, and B indicates a lepton that meets the *Baseline* selection without additional tightness requirements. The lower indices specify whether an event is from data or MC simulation. For MC events, they also indicate whether the lepton is real (R), fake (F), or has no specific 'truth' requirement (X). The first index always refers to the electron, and the second to the muon.

For example, $N^{\mathrm{TL}}_{\mathrm{FX}}$ is the number of MC events with a *Tight* fake electron and a muon that passes the baseline selection, and $N^{\mathrm{\overline{T}T}}_{\mathrm{Data}}$ is the number of data events with a *Non-tight* electron and a *Tight* muon.

Inverting the matrix from Equation 6.1 allows an estimation of the event numbers of real- and fake-lepton events:

$$\mathbf{N}^{\mathrm{R}} = \mathbf{M}^{-1} \cdot \mathbf{N}^{\mathrm{T}},$$

with the inverted matrix

$$\mathbf{M}^{-1} = \frac{1}{(\varepsilon^e_{\text{real}} - \varepsilon^e_{\text{fake}})(\varepsilon^\mu_{\text{real}} - \varepsilon^\mu_{\text{fake}})} \begin{pmatrix} \bar{\varepsilon}^e_{\text{fake}}\bar{\varepsilon}^\mu_{\text{fake}} & -\bar{\varepsilon}^e_{\text{fake}}\varepsilon^\mu_{\text{fake}} & -\varepsilon^e_{\text{fake}}\bar{\varepsilon}^\mu_{\text{fake}} & \varepsilon^e_{\text{fake}}\varepsilon^\mu_{\text{fake}} \\ -\bar{\varepsilon}^e_{\text{fake}}\bar{\varepsilon}^\mu_{\text{real}} & \bar{\varepsilon}^e_{\text{fake}}\varepsilon^\mu_{\text{real}} & \varepsilon^e_{\text{fake}}\bar{\varepsilon}^\mu_{\text{real}} & -\varepsilon^e_{\text{fake}}\varepsilon^\mu_{\text{real}} \\ -\bar{\varepsilon}^e_{\text{real}}\bar{\varepsilon}^\mu_{\text{fake}} & \bar{\varepsilon}^e_{\text{real}}\varepsilon^\mu_{\text{fake}} & \varepsilon^e_{\text{real}}\bar{\varepsilon}^\mu_{\text{fake}} & -\varepsilon^e_{\text{real}}\varepsilon^\mu_{\text{fake}} \\ \bar{\varepsilon}^e_{\text{real}}\bar{\varepsilon}^\mu_{\text{real}} & -\bar{\varepsilon}^e_{\text{real}}\varepsilon^\mu_{\text{real}} & -\varepsilon^e_{\text{real}}\bar{\varepsilon}^\mu_{\text{real}} & \varepsilon^e_{\text{real}}\varepsilon^\mu_{\text{real}} \end{pmatrix}.$$

The total fake-lepton background is obtained by summing the fake-electron, fake-muon, and double-fake-lepton backgrounds:

$$N^{\mathrm{TT}}_{\text{fake}} = \varepsilon^e_{\text{real}}\varepsilon^\mu_{\text{fake}} N^{\mathrm{BB}}_{\mathrm{RF}} + \varepsilon^e_{\text{fake}}\varepsilon^\mu_{\text{real}} N^{\mathrm{BB}}_{\mathrm{FR}} + \varepsilon^e_{\text{fake}}\varepsilon^\mu_{\text{fake}} N^{\mathrm{BB}}_{\mathrm{FF}},$$

with the individual contributions to the fake-electron, fake-muon, and double-fake-lepton backgrounds:

$$\begin{aligned} N^{\mathrm{BB}}_{\mathrm{RF}} &= \frac{-\bar{\varepsilon}^e_{\text{fake}}\bar{\varepsilon}^\mu_{\text{real}} N^{\mathrm{TT}}_{\mathrm{XX}} + \bar{\varepsilon}^e_{\text{fake}}\varepsilon^\mu_{\text{real}} N^{\mathrm{T\overline{T}}}_{\mathrm{XX}} + \varepsilon^e_{\text{fake}}\bar{\varepsilon}^\mu_{\text{real}} N^{\mathrm{\overline{T}T}}_{\mathrm{XX}} - \varepsilon^e_{\text{fake}}\varepsilon^\mu_{\text{real}} N^{\mathrm{\overline{TT}}}_{\mathrm{XX}}}{(\varepsilon^e_{\text{real}} - \varepsilon^e_{\text{fake}})(\varepsilon^\mu_{\text{real}} - \varepsilon^\mu_{\text{fake}})}, \\ N^{\mathrm{BB}}_{\mathrm{FR}} &= \frac{-\bar{\varepsilon}^e_{\text{real}}\bar{\varepsilon}^\mu_{\text{fake}} N^{\mathrm{TT}}_{\mathrm{XX}} + \bar{\varepsilon}^e_{\text{real}}\varepsilon^\mu_{\text{fake}} N^{\mathrm{T\overline{T}}}_{\mathrm{XX}} + \varepsilon^e_{\text{real}}\bar{\varepsilon}^\mu_{\text{fake}} N^{\mathrm{\overline{T}T}}_{\mathrm{XX}} - \varepsilon^e_{\text{real}}\varepsilon^\mu_{\text{fake}} N^{\mathrm{\overline{TT}}}_{\mathrm{XX}}}{(\varepsilon^e_{\text{real}} - \varepsilon^e_{\text{fake}})(\varepsilon^\mu_{\text{real}} - \varepsilon^\mu_{\text{fake}})}, \\ N^{\mathrm{BB}}_{\mathrm{FF}} &= \frac{\bar{\varepsilon}^e_{\text{real}}\bar{\varepsilon}^\mu_{\text{real}} N^{\mathrm{TT}}_{\mathrm{XX}} - \bar{\varepsilon}^e_{\text{real}}\varepsilon^\mu_{\text{real}} N^{\mathrm{T\overline{T}}}_{\mathrm{XX}} - \varepsilon^e_{\text{real}}\bar{\varepsilon}^\mu_{\text{real}} N^{\mathrm{\overline{T}T}}_{\mathrm{XX}} + \varepsilon^e_{\text{real}}\varepsilon^\mu_{\text{real}} N^{\mathrm{\overline{TT}}}_{\mathrm{XX}}}{(\varepsilon^e_{\text{real}} - \varepsilon^e_{\text{fake}})(\varepsilon^\mu_{\text{real}} - \varepsilon^\mu_{\text{fake}})}. \end{aligned} \tag{6.2}$$

While the matrix method is capable of giving a good estimate of the fake-lepton background, it also has possible drawbacks. The Equation 6.2 shows that the obtained background yields are not necessarily positive. This is because $\varepsilon^\ell_{\text{real}} \in [0,1]$ and $\varepsilon^\ell_{\text{fake}} \in \left[0, \varepsilon^\ell_{\text{real}}\right)$, such that TT and $\overline{\mathrm{TT}}$ events contribute positively to double-fake-lepton but negatively to single-fake-lepton events, while it is the opposite for $\overline{\mathrm{T}}\mathrm{T}$ and $\mathrm{T}\overline{\mathrm{T}}$ events. Due to uncertainties on event counts and efficiencies, this can sometimes yield negative total event numbers, especially in low-statistics bins.

6.3.4 Calculation of real- and fake-lepton efficiencies for the matrix method

The fake- and real-lepton efficiencies are essential inputs to the matrix method and need to be measured. They are defined as the fraction of *Tight* leptons to the *Baseline* leptons. In the conventional matrix method, the efficiencies of the two leptons are considered independent. However, in this analysis it was observed that the efficiencies of fake leptons are showing a slight dependence on the other (fake) lepton in the event. To account for this behavior, a parametrization is introduced, which considers the tightness of the other lepton. This means that the electron efficiencies are dependent on the muon's tightness, and vice versa:

$$\varepsilon^{e}_{\text{real}}(\mu) = \begin{cases} \dfrac{N^{\text{TT}}_{\text{RX}}}{N^{\text{BT}}_{\text{RX}}}, & \mu \text{ Tight} \\[2ex] \dfrac{N^{\text{T}\bar{\text{T}}}_{\text{RX}}}{N^{\text{B}\bar{\text{T}}}_{\text{RX}}}, & \mu \text{ Non-tight} \end{cases}, \quad \varepsilon^{e}_{\text{fake}}(\mu) = \begin{cases} \dfrac{N^{\text{TT}}_{\text{Data}} - N^{\text{TT}}_{\text{RX}}}{N^{\text{BT}}_{\text{Data}} - N^{\text{BT}}_{\text{RX}}}, & \mu \text{ Tight} \\[2ex] \dfrac{N^{\text{T}\bar{\text{T}}}_{\text{Data}} - N^{\text{T}\bar{\text{T}}}_{\text{RX}}}{N^{\text{B}\bar{\text{T}}}_{\text{Data}} - N^{\text{B}\bar{\text{T}}}_{\text{RX}}}, & \mu \text{ Non-tight} \end{cases},$$

$$\varepsilon^{\mu}_{\text{real}}(e) = \begin{cases} \dfrac{N^{\text{TT}}_{\text{XR}}}{N^{\text{TB}}_{\text{XR}}}, & e \text{ Tight} \\[2ex] \dfrac{N^{\bar{\text{T}}\text{T}}_{\text{XR}}}{N^{\bar{\text{T}}\text{B}}_{\text{XR}}}, & e \text{ Non-tight} \end{cases}, \quad \varepsilon^{\mu}_{\text{fake}}(e) = \begin{cases} \dfrac{N^{\text{TT}}_{\text{Data}} - N^{\text{TT}}_{\text{XR}}}{N^{\text{TB}}_{\text{Data}} - N^{\text{TB}}_{\text{XR}}}, & e \text{ Tight} \\[2ex] \dfrac{N^{\bar{\text{T}}\text{T}}_{\text{Data}} - N^{\bar{\text{T}}\text{T}}_{\text{XR}}}{N^{\bar{\text{T}}\text{B}}_{\text{Data}} - N^{\bar{\text{T}}\text{B}}_{\text{XR}}}, & e \text{ Non-tight} \end{cases}.$$

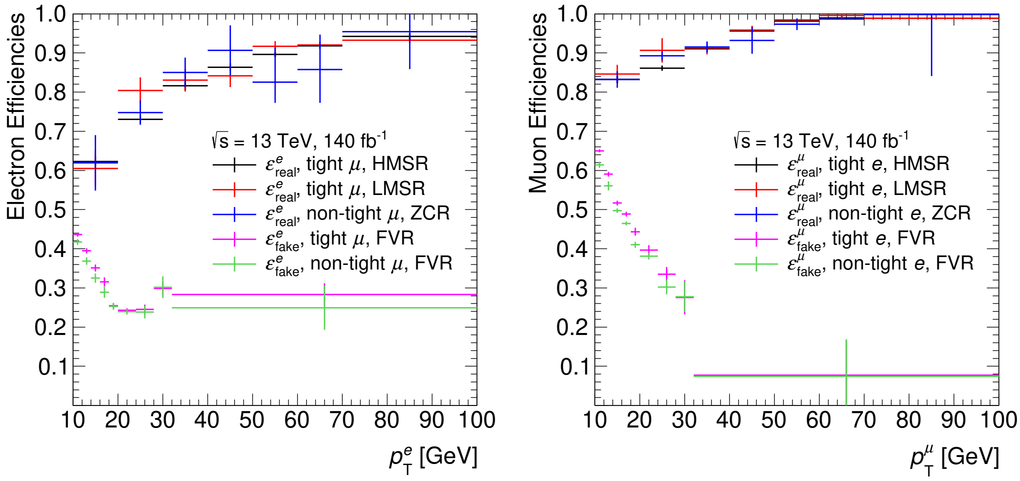

(a) (b)

Figure 6.6: Real- and fake-lepton efficiencies for (a) electrons and (b) muons that have a *Tight* or *Non-tight* accompanying (a) muon and (b) electron, binned in p_{T}^{e} and p_{T}^{μ}, respectively. The real-lepton efficiencies for a *Tight* accompanying lepton are obtained from the HMSR and LMSR, the real-lepton efficiencies for a *Non-tight* accompanying lepton are measured in the ZCR, and fake-lepton efficiencies are retrieved from the FVR.

As the efficiencies can depend on several parameters, they need to be calculated as close to the SR as possible. For the real-lepton efficiencies accompanied by a

Tight lepton, it is possible to extract them directly from there, as the SR contains a sufficient number of well-modeled MC events with prompt leptons. Different real-lepton efficiencies were calculated for the LMSR and HMSR, where for the former the cut on $E_{\mathrm{T}}^{\mathrm{miss}}$ was removed to gain more statistics. The real efficiencies with an accompanying *Non-tight* lepton are calculated in the ZCR because of the much better statistics compared to the SR.
For the calculation of the fake-lepton efficiencies, however, one needs a region enriched in fake leptons, the closest to the SR with sufficient statistics being the FVR. Furthermore, fake leptons are generally not modeled well in MC simulation. Hence, they have to be measured in data. To ensure that only fake leptons are used in the calculations, the real lepton contamination, as taken from the MC truth record, is subtracted from the events first. Both efficiencies with an accompanying *Tight* and *Non-tight* lepton are measured in the FVR.
The measured efficiencies, binned in the p_{T} of the respective lepton, are shown in Figure 6.6. It is visible that the fake-lepton efficiencies depend on the tightness of the accompanying lepton for low p_{T} values, while the real-lepton efficiencies are statistically compatible within the tightness. Additional parametrizations were not feasible due to the limited number of event in the available regions. The dependence on η^{ℓ}, $E_{\mathrm{T}}^{\mathrm{miss}}$ and the number of jets in the event are added as systematic uncertainties. Various studies have been done to check the behavior of the efficiencies in dependence of variables or data-taking conditions. They are summarized in Section B.3.2 to Section B.3.5 and cover efficiencies measured in different analysis regions, data-taking years and for various n_{jets} and $\Delta R_{\ell\ell}$ values.

6.3.5 Data-driven $Z \to \tau\tau$ reweighting

The distribution of different variables in the ZCR using the standard selection criteria can be seen in Figure 6.7. It is apparent that a mismodeling can be observed for $E_{\mathrm{T}}^{\mathrm{miss}}$ in the range from 30 to 100 GeV. This region is especially important for this analysis since the HMSR starts only at $E_{\mathrm{T}}^{\mathrm{miss}} > 30\,\mathrm{GeV}$, the LMSR only at $E_{\mathrm{T}}^{\mathrm{miss}} > 50\,\mathrm{GeV}$, and $Z \to \tau\tau$ is the main background in the SRs. It seems like the MC generator does not model $p_{\mathrm{T}}^{\tau\tau}$ and the interplay with jets well. However, other distributions, like the p_{T} of the leading lepton, and the overall normalization show a good modeling. A number of studies has been carried out to investigate the cause of this behavior. They are summarized in Section B.6. As no satisfactory conclusion has been found, a data-driven reweighting method is chosen to improve the agreement between data and prediction in the ZCR.
None of the other backgrounds contribute enough to cover the whole difference between data and background, hence it was assumed that the major cause of this mismodeling lies in the $Z \to \tau\tau$ MC sample. A data-driven approach is used to reweight all $Z \to \tau\tau$ MC events, similar to the one done in the ATLAS $Z \to \ell\ell\gamma$

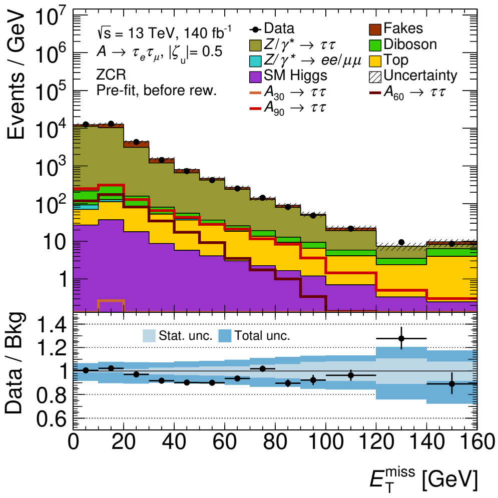

(a)

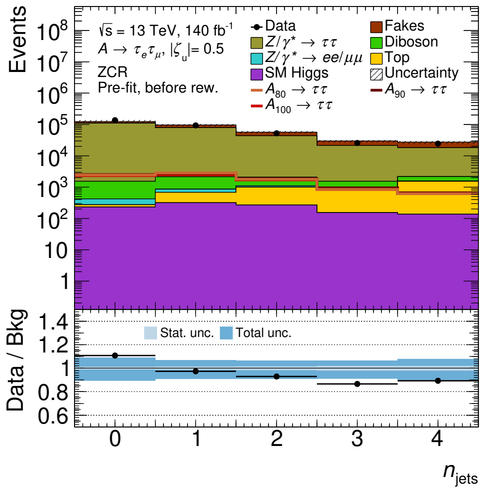

(b)

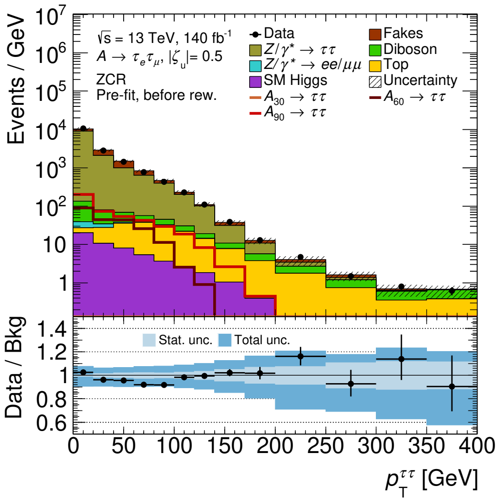

(c)

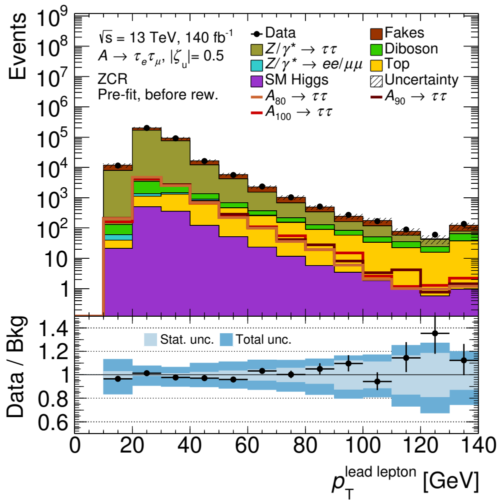

(d)

Figure 6.7: Variable distributions in the ZCR after complete selection criteria but without reweighting of the $Z \to \tau\tau$ events as described in Section 6.3.5: (a) E_T^{miss}, (b) n_{jets}, (c) $p_T^{\tau\tau}$, (d) $p_T^{\text{lead lepton}}$. A mismodeling is observed in the E_T^{miss} and n_{jets} distributions which is not entirely covered by the uncertainties. Other distributions, like $p_T^{\text{lead lepton}}$, show a good modeling. The distribution of $p_T^{\tau\tau}$ shows some features in the data-to-background ratio, but these are well covered by the uncertainties.

measurement [211]. The weights are calculated as the ratio of expected number of

$Z \to \tau\tau$ events over the simulated number in the ZCR:

$$\text{weight} = \frac{(\text{Data} - \sum_{i \neq Z \to \tau\tau} \text{Background}_i)}{\text{Background}_{Z \to \tau\tau}}. \tag{6.3}$$

The expected events are obtained from the difference between data and other predicted background events that do not originate from $Z \to \tau\tau$. The fake-lepton background (see Section 6.3.3) also needs to be taken into account here, which means that the efficiencies for the matrix method need to be determined prior to the calculation of the $Z \to \tau\tau$ reweighting weights.

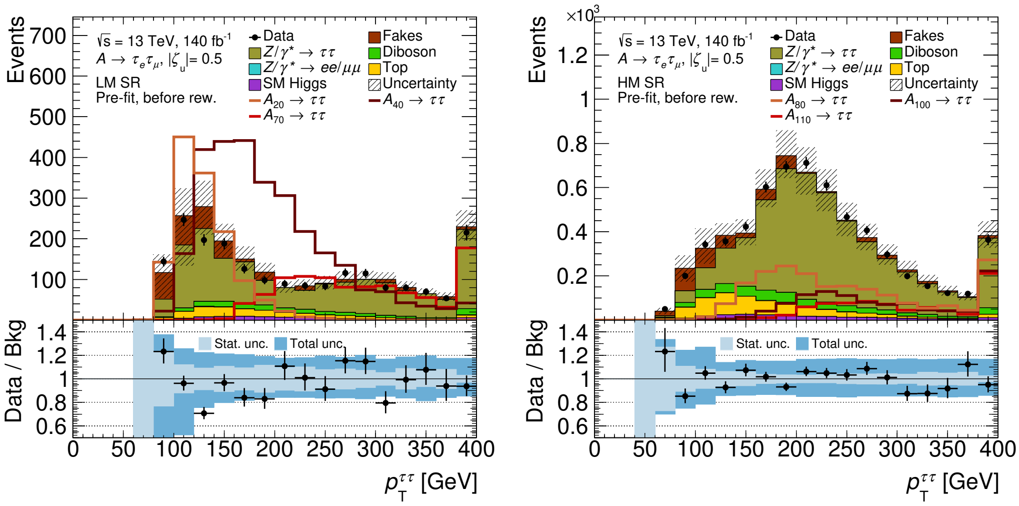

(a) (b)

Figure 6.8: Distributions of the p_{T} of the reconstructed ditau system in (a) the LMSR and (b) the HMSR before the reweighting of the $Z \to \tau\tau$ events. Due to the cut on $\Delta R_{\ell\ell}$, the ditau system has a significant p_{T} in both regions.

The calculation of these weights is performed in the ZCR where the $Z \to \tau\tau$ background is most prevalent and the mismodeling appears. The weights are binned in the number of jets as seen in Figure 6.9. Other searches use the p_{T}^{Z} distribution instead (which can best be approximated in this analysis with $p_{\mathrm{T}}^{\tau\tau}$) to bin their weights. However, this is not feasible here, as the ZCR and SRs are separated by $\Delta R_{\ell\ell}$, which correlates strongly with $p_{\mathrm{T}}^{\tau\tau}$, such that weights calculated in the ZCR would not be applicable in the SRs. The distributions of $p_{\mathrm{T}}^{\tau\tau}$ in the SRs are shown in Figure 6.8. They peak at around 125 GeV and 200 GeV, respectively, which is in a regime where the number of events in the ZCR has already decreased

drastically (see Figure 6.7c), hence the extrapolation of weights would not be reliably possible.
The weights are then applied to all $Z \to \tau\tau$ MC events according to their number of jets. The same weights are used in all regions, including the SR, assuming the

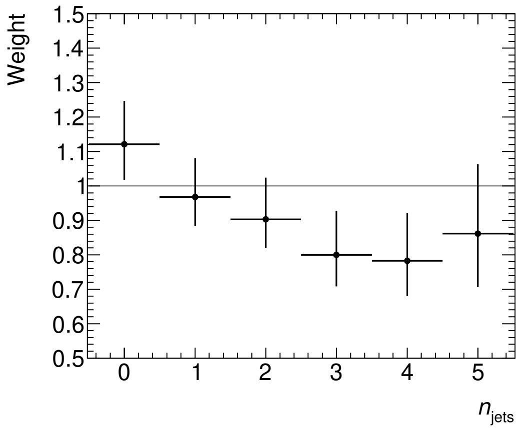

Figure 6.9: Reweighting weights for the $Z \to \tau\tau$ MC background, binned in the number of jets and calculated according to Equation 6.3. They are shown with their total uncertainty. The displayed weight for $n_{\text{jets}} = 5$ contains also all larger jet multiplicities.

mismodeling in the $Z \to \tau\tau$ sample is independent of the cuts used to separate them. A study has been done (see Section B.3.1) on whether there is any impact of this reweighting procedure on the efficiencies for the matrix method, and vice versa. It was found that the efficiencies are only very marginally affected and the changes are not seen in the plots or final event numbers. This has two reasons: For the real efficiencies one divides the number of *Tight* leptons by the number of *Baseline* leptons and the reweighting is basically independent of this ratio. For the fake efficiencies data is used, so the reweighting only could depend on the real MC events that are subtracted from data. $Z \to \tau\tau$ contributes only to 0.2 % to the background in the FVR where the fake efficiencies are measured, so no impact is expected there. Therefore, no iteration of determining efficiencies and reweighting weights needs to be done.
This $Z \to \tau\tau$ MC reweighting method leads to an improved modeling not only of n_{jets} and $p_{\text{T}}^{\tau\tau}$, but also of $E_{\text{T}}^{\text{miss}}$ and other variables as is shown in Figure 6.17 and Figure B.13. While the reweighting works well in the ZCR, extrapolations to the other regions could lead to unwanted effects. In particular, the weights reduce the $Z \to \tau\tau$ background in regions with one or more jets, which is the case for both SRs, by 5–20 %. Hence, a general excess observed in the SRs might be caused by

this reweighting procedure and would need a careful examination. However, as the uncertainties on the reweighting weights (which are further detailed in Section 6.4.6) cover unity in most cases, the effect is expected to be insignificant.

6.4 Systematic uncertainties

All measurements carried out in the CRs, VRs and SRs come with various uncertainties. One differentiates between statistical and systematic uncertainties, which are treated separately. Events that pass the selection are assumed to be uncorrelated, so the event yield probabilities follow a Poisson distribution around the measured value n_i. For statistical uncertainties on the data, n_i represents the number of measured events, while for MC generated samples, it is the sum of all event weights for the specific bin.
Systematic uncertainties arise from a number of different sources and can be categorized into 'experimental uncertainties', which originate from measurements, and 'theoretical uncertainties', which stem from the modeling of processes. While the latter are specific to a single process or a group of processes, the former ones depend on detector simulations and object reconstruction, and are therefore process independent.
The experimental uncertainties are further split into 'factor systematics' and 'calibration systematics'. For the factor systematics, the same set of events are used and only a multiplicative factor is varied. This could for example be the data/MC scale factor of the muon trigger efficiency. When computing calibration systematics, the whole analysis chain needs to be repeated because varying the calibration of objects can change the selected events. An example for this would be the momentum scale calibration of muons.
The full statistical model is explained later in this chapter in Section 6.6 and the fit setup is given in Section 6.6.2. For the understanding of this section, it is sufficient to point out that a binned likelihood function is used and for each systematic uncertainty, a nuisance parameter (NP) is assigned using a Gaussian prior.

6.4.1 Experimental uncertainties

Experimental uncertainties can be centrally estimated because they apply to all simulations rather than specific processes. Typically, these uncertainties are determined by the ATLAS combined performance group responsible for the relevant object or parameter. They recommend various sets of variations to be applied to each simulated data set. These uncertainties are grouped based on their type and the related physics object. The following paragraphs briefly explain these groups. Unless otherwise stated, the uncertainties are considered as both 'up' and 'down'

Table 6.5: Summary of all the experimental systematics groups and numbers of considered NPs.

NP group	Description	Number of NPs
LUMI	integrated luminosity measurement	1
MUON	muon resolution and energy scale	4
MUON_EFF	muon systematics from trigger, reconstruction, isolation and identification	9
EG	electron resolution and energy scale	3
EL_EFF	electron systematics from trigger, reconstruction, isolation and identification	176
MET	E_T^{miss} soft term resolution and scale	3
JET	jet energy scale and resolution	17
JET_EFF	jet vertex tagging efficiency	2
FT	flavor-tagging efficiency	11
PRW	pile-up reweighting	1

variations. This analysis follows the latest available ATLAS combined performance group recommendations. A summary of these systematics is provided in Table 6.5, and the detailed names of the NPs are listed in Section C.1.

Electron calibration (EG)

This group covers all systematics related to the calibration of electrons [212].[2] Systematic uncertainties are applied for electron energy resolution (`EG_RESOLUTION_ALL`) and the energy scale (`EG_SCALE_ALL` for samples using the full detector simulation and `EG_SCALE_AF2` for samples using the Atlfast-ii simulation) variations. In these simplified sets, multiple variations of the electron energy scale are combined.

Electron efficiencies (EL_EFF)

This group incorporates variations that account for the effects of electron

[2]It also includes the calibration of photons but they are not relevant in this analysis.

efficiency measurements [124, 133]. Each efficiency is divided into several NPs and categorized into correlated and uncorrelated uncertainties. The `SIMPLIFIED` correlation model is applied to the correlated variations. These sets contain systematic uncertainties arising from measurements of reconstruction (18 NPs for `EL_EFF_Reco_SIMPLIFIED_UncorrUncertainty` and 7 NPs for `EL_EFF_Reco_CorrUncertainty`), identification (18 NPs for `EL_EFF_ID_SIMPLIFIED_UncorrUncertainty` and 16 NPs for `EL_EFF_ID_CorrUncertainty`), isolation (18 NPs for `EL_EFF_Iso_SIMPLIFIED_UncorrUncertainty` and 11 NPs for `EL_EFF_Iso_CorrUncertainty`), and trigger (18 NPs for `EL_EFF_Trigger_SIMPLIFIED_UncorrUncertainty` and 11 NPs for `EL_EFF_Trigger_CorrUncertainty`) efficiencies.

Muon calibration (MUON)

Variations covering the systematic uncertainties of muon measurements are contained in this group [213]. Uncertainties in the muon calibration arise from the smearing of MS and ID tracks (`MUON_CB`), the muon momentum scale (`MUON_SCALE`), a charge-dependent momentum scale correction (`MUON_SAGITTA_DATASTAT`) and the remaining bias after applying the charge-dependent momentum scale corrections (`MUON_SAGITTA_RESBIAS`).

Muon efficiencies (MUON_EFF)

This set collects the uncertainties on muon efficiencies [125, 134]. The uncertainties are split into a statistical (`STAT`) and a systematic (`SYS`) part for each efficiency. The variations provide uncertainties for muon reconstruction (`MUON_EFF_RECO_SYS` and `MUON_EFF_RECO_STAT`), isolation (`MUON_EFF_ISO_SYS` and `MUON_EFF_ISO_STAT`) and trigger (`MUON_EFF_TrigSystUncertainty` and `MUON_EFF_TrigStatUncertainty`) efficiencies. In addition to that, separate reconstruction efficiency uncertainties for low-p_{T} muons are used (`MUON_EFF_RECO_STAT_LOWPT` and `MUON_EFF_RECO_SYS_LOWPT`).

Jet calibration (JET)

This group assembles the systematic uncertainties from the jet energy scale and resolution calibration [128]. As jets only play a minor role in the analysis, it is sufficient to use the reduced set of variations. This results in eight effective parameters for the jet energy scale: four for the η-intercalibration (`JET_EtaIntercalibration_NonClosure_posEta`, `JET_EtaIntercalibration_NonClosure_negEta`, `JET_EtaIntercalibration_`

NonClosure_highE and JET_EtaIntercalibration_NonClosure_2018data), one for flavor response (JET_Flavour_Response) and three supplementary grouped parameters (JET_Grouped). The jet energy resolution uncertainties are represented by seven effective NPs (JET_JER_Effective), one NP for the data–vs–MC divergence (JET_JER_DataVsMC_MC16) and one residual NP (JET_JER_SINGLE_NP).

Jet efficiencies (JET_EFF)

The systematic uncertainties from efficiency variations in the jet vertex tagging are grouped in this collection [130]. Variations are taken into account for the efficiency of the jet vertex tagging (JET_JvtEfficiency, with a separate NP for the forward region JET_fJvtEfficiency).

Missing transverse momentum (MET)

The uncertainties of the hard terms for the $E_{\mathrm{T}}^{\mathrm{miss}}$ calculation are already included through the relevant objects. For the track-based soft term, uncertainties from the scale (MET_SoftTrk_Scale) and resolution (MET_SoftTrk_ResoPara and MET_SoftTrk_ResoPerp) are considered [137]. The latter ones are one-sided uncertainties.

Flavor-tagging efficiencies (FT_EFF)

A reduced set of variations is used to model the uncertainties on the efficiencies for the flavor-tagging of jets [136]. The uncertainties are evaluated separately for the jet flavor. Two NPs are used for b-quark jets (FT_EFF_Eigen_B), three NPs for c-quark-jets (FT_EFF_Eigen_C) and four NPs for jets originating from light quarks (FT_EFF_Eigen_Light). Additional uncertainties are added for the extrapolation into high-p_{T} regimes for b-tagging weights (FT_EFF_extrapolation with two NPs), and for covering the mistagging of c-quark-jets (FT_EFF_extrapolation_from_charm).

Pile-up reweighting (PRW)

One systematic uncertainty is included for the reweighting procedure that corrects the pile-up profile in MC to match the pile-up observed in data (PRW_DATASF). It covers the uncertainties from the measurement of the data-to-MC scale factor.

Luminosity (LUMI)

The simulated events are scaled to the recorded data using the integrated luminosity. It has been measured with an uncertainty of 0.83 % [91, 97]. In this analysis, this luminosity uncertainty only appears in the fitting and limit calculation, but not in the variable distribution plots, where it is negligible.

6.4.2 Cross-section uncertainties for background processes

Cross-section uncertainties are added for the relevant background processes according to recommendations from the responsible ATLAS working groups. Same as for the luminosity, they are only added in the fitting procedure and limit calculation.

$Z \to \tau\tau$ background

Systematic uncertainties on the production cross-section arise from missing higher order (MHO) corrections, PDFs and chosen input parameters. The relative uncertainties on the production cross-section for $Z \to \tau\tau$ are 1.9 % for $m_{\ell\ell} > 66\,\text{GeV}$ and 5 % for $m_{\ell\ell} < 66\,\text{GeV}$ [214].

Top-quark processes background

The top-quark processes are heavily (>90 %) dominated by $t\bar{t}$, hence the production cross-section uncertainty for $t\bar{t}$ is taken for all top-quark processes. The other production modes single-top in s-channel, t-channel and W-associated production have similar uncertainty predictions and tests have shown that using the exact values does not have any influence on the fit results.
The $t\bar{t}$ production cross-section is $\sigma_{t\bar{t}} = 833.9^{+20.5}_{-30.0}$ (scale) $\pm\,21.0$ (PDF + α_s) pb as calculated with the `Top++2.0` program to NNLO in perturbative QCD, including soft-gluon resummation to next-to-next-to-leading-log order (see Ref. [215] and references therein), and assuming a top-quark mass $m_t = 172.5\,\text{GeV}$. The first uncertainty comes from the independent variation of the factorization and renormalization scales, μ_F and μ_R, while the second one is associated to variations in the PDFs and α_s, following the PDF4LHC prescription with the MSTW2008NNLO 68 % confidence level (CL), CT10NNLO and NNPDF2.3 PDF sets (see Ref. [216] and references therein, and Ref. [178, 217, 218]). The envelope of 4.4 % is taken as the production cross-section uncertainty for the top-quark processes.

Diboson background

Diboson processes include decays of the vector-boson pairs WW, WZ and ZZ. The systematic uncertainties on the different production cross-sections vary slightly. The relative uncertainties of the measured cross-sections are 7.1 % (WW) [219], 4.5 % (WZ) [220], 6.8 % (ZZ) [221] and 8.6 % for the rare $Z \to 4\ell$ decay [222]. The envelope of 7.1 % is taken as the cross-section uncertainty for all diboson processes in this analysis as the $Z \to 4\ell$ decay is very rare and does not play a role with the analysis selection criteria.

6.4.3 Cross-section uncertainties for signal processes

Systematic uncertainties on the signal production cross-section stem from various sources: uncertainties on input parameters used in the calculation, the PDF used and MHOs. All of these are calculated with `ggHiggs`, similar to the nominal cross-sections.
Uncertainties from MHOs are determined by varying the renormalization scale μ_{R} from 0.5 to 2.0. The envelope of all combinations gives a good estimate for the MHO systematic uncertainty. [190] In `ggHiggs`, the N^{3}LO variation for the factorization scale μ_{F} for CP-odd Higgs bosons is only implemented with approximations which are not fully valid in the mass range probed here. Therefore, only the renormalization scale is varied and an additional factorization scale factor is added to account for factorization scale effects at N^{3}LO. This factorization scale factor is calculated as the ratio of the 7-point variation over the variation of the renormalization scale for CP-even Higgs bosons. For CP-even Higgs bosons, the calculation in `ggHiggs` up to N^{3}LO is exact without approximations. The obtained factorization scale factor is exactly 1.0 which is expected as the factorization scale becomes less important compared to the renormalization scale for higher orders. The MHO uncertainty is the most significant contribution to the overall uncertainty of the production cross-section for the signal process, as detailed in Table 6.6.
The uncertainty on the PDF (in this case PDF4LHC15NNLO) can be estimated by computing the cross-section for the 100 eigenvariations of the PDF and calculating the standard deviation of the resulting distribution. [182]
For the third sort of uncertainties stemming from input parameters, only two are relevant: the strong coupling α_s and the top-quark mass. The top-quark mass is varied around its nominal value by $m_t = (172.5 \pm 1.0)$ GeV and the strong coupling constant by $\alpha_s = 0.1180 \pm 0.0015$ (at m_Z) as outlined in Ref. [190]. Adjusting the top-quark mass is straightforward, but for the α_s uncertainty, the PDF must be matched to the new α_s value.
The results are summarized in Table 6.6. These uncertainties are considered only for the fit in the model-dependent case and for limits on $|\zeta_{\mathrm{u}}|$, but not for the

Table 6.6: N^{3}LO calculation and systematic uncertainties on the A boson production cross-section within the probed mass range. The values are determined using `ggHiggs` version v4.0, thereby setting the coupling strength parameters of the A boson to up-type quarks to $\cot\beta = \zeta_\mathrm{u} = 1$. The largest uncertainties originate from MHOs, while the contributions from PDFs and m_t uncertainties are insignificant.

m_A	Nominal	Production cross-section uncertainty [pb]					Relative
[GeV]	[pb]	MHO	PDF	m_t	α_S	Total	uncertainty [%]
20	1850	200	6.8	0.20	67	210	11
25	1390	140	4.4	0.17	48	140	10
30	1090	99	3.1	0.15	37	105	9.7
40	722	59	1.8	0.13	23	63	8.8
50	514	39	1.2	0.12	16	42	8.2
60	385	28	0.85	0.12	11	30	7.7
70	299	20	0.62	0.12	8.4	22	7.4
75	266	18	0.54	0.12	7.4	19	7.2
80	239	16	0.49	0.12	6.5	17	7.0
85	215	14	0.43	0.12	5.8	15	7.0
90	195	12	0.39	0.12	5.2	13	6.9
95	178	11	0.35	0.12	4.7	12	6.8
100	162	10	0.31	0.12	4.3	11	6.7
105	149	9.0	0.28	0.12	3.9	9.8	6.6
110	137	8.2	0.26	0.12	3.5	8.9	6.5

model-independent fit and cross-section limits.

6.4.4 Modeling uncertainties

The systematic uncertainties arising from the background modeling can be split into two categories: uncertainties related to the MC samples generator and uncertainties

Table 6.7: Summary of all the theoretical background modeling systematics groups and numbers of considered NPs.

NP group	Description	Number of NPs
xsec_Ztautau	Cross-section uncertainty for $Z \to \tau\tau$	1
xsec_Diboson	Cross-section uncertainty for diboson	1
xsec_Top	Cross-section uncertainty for $t\bar{t}$	1
FAKEBGK_STAT	Statistical uncertainties on the matrix method	64
FAKEBGK_SYS	Systematic uncertainties on the matrix method	4
TTBar	$t\bar{t}$ modeling systematics	5
Ztautau_MCGenSys	$Z \to \tau\tau$ generator systematics	5
Diboson_MCGenSys	Diboson generator systematics	3
Ztautau_NJetWt	$Z \to \tau\tau$ N_{Jets} reweighting uncertainty	3

associated to the reweighting of the $Z \to \tau\tau$ background. The former ones were largely computed by other members of the analysis team. They are outlined here briefly, and further details can be found in the relevant theses. The top-quark generator uncertainties were computed in the master's thesis of Christian Schmidt [146] under the supervision of the author. The generator systematics for $Z \to \tau\tau$ and diboson processes, as well as the signal acceptance uncertainties were calculated by Manuel Gutsche and will be explained in detail in his doctoral thesis. All background generator uncertainties are calculated in bins of m_{MMC}. A summary of all background modeling systematics is given in Table 6.7

$Z \to \tau\tau$ generator uncertainties

Systematic uncertainties in the generation of the $Z \to \tau\tau$ processes mainly arise from the renormalization and factorization scales (μ_{R} and μ_{F}), α_s uncertainties, choices of PDFs parameters, and uncertainties in the soft-gluon emission resummation (QSF) and matrix element matching (CKKW [223]) scales.
The event samples were generated using Sherpa 2.2.1 respectively. Systematic uncertainties related to renormalization and factorization scales, PDF, and α_s variations are evaluated using the event weights which are produces in conjunction with the nominal samples. All uncertainties are determined in the HMSR and ZCR, with the latter ones being applied in the ZCR and FVR. In other regions, those calculated in the HMSR are utilized.

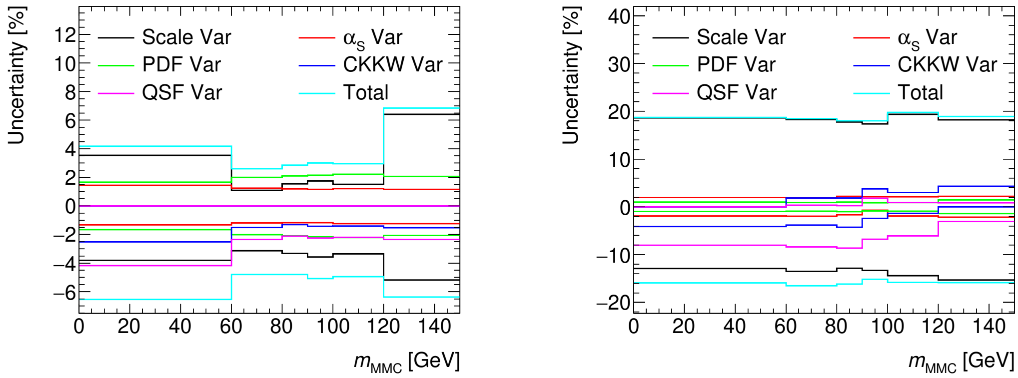

(a)

(b)

Figure 6.10: Relative systematic generator uncertainties on the $Z \to \tau\tau$ production determined in (a) the ZCR and (b) the HMSR, binned in m_{MMC}.

For QCD scale uncertainties, a 7-point variation is carried out by varying μ_{R} and μ_{F} by factors of 2 and 0.5 in all but the two extreme combinations (0.5,0.5) and (2,2). The uncertainty for each bin is given by the maximum positive and negative changes occurring during these variations.
The uncertainty from the scale variations is decorrelated between the different regions because it shows a largely different structure between the ZCR and the HMSR, and to prevent potential issues when extrapolating the n_{jets} weights from the ZCR to the SRs.
The PDF uncertainty is calculated as the standard deviation of 100 PDF variations, with the nominal PDF being NNPDF3.0NLO and using the strong coupling value $\alpha_s(m_Z) = 0.118$. Additionally, α_s is varied by 0.118 ± 0.001. As a cross-check, the obtained results are compared with the CT14NNLO [224] and MMHT2014NNLO PDF sets with associated 68 % CL uncertainty bands [225].
A parametrization method is used to evaluate the CKKW and QSF scale variations. To retrieve the CKKW uncertainty, the scale used for the jet overlap calculation from ME and PS is varied between 15 GeV and 30 GeV around the central value of 20 GeV. For the QSF uncertainty, factors of 0.5 and 2 are taken as variations.
The computed uncertainties are displayed in Figure 6.10 for both the uncertainties in the HMSR and in the ZCR.

Diboson generator uncertainties

The generator uncertainties for diboson processes are similarly to the $Z \to \tau\tau$ processes arising from renormalization and factorization scales, α_s uncertainties, choices of PDFs parameters, and uncertainties in the QSF and CKKW scales. They are determined analogously to the $Z \to \tau\tau$ uncertainties described in the previous paragraph. The differences are that Sherpa 2.2.2 was used in addition, and the QSF and CKKW uncertainties are not taken into account. The relevant weights were not provided yet by the ATLAS physics modeling group. As diboson processes only form a minor background in the analysis and the QSF and CKKW uncertainties are not the leading uncertainties, it was decided that these can be dropped without any influence on the results. The resulting uncertainties as calculated in the HMSR and in the ZCR are shown in Figure 6.11.

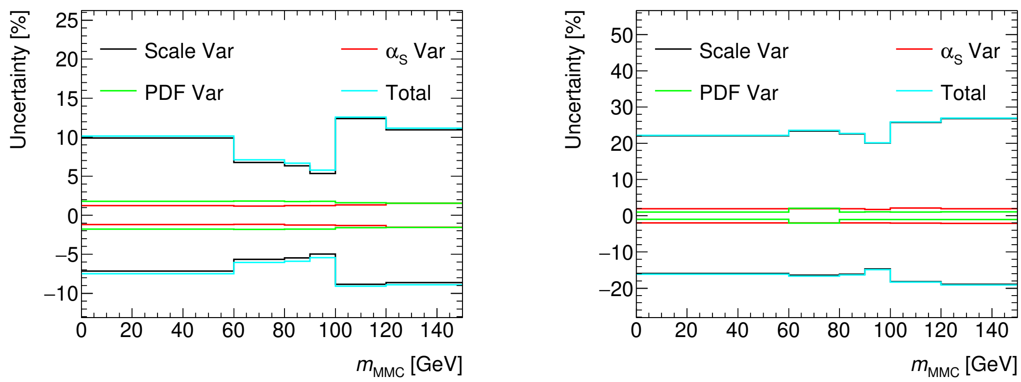

(a) (b)

Figure 6.11: Relative systematic generator uncertainties on the diboson production determined in (a) the ZCR and (b) the HMSR, binned in m_{MMC}.

Top-quark production generator uncertainties

The modeling of top-quark processes involves uncertainties from various sources. These uncertainties are estimated by comparing the nominal sample (simulated using Powheg Box v2 at NLO with NNPDF3.0nlo and $h_{\mathrm{damp}} = 1.5\,m_t$, Pythia 8.230 with the A14 tune and NNPDF2.3lo, and EvtGen 1.6.0) with several variations. The uncertainties are assessed in a modified TCR, where the requirement for the number of b-tagged jets is relaxed to $\geq$1 b-tagged jet to increase the sample size.[3]
To estimate the uncertainties on the PS and hadronization model, Pythia is replaced by Herwig 7.13 [226, 227] and the MMHT2014lo PDF set is used. The

[3]As systematic variations are performed using only simulated top-quark processes only, any potential signal contamination in an extended TCR has no effect on this study.

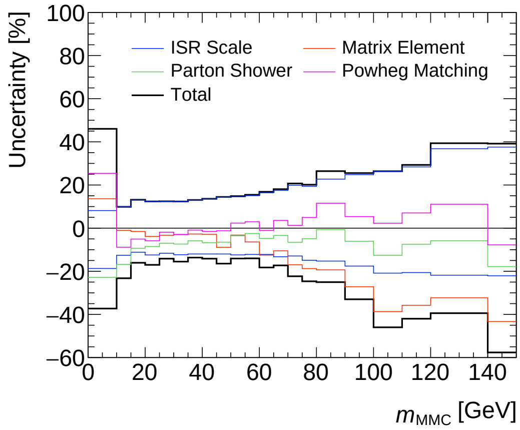

Figure 6.12: Relative systematic generator uncertainties on the top-quark pair production determined in the extended TCR, binned in m_{MMC}. For the sake of clarity, the two smallest contributions, from FSR and the *Var3c* variation, have been omitted from the plot. They only have a significant contribution in the first bin with $m_{\text{MMC}} < 10\,\text{GeV}$, which is not relevant in the analysis.

uncertainties in the ME generation and matching to the PS are evaluated by using MadGraph5_aMC@NLO 2.6.0 [228] instead of Powheg Box. The impact of the h_{damp} parameter value is determined by utilizing a sample with $h_{\text{damp}} = 3\,m_t$. For each of the variations, separate alternative data sets were simulated.
The uncertainties on the ISR are estimated through halving and doubling μ_{F} and μ_{R}, and by using the *Var3cUp* and *Var3cDown* variations of Pythia 8's A14 tune, which corresponds to α_s variations in the ISR.
For the FSR, the uncertainties are calculated by similarly halving and doubling the renormalization scale for PS emissions. These variations in α_s and scales are applied using alternative event weights recorded in the nominal simulation samples. The summary of all obtained systematic uncertainties is displayed in Figure 6.12.

Signal generator acceptance uncertainties

A variety of sources contribute to the uncertainties in the signal modeling: the PDFs, the color reconnection parameters, MHO corrections, and α_{s}. Additionally, the modeling of MPIs, PS, hadronization, ISR and FSR leads to further uncertainties. These uncertainties are estimated by comparing the acceptance ratios of nominal-sample events to variation-sample events, dependent on the transverse momentum of the CP-odd Higgs boson p_{T}^{A}. Two regions are defined, split by the transverse momentum splitting point p^A_{Sp}. It is chosen individually for each mass point in a way that 1 % of the events lie in the first bin and the remaining 99 % in the second bin. This separation is necessary, because the low-p_{T} spectrum of

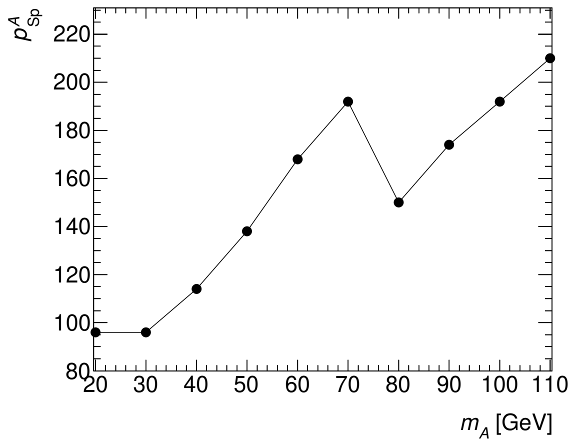

Figure 6.13: Dependence of the transverse momentum splitting point p^A_{Sp} on the mass of the A boson m_A. The value decreases from 70 GeV to 80 GeV due to differences in selection criteria between the LMSR and HMSR. For the mass points 25, 75, 85, 95 and 105 GeV, which were added to the analysis in a later stage, p^A_{Sp} is interpolated.

the A boson has significantly worse statistics and splitting the spectrum in two bins enables to largely reduce the systematic uncertainties for the main part of the spectrum.
Uncertainties from the modeling of MPI, color reconnection, ISR, and FSR are estimated by combining the effects of the *Var1*, *Var2*, *Var3a*, *Var3b*, and *Var3c* up and down eigenvariations of PYTHIA 8's A14 tune in quadrature.
The scale uncertainties due to MHO corrections are derived from event weights provided for 7-point combinations of different μ_{R} and μ_{F} values [190].
Similarly, the uncertainties from PDF and α_{s} are determined using event weight variations, with the NNPDF2.3LO PDF as the reference. This includes two α_{s} values, 0.119 and 0.130, and 100 variations of the PDF set.
For each m_A value and systematic variation, approximately 5 million events were generated to minimize statistical effects. Finally, the results are smoothed, considering neighboring mass hypotheses, to further reduce statistical fluctuations.
Figure 6.14 shows all calculated systematic uncertainties. The mass points 25, 75, 85, 95 and 105 GeV were added to the analysis at a later stage. Their uncertainties are interpolated from neighboring mass points.

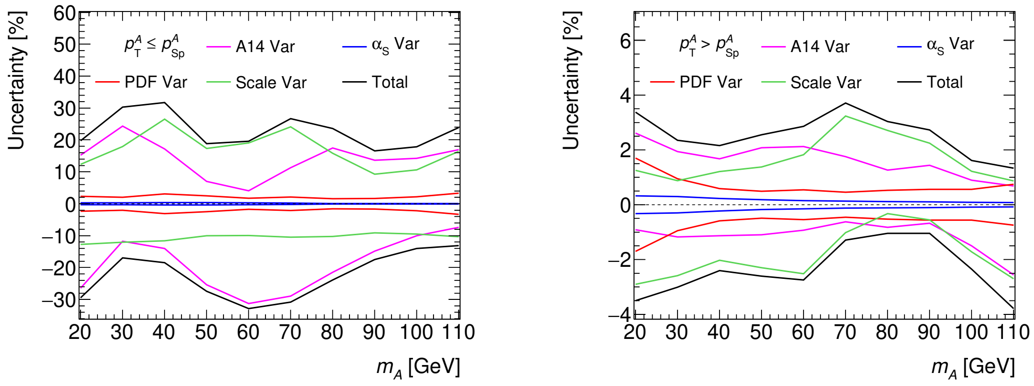

(a) (b)

Figure 6.14: Relative acceptance uncertainties for the signal samples depending on m_A (a) $p_{\mathrm{T}}^A \le p_{\mathrm{Sp}}^A$ and (b) $p_{\mathrm{T}}^A > p_{\mathrm{Sp}}^A$. 99 % of the events fall into the case (b) $p_{\mathrm{T}}^A > p_{\mathrm{Sp}}^A$, which shows much lower uncertainties. For the mass points 25, 75, 85, 95 and 105 GeV the uncertainty is interpolated from neighboring masses.

6.4.5 Uncertainties on the matrix method

The underlying idea for systematics on the Matrix Method (MM) is to vary the lepton efficiencies for different systematics reasons and propagate the changes through the method to changes in the event yield for the fake-lepton background. The resulting uncertainties are summarized in Figure 6.15 for the FVR and the LMSR, while plots for the individual contributions are shown in Section C.2 in Appendix C.
The following systematics are considered:

Statistical uncertainties of efficiencies

The efficiencies have statistical uncertainties which are propagated as one single systematic for each p_{T} bin. It depends on the lepton type (electron or muon), if the efficiency is for real or fake leptons and the tightness of the accompanying lepton. The efficiencies and statistical uncertainties that are used for these NPs are shown in Figure 6.6. Its propagated uncertainty on the fake-lepton background is summarized in Figure C.1 in Appendix C.

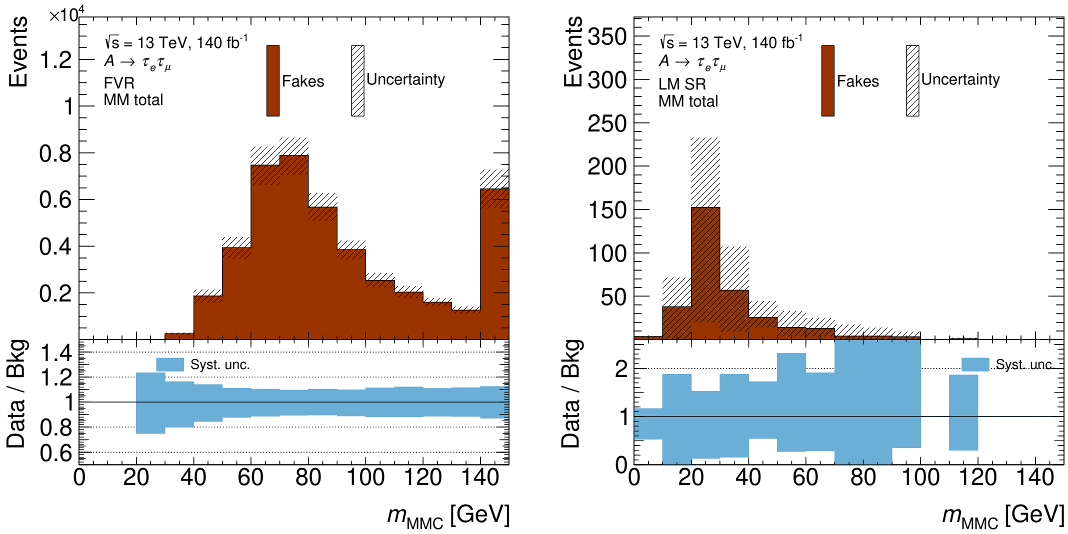

Figure 6.15: Distribution of m_{MMC} for the fake-lepton background estimated with the MM in (a) the FVR and (b) the LMSR. The shown uncertainties comprise the total systematic uncertainties on the fake-lepton background.

Parametrization uncertainties

The efficiencies have a slight dependence on other variables than just the p_{T} binning used in this implementation. Due to statistical limitations, it is not possible to split up the efficiencies further, therefore systematic uncertainties are added to cover unaccounted dependencies on η^{ℓ}, n_{jets} and $E_{\mathrm{T}}^{\mathrm{miss}}$.
The η^{ℓ} dependence is taken into account by using three different ranges of absolute η values: $[0, 0.8)$, $[0.8, 1.7)$ and $[1.7, 2.7]$.
The n_{jets} dependence considered by introducing the following n_{jets} bins: {0,1,2,>3} for the fake-lepton efficiencies and {1,2,3,>4} for the real-lepton efficiencies. For real-lepton efficiencies, the binning starts at $n_{\mathrm{jets}} = 1$ because the SRs have no events without any jets.
For the $E_{\mathrm{T}}^{\mathrm{miss}}$ dependence, the $E_{\mathrm{T}}^{\mathrm{miss}}$ spectrum is split into four bins: $[0, 10)$ GeV, $[10, 20)$ GeV, $[20, 30)$ GeV and $[30, \infty)$ GeV.
The weighted standard deviations are calculated for all cases and used as an estimate of the parametrization uncertainty. To avoid overly constraining the parametrization NPs, they are decorrelated between the regions. This is advised because the regions use independent data. The size of the uncertainties are displayed in Section C.2 in Appendix C.

Systematic uncertainties on subtracted MC background

When estimating the fake-lepton efficiencies, the contribution from processes modeled by MC needs to be subtracted. Uncertainties on this MC background should be considered as uncertainties on the fake-lepton efficiencies. However, for this analysis the MC contamination in the FVR, where the fake efficiencies are measured, is only 3 %. As there would not be a resulting systematic of significant size, it is omitted.

Composition

The composition between the region where the efficiencies are measured and the SR could vary. To compensate for this variation, a composition systematic is added. It is estimated by measuring the efficiencies in a region closer to the SRs.

Table 6.8: Summary table for the composition systematics of the MM for all efficiencies. An asterisk * indicates that the $E_{\mathrm{T}}^{\mathrm{miss}}$ and MMC cuts in that region are disregarded to increase the available statistics.

Lepton truth type	Tightness of accompanying lepton	Applied in	Nominal	→	Variation
Real	*Tight*	LMSR	LMSR*	→	LMSR*
Real	*Tight*	HMSR	HMSR	→	HMSR
Real	*Non-tight*	LMSR, HMSR	ZCR	→	HMSR*
Fake	*Tight*	LMSR, HMSR	FVR	→	HMSSVR*
Fake	*Non-tight*	LMSR, HMSR	FVR	→	HMSSVR*

The real-lepton efficiencies are already calculated in the LMSR or HMSR for a *Tight* accompanying lepton, thus no uncertainty is needed. For the case of the *Non-tight* efficiencies, the region is changed from the ZCR to the HMSR.
The fake-lepton efficiencies are calculated in the HMSSVR instead of the FVR. As there are statistical limits in the new regions, the $E_{\mathrm{T}}^{\mathrm{miss}}$ and MMC cuts are omitted. This is still giving a good estimate for the composition uncertainty because the $E_{\mathrm{T}}^{\mathrm{miss}}$ bias is already accounted for as an parametrization uncertainty.
Like for the parametrization uncertainties, the composition uncertainty is decorrelated across the regions for the fit because this uncertainty is by definition different

in different regions. An overview of the nominal and alternative regions used to calculate the efficiencies for the composition uncertainty is given in Table 6.8. The resulting uncertainties on the fake-lepton background are shown in Figure C.5 in Appendix C.

Summary of systematic uncertainties on the matrix method

The different systematic uncertainties on the MM are relevant in different parts of the m_{MMC} spectrum in the SRs. On the lower end of the spectrum, the $E_{\text{T}}^{\text{miss}}$ parametrization and the composition uncertainty are most relevant, while in the high-mass regime the n_{jets} and η^{ℓ} parametrizations take over. The systematic uncertainty from the statistical uncertainties in the efficiency measurements is negligible over the whole mass range.

6.4.6 Uncertainties on the $Z \to \tau\tau$ reweighting

The weights for the $Z \to \tau\tau$ reweighting are influenced by statistical uncertainties on MC and data events, as well as systematic uncertainties on MC. Hence, three NPs are calculated by propagating the uncertainties through the formula for the weight calculation Equation 6.3. For the two statistical uncertainties this is straight forward as each bin only has a single uncertainty.
The MC systematics part, however, consists of more than one uncertainty. All MC systematics from experimental and generator sources are combined quadratically into one single uncertainty. This is propagated through Equation 6.3 as well to get the resulting NP for the $Z \to \tau\tau$ reweighting. The resulting uncertainties can be seen in Figure 6.16. They cover unity in most n_{jets} bins. To prevent double-counting the propagation of issues from the ZCR (where the weights were measured) to the SR, the NPs are decorrelated between the regions.

6.5 Analysis results

Particle searches are typically performed in a *blinded* setup [229]. This approach keeps the data yields in the signal regions — those most sensitive to the expected signal — hidden until the background modeling is complete. Revealing this data earlier could introduce biases, as the background modeling might be influenced by directly or indirectly comparing it with the observed signal region data.
Before *unblinding* the data, the background modeling in the various control and validation regions is scrutinized. The results in these regions are shown in Section 6.5.1.

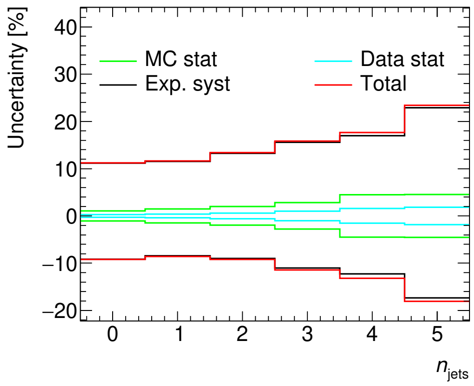

Figure 6.16: Relative uncertainties on the weights for the $Z \to \tau\tau$ MC background reweighting, split by their origin.

After the background modeling has been validated, the results in the SRs are analyzed with a statistical analysis. The unblinded results in the SRs are given in Section 6.5.2. The mass obtained from the MMC, m_{MMC}, is used as the final discriminating variable. As shown in Section 5.2.7, the MMC is a very useful tool to reconstruct the mass of the mother particle in ditau decay systems.

The event yields from the signal predictions in all the regions are summarized in Table 6.9, while the background predictions are given in Table 6.10 for the CRs and VRs, and in Table 6.11 for the SRs.

The signal has a high abundance in both the SRs by construction. While the absolute signal event yields are larger in the ZCR, the background is also much larger too, leading to a maximum possible signal contamination in the ZCR of 2.6 % for $m_A = 90\,\text{GeV}$. The largest signal contributions in the ZCR are reached for masses close to the Z boson mass. In the TCR, the different signal masses have a more uniform contribution, reaching its maximum of 1 % for $m_A = 40\,\text{GeV}$.

The largest background in the SRs is $Z \to \tau\tau$ with more than 60 %. Other significant backgrounds come from fake-lepton, diboson and top-quark processes. The SM Higgs boson decays only contribute as a minor background, while $Z \to \ell\ell$ decays are negligible.

The CRs have a high abundance in their respective backgrounds: $Z \to \tau\tau$ for the ZCR and top-quark processes for the TCR. Similarly, the fake-lepton background dominates in the three same-sign (SS) VRs. In most of these regions, the respective other background are negligible, with the exceptions being the fake-lepton background in the ZCR and the diboson background in the LMSSVR and HMSSVR.

Table 6.9: Pre-fit signal yields in all the analysis regions for an integrated luminosity of $140\,\mathrm{fb}^{-1}$. The stated uncertainties are the statistical uncertainties which result from the finite number of events generated in the simulated samples. No signal is expected in the three same-sign validation regions: FVR, LMSSVR and HMSSVR. The cross-sections for the signal process are calculated in $\mathrm{N^3LO}$, as given in Table 6.1. These cross-section values are multiplied with the highest not-already-excluded value of $|\zeta_\mathrm{u}|^2$ of $0.25 = |\zeta_\mathrm{u}|^2 = \cot^2\beta$ [58].

m_A [GeV]	ZCR	TCR	Low-mass SR	High-mass SR
20	0.0 ± 0.0	15.4 ± 3.0	1355 ± 27	-
25	0.3 ± 0.3	30.8 ± 3.3	2326 ± 28	-
30	4.7 ± 1.8	39.6 ± 5.3	2865 ± 44	-
40	314 ± 17	59.4 ± 7.6	2940 ± 52	-
50	1706 ± 43	51.2 ± 7.5	2293 ± 51	-
60	4396 ± 71	39.6 ± 7.1	1516 ± 43	-
70	7242 ± 91	53.6 ± 8.1	1002 ± 35	-
75	8083 ± 75	53.9 ± 6.5	774 ± 23	2312 ± 41
80	8520 ± 96	49.9 ± 7.5	-	2011 ± 47
85	8706 ± 76	39.1 ± 5.4	-	1771 ± 35
90	8710 ± 93	39.6 ± 6.3	-	1512 ± 39
95	8460 ± 73	22.0 ± 3.8	-	1259 ± 29
100	7985 ± 78	15.7 ± 3.7	-	1067 ± 29
105	7509 ± 67	21.4 ± 3.7	-	893 ± 23
110	7056 ± 69	14.9 ± 3.3	-	789 ± 24

Table 6.10: Pre-fit background event yields for all the CRs and VRs for an integrated luminosity of $140\,\mathrm{fb}^{-1}$. The stated uncertainties are the statistical uncertainties which result from the finite number of events generated in the simulated samples. In case of the fake-lepton background, they result from the statistical uncertainties of the measured input data to the MM. The numbers in parentheses indicate the fraction of each specific background relative to the overall background in each region. In the $Z \to \ell\ell$ background, $\ell\ell$ stands for both e^+e^- and $\mu^+\mu^-$.

	ZCR	FVR	TCR	LMSSVR	HMSSVR
Fakes	$59{,}680 \pm 690$	$44{,}850 \pm 430$	213 ± 50	198 ± 27	447 ± 33
	(18%)	(97%)	(3.5%)	(89%)	(86%)
$Z \to \tau\tau$	$262{,}700 \pm 1800$	82 ± 27	116.1 ± 4.0	0.2 ± 1.0	1.2 ± 3.5
	(79%)	(0.18%)	(1.9%)	(0.14%)	(0.28%)
Diboson	4552 ± 26	747.3 ± 7.4	10.82 ± 0.50	23.5 ± 0.79	59.0 ± 1.3
	(1.4%)	(1.6%)	(0.18%)	(11%)	(11%)
$Z \to \ell\ell$	468 ± 71	354 ± 68	0.28 ± 0.12	0.23 ± 0.87	12.3 ± 2.7
	(0.14%)	(0.77%)	($< 0.1\%$)	($< 0.1\%$)	(2.4%)
Top	3327 ± 22	2.02 ± 0.51	5653 ± 28	0.35 ± 0.27	0.77 ± 0.30
	(1.0%)	($< 0.1\%$)	(94%)	(0.10%)	(0.20%)
SM Higgs	1108.7 ± 2.6	3.63 ± 0.18	5.79 ± 0.23	0.15 ± 0.11	0.6 ± 1.4
	(0.33%)	($< 0.1\%$)	($< 0.1\%$)	(0.10%)	(0.10%)
Total	$331{,}800 \pm 2000$	$46{,}040 \pm 440$	5999 ± 57	222 ± 34	519 ± 33
Data	331,797	44,587	6227	213	422

6.5.1 Background modeling in the validation and control regions

The modeling of the $Z \to \tau\tau$ background is validated in the ZCR, which is later also used in the statistical analysis. Similarly, the TCR, in which the top-quark background modeling is verified, is used in the statistical analysis. On the other hand, the three same-sign regions FVR, LMSSVR and HMSSVR are only used to validate the background from the fake-lepton estimation and do not enter the fit. Using them to set up a normalization factor for the fake-lepton background does not seem justifiable because the fake-lepton background depends on statistically independent data in each of the regions.

$Z \to \tau\tau$ control region

The distributions of the p_T of the leading and subleading lepton, as well as the $E_\mathrm{T}^\mathrm{miss}$ and m_MMC variables in the ZCR are displayed in Figure 6.17. Additional distributions are shown in Figure B.13 in Appendix B. After applying the $Z \to \tau\tau$ reweighting, the agreement of the observed data with the expected background is good within the given uncertainties. The best agreement is observed in the bins with the largest $Z \to \tau\tau$ contributions. The purity in $Z \to \tau\tau$ processes reaches 79 %, while the expected signal contributions stay below 3 % even for the largest possible coupling values. This makes the ZCR an ideal control region for the $Z \to \tau\tau$ background process and shows that the $Z \to \tau\tau$ reweighting procedure works well. It also enables the extraction of a normalization factor for the fit and allows constraining the $Z \to \tau\tau$ background related NPs.

Top control region

The p_T distributions of both the leading and subleading lepton, in addition to the $E_\mathrm{T}^\mathrm{miss}$ and m_MMC variables in the TCR, are presented in Figure 6.18. Supplementary distributions are shown in Figure B.14 in Appendix B. The observed data agrees well with the predicted background within their respective uncertainties. A small slope is still visible in the data-to background ratio for the p_T of the leading lepton after the reweighting with higher orders, but the method has nevertheless improved the agreement. A purity in top-quark processes of 94 % is reached, while the expected signal contributions stays below 1 %. Both characteristics make the TCR an excellent control region for the top-quark background processes and the extraction of a normalization factor for the fit.

Fake-lepton validation region

The distributions for the p_T of the leading and subleading lepton, along with the $E_\mathrm{T}^\mathrm{miss}$ and m_MMC variables in the FVR, are illustrated in Figure 6.19. Additional distributions are displayed in Figure B.15 in Appendix B. The FVR has a very high purity in the fake-lepton background of 97 %, while not expecting any signal contribution. The observed data agrees well with the background predictions, and hence validating the fake-lepton background estimation for this analysis. The best agreement is reached for bins with large event numbers, while the agreement becomes slightly worse in the tails of the distributions.

Low-mass same-sign validation region

Figure 6.20 shows the distribution of the main variables leading and subleading lepton p_T, m_MMC, and $E_\mathrm{T}^\mathrm{miss}$ in the LMSSVR. Additional distributions are given in Figure B.16 in Appendix B. A purity in the fake-lepton background of 89 % is reached, while at the same time no signal is expected. Due to the low statistics, the uncertainties in this region are quite large. Nevertheless, it is important to see that the background prediction and observed data agree within the uncertainties, because the LMSSVR is closer to the LMSR than the FVR and provides a good cross-check for the validation of the fake-lepton background estimation.

High-mass same-sign validation region

In Figure 6.21, the distributions for the p_T of the leading and subleading lepton, as well as the $E_\mathrm{T}^\mathrm{miss}$ and m_MMC variables in the HMSSVR, are displayed. Additional distributions are shown in Figure B.17 in Appendix B. In the HMSSVR, a purity in the fake-lepton background of 86 % is reached, expecting simultaneously zero signal. Due to the small available dataset, the uncertainties in this region are quite large. However, the agreement between data and background within the uncertainties still provides a good validation of the fake-lepton background in a region closer to the HMSR.

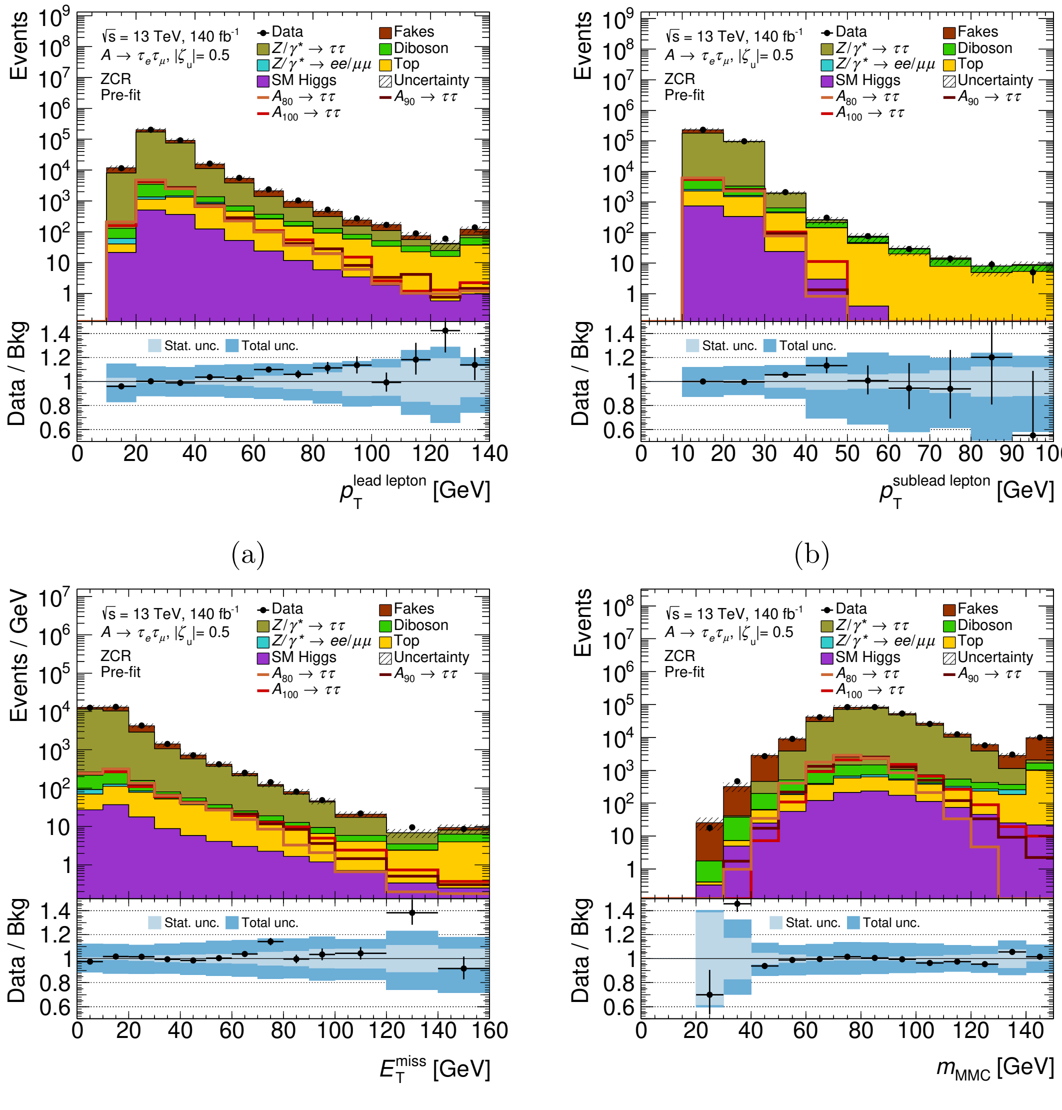

(a) (b) (c) (d)

Figure 6.17: Variable distributions in the ZCR after complete selection criteria: (a) leading lepton p_{T}, (b) subleading lepton p_{T}, (c) $E_{\mathrm{T}}^{\mathrm{miss}}$ and (d) m_{MMC}. The background is estimated by using MC simulation and data-driven methods (for details see Section 6.3). The expected signal contributions for the masses $m_A = 80,\ 90$ and $100\,\mathrm{GeV}$ are displayed for $|\zeta_{\mathrm{u}}| = 0.5$. Events with values beyond the x-axis range are shown in the last bin of each distribution. The dark blue bands in the ratio plot visualize the total uncertainty of the background estimate from both statistical and systematic sources. The statistical uncertainty is overlaid as the light blue band.

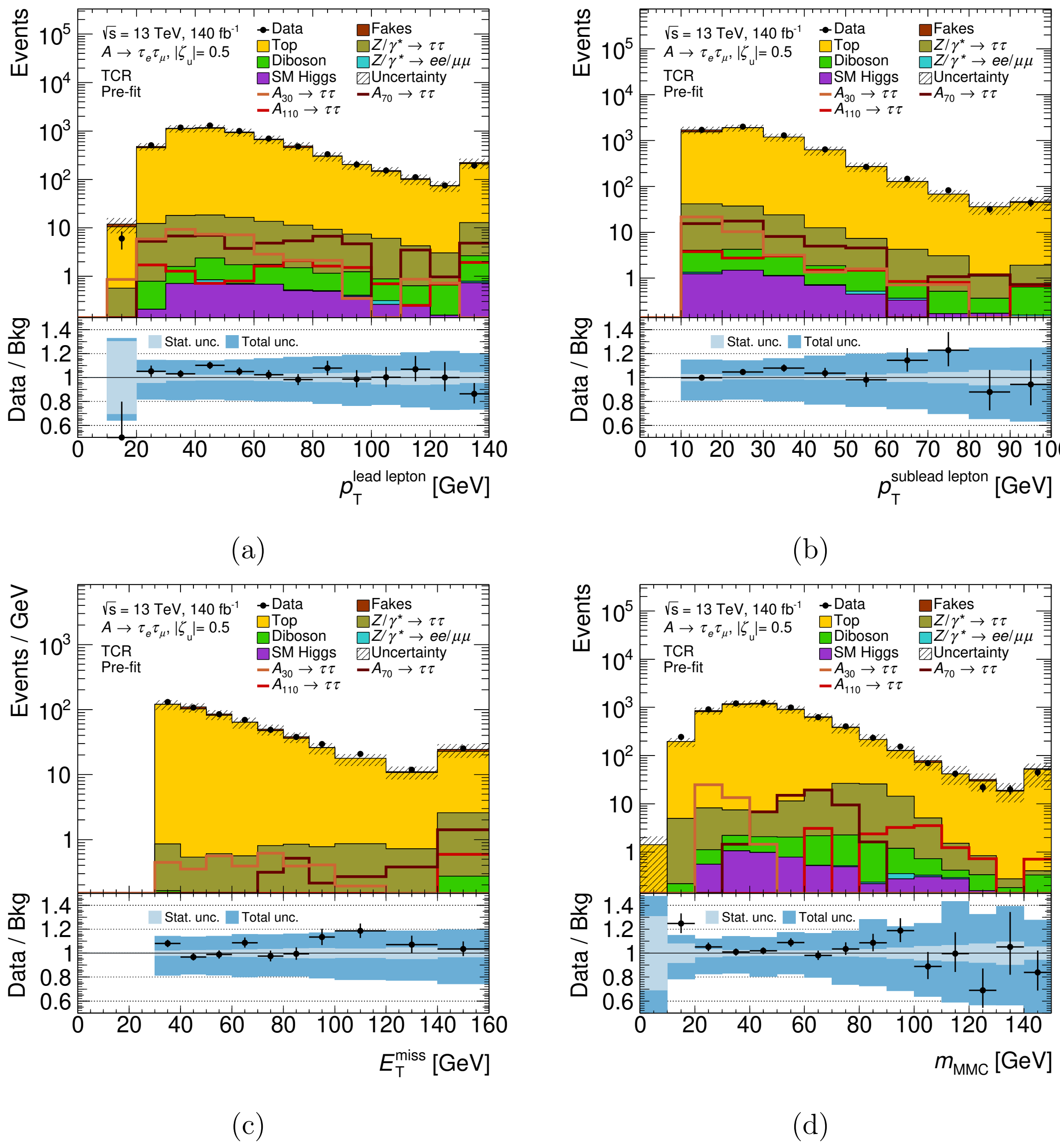

Figure 6.18: Variable distributions in the TCR after complete selection criteria: (a) leading lepton p_{T}, (b) subleading lepton p_{T}, (c) $E_{\mathrm{T}}^{\mathrm{miss}}$ and (d) m_{MMC}. The background is estimated by using MC simulation and data-driven methods (for details see Section 6.3). The expected signal contributions for the masses $m_A = 30,\ 70$ and $110\,\mathrm{GeV}$ are displayed for $|\zeta_{\mathrm{u}}| = 0.5$. Events with values beyond the x-axis range are shown in the last bin of each distribution. The dark blue bands in the ratio plot visualize the total uncertainty of the background estimate from both statistical and systematic sources. The statistical uncertainty is overlaid as the light blue band.

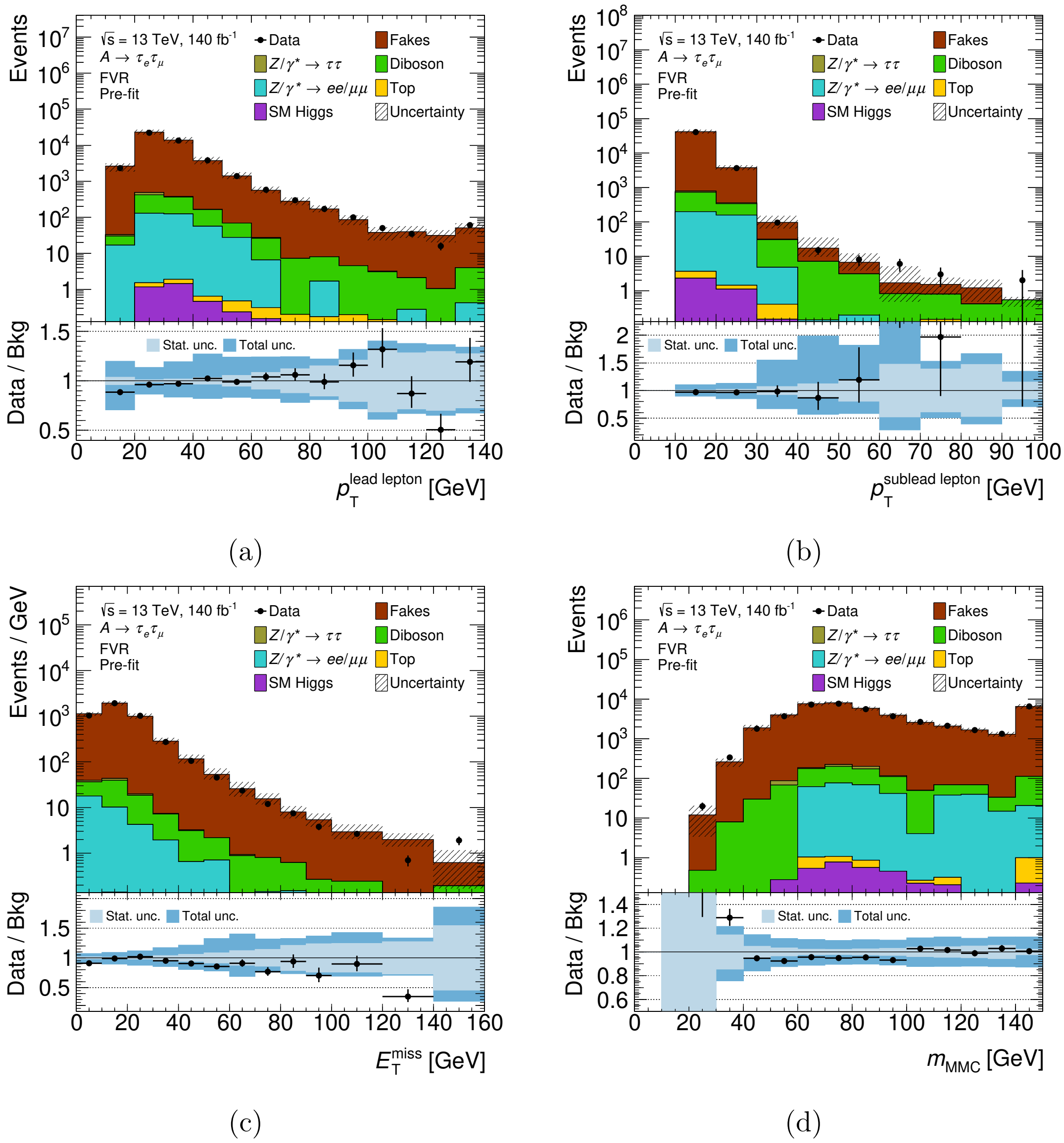

(a) (b) (c) (d)

Figure 6.19: Variable distributions in the FVR after complete selection criteria: (a) leading lepton p_{T}, (b) subleading lepton p_{T}, (c) $E_{\mathrm{T}}^{\mathrm{miss}}$ and (d) m_{MMC}. The background is estimated by using MC simulation and data-driven methods (for details see Section 6.3). No signal contribution is expected in this region. Events with values beyond the x-axis range are shown in the last bin of each distribution. The dark blue bands in the ratio plot visualize the total uncertainty of the background estimate from both statistical and systematic sources. The statistical uncertainty is overlaid as the light blue band.

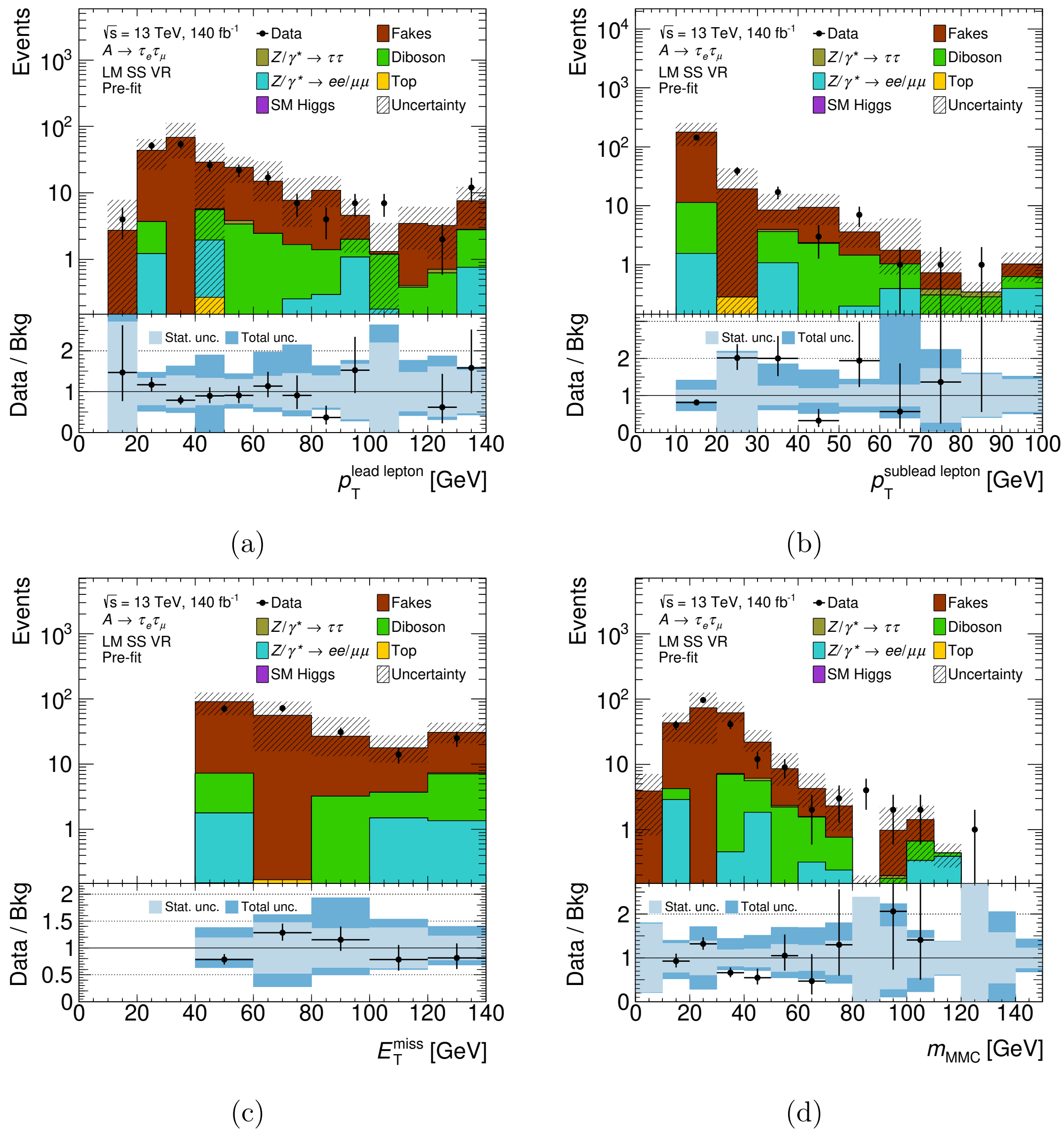

Figure 6.20: Variable distributions in the LMSSVR after complete selection criteria: (a) leading lepton p_{T}, (b) subleading lepton p_{T}, (c) $E_{\mathrm{T}}^{\mathrm{miss}}$ and (d) m_{MMC}. The background is estimated by using MC simulation and data-driven methods (for details see Section 6.3). No signal contribution is expected in this region. Events with values beyond the x-axis range are shown in the last bin of each distribution. The dark blue bands in the ratio plot visualize the total uncertainty of the background estimate from both statistical and systematic sources. The statistical uncertainty is overlaid as the light blue band.

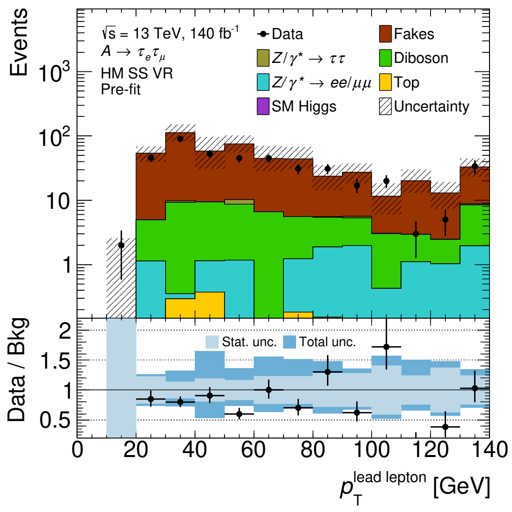

(a)

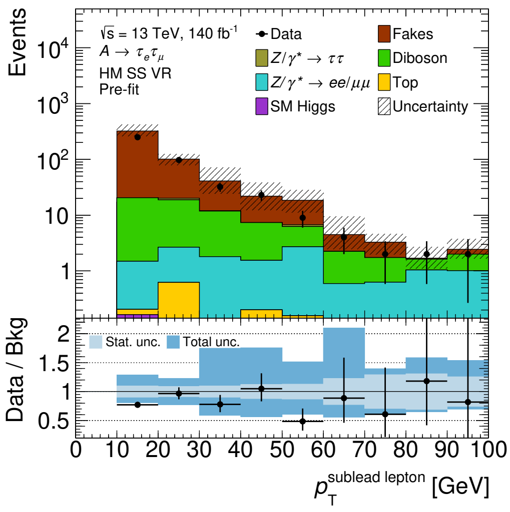

(b)

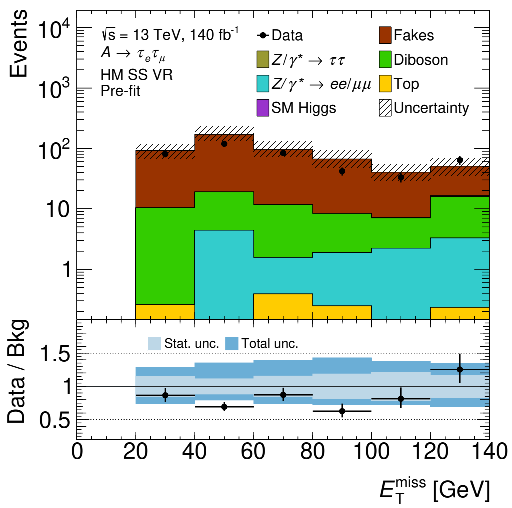

(c)

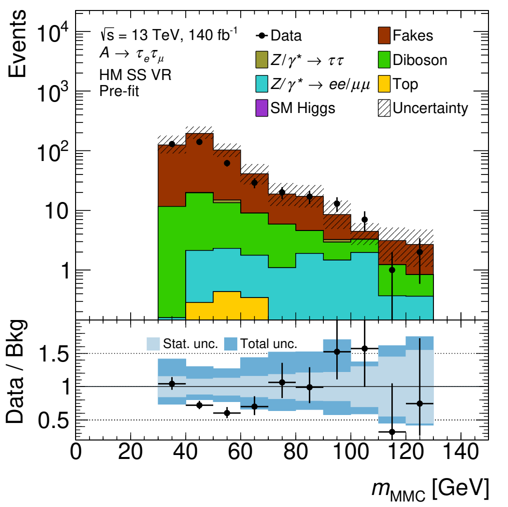

(d)

Figure 6.21: Variable distributions in the HMSSVR after complete selection criteria: (a) leading lepton p_{T}, (b) subleading lepton p_{T}, (c) $E_{\mathrm{T}}^{\mathrm{miss}}$ and (d) m_{MMC}. The background is estimated by using MC simulation and data-driven methods (for details see Section 6.3). No signal contribution is expected in this region. Events with values beyond the x-axis range are shown in the last bin of each distribution. The dark blue bands in the ratio plot visualize the total uncertainty of the background estimate from both statistical and systematic sources. The statistical uncertainty is overlaid as the light blue band.

6.5.2 Signal region results

Low-mass signal region

The distributions for the main variables p_{T} of the leading and subleading lepton, $E_{\mathrm{T}}^{\mathrm{miss}}$ and m_{MMC} in the LMSR are shown in Figure 6.22. Additional distributions are shown in Figure B.11 in Appendix B. Even at pre-fit stage, a good agreement between background estimation and observed data withing their respective uncertainties is reached. A small overshoot of data over the modeled background is seen for large values of $E_{\mathrm{T}}^{\mathrm{miss}}$ and the p_{T} of the subleading lepton, as well as for intermediate m_{MMC} values. Assuming the highest currently allowed value of $|\zeta_{\mathrm{u}}| = 0.5$, a signal contribution as large as the predicted background can be reached. The best separation power of signal and background is obtained from the distribution of m_{MMC}, which is therefore used as the final discriminating variable in the fit.

High-mass signal region

Figure 6.23 displays the distributions of the important variables p_{T} of the leading and subleading lepton, $E_{\mathrm{T}}^{\mathrm{miss}}$ and m_{MMC} in the HMSR. Additional distributions are shown in Figure B.12 in Appendix B. Overall, all distributions show a slightly larger number of data events compared to the estimated background. This could partially result from the $Z \rightarrow \tau\tau$ reweighting, since it reduces the dominant $Z \rightarrow \tau\tau$ background. However, the data still agrees with the estimated background within their respective uncertainties. Assuming the highest currently allowed value of $|\zeta_{\mathrm{u}}| = 0.5$, a signal contribution as large as 42 % is possible. Similar to the LMSR, the distribution of m_{MMC} shows the best separation power for signal and background, and is consequently used in the fit as the final discriminating variable.

Table 6.11: Pre-fit background event yields for the SRs for an integrated luminosity of $140\,\mathrm{fb}^{-1}$. The stated uncertainties are the statistical uncertainties which result from the finite number of events generated in the simulated samples. In case of the fake-lepton background, they result from the statistical uncertainties of the measured input data to the MM. The numbers in parentheses indicate the fraction of each specific background relative to the overall background in each region. In the $Z \to \ell\ell$ background, $\ell\ell$ stands for both e^+e^- and $\mu^+\mu^-$.

	Low-mass SR	High-mass SR
Fakes	316 ± 45	495 ± 55
	(17%)	(9.0%)
$Z/\gamma^* \to \tau^+\tau^-$	1210 ± 36	3701 ± 46
	(63%)	(67%)
Diboson	139.1 ± 2.4	449.2 ± 4.4
	(7.3%)	(8.2%)
$Z/\gamma^* \to \ell^+\ell^-$	4.0 ± 1.7	9.8 ± 3.3
	(0.21%)	(0.18%)
Top	162.9 ± 4.7	611.4 ± 9.3
	(8.5%)	(11%)
SM Higgs	76.86 ± 0.79	227.4 ± 1.3
	(4.0%)	(4.1%)
Total	1908 ± 58	5494 ± 73
Data	1987	6119

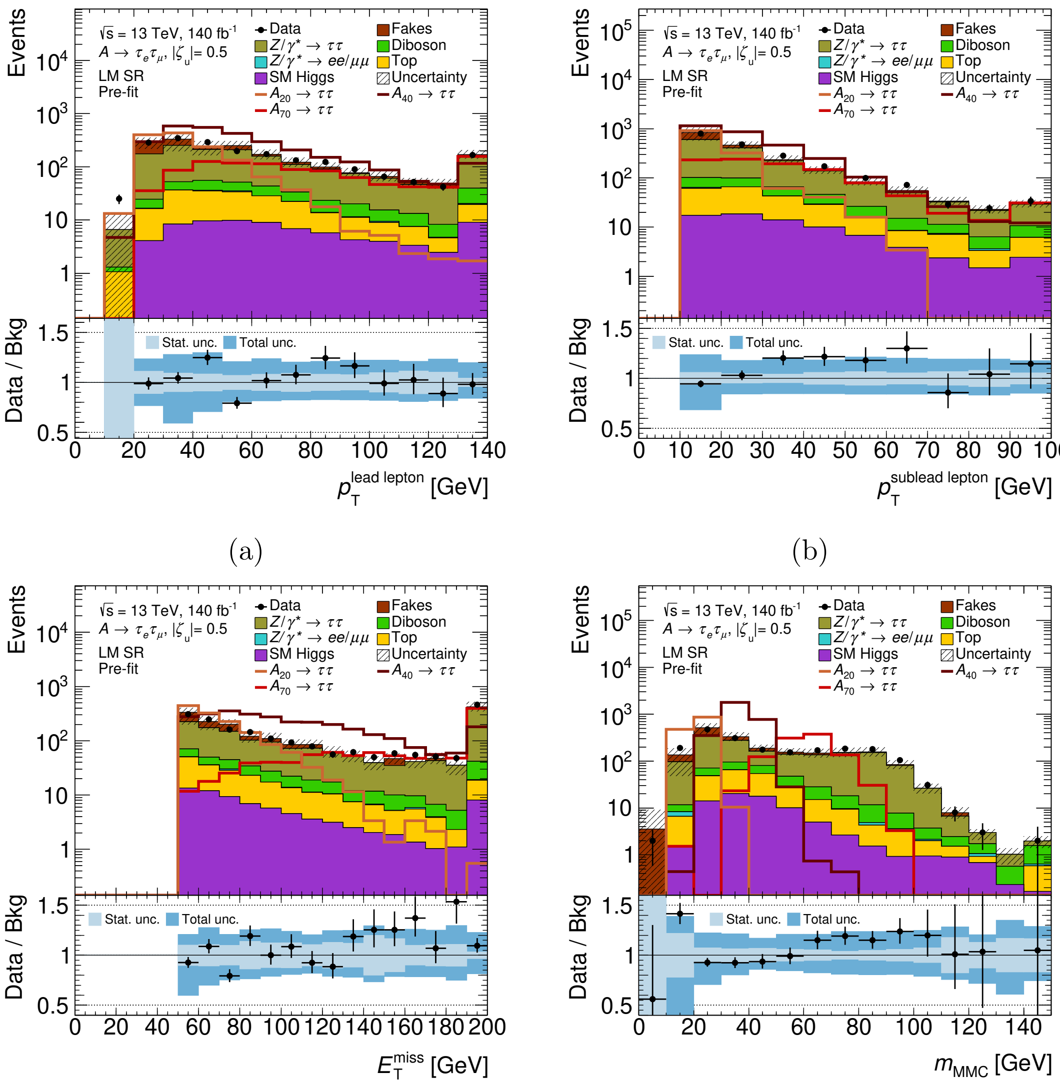

(a) (b) (c) (d)

Figure 6.22: Variable distributions in the LMSR after complete selection criteria: (a) leading lepton p_{T}, (b) subleading lepton p_{T}, (c) $E_{\mathrm{T}}^{\mathrm{miss}}$ and (d) m_{MMC}. The background is estimated by using MC simulation and data-driven methods (for details see Section 6.3). The expected signal contributions for the masses $m_A = 20,\ 40$ and $70\,\mathrm{GeV}$ are displayed for $|\zeta_{\mathrm{u}}| = 0.5$. Events with values beyond the x-axis range are shown in the last bin of each distribution. The dark blue bands in the ratio plot visualize the total uncertainty of the background estimate from both statistical and systematic sources. The statistical uncertainty is overlaid as the light blue band.

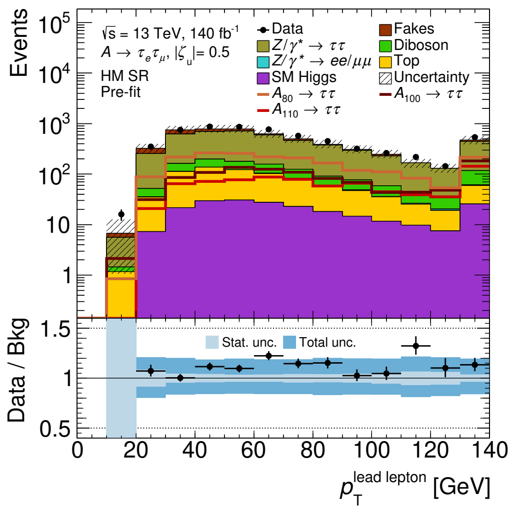

(a)

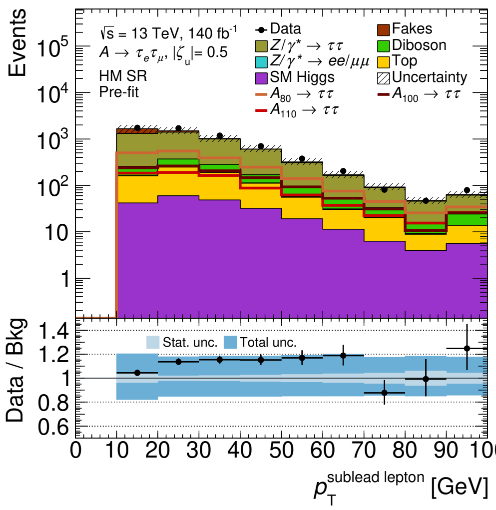

(b)

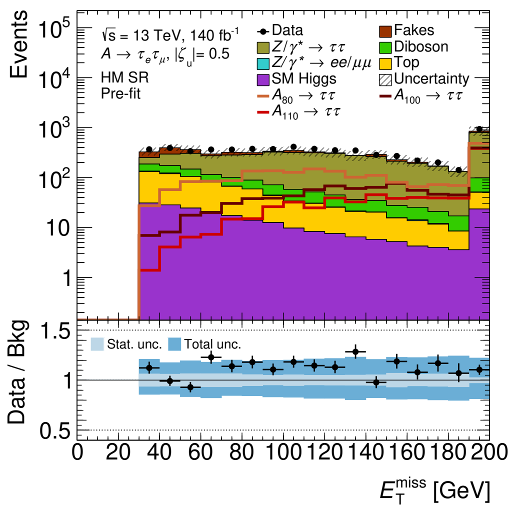

(c)

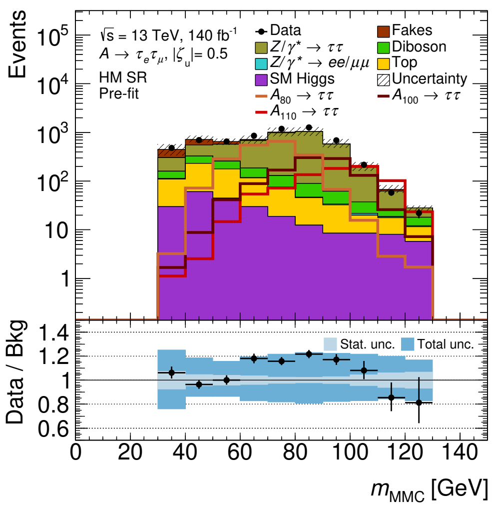

(d)

Figure 6.23: Variable distributions in the HMSR after complete selection criteria: (a) leading lepton p_{T}, (b) subleading lepton p_{T}, (c) $E_{\mathrm{T}}^{\mathrm{miss}}$ and (d) m_{MMC}. The background is estimated by using MC simulation and data-driven methods (for details see Section 6.3). The expected signal contributions for the masses $m_A = 80$, 100 and 110 GeV are displayed for $|\zeta_{\mathrm{u}}| = 0.5$. Events with values beyond the x-axis range are shown in the last bin of each distribution. The dark blue bands in the ratio plot visualize the total uncertainty of the background estimate from both statistical and systematic sources. The statistical uncertainty is overlaid as the light blue band.

6.6 Statistical evaluation

The statistical analysis of the data employs a binned likelihood function constructed as the product of Poisson probability terms. Signal and background predictions depend on systematic uncertainties, which are parameterized as NPs and are constrained using Gaussian functions. The binned likelihood function is constructed in bins of the mass obtained from the MMC. In the following sections, first the statistical framework is explained, then the fit setup is given and finally the results are presented and discussed.

6.6.1 The statistical analysis framework

For the search of new particles, a statistical profile likelihood test [230] is carried out, which is outlined here. Two hypotheses are defined. The null hypothesis $\mathcal{H}_0$ describes all known phenomena, generally summarized as background. It is tested against the alternative hypothesis $\mathcal{H}_1$, which includes both the background and the new signature, here the CP-odd Higgs boson A.

The likelihood function

Different signal hypotheses can be tested by introducing the signal strength scale factor μ. Using this, the expectation value for each bin n_i of a histogram $\boldsymbol{n} = (n_1, \ldots, n_N)$ can be described as

$$E\left[n_i\right] = \mu s_i + b_i$$

with the expected signal and background yields in the ith bin s_i and b_i. A value of $\mu = 0$ represents the background hypothesis, while $\mu = 1$ describes the nominal signal hypothesis.
Assuming uncorrelated bins, the probability of the measured data yields follows a Poisson distribution, and the likelihood function for each bin can be written as

$$\mathcal{L}_i(\mu) = \mathrm{Pois}\left(n_i, \mu s_i + b_i\right),$$

with the Poisson distribution defined by:

$$\mathrm{Pois}\left(m, n\right) = \frac{n^m}{m!} e^{-n}.$$

The total likelihood for the distribution is then the product over the likelihoods for each bin:

$$\mathcal{L}(\mu) = \prod_{i=1}^{N} \mathcal{L}_i(\mu).$$

This likelihood depends only on the expected signal and background yields, as well as the measured data. To account for statistical and systematic uncertainties, additional dependencies need to be added. Each uncertainty is represented by a NP θ. The full set of nuisance parameters $\boldsymbol{\theta} = (\boldsymbol{\alpha}, \boldsymbol{\gamma})$ consists of the M systematic uncertainties $\alpha_j \in \{\alpha_1, \ldots, \alpha_M\}$ and the N statistical uncertainties $\gamma_i \in \{\gamma_1, \ldots, \gamma_N\}$.
The systematic uncertainties α_j are obtained from auxiliary measurements and are constrained using Gaussian functions:

$$\mathrm{Gauss}(x, \mu, \sigma) = \frac{1}{\sigma\sqrt{2\pi}} e^{-\frac{1}{2}\frac{(x-\mu)^2}{\sigma^2}}.$$

The statistical uncertainties γ_i on the MC generated signal and background, as well as the data-driven background are constraint by Poisson distributions using a light version of the Barlow and Beeston method [231]. For the full likelihood, the likelihood product over all regions r needs to be built:

$$\mathcal{L}(\mu, \boldsymbol{\theta}) = \mathcal{C} \prod_r \prod_i \mathrm{Pois}_r\left(n_i, \mu s_i(\boldsymbol{\theta}) + b_i(\boldsymbol{\theta})\right) \cdot \mathrm{Pois}_r\left(\gamma_i m_i, m_i\right) \times \prod_j \mathrm{Gauss}\left(\alpha_j, 0, 1\right), \tag{6.4}$$

where $\mathcal{C}$ is a scaling factor and $m_i = \frac{b_i^2}{\delta_i^2}$ with δ_i being the statistical uncertainty of the ith bin of the background prediction.

The test statistic

Using the likelihood distribution, the profile likelihood ratio $\tilde{\lambda}(\mu)$ can be constructed [230]:

$$\tilde{\lambda}(\mu) = \begin{cases} \dfrac{\mathcal{L}(\mu, \hat{\hat{\boldsymbol{\theta}}}(\mu))}{\mathcal{L}(\hat{\mu}, \hat{\boldsymbol{\theta}})} & \hat{\mu} \geq 0, \\[2ex] \dfrac{\mathcal{L}(\mu, \hat{\hat{\boldsymbol{\theta}}}(\mu))}{\mathcal{L}(0, \hat{\hat{\boldsymbol{\theta}}}(0))} & \hat{\mu} < 0. \end{cases} \tag{6.5}$$

Here, $\hat{\hat{\boldsymbol{\theta}}}(0)$ and $\hat{\hat{\boldsymbol{\theta}}}(\mu)$ are the conditional maximum-likelihood estimators (MLEs) of $\boldsymbol{\theta}$ for a strength parameter 0 or μ, respectively. The terms $\hat{\mu}$ and $\hat{\boldsymbol{\theta}}$ refer to the MLEs of $\mathcal{L}$. As only positive signal contributions are expected, the test statistic $\tilde{\lambda}$ is bound from below. For cases where the data fluctuates in a way that $\hat{\mu} < 0$, the closest value of $\mu = 0$ is the best estimate.
For carrying out the calculations, it is more convenient to modify the test statistic

from Equation 6.5 to

$$\tilde{t}_\mu = -2\ln\tilde{\lambda}(\mu) = \begin{cases} -2\ln\dfrac{\mathcal{L}(\mu,\hat{\hat{\boldsymbol{\theta}}}(\mu))}{\mathcal{L}(\hat{\mu},\hat{\boldsymbol{\theta}})} & \hat{\mu}\geq 0, \\ -2\ln\dfrac{\mathcal{L}(\mu,\hat{\hat{\boldsymbol{\theta}}}(\mu))}{\mathcal{L}(0,\hat{\hat{\boldsymbol{\theta}}}(0))} & \hat{\mu}< 0, \end{cases} \tag{6.6}$$

in which the natural logarithm is making it easier to deal with the products from the likelihood function.
To test the level of agreement between the data and a hypothesized value of μ, the p-value is introduced:

$$p_\mu = \int_{\tilde{t}_{\mu,\mathrm{obs}}}^{\infty} f(\tilde{t}_\mu|\mu)\ \mathrm{d}\tilde{t}_\mu. \tag{6.7}$$

with $\tilde{t}_{\mu|\mathrm{obs}}$ representing the value of the statistic $\tilde{t}_\mu$ observed in data and $f(\tilde{t}_\mu|\mu)$ the pdf of $\tilde{t}_\mu$ under the assumption of a signal strength μ. Typically, the pdfs are not known and need to be determined. One way to achieve this is by creating pseudo data, also known as toy MC, where random numbers are generated according to the underlying probability functions. However, this method is very CPU-intensive, so an alternative approach is often preferred. By applying Wilks' theorem [232] and the Wald approximation [233] for logarithmic likelihood functions, the test statistic can be expressed as

$$\tilde{t}_\mu = \begin{cases} \dfrac{(\mu-\hat{\mu})^2}{\sigma^2} & \hat{\mu}\geq 0, \\ \dfrac{\mu^2}{\sigma^2} - \dfrac{2\mu\hat{\mu}}{\sigma^2} & \hat{\mu}< 0. \end{cases} \tag{6.8}$$

The underlying assumption is that $\tilde{t}_\mu$ approaches the asymptotic approximation in Equation 6.8 once the sample reaches a reasonably large size. The major benefit of the approximation is that Equation 6.8 is independent of the NPs.
The MLE $\hat{\mu}$ is assumed to follow a Gaussian distribution around the mean value μ'

with the standard deviation σ. The corresponding pdf is found to be

$$f\left(\tilde{t}_\mu|\mu'\right) = \frac{1}{2\sqrt{2\pi\tilde{t}_\mu}} \exp\left[-\frac{1}{2}\left(\sqrt{\tilde{t}_\mu} + \frac{\mu-\mu'}{\sigma}\right)^2\right] + \begin{cases} \frac{1}{2\sqrt{2\pi\tilde{t}_\mu}} \exp\left[-\frac{1}{2}\left(\sqrt{\tilde{t}_\mu} + \frac{\mu-\mu'}{\sigma}\right)^2\right] & \tilde{t}_\mu \leq \mu^2/\sigma^2, \\ \frac{1}{\sqrt{2\pi}(2\mu/\sigma)} \exp\left[-\frac{1}{2}\frac{\left(\tilde{t}_\mu - \frac{\mu^2-2\mu\mu'}{\sigma^2}\right)^2}{(2\mu/\sigma)^2}\right] & \tilde{t}_\mu > \mu^2/\sigma^2. \end{cases} \tag{6.9}$$

This method of determining the pdf is much more efficient than generating pseudo data, as only μ' and σ are needed, which can be measured in data.

Exclusion limit calculation

If no significant excess above the SM predictions is observed, exclusion limits can be set. Setting upper limits on the signal strength μ is very similar to the p-value calculation [230]. Only the test statistic $\tilde{t}_\mu$ from Equation 6.6 is modified to become zero for $\hat{\mu} > \mu$ to not consider more compatible estimates than the hypothesized value of μ as evidence against the hypothesis:

$$\tilde{q}_\mu = \begin{cases} -2\ln\tilde{\lambda}(\mu) & \hat{\mu} \leq \mu, \\ 0 & \hat{\mu} > \mu, \end{cases} = \begin{cases} -2\ln\frac{\mathcal{L}(\mu,\hat{\hat{\boldsymbol{\theta}}}(\mu))}{\mathcal{L}(0,\hat{\hat{\boldsymbol{\theta}}}(0))} & \hat{\mu} < 0, \\ -2\ln\frac{\mathcal{L}(\mu,\hat{\hat{\boldsymbol{\theta}}}(\mu))}{\mathcal{L}(\hat{\mu},\hat{\boldsymbol{\theta}})} & 0 \leq \hat{\mu} \leq \mu, \\ 0 & \hat{\mu} > \mu. \end{cases}$$

This test statistic can be used to calculate the p-value similar to Equation 6.7 with the pdf $f(\tilde{q}_\mu|\mu,\hat{\hat{\boldsymbol{\theta}}}(\mu|\text{obs}))$, in which $\hat{\hat{\boldsymbol{\theta}}}(\mu|\text{obs})$ represents the NPs that maximize the likelihood function for a specific value of μ under the condition of the observed data. Again, Wilks' theorem [232] and the Wald approximation [233] can be used to get an approximation for $\tilde{q}_\mu$, similar to Equation 6.8:

$$\tilde{q}_\mu = \begin{cases} \frac{\mu^2}{\sigma^2} - \frac{2\mu\hat{\mu}}{\sigma^2} & \hat{\mu} < 0, \\ \frac{(\mu - \hat{\mu})^2}{\sigma^2} & 0 \leq \hat{\mu} \leq \mu, \\ 0 & \hat{\mu} > \mu. \end{cases} \tag{6.10}$$

The resulting pdf is

$$f\left(\tilde{q}_\mu|\mu'\right) = \Phi\left(\frac{\mu' - \mu}{\sigma}\right)\delta(\tilde{q}_\mu)$$
$$+ \begin{cases} \frac{1}{2}\frac{1}{\sqrt{2\pi}}\frac{1}{\sqrt{\tilde{q}_\mu}}\exp\left[-\frac{1}{2}\left(\sqrt{\tilde{q}_\mu} + \frac{\mu - \mu'}{\sigma}\right)^2\right] & 0 < \tilde{q}_\mu \leq \mu^2/\sigma^2, \\ \frac{1}{\sqrt{2\pi}(2\mu/\sigma)}\exp\left[-\frac{1}{2}\frac{\left(\tilde{q}_\mu - \frac{\mu^2 - 2\mu\mu'}{\sigma^2}\right)^2}{(2\mu/\sigma)^2}\right] & \tilde{q}_\mu > \mu^2/\sigma^2, \end{cases}$$

with Φ being the cumulative distribution of the standard Gaussian (zero mean, unit variance). Using this pdf, the p-value can be calculated with Equation 6.7 and setting $\mu' = \mu$. To obtain an exclusion limit, one defines the threshold parameter α in a way that all values $p_\mu < \alpha$ are excluded with a CL of $1 - \alpha$. A common choice for the threshold parameter is $\alpha = 0.05$, corresponding to a 2σ deviation and resulting in a 95 % CL. The upper limit on μ is the largest value μ for which $p_\mu \leq \alpha$.

The limit procedure described up to this point rejects the signal-plus-background hypothesis, and hence the CL is referred to as $\mathrm{CL_{s+b}}$. This method has one drawback: in the case of a small signal compared to the background and low statistics, the signal could be excluded due to downward fluctuations of the background in data. To compensate for this, the $\mathrm{CL_s}$ method [234] in introduced:

$$\mathrm{CL_s} = \frac{\mathrm{CL_{s+b}}}{\mathrm{CL_b}}, \tag{6.11}$$

normalizing $\mathrm{CL_{s+b}}$ by dividing it through the CL of the background-only hypothesis. This is accomplished by adjusting the p-value to

$$p'_\mu = \frac{p_\mu}{1 - p_b}$$

with

$$p_b = 1 - \int_{\tilde{q}_{\mu,\mathrm{obs}}}^{\infty} f(\tilde{q}_\mu|0, \hat{\hat{\boldsymbol{\theta}}}(0|\mathrm{obs}))\,\mathrm{d}\tilde{q}_\mu,$$

and μ' set to zero.

Expected limits

In many cases it is useful to calculate expected limits without using any observed data. Instead of the observed data, an artificial data set called the *Asimov data set* [230] is used. It is constructed in a way such that when it is used to evaluate the MLEs for all parameters, the true parameter values are obtained. This is achieved by setting the Asimov data to their expectation value for a specific signal strength parameter μ'

$$
\begin{aligned}
n_{i,\mathrm{A}} &= E\left[n_i\right] = \mu' s_i + b_i, \\
m_{i,\mathrm{A}} &= E\left[m_i\right] = u_i(\boldsymbol{\theta}).
\end{aligned}
$$

This Asimov data set is used to evaluate an Asimov likelihood $\mathcal{L}_\mathrm{A}$ similar to Equation 6.4 and subsequently construct the Asimov profile likelihood ratio $\tilde{\lambda}_\mathrm{A}(\mu)$ following Equation 6.5. The variance describing the distribution of $\hat{\mu}$ is derived to

$$\sigma_\mathrm{A}^2 = \frac{(\mu - \mu')^2}{\tilde{q}_{\mu,\mathrm{A}}},$$

where $\tilde{q}_{\mu,\mathrm{A}} = -2\ln\tilde{\lambda}_\mathrm{A}(\mu)$. The variance is simplified for the important case of no signal by setting $\mu' = 0$

$$\sigma_\mathrm{A}^2 = \frac{\mu^2}{\tilde{q}_{\mu,\mathrm{A}}}.$$

The $\mathrm{CL_s}$ limits on μ obtained through this method are referred to as expected limits. They represent the minimum limits that reject the signal hypothesis, assuming the data follows the background prediction. Furthermore, error bands on the expected upper limits with $\pm N\sigma$ can be calculated through variations of $\hat{\mu}$ by $\pm N\sigma_\mathrm{A}$ around μ'.

6.6.2 Fit setup

The fit model for this search consists of three regions: the LMSR or HMSR, chosen dependent on the evaluated signal mass hypothesis, and the two control regions TCR and ZCR.

The distribution of m_MMC is used for the statistical analysis of the data in the SRs. As the signal distribution is expected to have a different shape than the background, it is beneficial to use a high number of bins, while fulfilling the statistical requirements. The binning strategy chooses the bins in a way that the background statistical uncertainty per bin does not exceed 10 %. At the same time, each bin must have at least 10 background events as required by the statistical analysis. Additionally, there has to be at least one fake-lepton event per bin in order to avoid high statistical uncertainties for the statistical analysis. Furthermore, the minimum bin width is set to 2 GeV, which prevents bin migration effects that have been visible in finer binned distributions. Figure 6.24 shows the m_{MMC} distributions in the obtained binnings, with the bin borders listed here (in [GeV]):

- low-mass SR: (10.0, 26.2, 30.1, 34.3, 38.3, 44.4, 49.1, 54.0, 57.0, 59.5, 61.5, 64.7, 68.3, 74.1, 76.6, 78.6, 81.6, 85.3, 87.3, 91.7, 110.0)
- high-mass SR: (35.0, 37.4, 40.2, 42.3, 44.7, 47.3, 50.0, 52.1, 54.2, 56.2, 58.2, 60.2, 62.4, 66.2, 70.7, 72.7, 74.7, 77.2, 79.2, 86.0, 90.0, 92.0, 94.1, 99.3, 102.3, 104.3, 107.1, 110.1, 130.0).

The control regions are included to extract a normalization factor for the top-quark and the $Z \to \tau\tau$ background, respectively, and to constrain systematic uncertainties. To take into account shape effects, the CRs are split into multiple bins in m_{MMC}. The binning was chosen in a way to reflect the shape of the distribution while ensuring sufficient statistical coverage in each bin. It is shown in Figure 6.24 with the following bin borders (in [GeV]):

- TCR: (0.0, 30.0, 45.0, 65.0, 90.0, 150.0)
- ZCR: (0.0, 50.0, 70.0, 80.0, 90.0, 110.0, 150.0).

While the signal contributions in the CRs are small, they are still taken into account in the fit properly.
The validation regions FVR, LMSSVR and HMSSVR are not included in the fit. While it would be beneficial to have a normalization factor for the fake-lepton background as well, they cannot be used for this purpose because this background is obtained using independent data and the composition of the fake leptons is too different compared to the SRs.
The statistical uncertainties of the backgrounds and signals arise from the finite number of simulated MC events and the statistical uncertainties of the data entering the matrix method. They are modeled by NPs which use Poisson constraints and are separately introduced for the signals and the combined backgrounds.
In the general fit, all the systematic uncertainties described in Section 6.4 are used, except for the uncertainties on the signal cross-section. These signal cross-section uncertainties are added in the second fit, which is probing $|\zeta_{\text{u}}|$ parameter values.
In order to reduce the impact of statistical fluctuation and small systematic variations, a smoothing and pruning procedure is put in place for the systematic uncertainties. It was inspired by the ATLAS $VHbb$ Run 1 analysis [235]. The smoothing is done using the `353QH twice` algorithm [236] for the relative uncertainty size of each NP using neighboring bins in the m_{MMC} distributions. The pruning happens in two steps:

1. Drop the shape uncertainty if no single bin has a deviation greater than 0.5 % for a given process.
2. Drop the normalization uncertainty if it is smaller than 0.5 % for a given process.

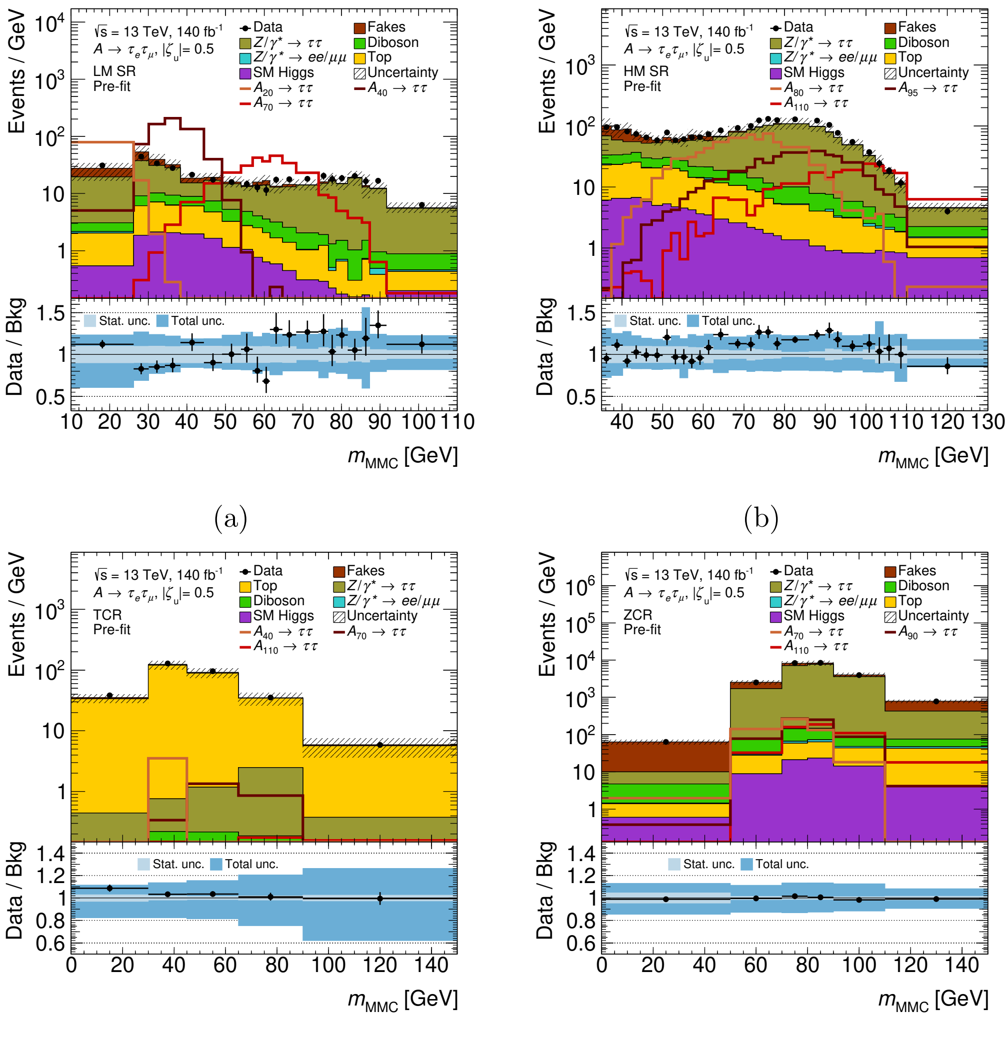

Figure 6.24: Input m_{MMC} distributions for the statistical analysis (pre-fit). Either (a) the LMSR or (b) the HMSR is chosen, dependent on the signal mass hypothesis as the SR. The two CRs (c) TCR and (d) ZCR are used in all cases. The signals are scaled with $|\zeta_{\mathrm{u}}| = 0.5$ and displayed here only for comparison. In the statistical analysis, only one signal hypothesis is used at a time and tested with the here shown backgrounds.

6.6.3 Fit results

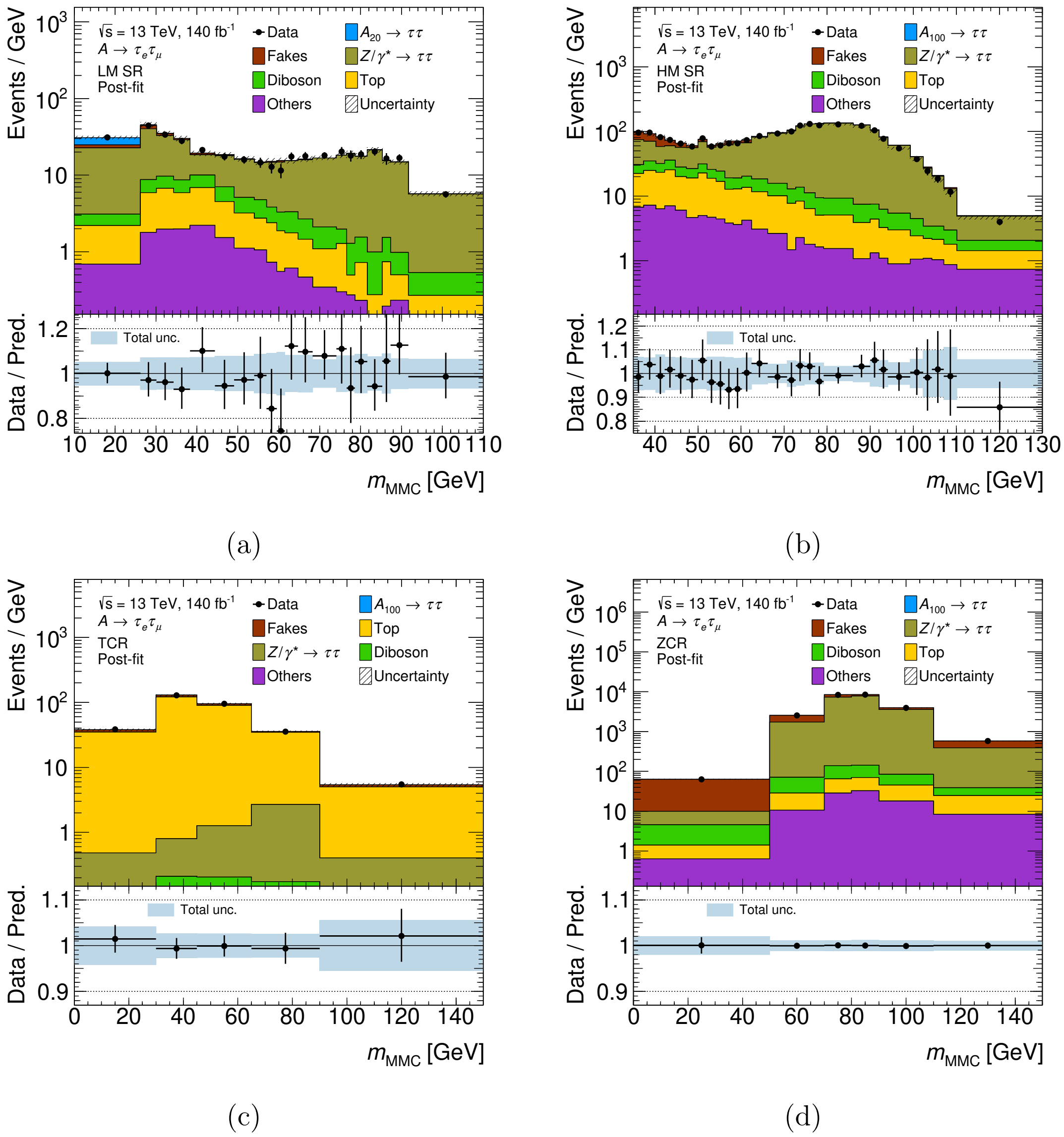

Figure 6.25: Post-fit m_{MMC} distributions in (a) the LMSR for $m_A = 20\,\mathrm{GeV}$ and (b) the HMSR for $m_A = 100\,\mathrm{GeV}$. The fit results in the CRs are shown for $m_A = 100\,\mathrm{GeV}$ in (c) for the TCR and (d) for the ZCR. The signal-plus-background hypothesis is used for the fits with the respective m_A. The processes $Z/\gamma^* \to \ell^+\ell^-$ and SM Higgs production are summarized to the 'Others' background. Events with values beyond the x-axis range are shown in the last bin of each distribution. The blue band in the ratio plot shows the total uncertainty of the background estimate.

Table 6.12: Post-fit event yields for the background-only fit in the LMSR and the two CRs (TCR and ZCR).

	LMSR			ZCR			TCR		
Signal	0.0			0.0			0.0		
Fake leptons	143	$\pm$	64	51,600	$\pm$	3300	350	$\pm$	280
$Z \to \tau\tau$	1458	$\pm$	75	264,100	$\pm$	3700	123	$\pm$	29
Diboson	131	$\pm$	24	3950	$\pm$	380	10.3	$\pm$	2.1
Top	161	$\pm$	20	2420	$\pm$	310	5710	$\pm$	230
$H_{125} + Z \to \ell\ell$	79.0	$\pm$	2.5	1562	$\pm$	37	6.09	$\pm$	0.32
Total	1972	$\pm$	50	323,700	$\pm$	1800	6200	$\pm$	110
Data	1972			323,650			6204		

The fit results are shown in Figure 6.25 for the signal mass hypothesis $m_A = 20\,\text{GeV}$ in the LMSR and for the hypothesis $m_A = 100\,\text{GeV}$ in the HMSR, as well as in the TCR and ZCR, including both statistical and systematic uncertainties in all cases. The data agree well with the predictions in all cases within the respective uncertainties. The uncertainties are largely reduced compared to the pre-fit plots shown in Figure 6.24. After carrying out the fit, they are now in the order of 10 % in the SRs and $2-5\,\%$ in the CRs. The fit results in the CRs are in general very similar for the different mass hypotheses. Section D.3.1 in Appendix D shows additional post-fit plots: The comparison between pre-fit and post-fit distributions in the CRs is shown for $m_A = 20\,\text{GeV}$ in Figure D.2 and for $m_A = 100\,\text{GeV}$ in Figure D.3, while the results in the SRs for the additional mass hypotheses are shown in Figure D.4 and Figure D.5.

The post-fit event yields for the background-only fit are listed in Table 6.12 for the LMSR and in Table 6.13 for the HMSR. In both cases, the fit is carried out simultaneously in the respective SR and the two CRs, TCR and ZCR. In all regions, the prediction agrees very well with the observed data. The overall largest uncertainties arise from the fake-lepton and $Z \to \tau\tau$ backgrounds, with the top process uncertainties additionally playing an important role in the TCR.

The largest uncertainties are measured by their post-fit impact on the signal strength. Table 6.14 lists the NP groups according to their relative contribution to the post-fit impact for $m_A = 20\,\text{GeV}$ and $m_A = 100\,\text{GeV}$. In both cases it can be seen that the uncertainties are dominated by systematic uncertainties and the

Table 6.13: Post-fit event yields for the background-only fit in the HMSR and the two CRs (TCR and ZCR).

	HMSR			ZCR			TCR		
Signal	0.0			0.0			0.0		
Fake leptons	390	$\pm$	89	51,900	$\pm$	5500	350	$\pm$	350
$Z \to \tau\tau$	4490	$\pm$	100	264,000	$\pm$	6000	125	$\pm$	32
Diboson	411	$\pm$	75	3860	$\pm$	380	9.8	$\pm$	2.0
Top	592	$\pm$	78	2360	$\pm$	310	5710	$\pm$	260
$H_{125} + Z \to \ell\ell$	237.1	$\pm$	6.8	1557	$\pm$	55	6.13	$\pm$	0.34
Total	6123	$\pm$	94	323,700	$\pm$	2500	6200	$\pm$	140
Data	6119			323,650			6204		

data statistical uncertainties only play a minor direct role. However, the data statistics also enter indirectly through the fake-lepton background estimation ('Fake-lepton statistical' and 'Fake-lepton systematic'), which forms one of the three most important groups. The other two significant groups are the '$Z \to \tau\tau$ modeling' and the $Z \to \tau\tau$ MC sample size ('$Z \to \tau\tau$ statistical'). The latter is the most impactful NP group. To mitigate its impact, dedicated low-$m_{\ell\ell}$ samples with increased statistics are already in use. Its impact is augmented by the relatively fine binning that is in use in the SRs. However, while a wider binning might attenuate the impact of the $Z \to \tau\tau$ MC sample size, studies have shown that this would come with overall loss of signal sensitivity and ultimately worse exclusion limits.

The $Z \to \tau\tau$ modeling ranks highly because $Z \to \tau\tau$ is the main background in the analysis and it gets increasingly difficult to model it in the low $\Delta R_{\ell\ell}$ regions used for the SRs. It shows up a bit further down in the ranking in the LMSR because there the fake-lepton background becomes more significant. As a data-driven method, the fake-lepton estimation naturally suffers from the low statistics in the regions where the lepton efficiencies are calculated, and hence its uncertainties have a measurable impact on the fit results.

Table 6.14: Relative contributions to the uncertainty of the extracted signal strength μ from the likelihood fit to the data for the hypothesis $m_A = 20\,\text{GeV}$ and $m_A = 100\,\text{GeV}$. The contributions are calculated by fixing the relevant NPs to their post-fit values in the likelihood fit. The relative impact is obtained as the square-root of the difference of the squares of the nominal uncertainty and the obtained uncertainty, then dividing by the nominal uncertainty. The total uncertainty differs from the sum of all squared individual uncertainties due to correlations between uncertainties. The impact of data statistical uncertainties is determined by fitting with all NPs fixed to their post-fit values. The background statistical uncertainty includes the uncertainties from background MC statistics as well as the statistical uncertainty from the fake-lepton background determination. NP groups are only listed if they have a relative impact larger than 5%.

$m_A = 20\,\text{GeV}$		$m_A = 100\,\text{GeV}$	
Category	Relative contribution to $\Delta\mu$	Category	Relative contribution to $\Delta\mu$
Data statistical	42%	**Data statistical**	27%
Systematic	91%	**Systematic**	96%
Background statistical	81%	Background statistical	58%
$Z \to \tau\tau$ statistical	75%	*$Z \to \tau\tau$ statistical*	44%
Fake-lepton statistical	30%	*Fake-lepton statistical*	37%
Other background stat.	7%	*Other background stat.*	8%
Fake-lepton systematic	37%	$Z \to \tau\tau$ modeling	37%
Signal modeling	11%	Fake-lepton systematic	19%
$Z \to \tau\tau$ modeling	9%	Signal statistical	18%
Muon efficiencies	8%	Muon calibration	18%
Diboson modeling	8%	$Z \to \tau\tau$ and $t\bar{t}$ norm.	12%
		$Z \to \tau\tau$ reweighting	12%
		Muon efficiencies	11%
		Electron calibration	10%
		Flavor tagging	6%

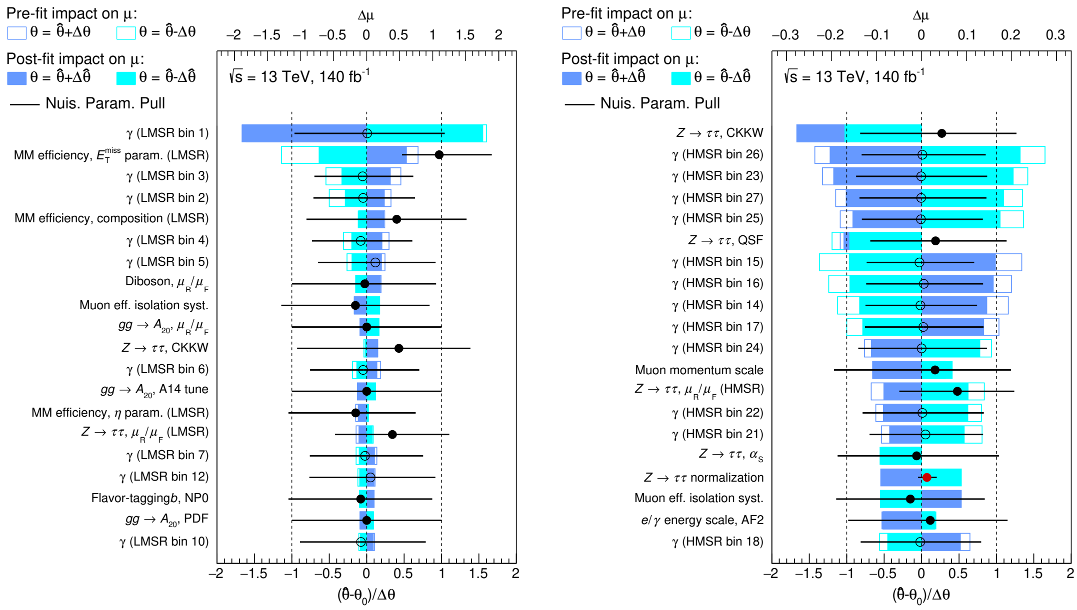

(a) (b)

Figure 6.26: Ranking of systematic uncertainties based on their post-fit impact on the signal strength μ in the model-independent fit. The 20 NPs with the highest impact are displayed in (a) the LMSR for the $m_A = 20\,\text{GeV}$ signal and (b) the HMSR for the $m_A = 100\,\text{GeV}$ signal. The top axis measures the pre- and post-fit impact $\Delta\mu$ of each NP, while the bottom axis parametrizes the NP pulls and constraints of each NP in standard deviations $\Delta\theta$ of its pre-fit value θ_0. The pre-fit (post-fit) impact of a NP is determined as the difference between the fitted μ value in the nominal fit and a fit when fixing the NP to $\hat{\theta} \pm \Delta\theta$ ($\hat{\theta} \pm \Delta\hat{\theta}$), with $\hat{\theta}$ being the best-fit value of the NP and $\Delta\theta$ ($\Delta\hat{\theta}$) representing its pre-fit (post-fit) uncertainty.

The grouped impacts for the additional mass hypotheses are listed in Section D.3.2 in Appendix D. Overall, the $Z \to \tau\tau$ MC sample size and fake-lepton background uncertainties dominate throughout the full mass range. For the higher mass points of the LMSR, the $Z \to \tau\tau$ modeling is replaced by uncertainties on diboson modeling and $E_{\mathrm{T}}^{\mathrm{miss}}$ as the following NP group. Around the Z boson mass, the $Z \to \tau\tau$ reweighting becomes an important NP group.
The rankings of the individual NPs with the highest impact on the signal strength are shown in Figure 6.26 for $m_A = 20\,\text{GeV}$ and $m_A = 100\,\text{GeV}$. They break down the impacts of the NP groups described in the previous paragraph and also provide additional information about pulls and constraints. In both cases, the γ NPs, which

incorporate the statistical uncertainties on the combined backgrounds, are very important. They relate to the fake-lepton background statistical uncertainties and the uncertainties introduced due to the $Z \to \tau\tau$ MC sample size.
For the $m_A = 20\,\text{GeV}$ mass point, the fake-lepton composition and $E_{\text{T}}^{\text{miss}}$ parametrization uncertainties rank highly. This is expected as almost all of the signal is found in the first bin of the m_{MMC} distribution, which has a high abundance of fake leptons that comes with various uncertainties. For the $m_A = 100\,\text{GeV}$ mass hypothesis, the $Z \to \tau\tau$ modeling uncertainties from ME matching (CKKW) and soft-gluon emission resummation (QSF) scales play the most significant role due to the importance of the $Z \to \tau\tau$ background in that mass regime. They show a one-sided behavior because the variations of these scales produce highly asymmetric resulting uncertainty distributions coming from the variations of the input parameters. This behavior has been investigated further in Section C.3.
The systematic uncertainty rankings for the additional mass hypotheses are shown in Section D.3.3 in Appendix D. In general, the γ NPs are important for all masses. Other important NPs are related to MM efficiencies for low masses, to diboson modeling, flavor-tagging and $E_{\text{T}}^{\text{miss}}$ for the intermediate mass range, and to the $Z \to \tau\tau$ modeling scales for the higher mass points.
Generally, the fit shows a good behavior, as no NPs are strongly pulled or constrained. The largest pull is observed for the $E_{\text{T}}^{\text{miss}}$ parametrization uncertainty of the MM efficiencies for $m_A = 20\,\text{GeV}$. It is caused by the overshoot of data in the first bin in the m_{MMC} distribution in the LMSR, shown in Figure 6.24(a), which puts a tension on the $E_{\text{T}}^{\text{miss}}$ parametrization because this favors a downward tendency, as seen in Figure C.4.
On top of the pulls and constraints between NPs, their correlations can be calculated by using the covariance of two NPs θ_i and θ_j:

$$\text{corr}\left[\theta_i, \theta_j\right] = \frac{\text{cov}\left[\theta_i, \theta_j\right]}{\sqrt{\left[\theta_i, \theta_i\right] \cdot \left[\theta_j, \theta_j\right]}}.$$

The parameter of interest μ is included in these evaluations. Figure 6.27 shows the correlation matrices for all NPs that have at least one correlation $> 20\,\%$, for $m_A = 20\,\text{GeV}$ and $m_A = 100\,\text{GeV}$. Generally, the correlations are low and no striking patterns are observed. The few higher correlations can be explained with the nature of the involved NPs. Correlations are expected for NPs that are similar in shape and/or magnitude and affect the same background process, for example ISR and ME uncertainties on the top background, or n_{jets} reweighting and scale uncertainties on the $Z \to \tau\tau$ background. The γ NPs can be correlated with each other (within the same region) and with the fake-lepton background systematics because they might use the same data to calculate the lepton efficiencies for the MM or because the same *Non-tight* lepton data is used to calculate the fake-lepton

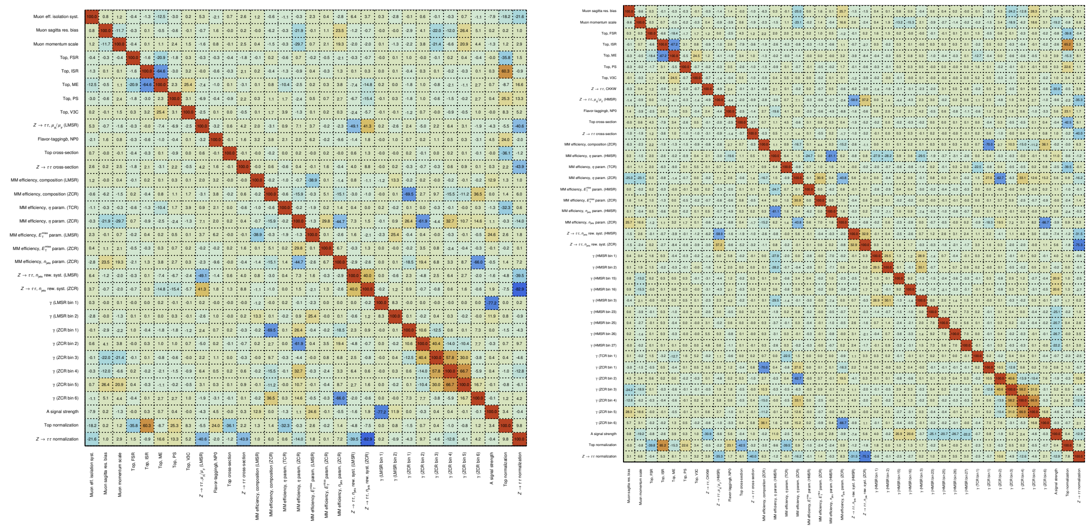

(a) (b)

Figure 6.27: Correlation matrices for all NPs with a correlation > 20% of the fit to data. The considered signals are (a) $m_A = 20\,\mathrm{GeV}$ in the LMSR and (b) $m_A = 100\,\mathrm{GeV}$ in the HMSR.

content for multiple bins. The signal strength is correlated with NPs that have a large impact on the fit result. The correlation matrices for the additional mass hypotheses are given in Section D.3.5 in Appendix D.

The compatibility of the observed data in the m_{MMC} distribution with the background-only hypothesis is evaluated by calculating the local p_0-value according to Equation 6.7. This is carried out individually for each A boson mass hypothesis in the corresponding SR. The results are displayed in Figure 6.28, which shows the local p_0-values together with the corresponding significances. No substantial excess above the background-only hypothesis is observed. The most significant local excess of events is observed for $m_A = 20\,\mathrm{GeV}$ with $1.8\,\sigma$, followed by a $1.3\,\sigma$ local excess for $m_A = 85\,\mathrm{GeV}$. The exact numbers for the p_0-values and significances are listed in Section D.1 in Appendix D.

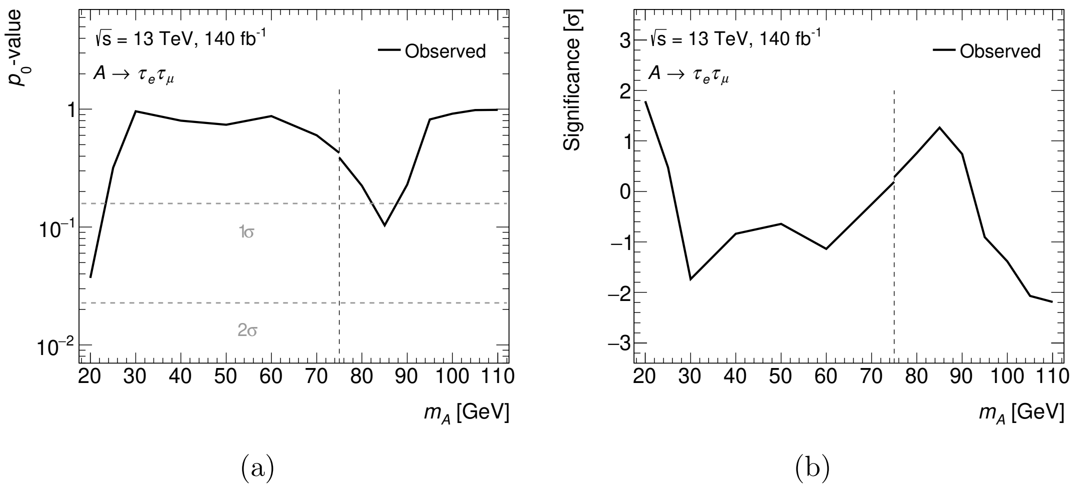

Figure 6.28: Observed (a) p_0-values and (b) discovery significance for the production cross-section for $gg \to A$ times the branching ratio for A decaying into two τ-leptons for A boson masses from 20 to 110 GeV. The solid line represents the observed p_0-values. The horizontal dashed lines visualize the values corresponding to $1\,\sigma$ and $2\,\sigma$ excesses. The vertical dashed line visualizes the split into two SRs: the mass points on the left side are analyzed within the LMSR and the ones on the right side in the HMSR.

6.6.4 Cross-section limits

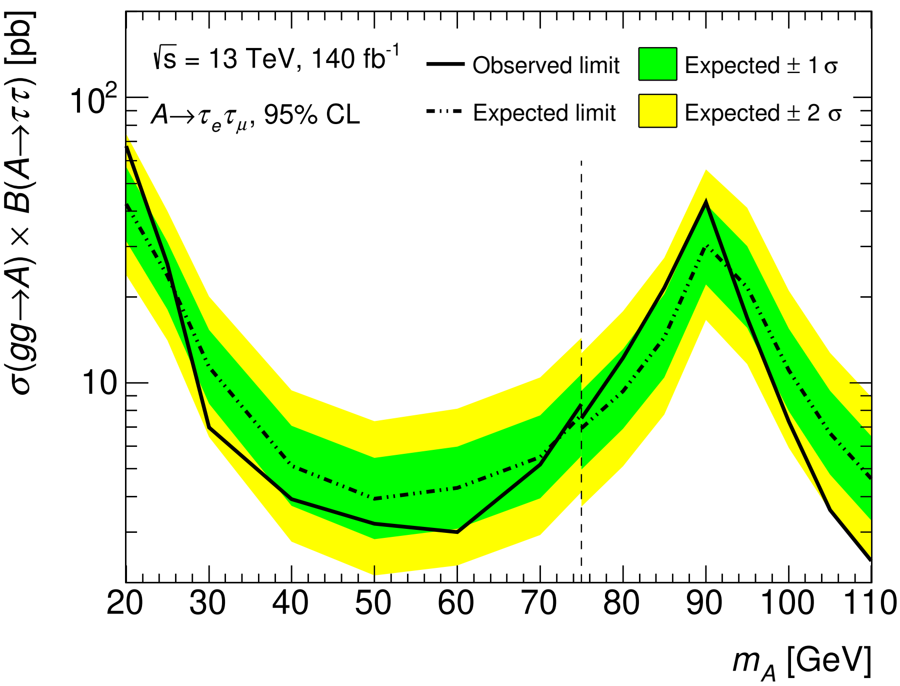

Figure 6.29: Expected and observed upper limits on the production cross-section for $gg \to A$ times the branching ratio for A decaying into two τ-leptons for A boson masses from 20 to 110 GeV. The dash-dotted line shows the expected limit set by analyzing the shape of the m_{MMC} distribution with its $1\,\sigma$ and $2\,\sigma$ uncertainty bands in green and yellow, respectively. The observed limits are shown by the solid line. The vertical dashed line visualizes the split into two SRs: the mass points on the left side are analyzed within the LMSR and the ones on the right side in the HMSR.

As no significant excess of data events over the prediction has been observed, limits can be set on the signal strength μ. The expected and observed 95 % CL limits are calculated with the $\mathrm{CL_s}$ method according to Equation 6.11. The limits on the signal strength are translated into limits on the gluon–gluon fusion production cross-section $\sigma(gg \to A)$ times the branching ratio for A boson decay into two τ-leptons, $\mathcal{B}(A \to \tau\tau)$. The obtained results are shown in Figure 6.29. They include all systematic uncertainties described in Section 6.4, except for the signal cross-section uncertainties.
The observed limits range from 2.4 pb for $m_A = 110\,\mathrm{GeV}$ to 67 pb for $m_A = 20\,\mathrm{GeV}$.

The worst limits are set for the low mass points because the statistics are limited with lots of events getting rejected by the triggers. The limits then improve towards higher masses as the statistics get better and the fake-lepton background loses influence. Towards the Z boson resonance, the sensitivity is largely reduced due to the huge background from $Z \to \tau\tau$ decays and its accompanying uncertainties. Above 90 GeV, the sensitivity quickly increases again and reaches its best value for $m_A = 110\,\text{GeV}$.
The exact values for the expected and observed limits are listed in Table D.3 in Appendix D. The appendix also shows the comparison of the expected limit with the STAT-only limit in Figure D.1.

6.6.5 Fit results for the model-dependent evaluation

The model-dependent fit differs from the model-independent fit only by including one additional NP per mass point for the signal cross-section uncertainty. This only marginally changes the fit behavior, so that the fit results and checks can almost be taken entirely from the model-independent fit. In the NP ranking, the additional NP shows up only for mass points that are not too close to the Z boson mass: $m_A = 20, 25, 30, 40, 50, 60, 105$ and $110\,\text{GeV}$. It is shown for $m_A = 20\,\text{GeV}$ and $m_A = 110\,\text{GeV}$ in Figure 6.30, where the signal cross-section uncertainty shows up on positions three and eight, respectively. All other NP impacts, pulls and constraints are identical to the model-independent fit (compare to Figure 6.26(a) for $m_A = 20\,\text{GeV}$ and Figure D.9(d) for $m_A = 110\,\text{GeV}$). The ranking plots for the additional mass points are shown in Section D.3.4 in Appendix D.

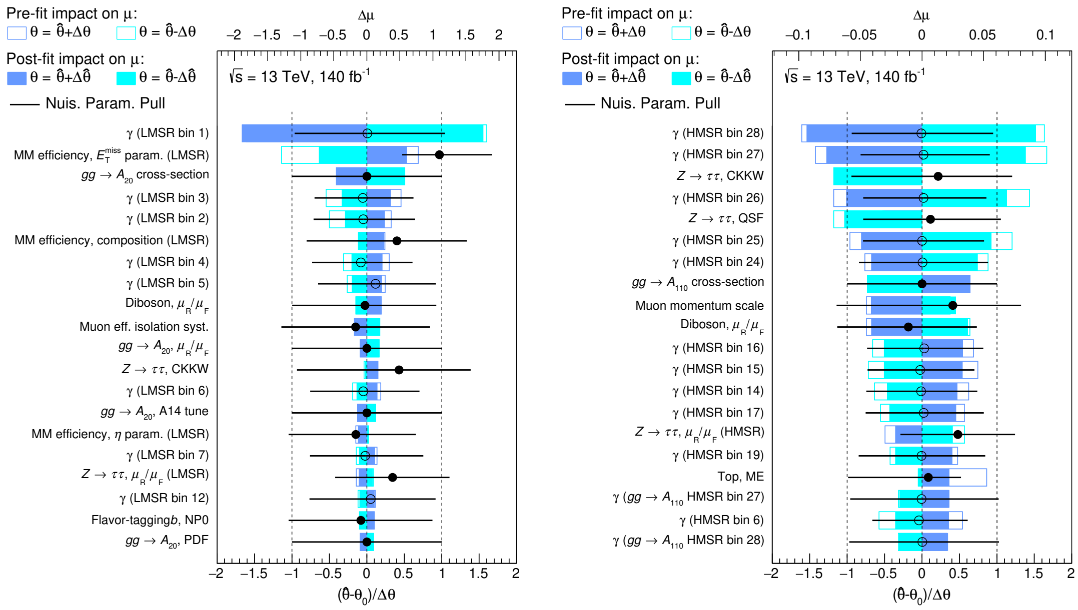

(a) (b)

Figure 6.30: Ranking of systematic uncertainties based on their post-fit impact on the signal strength μ in the model-dependent fit. The 20 NPs with the highest impact are displayed in (a) the LMSR for the $m_A = 20\,\text{GeV}$ signal and (b) the HMSR for the $m_A = 110\,\text{GeV}$ signal. The top axis measures the pre- and post-fit impact $\Delta\mu$ of each NP, while the bottom axis parametrizes the NP pulls and constraints of each NP in standard deviations $\Delta\theta$ of its pre-fit value θ_0. The pre-fit (post-fit) impact of a NP is determined as the difference between the fitted μ value in the nominal fit and a fit when fixing the NP to $\hat{\theta} \pm \Delta\theta$ ($\hat{\theta} \pm \Delta\hat{\theta}$), with $\hat{\theta}$ being the best-fit value of the NP and $\Delta\theta$ ($\Delta\hat{\theta}$) representing its pre-fit (post-fit) uncertainty.

6.6.6 $|\zeta_\mathrm{u}|$ limits

In addition to the cross-section limit, an upper limit is set on the absolute values of the up-type quark coupling parameter $|\zeta_\mathrm{u}|$ within the flavor-aligned 2HDM. According to the model constraints discussed in Section 2.2.4, only gluon–gluon fusion production via a top-quark loop is assumed for the A boson and its decay is set to be exclusive into a $\tau^+\tau^-$ pair with $\mathcal{B}(A \to \tau\tau) = 1$. The obtained limits σ_fit is then transformed into limits on $|\zeta_\mathrm{u}|$ via

$$|\zeta_\mathrm{u}| = \sqrt{\frac{\sigma_\mathrm{fit}}{\sigma_\mathrm{ref}}}.$$

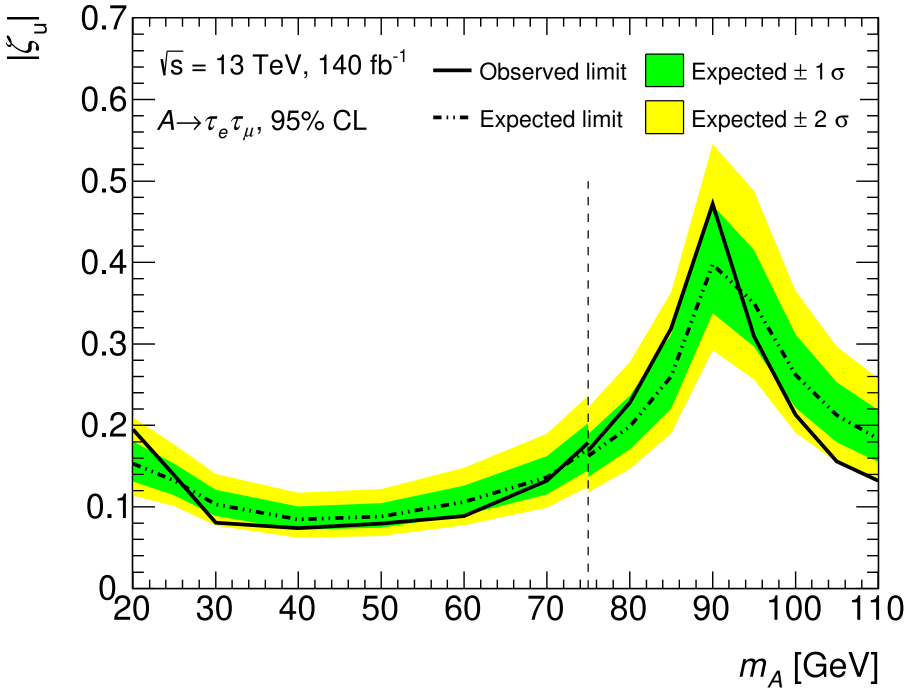

Figure 6.31: Expected and observed upper limits on the absolute value of the up-type quark coupling parameter $|\zeta_{\mathrm{u}}|$ for A boson masses from 20 to 110 GeV, assuming the A boson decays exclusively into a $\tau^+\tau^-$ pair. The dash-dotted line shows the expected limit set by analyzing the shape of the m_{MMC} distribution with its $1\,\sigma$ and $2\,\sigma$ uncertainty bands in green and yellow, respectively. The observed limits are shown by the solid line. The vertical dashed line visualizes the split into two SRs: the mass points on the left side are analyzed within the LMSR and the ones on the right side in the HMSR.

Here, σ_{ref} is the N^{3}LO signal cross-section as calculated with `ggHiggs` according to Table 6.6. The results for the expected and observed limits are displayed in Figure 6.31. The observed limits on $|\zeta_{\mathrm{u}}|$ range from 0.074 for $m_A = 40$ GeV to 0.47 for $m_A = 90$ GeV. The shape of the limit is relatively flat in the LMSR and shows a reduced sensitivity around the Z boson resonance in the HMSR. The low mass points can compete with the rest of the mass points LMSR, because the signal cross-sections are much higher for low masses and compensate the inferior statistics.
The detailed limit values for the expected and observed limits on $|\zeta_{\mathrm{u}}|$ can be found in Table D.5 in Appendix D.

6.7 Results in the context of previous publications

This section discusses the results obtained in this analysis in the context of preceding publications. First, the cross-section limit is compared with previous limits in Section 6.7.1 and then the limit improvements for $|\zeta_\mathrm{u}|$ are reviewed in Section 6.7.2.

6.7.1 Model-independent limit

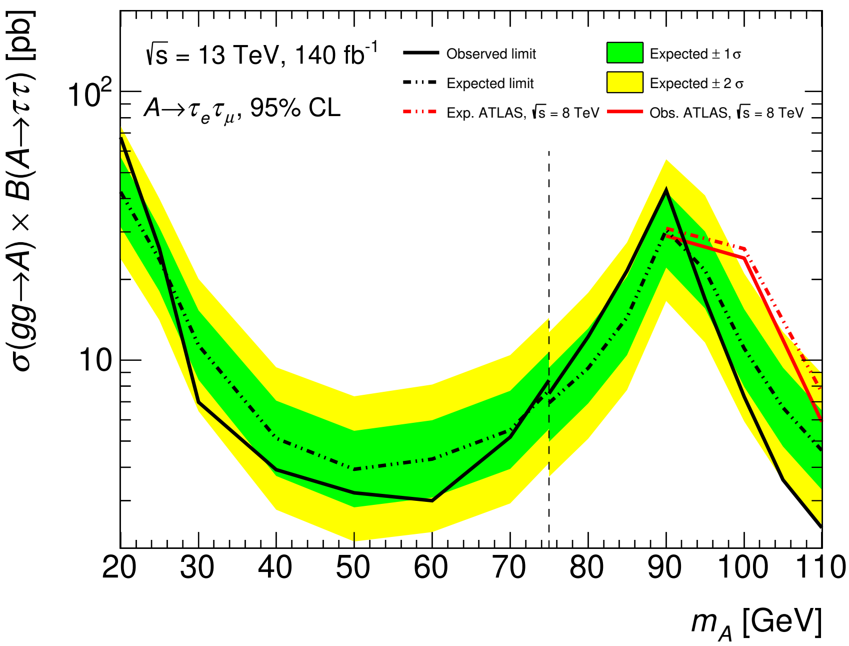

Figure 6.32: Comparison of the expected and observed upper limits on the production cross-section for $gg \to A$ times the branching ratio for A decaying into two τ-leptons for A boson masses from 20 to 110 GeV with the previous ATLAS limits for $\sqrt{s} = 8\,\mathrm{TeV}$ [14]. The dash-dotted lines show the expected limits with its $1\,\sigma$ and $2\,\sigma$ uncertainty bands in green and yellow, respectively, while the solid lines show the observed limits. The results obtained in this search are shown in black and the $\sqrt{s} = 8\,\mathrm{TeV}$ results are shown in red. The vertical dashed line visualizes the split into two SRs: the mass points on the left side are analyzed within the LMSR and the ones on the right side in the HMSR.

Earlier searches for the production of neutral Higgs bosons via gluon–gluon fusion in proton–proton collisions with a subsequent decay into a $\tau^+\tau^-$ pair were presented by the ATLAS and CMS collaborations. The ATLAS results start with Higgs boson masses of 90 GeV for the $\sqrt{s} = 7$ TeV search with 36 pb^{-1} [13] and the $\sqrt{s} = 8$ TeV search with 20 fb^{-1} [14], and 200 GeV for the previous $\sqrt{s} = 13$ TeV search [15]. The CMS searches at $\sqrt{s} = 13$ TeV start at 90 GeV for the early Run 2 result with 36 fb^{-1} [16] and at 60 GeV for the full Run 2 result with 138 fb^{-1} [17]. This shows the first major achievement of this analysis. It is the first ever search for neutral Higgs bosons produced via gluon–gluon fusion and decaying into a $\tau^+\tau^-$ pair for the mass range 20 GeV to 60 GeV, and in addition the first ATLAS result for 60 GeV to 90 GeV.

The results for the overlapping regions can be compared to the results in the previous publications. The ATLAS result for $\sqrt{s} = 8$ TeV was combining the

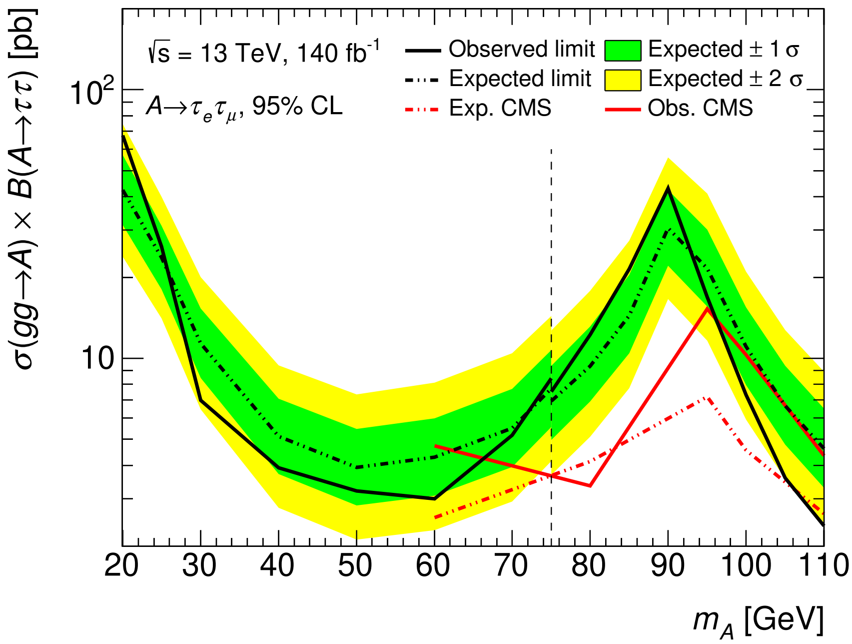

Figure 6.33: Comparison of the expected and observed upper limits on the production cross-section for $gg \to A$ times the branching ratio for A decaying into two τ-leptons for A boson masses from 20 to 110 GeV with the current limits from CMS [17]. The dash-dotted lines show the expected limits with its $1\,\sigma$ and $2\,\sigma$ uncertainty bands in green and yellow, respectively, while the solid lines show the observed limits. The results obtained in this search are shown in black and the CMS results are shown in red. The vertical dashed line visualizes the split into two SRs: the mass points on the left side are analyzed within the LMSR and the ones on the right side in the HMSR.

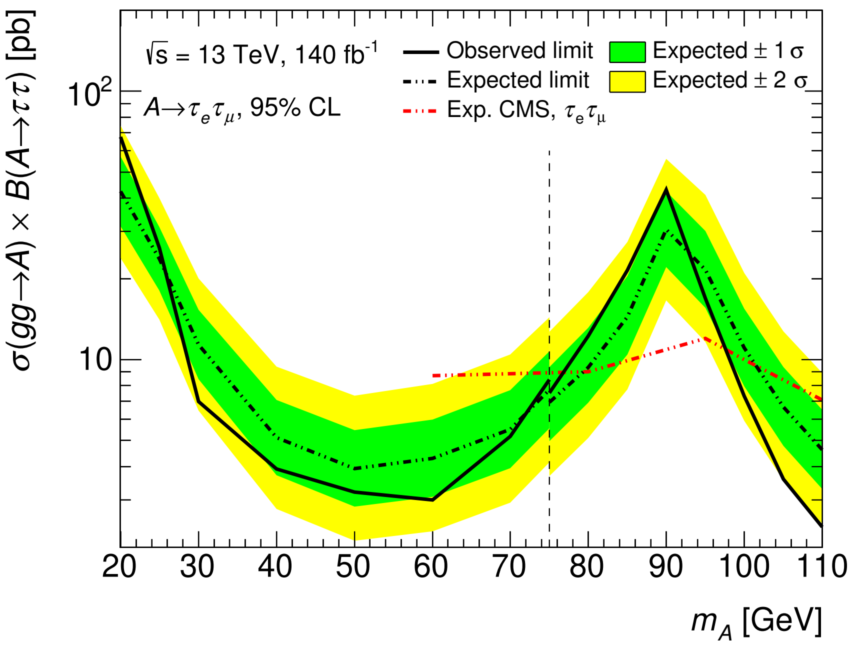

Figure 6.34: Comparison of the expected and observed upper limits on the production cross-section for $gg \to A$ times the branching ratio for A decaying into two τ-leptons for A boson masses from 20 to 110 GeV with the limits obtained by CMS in the $\tau_e\tau_\mu$ channel [17]. The dash-dotted lines show the expected limits with its $1\,\sigma$ and $2\,\sigma$ uncertainty bands in green and yellow, respectively, while the solid line shows the observed limits. The results obtained in this search are shown in black and the CMS results in the $\tau_e\tau_\mu$ channel are shown in red. Only the expected limits were made public by CMS for this channel. The vertical dashed line visualizes the split into two SRs: the mass points on the left side are analyzed within the LMSR and the ones on the right side in the HMSR.

$\tau_{\text{lep}}\tau_{\text{lep}}$ channel, which is used as the only channel in this analysis, with the $\tau_{\text{lep}}\tau_{\text{had}}$ channel. The expected and observed limits are compared to the results of this analysis in Figure 6.32. Similar limits are expected for $m_A = 90\,\text{GeV}$, but the previous observed limit is 33 % better. For the mass points with $m_A > 90\,\text{GeV}$, this analysis improves the expected and observed results by a factor of 1.7–3.3. This is a strong improvement, considering the fact that the analysis focus was on the lower mass points and only the $\tau_{\text{lep}}\tau_{\text{lep}}$ decay channel less was used.
The comparison of the cross-section limit result of this search with the best CMS result [17] is shown in Figure 6.33. It can clearly be seen that the expected limits

by CMS are better by a factor of 1.7–3.0 in the mass range of 60 to 110 GeV. The picture is slightly different for the observed limits, where this analysis observed a very similar limit for $m_A = 95$ GeV, better limits for $m_A = 60$ GeV and $m_A > 95$ GeV, and worse limits for the other mass points.

The difference in the expected limits comes mostly from the different channel used in the analyses. While this analysis only uses the $\tau_{\text{lep}}\tau_{\text{lep}}$ channel, the CMS result combines this channel with a $\tau_{\text{lep}}\tau_{\text{had}}$ channel and a $\tau_{\text{had}}\tau_{\text{had}}$ channel. Looking at the auxiliary material of Ref. [17] shows that the $\tau_{\text{lep}}\tau_{\text{lep}}$ has the worst sensitivity of all channels over the whole mass range, except for $m_A > 95$ GeV, where the $\tau_{\text{had}}\tau_{\text{had}}$ gives a weaker limit.

Hence, to make a fair comparison, the results from the analysis presented here are compared directly with the $\tau_{\text{lep}}\tau_{\text{lep}}$ channel results from CMS in Figure 6.34. CMS only published the expected limits for the single channels, which are almost identical for $m_A = 80$ GeV and $m_A = 100$ GeV. In between these mass points, closer to the Z boson mass, CMS expects a better limit, while for masses below 80 GeV and above 100 GeV, this analysis gives up to a factor of two better expected limits. This shows that the main goal of this analysis, which is improving the limits in the low-mass regions, has been successful.

When comparing this analysis results with the CMS results in Figure 6.33 and Figure 6.34, the mass point of $m_A = 90$ GeV, right at the Z boson mass, should be taken with care. While this analysis provides a signal mass point directly for $m_A = 90$ GeV, CMS only has the points $m_A = 80$ GeV and $m_A = 95$ GeV, and an interpolation between these points neglects the fact that the background at the Z boson mass is highly increased.

The CMS result has drawn special attention, because for $m_A = 100$ GeV, it reports a p-value equivalent to a local excess of $3.1\,\sigma$ ($2.7\,\sigma$ global). This analysis unfortunately cannot confirm or reject this finding since CMS reports a 2.4 times better expected limit due to the additional channels. However, no excess of data events is seen in this analysis within its sensitivity.

6.7.2 Model-dependent limit

This analysis reports the first direct limits on the absolute value of the up-type quark coupling parameter $|\zeta_{\text{u}}|$. Previous limits have been obtained by theoretical arguments and the analysis of constraints coming from LHC collider experiment and constraints arising from b-physics. Ref. [58] summarizes these findings and reports a general upper limit of $|\zeta_{\text{u}}| < 0.5$. This is improved by this analysis over the whole probed mass range of $m_A = 20$ GeV to $m_A = 110$ GeV, with reduced sensitivity close to the Z boson resonance and strong improvements up to factor five elsewhere.

The deviation of a_μ between the theoretical SM value and the experiment could be explained by finding evidence for a CP-odd Higgs boson within the flavor-aligned 2HDM, assuming near-maximal couplings. As no evidence for this particle has been found within this analysis, further parameter spaces become unavailable for explaining the deviation in a_μ with a CP-odd Higgs boson. Quantifying the impact of the new limits on $|\zeta_\mathrm{u}|$ goes well beyond the scope of this thesis, but provides an exciting basis for further theoretical modeling and calculations.

7 Summary and outlook

The main part of this thesis presents the search for a light CP-odd Higgs boson A, which is produced via gluon–gluon fusion in proton–proton collisions at a center-of-mass energy of 13 TeV. The search is carried out using the 140 fb^{-1} dataset collected with the ATLAS detector during Run 2 of the LHC between 2015 and 2018. The results are reported for A boson decay into a $\tau^+\tau^-$ pair with subsequent decay into the fully leptonic final states $gg \to A \to \tau^+\tau^- \to \mu^+\nu_\mu\bar{\nu}_\tau e^-\bar{\nu}_e\nu_\tau$ or $gg \to A \to \tau^+\tau^- \to e^+\nu_e\bar{\nu}_\tau\mu^-\bar{\nu}_\mu\nu_\tau$. During the course of this thesis, the feasibility study of the analysis [143] has been shaped, refined and improved into a fully mature physics analysis, which was finally brought to publication in *JHEP* [19].
The analysis is tailored to the specific challenges that arise from searching for light Higgs bosons in the range of 20 GeV to 110 GeV. First and foremost, leptonic triggers are used to benefit from the lower p_T thresholds compared to the hadronic τ-lepton triggers and be able to push the mass range for the A boson down to the unexplored 20 GeV region. The second challenge is the large background contribution from the SM backgrounds, most notably from Z/γ^* decays. They are suppressed by requiring exactly one electron and one muon in the final state. However, the $Z/\gamma^* \to \tau\tau$ process still remains the main background, as its final state is very similar to the signal process.
Several methods are introduced to maximize the signal sensitivity. Angular and mass cuts are applied to exploit the small differences between the signal and background processes. In order to optimize the signal sensitivity further, the search is split into a low-mass SR and a high-mass SR. Dedicated CRs are used for the $Z \to \tau\tau$ (ZCR) and top-quark (TCR) backgrounds to ensure good modeling of these main backgrounds and help constrain systematic uncertainties. The ZCR is furthermore utilized to extract a data-driven reweighting factor for the $Z \to \tau\tau$ background to improve agreement of the background predictions with data. Another challenge for the analysis is the occurrence of fake and non-prompt leptons, which are physics objects falsely identified as leptons, as well as leptons from non-prompt decays and charge flips. This generally happens more frequently for the here present abundance of low-p_T leptons. To address this fake-lepton background, a dedicated data-driven matrix method is set up. This is necessary, because MC simulations can not reliably model background from fake leptons. A validation region is designed to estimate the fake-lepton background, validate it and provide systematic uncertainties on the method. The mass obtained with the MMC algorithm is used as an estimator of

the invariant mass of the τ-lepton pair. Due to its likelihood approach taking into account the momentum of the four neutrinos in the final state, it is well suited for this task.
The distributions of this m_{MMC} variable in the SRs and CRs are used for the statistical interpretation of the data. It yields no significant excess of events above the SM background. Hence, 95 % CL upper limits are set on the production cross-section of a CP-odd Higgs boson via gluon–gluon fusion which decays into the $\tau^+\tau^-$ final state. The observed limits range from 67 pb for $m_A = 20\,\mathrm{GeV}$ to 2.4 pb for $m_A = 110\,\mathrm{GeV}$, with reduced sensitivity around the Z boson resonance. This search probes the mass range from 20 to 60 GeV for the first time for this production and decay mode across all LHC experiments. While CMS already had results for masses from 60 GeV upwards [17], the results shown here represent the first ATLAS search in the mass range up to 90 GeV. Hence, an important contribution is made to map out unexplored phase space for additional Higgs bosons. Simultaneously, the potential of using fully leptonic final states to explore low-mass regions for Higgs bosons decaying into a pair of τ-leptons is demonstrated. For the mass ranges overlapping with previous cross-section limits, a comparison is carried out. It shows that good improvements are achieved compared to the ATLAS result from Run 1 [14]. These improvements are accomplished despite the fact that the previous publication used the higher abundant hadronic τ-lepton decay channels in combination with the leptonic channels. These hadronic channels are also the reason that the combined CMS search [17] obtained better expected limits over the whole common mass range of 60 to 110 GeV. However, when comparing only the leptonic channels, this search yields better limits in the low-mass range where it is optimized for. The CMS result is still better around the Z resonance. The combined CMS result has drawn special attention, because it reported a p-value equivalent to a local (global) excess of $3.1\,\sigma$ $(2.7\,\sigma)$ for a Higgs boson with mass $m_A = 100\,\mathrm{GeV}$. The result obtained within this analysis cannot confirm or discard this excess, because CMS reaches a 2.4 times better expected limit due to a better signal sensitivity from the inclusion of hadronic τ-lepton decay channels. While no statistically significant conclusion can be drawn from this comparison, it can at least be mentioned that the presented result found no excess of any size in this region and even observed a lower limit than the CMS result.
In the model-dependent search, upper limits are set on the absolute value of the up-type quark coupling parameter ζ_{u}, ranging from 0.074 for $m_A = 40\,\mathrm{GeV}$ to 0.47 for $m_A = 90\,\mathrm{GeV}$. They represent the first limits on $|\zeta_{\mathrm{u}}|$ obtained by a direct search for a CP-odd Higgs boson. A significant improvement over previous limits, which were obtained by theoretical arguments and constraints arising from different experiments, is observed over the whole mass range. The available parameter space for explaining the deviation in the anomalous magnetic moment of the muon within

the flavor-aligned 2HDM is narrowed. The results can be utilized by theorists to perform an analysis of the exact impacts.

To come to a conclusive statement about the CMS excess mentioned above, and to enhance the obtained limits in general, several improvements to the analysis are possible. The first and very obvious choice would be to combine the search with the hadronic channels, where one or both of the τ-leptons decay hadronically. The easier case here is the semi-leptonic channel, where one could still use lepton triggers and make use of the lower p_{T} thresholds. A single-electron or single-muon trigger would be used for this, with the subsequent selection requirement of having an additional hadronic τ-lepton in the event. ATLAS is already carrying out a parallel search for neutral Higgs bosons in the range of 80 to 200 GeV, which includes hadronic channels and has the main focus of improving the ATLAS sensitivity to the 90 to 110 GeV mass range. This will hopefully shed light on the observed CMS excess to either reject it as a purely statistical fluctuation or support it and provide a basis for new theoretical ideas.

The comparison of the analysis result with other searches also reveals that the region around the Z resonance has potential to large improvements. Especially the large modeling systematics for the $Z \to \tau\tau$ background in the low $\Delta R_{\ell\ell}$ regions in the order of 20 % lead to a loss of sensitivity. Dedicated studies could be set up in order to reduce or constrain these uncertainties. Three possible approaches for this include: (i) an additional control region that is tailored to constrain the uncertainties; (ii) analyzing through the comparison of several MC event generators where the large uncertainties come from and how to circumvent them; or (iii) using $Z \to e^+e^-$ and $Z \to \mu^+\mu^-$ events to control the uncertainties. The latter approach is likely to also make the n_{jets} based reweighting of the $Z \to \tau\tau$ background obsolete.

The analysis sensitivity is also impacted by the relatively low statistics of the $Z \to \tau\tau$ MC background in the SRs. While the sample size of generated $Z \to \tau\tau$ events is around 300 million events, only about 3000 are selected for the HMSR, which represents roughly 0.01 %. A part of this difference is due to the necessary requirement of exactly one electron and one muon, but others, especially the low $\Delta R_{\ell\ell}$ cut are a design choice that leads to another significant drop in event numbers in the selection. A dedicated MC sample for the phase space of the SRs would help a lot to keep the statistical uncertainties from the $Z \to \tau\tau$ under control.

Another option to increase the analysis sensitivity is given by analyzing more data. The LHC continues to provide collisions and the ATLAS detector has already recorded 183 fb^{-1} [118] in the first three years (2022-2024) of the LHC Run 3. Until the end of Run 3 in 2026, this is expected to increase to 300 fb^{-1} [237]. Afterwards, an upgrade of the machine is planned to the High-Luminosity LHC (HL-LHC) [237], which is expected to deliver 3000 fb^{-1} over the course of twelve

years operation. While the data statistics in the SRs are not the dominant source of uncertainties, the search can still largely profit from the increased amount of data. More MC background events will be simulated to match the data, bringing down statistical uncertainties on the background. Additionally, the data-driven fake-lepton background estimation can profit immensely from additional statistics, as the efficiency estimation relies on rare events. An increase of the dataset would yield more precise estimations and simultaneously reduce systematic uncertainties.
In addition to the analysis of the Run 2 dataset, the ALTI board integration for the LAr calorimeter of the ATLAS detector is described as part of the detector upgrades prior to Run 3. It provides enhanced exchange of timing and trigger signals between the LAr system and the CTP, as well as other subdetectors. Besides ensuring smooth data-taking, it also comes with improved functionalities for testing, which proved very useful in the commissioning of the DT system during the LS2. The DT system as a major detector upgrade helps ATLAS to control the increased number of collisions in Run 3 and will continue to do so in the coming runs.
Overall, this thesis is significantly advancing the search for light CP-odd Higgs bosons, providing valuable insights and setting the stage for future investigations. Additionally, the integration of the ALTI board for the LAr calorimeter has enhanced the capabilities of the ATLAS detector, ensuring smooth data-taking for future analyses and improved functionalities for following runs.

A Units

As it is common practice in particle physics, natural units are chosen in this thesis. This implies that the speed of light, the Boltzmann constant and the reduced Planck constant are all set to be equal to one:

$$c = k_B = \hbar = 1.$$

This has the convenient consequence that all units of physical quantities can be written in powers of energy. The common choice in particle physics is to measure energy in electron volts, which converts to joules through

$$1\,\mathrm{eV} = 1.602,176,634 \times 10^{-19}\,\mathrm{J}.$$

B Additional details on the analysis setup

B.1 Analysis setup and configurations

Table B.1: Electron selection criteria.

Feature	Criterion
Pseudorapidity range	$\|\eta\| < 2.47$, veto electrons in $1.37 < \|\eta\| < 1.52$
Energy calibration	`es2018_R21_v0` (ES model)
Transverse momentum	$p_{\mathrm{T}} > 7\,\mathrm{GeV}$ (baseline), $p_{\mathrm{T}} > 10\,\mathrm{GeV}$ (after trigger), trigger dependent p_{T} cut applies according to Section 6.2.2
Object quality	remove electrons flagged with `DFCommonCrackVetoCleaning`
Identification	`DFCommonElectronsLHLoose` (baseline), `DFCommonElectronsLHMedium` (selection for regions)
Isolation	*Loose* (baseline), *Tight* (selection for regions)
Systematics scheme	`1NP_v1`

Table B.2: Electron analysis working points (WPs)

Analysis identification WP	Definition
Loose	`DFCommonElectronsLHLoose`
Medium	`DFCommonElectronsLHMedium`
Analysis isolation WP	
Loose	Electron WP *Loose*
Tight	Electron WP *Tight*

Table B.3: Muon selection criteria.

Feature	Criterion
Pseudorapidity range	$\|\eta\| < 2.7$
Energy calibration	`doDirectCBCalib = true`, `SagittaCorr = true`
Transverse momentum	$p_{\mathrm{T}} > 7\,\mathrm{GeV}$ (baseline), $p_{\mathrm{T}} > 10\,\mathrm{GeV}$ (after trigger), trigger dependent p_{T} cut applies according to Section 6.2.2
Object quality	remove muons flagged with `isBadMuon`
Identification	*Loose* (baseline),*Medium* (selection for regions)
Isolation	*Loose_ VarRad* (baseline), *Tight_ VarRad* (selection for regions)

Table B.4: Muon analysis WPs

Analysis identification WP	Definition
Loose	*Loose*
Medium	*Medium*
Analysis isolation WP	
Loose	Muon WP *Loose_ VarRad*
Tight	Muon WP *Tight_ VarRad*

Table B.5: Jet calibration configuration and selection criteria.

Parameter	Value
JetCalibrationTool	
Algorithm	Anti-k_t
R-parameter	0.4
Input constituent	PFlow
Analysis release number	21.2.202
Calibration configuration	`JES_MC16Recommendation_Consolidated_PFlow_Apr2019_Rel21.config`
Calibration configuration AF2	`JES_MC16Recommendation_AFII_PFlow_Apr2019_Rel21.config`
Calibration sequence (data)	`JetArea_Residual_EtaJES_GSC_Insitu`
Calibration sequence (MC)	`JetArea_Residual_EtaJES_GSC_Smear`
Selection requirements	
Jet cleaning	remove jets with flag `DFCommonJets_eventClean_LooseBad`
Pseudorapidity range	$\|\eta\| < 4.5$
Transverse momentum	$p_{\mathrm{T}} > 20\,\mathrm{GeV}$
Uncertainties	
Configuration file	`rel21/Summer2019/R4_SR_Scenario1_SimpleJER.config`
Calibration area	`CalibArea-08`
JVT SF File	`JetJvtEfficiency/Moriond2018/JvtSFFile_EMPFlowJets.root`
Max p_{T} for JVT	60 GeV
FJVT `UseTightOP`	true
FJVT SF File	`JetJvtEfficiency/May2020/fJvtSFFile.EMPFlow.root`
Max p_{T} for FJVT	60 GeV
FJVT property	`UseMuSFFormat = true`

Table B.6: b-tagging configuration.

Parameter	Value
Tagger	DL1r
Working point	FixedCutBEff_85
Jet collection	AntiKt4EMPFlowJets_BTagging201903
Transverse momentum	$p_{\mathrm{T}} > 20\,\mathrm{GeV}$
CDI file	xAODBTaggingEfficiency/13TeV/ 2020-21-13TeV-MC16-CDI-2021-04-16_v1.root
ConeFlavourLabel	true
SystematicsStrategy	SFEigen
EigenvectorReductionB	Tight
EigenvectorReductionC	Tight
EigenvectorReductionLight	Tight

Table B.7: $E_{\mathrm{T}}^{\mathrm{miss}}$ configuration.

Parameter	Value
JetRejectionDec	passFJVT
JetSelection	Tight
DoPFlow	true
AssocKey	METAssoc_AntiKt4EMPFlow
CoreKey	MET_Core_AntiKt4EMPFlow
softTerm	PVSoftTrk
totalName	FinalTrk
Uncertainties	
ConfigSoftTrkFile	TrackSoftTerms-pflow.config
ConfigPrefix	METUtilities/run2_13TeV/

Table B.8: Pile-up reweighting (PRW) configuration and luminosity calculation files.

File	Value
Luminosity calculation 2015	`PHYS_StandardGRL_All_Good_25ns_276262-284484_OflLumi-13TeV-008.root`
Luminosity calculation 2016	`PHYS_StandardGRL_All_Good_25ns_297730-311481_OflLumi-13TeV-009.root`
Luminosity calculation 2017	`physics_25ns_Triggerno17e33prim.lumicalc.OflLumi-13TeV-010.root`
Luminosity calculation 2018	`ilumicalc_histograms_None_348885-364292_OflLumi-13TeV-010.root`
Actual μ 2017	`physics_25ns_Triggerno17e33prim.actualMu.OflLumi-13TeV-010.root`
taken from	https://atlas-groupdata.web.cern.ch/atlas-groupdata/GoodRunsLists/ data17_13TeV/20180619
Actual μ 2018	`physics_25ns_Triggerno17e33prim.actualMu.OflLumi-13TeV-010.root`
taken from	https://atlas-groupdata.web.cern.ch/atlas-groupdata/GoodRunsLists/ data18_13TeV/20190318

B.2 List of data and Monte Carlo samples

B.2.1 Data samples

The data used for this analysis corresponds to $140\,\text{fb}^{-1}$, recorded by the ATLAS detector in $2015-2018$. Only data events within LBs that were recorded while all detector subsystems where operating in good conditions are considered. The luminosity tag used is `OflLumi-13TeV-011` and the files were processed with the tag 'p4165'. The LBs are filtered using the GRL files as listed in Table B.9.

Table B.9: GRLs used for the different data-taking years with their integrated luminosities.

Year	GRL	Integrated luminosity
2015	`data15_13TeV.periodAllYear_DetStatus-v89-pro21-02_Unknown_PHYS_StandardGRL_All_Good_25ns.xml`	$3.2\,\text{fb}^{-1}$
2016	`data16_13TeV.periodAllYear_DetStatus-v89-pro21-01_DQDefects-00-02-04_PHYS_StandardGRL_All_Good_25ns.xml`	$33.4\,\text{fb}^{-1}$
2017	`data17_13TeV.periodAllYear_DetStatus-v99-pro22-01_Unknown_PHYS_StandardGRL_All_Good_25ns_Triggerno17e33prim.xml`	$44.6\,\text{fb}^{-1}$
2018	`data18_13TeV.periodAllYear_DetStatus-v102-pro22-04_Unknown_PHYS_StandardGRL_All_Good_25ns_Triggerno17e33prim.xml`	$58.8\,\text{fb}^{-1}$

B.2.2 Monte Carlo samples

Detailed information on the simulated samples used in this thesis are listed in Section B.2.2.1 to Section B.2.2.8. Cross-sections, k-factors, and filter efficiencies are centrally provided by the ATLAS physics modeling group. These lists contain all samples for the `MC16a` campaign, which corresponds to data taken in $2015-2016$. The samples for the other campaigns (`MC16d` for 2017 data and `MC16e` for 2018 data) differ from the listed `MC16a` samples solely by their 'r-tags': `r9364` for `MC16a` needs to be replaced with `r10201` for `MC16d` or with `r10724` for `MC16e`.
For the signal samples, a k-factor of 1.0 is taken since already N^3LO cross-sections are used. The cross-sections are model parameter dependent and given in Table 6.1. For the mass points of 40, 50, 60, 70, 80 and 90 GeV, two samples with different lepton p_T filters are used. They are combined as indicated with the 'Fraction' in Section B.2.2.1.

B.2.2.1 Signal

Dataset name	Fraction	Filter efficiency
mc16_13TeV.801162.Py8EG_A14NNPDF23LO_ggA20_tautau_l1314.deriv.DAOD_HIGG3D1.e8307_a875_r9364_p4164.root	1.0	0.0288
mc16_13TeV.802413.Py8EG_A14NNPDF23LO_ggA25_tautau_l1516.deriv.DAOD_HIGG3D1.e8307_a906_r9364_p4164.root	1.0	0.0234
mc16_13TeV.801163.Py8EG_A14NNPDF23LO_ggA30_tautau_l1314.deriv.DAOD_HIGG3D1.e8307_a875_r9364_p4164.root	1.0	0.0609
mc16_13TeV.451705.Pythia8EvtGen_A14NNPDF23LO_ggA40_tautau_leplep.deriv.DAOD_HIGG3D1.e8139_a875_r9364_p4164.root	0.061	1.0
mc16_13TeV.802221.Py8EG_A14NNPDF23LO_ggA40_tautau_l1516.deriv.DAOD_HIGG3D1.e8307_a875_r9364_p4164.root	0.939	0.0645
mc16_13TeV.346375.Pythia8EvtGen_A14NNPDF23LO_ggA50_tautau_leplep.deriv.DAOD_HIGG3D1.e7122_a875_r9364_p4164.root	0.103	1.0
mc16_13TeV.802222.Py8EG_A14NNPDF23LO_ggA50_tautau_l1516.deriv.DAOD_HIGG3D1.e8307_a875_r9364_p4164.root	0.897	0.1148
mc16_13TeV.346025.Pythia8EvtGen_A14NNPDF23LO_ggA60_tautau_leplep.deriv.DAOD_HIGG3D1.e7122_a875_r9364_p4164.root	0.147	1.0
mc16_13TeV.802223.Py8EG_A14NNPDF23LO_ggA60_tautau_l1516.deriv.DAOD_HIGG3D1.e8307_a875_r9364_p4164.root	0.853	0.1723
mc16_13TeV.346026.Pythia8EvtGen_A14NNPDF23LO_ggA70_tautau_leplep.deriv.DAOD_HIGG3D1.e7122_a875_r9364_p4164.root	0.185	1.0
mc16_13TeV.802224.Py8EG_A14NNPDF23LO_ggA70_tautau_l1516.deriv.DAOD_HIGG3D1.e8307_a875_r9364_p4164.root	0.815	0.2277
mc16_13TeV.802414.Py8EG_A14NNPDF23LO_ggA75_tautau_l1516.deriv.DAOD_HIGG3D1.e8307_a906_r9364_p4164.root	1.0	0.253
mc16_13TeV.346027.Pythia8EvtGen_A14NNPDF23LO_ggA80_tautau_leplep.deriv.DAOD_HIGG3D1.e7122_a875_r9364_p4164.root	0.217	1.0
mc16_13TeV.802225.Py8EG_A14NNPDF23LO_ggA80_tautau_l1516.deriv.DAOD_HIGG3D1.e8307_a875_r9364_p4164.root	0.783	0.2776
mc16_13TeV.802415.Py8EG_A14NNPDF23LO_ggA85_tautau_l1516.deriv.DAOD_HIGG3D1.e8307_a906_r9364_p4164.root	1.0	0.3011
mc16_13TeV.346028.Pythia8EvtGen_A14NNPDF23LO_ggA90_tautau_leplep.deriv.DAOD_HIGG3D1.e7122_a875_r9364_p4164.root	0.244	1.0
mc16_13TeV.802226.Py8EG_A14NNPDF23LO_ggA90_tautau_l1516.deriv.DAOD_HIGG3D1.e8307_a875_r9364_p4164.root	0.756	0.3231
mc16_13TeV.802416.Py8EG_A14NNPDF23LO_ggA95_tautau_l1516.deriv.DAOD_HIGG3D1.e8307_a906_r9364_p4164.root	1.0	0.345
mc16_13TeV.801827.Py8EG_A14NNPDF23LO_ggA100_tautau_l1314.deriv.DAOD_HIGG3D1.e8307_a875_r9364_p4164.root	1.0	0.4508
mc16_13TeV.802412.Py8EG_A14NNPDF23LO_ggA105_tautau_l1516.deriv.DAOD_HIGG3D1.e8307_a906_r9364_p4164.root	1.0	0.3829
mc16_13TeV.801828.Py8EG_A14NNPDF23LO_ggA110_tautau_l1314.deriv.DAOD_HIGG3D1.e8307_a875_r9364_p4164.root	1.0	0.4843

B.2.2.2 H_{125}

Dataset name	Cross-section [pb]	k-factor	Filter efficiency
mc16_13TeV.345120.PowhegPy8EG_NNLOPS_nnlo_30_ggH125_tautaul13l7.deriv.DAOD_HIGG3D1.e5814_s3126_r9364_p4164.root	3.0469	1.0	0.0538
mc16_13TeV.345121.PowhegPy8EG_NNLOPS_nnlo_30_ggH125_tautaulm15hp20.deriv.DAOD_HIGG3D1.e5814_s3126_r9364_p4164.root	6.0938	1.0	0.0377
mc16_13TeV.345122.PowhegPy8EG_NNLOPS_nnlo_30_ggH125_tautaulp15hm20.deriv.DAOD_HIGG3D1.e5814_s3126_r9364_p4164.root	6.0938	1.0	0.0378
mc16_13TeV.345123.PowhegPy8EG_NNLOPS_nnlo_30_ggH125_tautauh30h20.deriv.DAOD_HIGG3D1.e5814_s3126_r9364_p4164.root	3.0469	1.0	0.1889
mc16_13TeV.345211.PowhegPy8EG_NNPDF30_AZNLO_WmH125J_Winc_MINLO_tautau.deriv.DAOD_HIGG3D1.e5808_s3126_r9364_p4164.root	0.0334	1.0	1.0
mc16_13TeV.345212.PowhegPy8EG_NNPDF30_AZNLO_WpH125J_Winc_MINLO_tautau.deriv.DAOD_HIGG3D1.e5808_s3126_r9364_p4164.root	0.0527	1.0	1.0
mc16_13TeV.345217.PowhegPy8EG_NNPDF30_AZNLO_ZH125J_Zinc_MINLO_tautau.deriv.DAOD_HIGG3D1.e5808_s3126_r9364_p4164.root	0.0554	1.0	1.0
mc16_13TeV.345324.PowhegPythia8EvtGen_NNLOPS_NN30_ggH125_WWlvlv_EF_15_5.deriv.DAOD_HIGG3D1.e5769_s3126_r9364_p4166.root	1.11	1.0	0.4937
mc16_13TeV.345948.PowhegPy8EG_NNPDF30_AZNLOCTEQ6L1_VBFH125_WWlvlv.deriv.DAOD_HIGG3D1.e7172_s3126_r9364_p4166.root	0.086	1.0	0.5103
mc16_13TeV.346190.PowhegPy8EG_NNPDF30_AZNLOCTEQ6L1_VBFH125_tautaul13l7.deriv.DAOD_HIGG3D1.e7259_s3126_r9364_p4164.root	0.2372	1.0	0.0579

B.2.2.3 $t\bar{t}$ and single top

Dataset name	Cross-section [pb]	k-factor	Filter efficiency
mc16_13TeV.410470.PhPy8EG_A14_ttbar_hdamp258p75_nonallhad.deriv.DAOD_HIGG3D1.e6337_s3126_r9364_p4164.root	729.77	1.1398	0.5438
mc16_13TeV.410644.PowhegPythia8EvtGen_A14_singletop_schan_lept_top.deriv.DAOD_HIGG3D1.e6527_s3126_r9364_p4164.root	2.027	1.017	1.0
mc16_13TeV.410645.PowhegPythia8EvtGen_A14_singletop_schan_lept_antitop.deriv.DAOD_HIGG3D1.e6527_s3126_r9364_p4164.root	1.2674	1.0167	1.0
mc16_13TeV.410648.PowhegPythia8EvtGen_A14_Wt_DR_dilepton_top.deriv.DAOD_HIGG3D1.e6615_s3126_r9364_p4164.root	3.997	0.9451	1.0
mc16_13TeV.410649.PowhegPythia8EvtGen_A14_Wt_DR_dilepton_antitop.deriv.DAOD_HIGG3D1.e6615_s3126_r9364_p4164.root	3.9939	0.9458	1.0
mc16_13TeV.410658.PhPy8EG_A14_tchan_BW50_lept_top.deriv.DAOD_HIGG3D1.e6671_s3126_r9364_p4164.root	36.996	1.1935	1.0
mc16_13TeV.410659.PhPy8EG_A14_tchan_BW50_lept_antitop.deriv.DAOD_HIGG3D1.e6671_s3126_r9364_p4164.root	22.173	1.1849	1.0

B.2.2.4 Alternative $t\bar{t}$ samples for top generator uncertainty studies

Dataset name	Cross-section [pb]	k-factor	Filter efficiency
mc16_13TeV.410482.PhPy8EG_A14_ttbar_hdamp517p5_dil.deriv.DAOD_HIGG3D1.e6454_a875_r9364_p4164	729.74	1.1398	0.1055
mc16_13TeV.410465.aMcAtNloPy8EvtGen_MEN30NLO_A14N23LO_ttbar_noShWe_dil.deriv.DAOD_HIGG3D1.e6762_a875_r9364_p4164	712.02	1.1681	0.1071
mc16_13TeV.411234.PowhegHerwig7EvtGen_tt_hdamp258p75_713_dil.deriv.DAOD_HIGG3D1.e7580_a875_r9364_p4164	730.15	1.1391	0.1054

B.2.2.5 Diboson

Dataset name	Cross-section [pb]	k-factor	Filter efficiency
mc16_13TeV.363355.Sherpa_221_NNPDF30NNLO_ZqqZvv.deriv.DAOD_HIGG3D1.e5525_s3126_r9364_p4164.root	15.561	1.0	0.28
mc16_13TeV.363356.Sherpa_221_NNPDF30NNLO_ZqqZll.deriv.DAOD_HIGG3D1.e5525_s3126_r9364_p4164.root	15.564	1.0	0.1416
mc16_13TeV.363357.Sherpa_221_NNPDF30NNLO_WqqZvv.deriv.DAOD_HIGG3D1.e5525_s3126_r9364_p4164.root	6.7975	1.0	1.0
mc16_13TeV.363358.Sherpa_221_NNPDF30NNLO_WqqZll.deriv.DAOD_HIGG3D1.e5525_s3126_r9364_p4164.root	3.4328	1.0	1.0
mc16_13TeV.363359.Sherpa_221_NNPDF30NNLO_WpqqWmlv.deriv.DAOD_HIGG3D1.e5583_s3126_r9364_p4164.root	24.708	1.0	1.0
mc16_13TeV.363360.Sherpa_221_NNPDF30NNLO_WplvWmqq.deriv.DAOD_HIGG3D1.e5983_s3126_r9364_p4164.root	24.724	1.0	1.0
mc16_13TeV.363489.Sherpa_221_NNPDF30NNLO_WlvZqq.deriv.DAOD_HIGG3D1.e5525_s3126_r9364_p4164.root	11.42	1.0	1.0
mc16_13TeV.364250.Sherpa_222_NNPDF30NNLO_llll.deriv.DAOD_HIGG3D1.e5894_s3126_r9364_p4164.root	1.2515	1.0	1.0
mc16_13TeV.364253.Sherpa_222_NNPDF30NNLO_lllv.deriv.DAOD_HIGG3D1.e5916_s3126_r9364_p4164.root	4.5725	1.0	1.0
mc16_13TeV.364254.Sherpa_222_NNPDF30NNLO_llvv.deriv.DAOD_HIGG3D1.e5916_s3126_r9364_p4166.root	12.5	1.0	1.0
mc16_13TeV.364255.Sherpa_222_NNPDF30NNLO_lvvv.deriv.DAOD_HIGG3D1.e5916_s3126_r9364_p4164.root	3.2341	1.0	1.0
mc16_13TeV.364286.Sherpa_222_NNPDF30NNLO_llvvjj_ss_EW4.deriv.DAOD_HIGG3D1.e6055_s3126_r9364_p4164.root	0.0252	1.0	1.0
mc16_13TeV.364288.Sherpa_222_NNPDF30NNLO_llll_lowMllPtComplement.deriv.DAOD_HIGG3D1.e6096_s3126_r9364_p4164.root	1.4496	1.0	1.0
mc16_13TeV.364289.Sherpa_222_NNPDF30NNLO_lllv_lowMllPtComplement.deriv.DAOD_HIGG3D1.e6133_s3126_r9364_p4164.root	2.9599	1.0	1.0
mc16_13TeV.364290.Sherpa_222_NNPDF30NNLO_llvv_lowMllPtComplement.deriv.DAOD_HIGG3D1.e6096_s3126_r9364_p4164.root	0.1715	1.0	1.0

B.2.2.6 $Z \to \tau\tau$

Dataset name	Cross-section [pb]	k-factor	Filter efficiency
mc16_13TeV.364128.Sherpa_221_NNPDF30NNLO_Ztautau_MAXHTPTV0_70_CVetoBVeto.deriv.DAOD_HIGG3D1.e5307_s3126_r9364_p4164.root	1982.1	0.9751	0.8213
mc16_13TeV.364129.Sherpa_221_NNPDF30NNLO_Ztautau_MAXHTPTV0_70_CFilterBVeto.deriv.DAOD_HIGG3D1.e5307_s3126_r9364_p4164.root	1981.7	0.9751	0.1095
mc16_13TeV.364130.Sherpa_221_NNPDF30NNLO_Ztautau_MAXHTPTV0_70_BFilter.deriv.DAOD_HIGG3D1.e5307_s3126_r9364_p4164.root	1981.9	0.9751	0.0658
mc16_13TeV.364131.Sherpa_221_NNPDF30NNLO_Ztautau_MAXHTPTV70_140_CVetoBVeto.deriv.DAOD_HIGG3D1.e5307_s3126_r9364_p4164.root	110.7	0.9751	0.6926
mc16_13TeV.364132.Sherpa_221_NNPDF30NNLO_Ztautau_MAXHTPTV70_140_CFilterBVeto.deriv.DAOD_HIGG3D1.e5307_s3126_r9364_p4164.root	110.46	0.9751	0.189
mc16_13TeV.364133.Sherpa_221_NNPDF30NNLO_Ztautau_MAXHTPTV70_140_BFilter.deriv.DAOD_HIGG3D1.e5307_s3126_r9364_p4164.root	110.7	0.9751	0.1183
mc16_13TeV.364134.Sherpa_221_NNPDF30NNLO_Ztautau_MAXHTPTV140_280_CVetoBVeto.deriv.DAOD_HIGG3D1.e5307_s3126_r9364_p4164.root	40.756	0.9751	0.617
mc16_13TeV.364135.Sherpa_221_NNPDF30NNLO_Ztautau_MAXHTPTV140_280_CFilterBVeto.deriv.DAOD_HIGG3D1.e5307_s3126_r9364_p4164.root	40.713	0.9751	0.2343
mc16_13TeV.364136.Sherpa_221_NNPDF30NNLO_Ztautau_MAXHTPTV140_280_BFilter.deriv.DAOD_HIGG3D1.e5307_s3126_r9364_p4164.root	40.741	0.9751	0.156
mc16_13TeV.364137.Sherpa_221_NNPDF30NNLO_Ztautau_MAXHTPTV280_500_CVetoBVeto.deriv.DAOD_HIGG3D1.e5307_s3126_r9364_p4164.root	8.6726	0.9751	0.5641
mc16_13TeV.364138.Sherpa_221_NNPDF30NNLO_Ztautau_MAXHTPTV280_500_CFilterBVeto.deriv.DAOD_HIGG3D1.e5313_s3126_r9364_p4164.root	8.6745	0.9751	0.2643
mc16_13TeV.364139.Sherpa_221_NNPDF30NNLO_Ztautau_MAXHTPTV280_500_BFilter.deriv.DAOD_HIGG3D1.e5313_s3126_r9364_p4164.root	8.6792	0.9751	0.1762
mc16_13TeV.364140.Sherpa_221_NNPDF30NNLO_Ztautau_MAXHTPTV500_1000.deriv.DAOD_HIGG3D1.e5307_s3126_r9364_p4164.root	1.8081	0.9751	1.0
mc16_13TeV.364141.Sherpa_221_NNPDF30NNLO_Ztautau_MAXHTPTV1000_E_CMS.deriv.DAOD_HIGG3D1.e5307_s3126_r9364_p4164.root	0.1482	0.9751	1.0
mc16_13TeV.364210.Sherpa_221_NN30NNLO_Ztt_Mll10_40_MAXHTPTV0_70_BVeto.deriv.DAOD_HIGG3D1.e5421_s3126_r9364_p4164.root	2416.0	0.9751	0.9653
mc16_13TeV.364211.Sherpa_221_NN30NNLO_Ztt_Mll10_40_MAXHTPTV0_70_BFilter.deriv.DAOD_HIGG3D1.e5421_s3126_r9364_p4164.root	2414.4	0.9751	0.0347
mc16_13TeV.364212.Sherpa_221_NN30NNLO_Ztt_Mll10_40_MAXHTPTV70_280_BVeto.deriv.DAOD_HIGG3D1.e5421_s3126_r9364_p4164.root	50.374	0.9751	0.8924
mc16_13TeV.364213.Sherpa_221_NN30NNLO_Ztt_Mll10_40_MAXHTPTV70_280_BFilter.deriv.DAOD_HIGG3D1.e5421_s3126_r9364_p4164.root	50.464	0.9751	0.1099
mc16_13TeV.364214.Sherpa_221_NN30NNLO_Ztt_Mll10_40_MAXHTPTV280_E_CMS_BVeto.deriv.DAOD_HIGG3D1.e5421_s3126_r9364_p4164.root	3.2852	0.9751	0.8542
mc16_13TeV.364215.Sherpa_221_NN30NNLO_Ztt_Mll10_40_MAXHTPTV280_E_CMS_BFilter.deriv.DAOD_HIGG3D1.e5421_s3126_r9364_p4164.root	3.2811	0.9751	0.1594
mc16_13TeV.364282.Sherpa_221_NNPDF30NNLO_Ztautau_Mll2Ml_MAXHTPTV280_E_CMS.deriv.DAOD_HIGG3D1.e6037_s3126_r9364_p4164.root	9.1472	1.0	1.0
mc16_13TeV.364360.Sherpa_221_NNPDF30NNLO_Ztautau_Mll2Ml_MAXHTPTV70_140.deriv.DAOD_HIGG3D1.e6544_a875_r9364_p4164.root	140.73	1.0	1.0
mc16_13TeV.364363.Sherpa_221_NNPDF30NNLO_Ztautau_Mll2Ml_MAXHTPTV140_280.deriv.DAOD_HIGG3D1.e6544_a875_r9364_p4164.root	43.265	1.0	1.0

B.2.2.7 $Z \to ee$

Dataset name	Cross-section [pb]	k-factor	Filter efficiency
mc16_13TeV.364114.Sherpa_221_NNPDF30NNLO_Zee_MAXHTPTV0_70_CVetoBVeto.deriv.DAOD_HIGG3D1.e5299_s3126_r9364_p4164.root	1981.6	0.9751	0.8212
mc16_13TeV.364115.Sherpa_221_NNPDF30NNLO_Zee_MAXHTPTV0_70_CFilterBVeto.deriv.DAOD_HIGG3D1.e5299_s3126_r9364_p4164.root	1981.7	0.9751	0.1139
mc16_13TeV.364116.Sherpa_221_NNPDF30NNLO_Zee_MAXHTPTV0_70_BFilter.deriv.DAOD_HIGG3D1.e5299_s3126_r9364_p4164.root	1982.0	0.9751	0.0658
mc16_13TeV.364117.Sherpa_221_NNPDF30NNLO_Zee_MAXHTPTV70_140_CVetoBVeto.deriv.DAOD_HIGG3D1.e5299_s3126_r9364_p4164.root	110.64	0.9751	0.6927
mc16_13TeV.364118.Sherpa_221_NNPDF30NNLO_Zee_MAXHTPTV70_140_CFilterBVeto.deriv.DAOD_HIGG3D1.e5299_s3126_r9364_p4164.root	110.5	0.9751	0.1907
mc16_13TeV.364119.Sherpa_221_NNPDF30NNLO_Zee_MAXHTPTV70_140_BFilter.deriv.DAOD_HIGG3D1.e5299_s3126_r9364_p4164.root	110.46	0.9751	0.1155
mc16_13TeV.364120.Sherpa_221_NNPDF30NNLO_Zee_MAXHTPTV140_280_CVetoBVeto.deriv.DAOD_HIGG3D1.e5299_s3126_r9364_p4164.root	40.645	0.9751	0.6161
mc16_13TeV.364121.Sherpa_221_NNPDF30NNLO_Zee_MAXHTPTV140_280_CFilterBVeto.deriv.DAOD_HIGG3D1.e5299_s3126_r9364_p4164.root	40.671	0.9751	0.2321
mc16_13TeV.364122.Sherpa_221_NNPDF30NNLO_Zee_MAXHTPTV140_280_BFilter.deriv.DAOD_HIGG3D1.e5299_s3126_r9364_p4164.root	40.675	0.9751	0.1524
mc16_13TeV.364123.Sherpa_221_NNPDF30NNLO_Zee_MAXHTPTV280_500_CVetoBVeto.deriv.DAOD_HIGG3D1.e5299_s3126_r9364_p4164.root	8.6703	0.9751	0.5635
mc16_13TeV.364124.Sherpa_221_NNPDF30NNLO_Zee_MAXHTPTV280_500_CFilterBVeto.deriv.DAOD_HIGG3D1.e5299_s3126_r9364_p4164.root	8.6668	0.9751	0.2653
mc16_13TeV.364125.Sherpa_221_NNPDF30NNLO_Zee_MAXHTPTV280_500_BFilter.deriv.DAOD_HIGG3D1.e5299_s3126_r9364_p4164.root	8.6799	0.9751	0.1758
mc16_13TeV.364126.Sherpa_221_NNPDF30NNLO_Zee_MAXHTPTV500_1000.deriv.DAOD_HIGG3D1.e5299_s3126_r9364_p4164.root	1.8087	0.9751	1.0
mc16_13TeV.364127.Sherpa_221_NNPDF30NNLO_Zee_MAXHTPTV1000_E_CMS.deriv.DAOD_HIGG3D1.e5299_s3126_r9364_p4164.root	0.1488	0.9751	1.0
mc16_13TeV.364204.Sherpa_221_NN30NNLO_Zee_Mll10_40_MAXHTPTV0_70_BVeto.deriv.DAOD_HIGG3D1.e5421_s3126_r9364_p4164.root	2415.3	0.9751	0.9652
mc16_13TeV.364205.Sherpa_221_NN30NNLO_Zee_Mll10_40_MAXHTPTV0_70_BFilter.deriv.DAOD_HIGG3D1.e5421_s3126_r9364_p4164.root	2415.5	0.9751	0.0347
mc16_13TeV.364206.Sherpa_221_NN30NNLO_Zee_Mll10_40_MAXHTPTV70_280_BVeto.deriv.DAOD_HIGG3D1.e5421_s3126_r9364_p4164.root	50.354	0.9751	0.8926
mc16_13TeV.364207.Sherpa_221_NN30NNLO_Zee_Mll10_40_MAXHTPTV70_280_BFilter.deriv.DAOD_HIGG3D1.e5421_s3126_r9364_p4164.root	50.484	0.9751	0.1087
mc16_13TeV.364208.Sherpa_221_NN30NNLO_Zee_Mll10_40_MAXHTPTV280_E_CMS_BVeto.deriv.DAOD_HIGG3D1.e5421_s3126_r9364_p4164.root	3.2539	0.9751	0.8548
mc16_13TeV.364209.Sherpa_221_NN30NNLO_Zee_Mll10_40_MAXHTPTV280_E_CMS_BFilter.deriv.DAOD_HIGG3D1.e5421_s3126_r9364_p4164.root	3.2526	0.9751	0.1535
mc16_13TeV.364280.Sherpa_221_NNPDF30NNLO_Zee_Mll2Ml_MAXHTPTV280_E_CMS.deriv.DAOD_HIGG3D1.e6037_s3126_r9364_p4164.root	46.031	0.9751	1.0
mc16_13TeV.364358.Sherpa_221_NNPDF30NNLO_Zee_Mll2Ml_MAXHTPTV70_140.deriv.DAOD_HIGG3D1.e6544_a875_r9364_p4164.root	568.84	1.0	1.0
mc16_13TeV.364361.Sherpa_221_NNPDF30NNLO_Zee_Mll2Ml_MAXHTPTV140_280.deriv.DAOD_HIGG3D1.e6544_a875_r9364_p4164.root	206.81	1.0	1.0

B.2.2.8 $Z \to \mu\mu$

Dataset name	Cross-section [pb]	k-factor	Filter efficiency
mc16_13TeV.364100.Sherpa_221_NNPDF30NNLO_Zmumu_MAXHTPTV0_70_CVetoBVeto.deriv.DAOD_HIGG3D1.e5271_s3126_r9364_p4164.root	1982.5	0.9751	0.8214
mc16_13TeV.364101.Sherpa_221_NNPDF30NNLO_Zmumu_MAXHTPTV0_70_CFilterBVeto.deriv.DAOD_HIGG3D1.e5271_s3126_r9364_p4164.root	1982.2	0.9751	0.1132
mc16_13TeV.364102.Sherpa_221_NNPDF30NNLO_Zmumu_MAXHTPTV0_70_BFilter.deriv.DAOD_HIGG3D1.e5271_s3126_r9364_p4164.root	1981.5	0.9751	0.0651
mc16_13TeV.364103.Sherpa_221_NNPDF30NNLO_Zmumu_MAXHTPTV70_140_CVetoBVeto.deriv.DAOD_HIGG3D1.e5271_s3126_r9364_p4164.root	109.14	0.9751	0.6879
mc16_13TeV.364104.Sherpa_221_NNPDF30NNLO_Zmumu_MAXHTPTV70_140_CFilterBVeto.deriv.DAOD_HIGG3D1.e5271_s3126_r9364_p4164.root	108.98	0.9751	0.1901
mc16_13TeV.364105.Sherpa_221_NNPDF30NNLO_Zmumu_MAXHTPTV70_140_BFilter.deriv.DAOD_HIGG3D1.e5271_s3126_r9364_p4164.root	109.04	0.9751	0.1173
mc16_13TeV.364106.Sherpa_221_NNPDF30NNLO_Zmumu_MAXHTPTV140_280_CVetoBVeto.deriv.DAOD_HIGG3D1.e5271_s3126_r9364_p4164.root	39.87	0.9751	0.5994
mc16_13TeV.364107.Sherpa_221_NNPDF30NNLO_Zmumu_MAXHTPTV140_280_CFilterBVeto.deriv.DAOD_HIGG3D1.e5271_s3126_r9364_p4164.root	39.857	0.9751	0.2336
mc16_13TeV.364108.Sherpa_221_NNPDF30NNLO_Zmumu_MAXHTPTV140_280_BFilter.deriv.DAOD_HIGG3D1.e5271_s3126_r9364_p4164.root	39.888	0.9751	0.1547
mc16_13TeV.364109.Sherpa_221_NNPDF30NNLO_Zmumu_MAXHTPTV280_500_CVetoBVeto.deriv.DAOD_HIGG3D1.e5271_s3126_r9364_p4164.root	8.5251	0.9751	0.5602
mc16_13TeV.364110.Sherpa_221_NNPDF30NNLO_Zmumu_MAXHTPTV280_500_CFilterBVeto.deriv.DAOD_HIGG3D1.e5271_s3126_r9364_p4164.root	8.5259	0.9751	0.2658
mc16_13TeV.364111.Sherpa_221_NNPDF30NNLO_Zmumu_MAXHTPTV280_500_BFilter.deriv.DAOD_HIGG3D1.e5271_s3126_r9364_p4164.root	8.5296	0.9751	0.1746
mc16_13TeV.364112.Sherpa_221_NNPDF30NNLO_Zmumu_MAXHTPTV500_1000.deriv.DAOD_HIGG3D1.e5271_s3126_r9364_p4164.root	1.7871	0.9751	1.0
mc16_13TeV.364113.Sherpa_221_NNPDF30NNLO_Zmumu_MAXHTPTV1000_E_CMS.deriv.DAOD_HIGG3D1.e5271_s3126_r9364_p4164.root	0.1476	0.9751	1.0
mc16_13TeV.364198.Sherpa_221_NN30NNLO_Zmm_Mll10_40_MAXHTPTV0_70_BVeto.deriv.DAOD_HIGG3D1.e5421_s3126_r9364_p4164.root	2414.3	0.9751	0.9654
mc16_13TeV.364199.Sherpa_221_NN30NNLO_Zmm_Mll10_40_MAXHTPTV0_70_BFilter.deriv.DAOD_HIGG3D1.e5421_s3126_r9364_p4164.root	2414.2	0.9751	0.0344
mc16_13TeV.364200.Sherpa_221_NN30NNLO_Zmm_Mll10_40_MAXHTPTV70_280_BVeto.deriv.DAOD_HIGG3D1.e5421_s3126_r9364_p4164.root	50.33	0.9751	0.8931
mc16_13TeV.364201.Sherpa_221_NN30NNLO_Zmm_Mll10_40_MAXHTPTV70_280_BFilter.deriv.DAOD_HIGG3D1.e5421_s3126_r9364_p4164.root	50.29	0.9751	0.1121
mc16_13TeV.364202.Sherpa_221_NN30NNLO_Zmm_Mll10_40_MAXHTPTV280_E_CMS_BVeto.deriv.DAOD_HIGG3D1.e5421_s3126_r9364_p4164.root	3.2398	0.9751	0.8537
mc16_13TeV.364203.Sherpa_221_NN30NNLO_Zmm_Mll10_40_MAXHTPTV280_E_CMS_BFilter.deriv.DAOD_HIGG3D1.e5421_s3126_r9364_p4164.root	3.2813	0.9751	0.1603
mc16_13TeV.364281.Sherpa_221_NNPDF30NNLO_Zmumu_Mll2Ml_MAXHTPTV280_E_CMS.deriv.DAOD_HIGG3D1.e6037_s3126_r9364_p4164.root	36.377	0.9751	1.0
mc16_13TeV.364359.Sherpa_221_NNPDF30NNLO_Zmumu_Mll2Ml_MAXHTPTV70_140.deriv.DAOD_HIGG3D1.e6544_a875_r9364_p4164.root	458.31	1.0	1.0
mc16_13TeV.364362.Sherpa_221_NNPDF30NNLO_Zmumu_Mll2Ml_MAXHTPTV140_280.deriv.DAOD_HIGG3D1.e6544_a875_r9364_p4164.root	163.96	1.0	1.0

B.3 Additional plots for data-driven background estimations

B.3.1 Studies on the dependence of lepton efficiencies on the reweighting of the $Z \to \tau\tau$ background

Because the reweighting procedure of the $Z \to \tau\tau$ background described in Section 6.3.5 relies on an already existing fake-lepton estimation, the fake- and real-lepton efficiencies used throughout the analysis are calculated before determining the $Z \to \tau\tau$ weights. As the efficiencies rely on the real MC events, they should change if calculated based on reweighted background. In an ideal scenario one would recalculate the weights and the fake-/real-lepton efficiencies in turn until they converge.

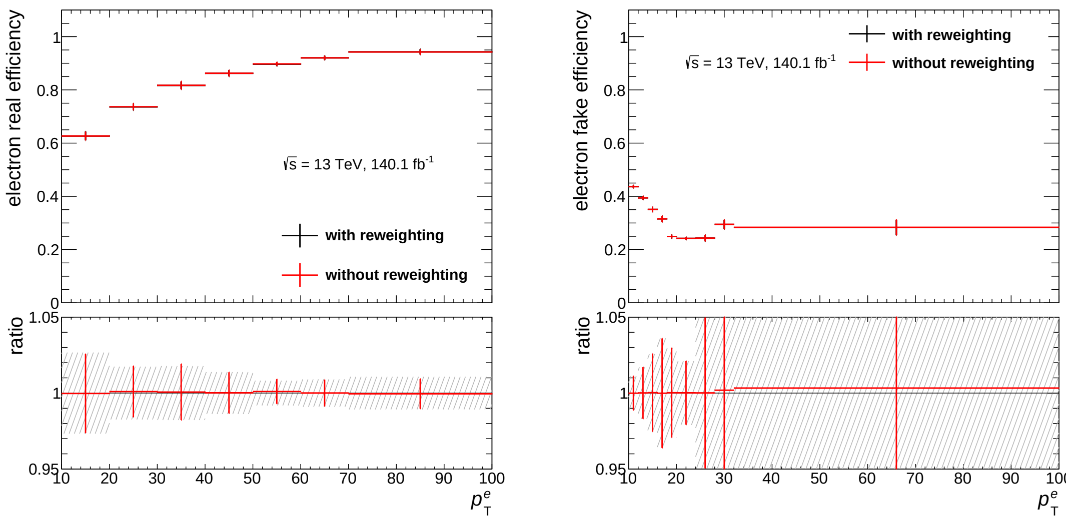

(a) (b)

Figure B.1: Electron (a) real-lepton and (b) fake-lepton efficiencies calculated with reweighting (in black) and without reweighting (in red) of the $Z \to \tau\tau$ background. The efficiencies were determined in (a) the HMSR and (b) the FVR with *Tight* muons. The ratio plot shows the efficiencies without reweighting divided by the efficiencies with applied reweighting. The hatched area visualizes the statistical uncertainties of the efficiencies with applied reweighting.

As the fake-lepton efficiencies are calculated in the FVR where $Z \to \tau\tau$ is only a very minor background, the impact of the reweighting is expected to be small.

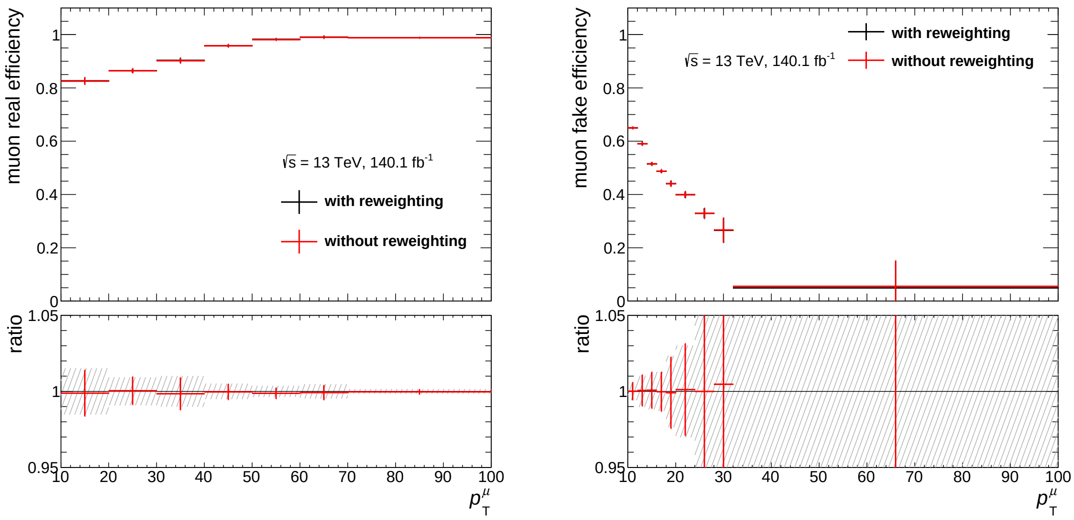

(a) (b)

Figure B.2: Muon (a) real-lepton and (b) fake-lepton efficiencies calculated with reweighting (in black) and without reweighting (in red) of the $Z \to \tau\tau$ background. The efficiencies were determined in (a) the HMSR and (b) the FVR with *Tight* electrons. The ratio plot shows the efficiencies without reweighting divided by the efficiencies with applied reweighting. The hatched area visualizes the statistical uncertainties of the efficiencies with applied reweighting.

Especially because the efficiencies are calculated as the ratio of events with *Tight* leptons over events with *Loose* leptons, the effect of the reweighting should also be small on the real-lepton efficiencies.
A comparison of the efficiencies calculated with and without considering the $Z \to \tau\tau$ reweighting can be seen in Figure B.1 and Figure B.2. The differences are very small, ranging well below 1 % in all bins for the majority of the efficiencies. Only for fake-muon efficiencies, the relative difference of the last bin reaches 10 % due to particularly small nominal efficiencies. All in all, calculating the efficiencies after the $Z \to \tau\tau$ reweighting leads to negligible changes. Therefore, it is sufficient to use the efficiencies calculated before the $Z \to \tau\tau$ reweighting and do no iteration of the two processes.

B.3.2 Efficiencies in different regions

The efficiencies needed for the MM have been calculated in all available regions and compared to each other. The real-lepton efficiencies are shown in Figure B.3. The

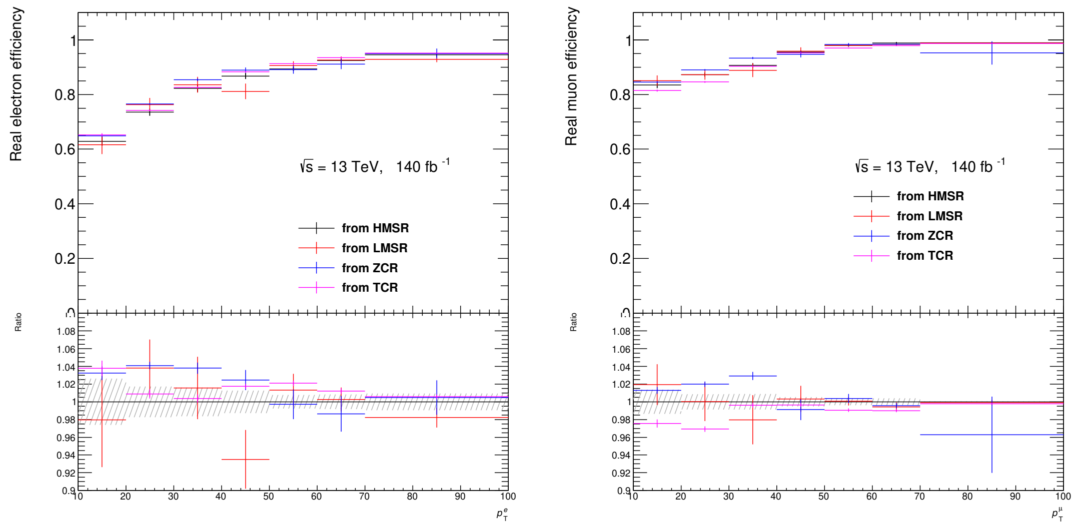

Figure B.3: Comparison of real-lepton efficiencies for (a) electrons and (b) muons, measured in different regions and binned in p_{T}^{e} or p_{T}^{μ}, respectively. The black line in the ratio plot represents the efficiencies measured in the HMSR, with its uncertainty visualized as the shaded area.

general shape of the distribution looks very similar between the regions. There are only very few cases where the statistical uncertainty bars do not touch each other, but these could still be statistical effects since the error bars only represent 68 % uncertainty intervals. Overall, it can be concluded that the real-lepton efficiencies do not change significantly between the regions.

Figure B.4 displays the comparison of the fake-electron and fake-muon efficiencies in the different SS regions. They have in general larger statistical uncertainties than the real-lepton efficiencies and are mostly statistically compatible throughout the regions. The only larger deviation is seen for the highest p_{T}^{μ} bin. There, all other regions differ significantly from the nominal value in the FVR. A test has shown that this comes from the $\Delta R_{\ell\ell}$ cut that is inverted in this region compared to the other regions. Raising the $\Delta R_{\ell\ell}$ cut in the HMSSVR would bring the efficiency down a bit and therefore closer to the efficiency in the FVR. However, no big impact on the overall fake-lepton background is expected from this change because high p_{T} fake muons are a very rare case.

Concluding from this, not every region needs to be included in the composition uncertainty. The most important change comes from the inverted $\Delta R_{\ell\ell}$ cut between the SRs and the ZCR as well as the FVR. Hence, for the composition uncertainty, the regions are changes as indicated in Table 6.8.

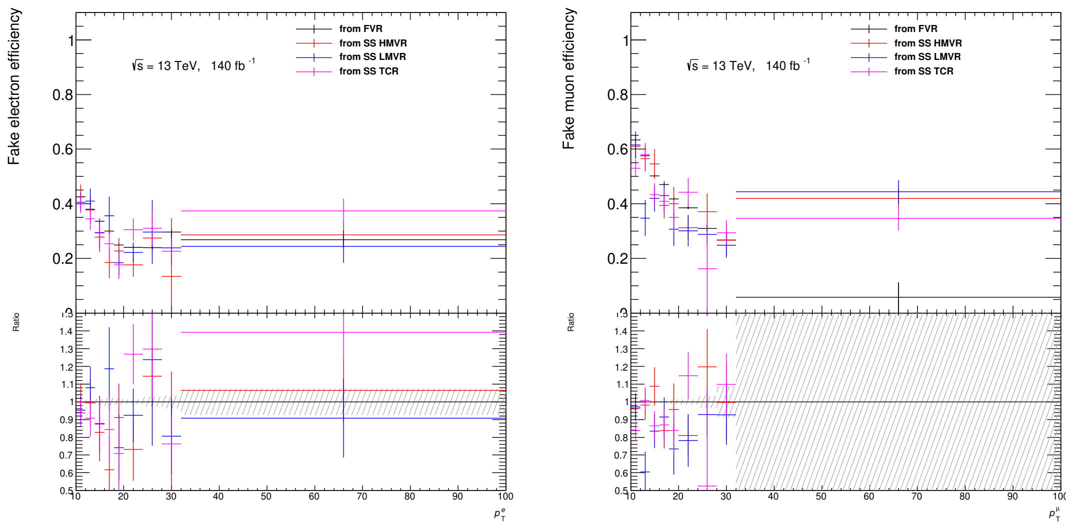

Figure B.4: Comparison of fake-lepton efficiencies for (a) electrons and (b) muons, measured in different regions and binned in p_{T}^{e} or p_{T}^{μ}, respectively. The black line in the ratio plot represents the efficiencies measured in the FVR, with its uncertainty visualized as the shaded area.

B.3.3 Efficiencies in dependence on jet multiplicity

The efficiencies needed for the MM have been calculated in dependence on the jet multiplicity and compared to each other. The real-lepton efficiencies are shown in Figure B.5 for electrons and in Figure B.6 for muons. The general shape of the distribution looks very similar between different jet numbers in the event. There are only a few cases where the statistical uncertainty bars do not touch each other, but these could still be statistical effects since the error bars only represent 68 % uncertainty intervals. Overall it can be concluded that the real-lepton efficiencies do not change significantly with the number of jets.

The fake-lepton efficiencies for different jet multiplicities are displayed in Figure B.5 for electrons and in Figure B.6 for muons efficiencies. There are multiple bins where the deviations between efficiencies from different jet numbers cannot be explained only with statistical fluctuations.

To account for these differences, a parametrization systematic is introduced since the statistics do not allow the full parametrization in jet multiplicity. It is determined by feeding the MM with varied efficiencies. The variations of the efficiencies are calculated as the root mean square (RMS) of the different jet multiplicities. The resulting systematic can be seen in Figure C.3 in the FVR. It can be seen that the systematic is quite small compared to other uncertainties for most m_{MMC} values.

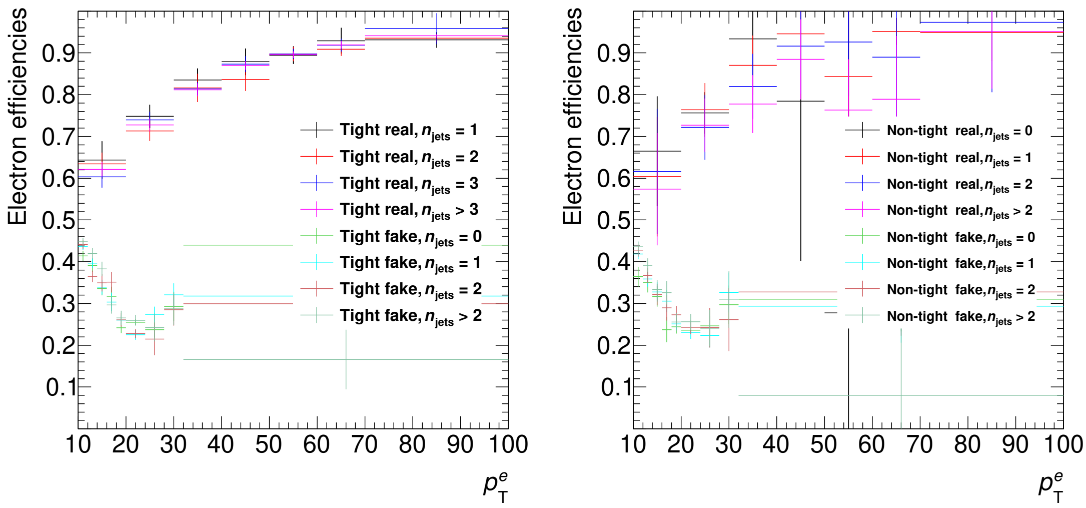

Figure B.5: Comparison of real-electron and fake-electron efficiencies for electrons accompanied by (a) a *Tight* and (b) a *Non-tight* muon, measured in dependence on jet multiplicity and binned in p_T^e.

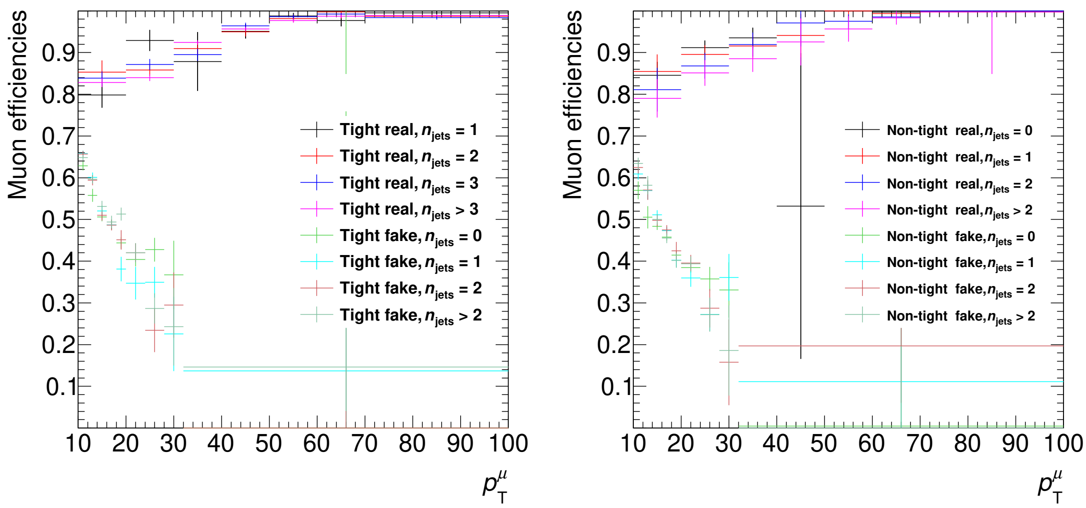

Figure B.6: Comparison of real-muon and fake-muon efficiencies for muons accompanied by (a) a *Tight* and (b) a *Non-tight* electron, measured in dependence on jet multiplicity and binned in p_T^μ.

B.3.4 Efficiencies in dependence on $\Delta R_{\ell\ell}$

The efficiencies needed for the MM have been calculated in dependence on $\Delta R_{\ell\ell}$ and compared to each other. The real-lepton efficiencies are shown in Figure B.7. There are a few outliers that do not agree statistically between high and low $\Delta R_{\ell\ell}$ values, although the general shape of the distribution stays similar. Figure B.8 displays the comparison of the fake-lepton efficiencies for electrons and muons for different $\Delta R_{\ell\ell}$ values. There are multiple bins where the deviations between efficiencies from different $\Delta R_{\ell\ell}$ values cannot be explained only with statistical fluctuations. Especially for high muon p_{T} the difference is large. These differences are mostly accounted for by composition systematics, as the various regions already have the $\Delta R_{\ell\ell}$ variations included.

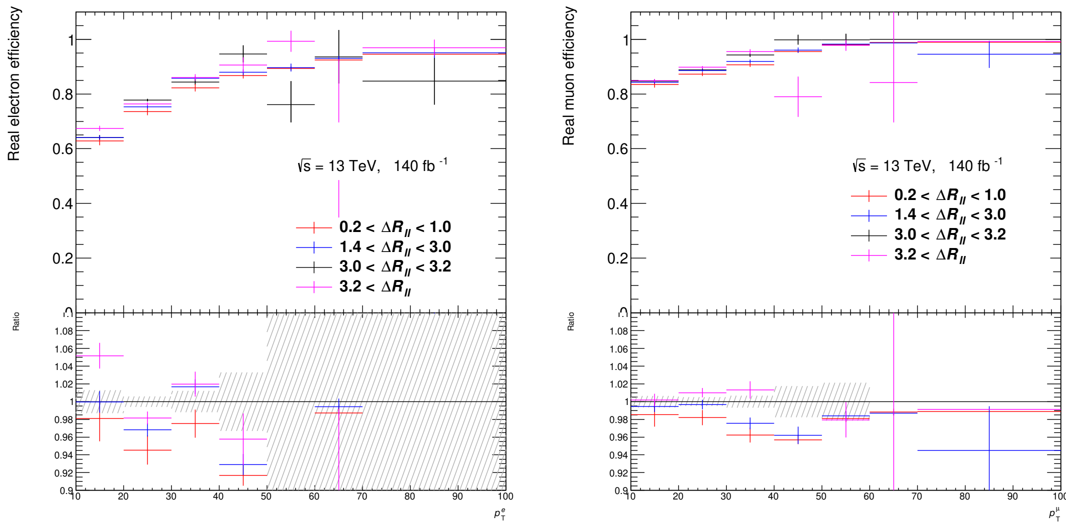

Figure B.7: Comparison of real-lepton efficiencies for (a) electrons and (b) muons, measured for different $\Delta R_{\ell\ell}$ values and binned in p_{T}^{e} or p_{T}^{μ}, respectively. The black line in the ratio plot represents the case of $3.0 < \Delta R_{ll} < 3.2$, with its uncertainty visualized as the shaded area. Efficiencies with $\Delta R_{ll} < 1.0$ are measured in the HMSR while efficiencies with $1.4 < \Delta R_{ll}$ are determined in the ZCR. There is no region in this analysis for the range $1.0 < \Delta R_{ll} < 1.4$.

B.3.5 Efficiencies throughout the years

The efficiencies needed for the MM have been calculated in the different data-taking periods and compared to each other. The real–lepton efficiencies are shown in Figure B.9. They mostly agree within their statistical uncertainties. Figure B.10

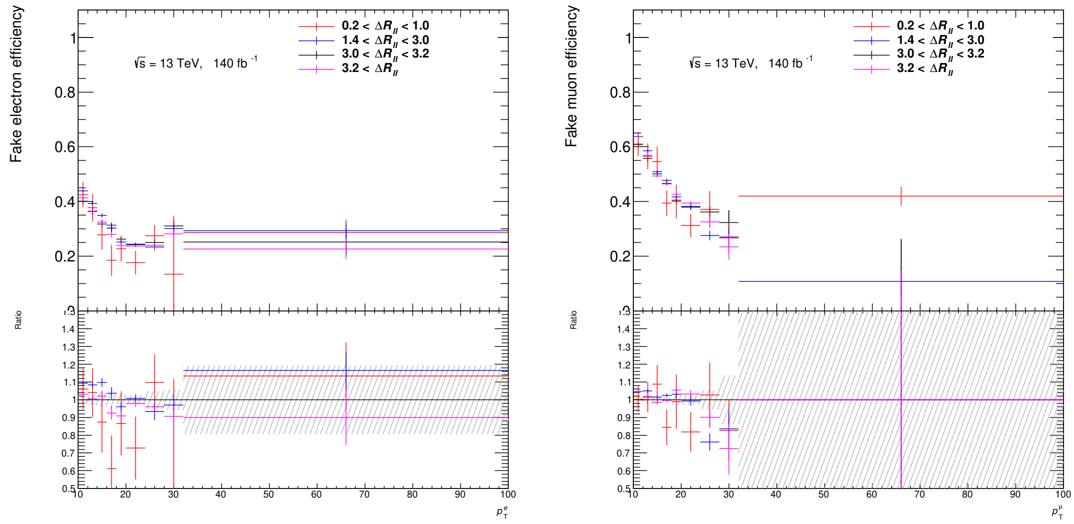

Figure B.8: Comparison of fake-lepton efficiencies for (a) electrons and (b) muons, measured for different $\Delta R_{\ell\ell}$ values and binned in p_{T}^{e} or p_{T}^{μ}, respectively. The black line in the ratio plot represents the case of $3.0 < \Delta R_{ll} < 3.2$, with its uncertainty visualized as the shaded area. Efficiencies with $\Delta R_{ll} < 1.0$ are measured in the HMSSVR while efficiencies with $1.4 < \Delta R_{ll}$ are determined in the FVR. There is no region in this analysis for the range $1.0 < \Delta R_{ll} < 1.4$.

displays the comparison of the fake-lepton efficiencies for electrons and muons for different data-taking years. There are only two bins for the fake-electron efficiencies, where the 2015+16 data yields slightly lower efficiencies, but in the overall picture one can conclude that the efficiencies are compatible throughout the different periods.

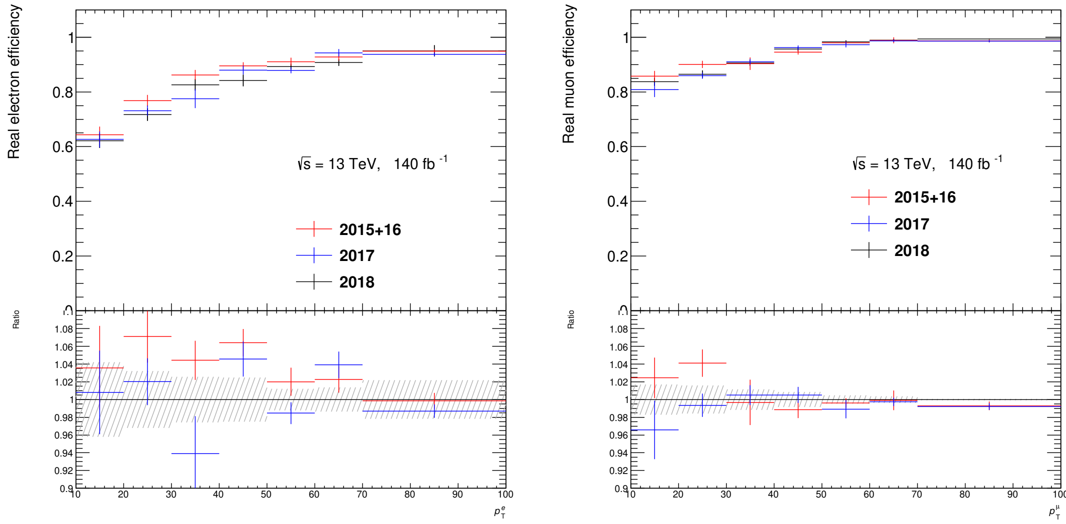

Figure B.9: Comparison of real-lepton efficiencies for (a) electrons and (b) muons, measured in different data-taking years and binned in p_{T}^{e} or p_{T}^{μ}, respectively. The black line in the ratio plot represents the efficiencies measured in 2018, with its uncertainty visualized as the shaded area.

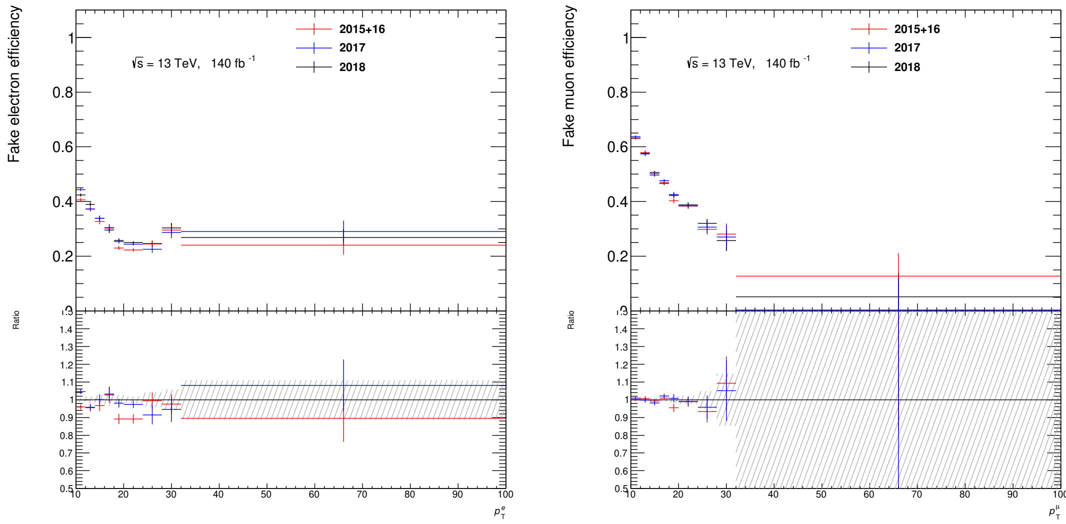

Figure B.10: Comparison of fake-lepton efficiencies for (a) electrons and (b) muons, measured in different data-taking years and binned in p_{T}^{e} or p_{T}^{μ}, respectively. The black line in the ratio plot represents the efficiencies measured in 2018, with its uncertainty visualized as the shaded area.

B.4 Additional variable distributions

B.4.1 Signal regions

Low-mass signal region

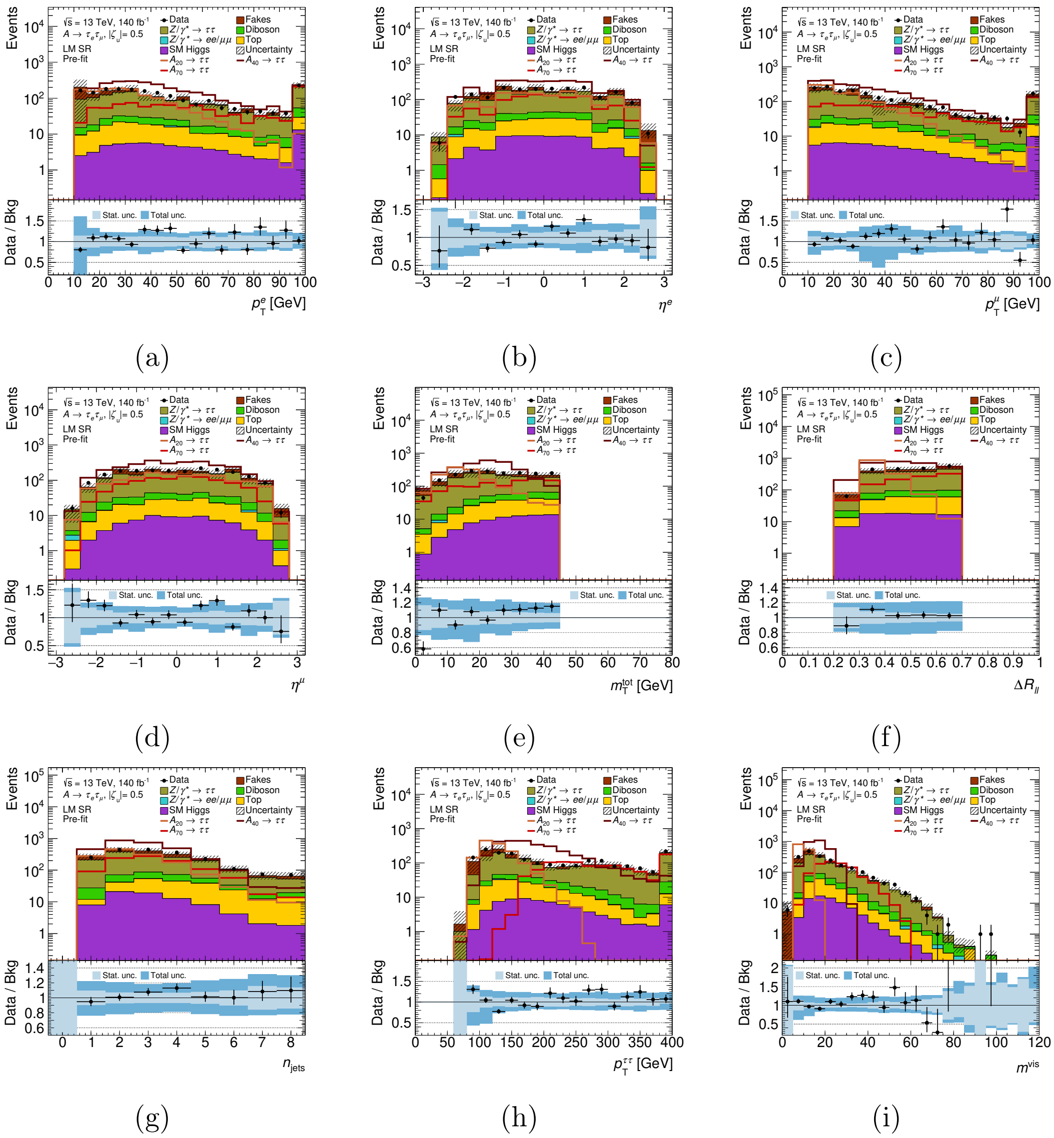

Figure B.11: Variable distributions in the LMSR after complete selection criteria: (a) electron p_{T}, (b) electron η, (c) muon p_{T}, (d) muon η (e) $m_{\mathrm{T}}^{\mathrm{tot}}$, (f) $\Delta R_{\ell\ell}$, (g) number of jets, (h) p_{T} of the di-tau system and (g) m^{vis}.

High-mass signal region

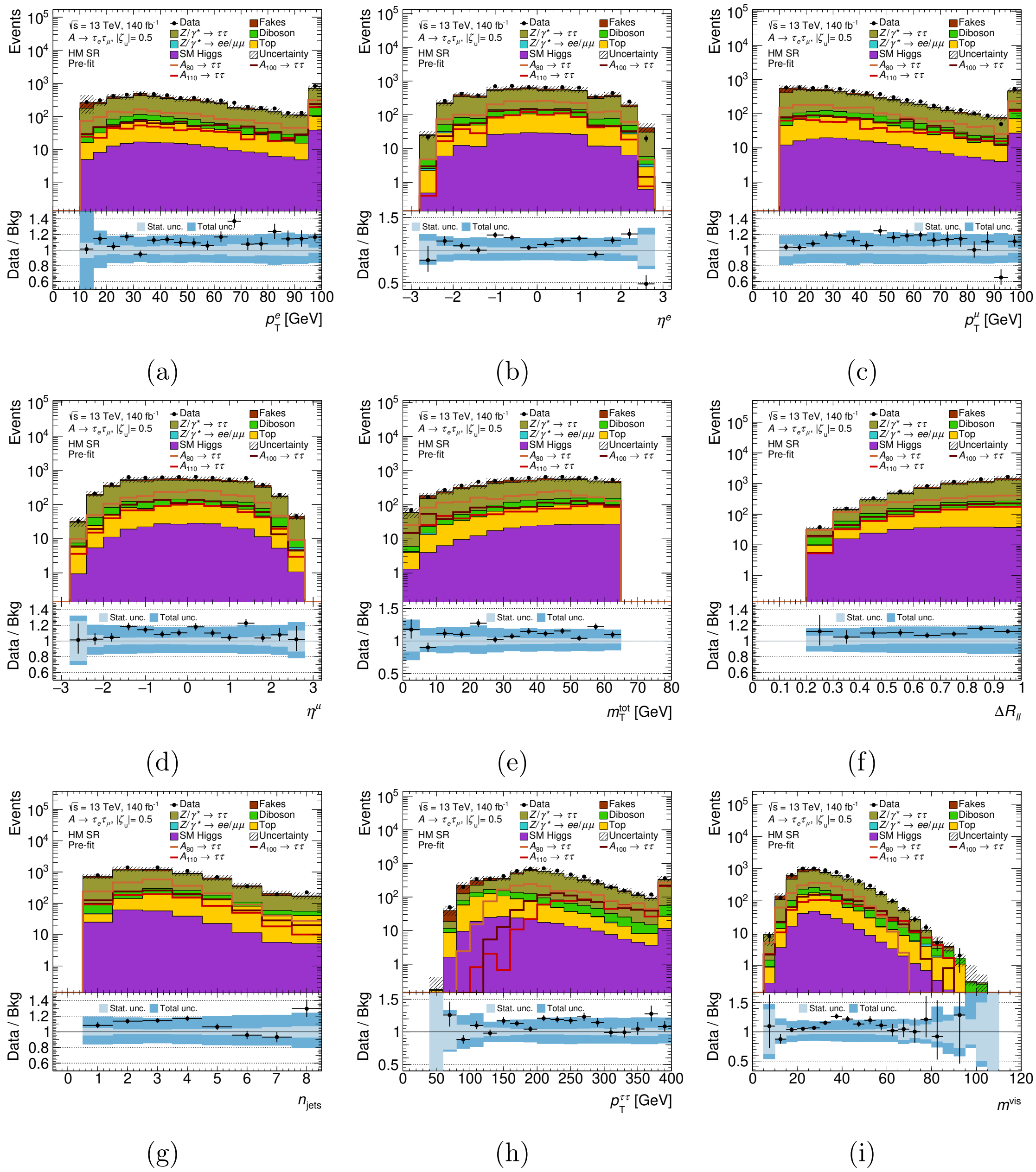

Figure B.12: Variable distributions in the HMSR after complete selection criteria: (a) electron p_{T}, (b) electron η, (c) muon p_{T}, (d) muon η (e) $m_{\mathrm{T}}^{\mathrm{tot}}$, (f) $\Delta R_{\ell\ell}$, (g) number of jets, (h) p_{T} of the di-tau system and (g) m^{vis}.

B.4.2 Control and validation regions

$Z \to \tau\tau$ control region

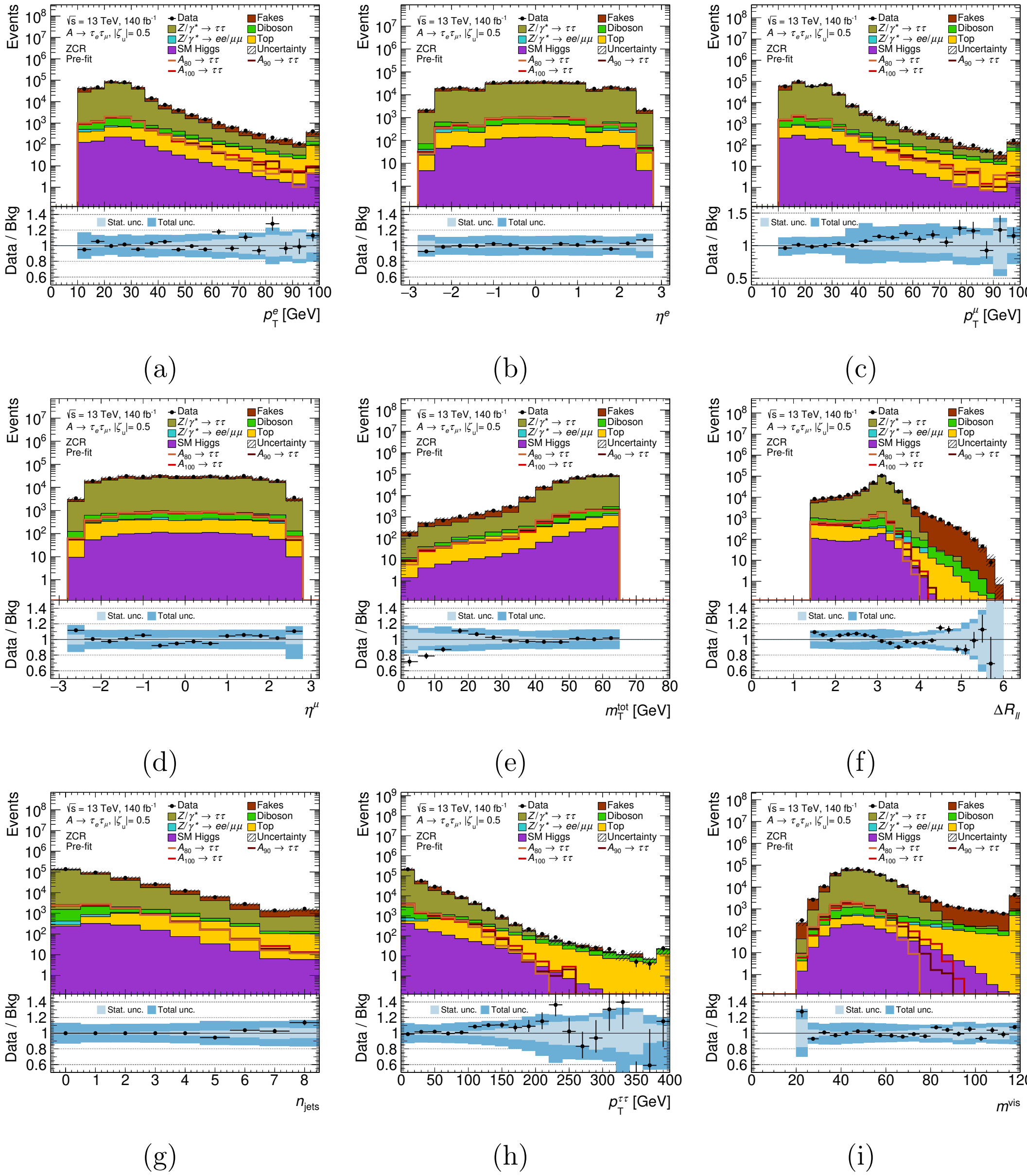

Figure B.13: Variable distributions in the ZCR after complete selection criteria: (a) electron p_{T}, (b) electron η, (c) muon p_{T}, (d) muon η (e) $m_{\mathrm{T}}^{\mathrm{tot}}$, (f) $\Delta R_{\ell\ell}$, (g) number of jets, (h) p_{T} of the di-tau system and (g) m^{vis}.

Top control region

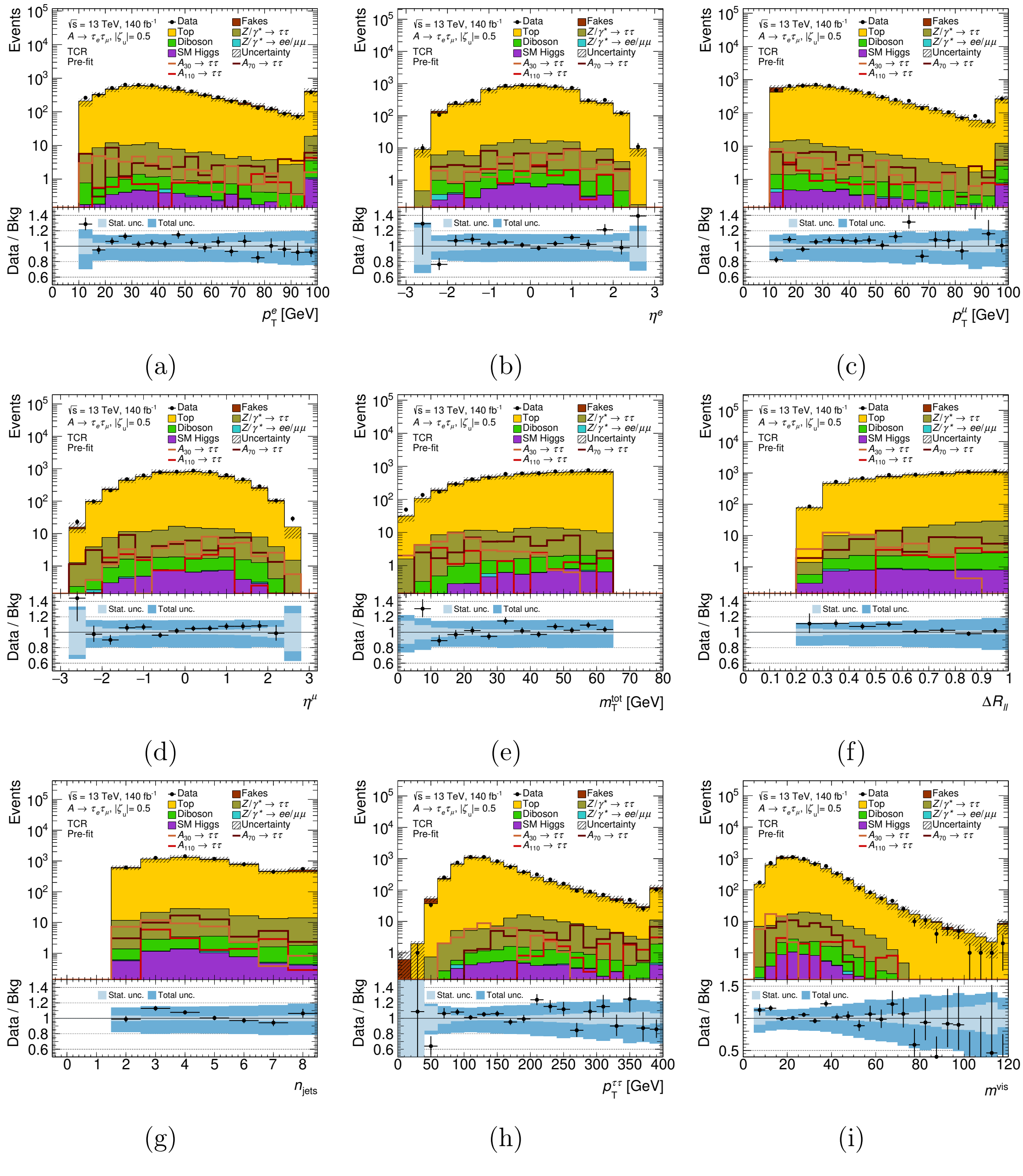

Figure B.14: Variable distributions in the TCR after complete selection criteria: (a) electron p_{T}, (b) electron η, (c) muon p_{T}, (d) muon η (e) $m_{\mathrm{T}}^{\mathrm{tot}}$, (f) $\Delta R_{\ell\ell}$, (g) number of jets, (h) p_{T} of the di-tau system and (g) m^{vis}.

Fake-lepton validation region

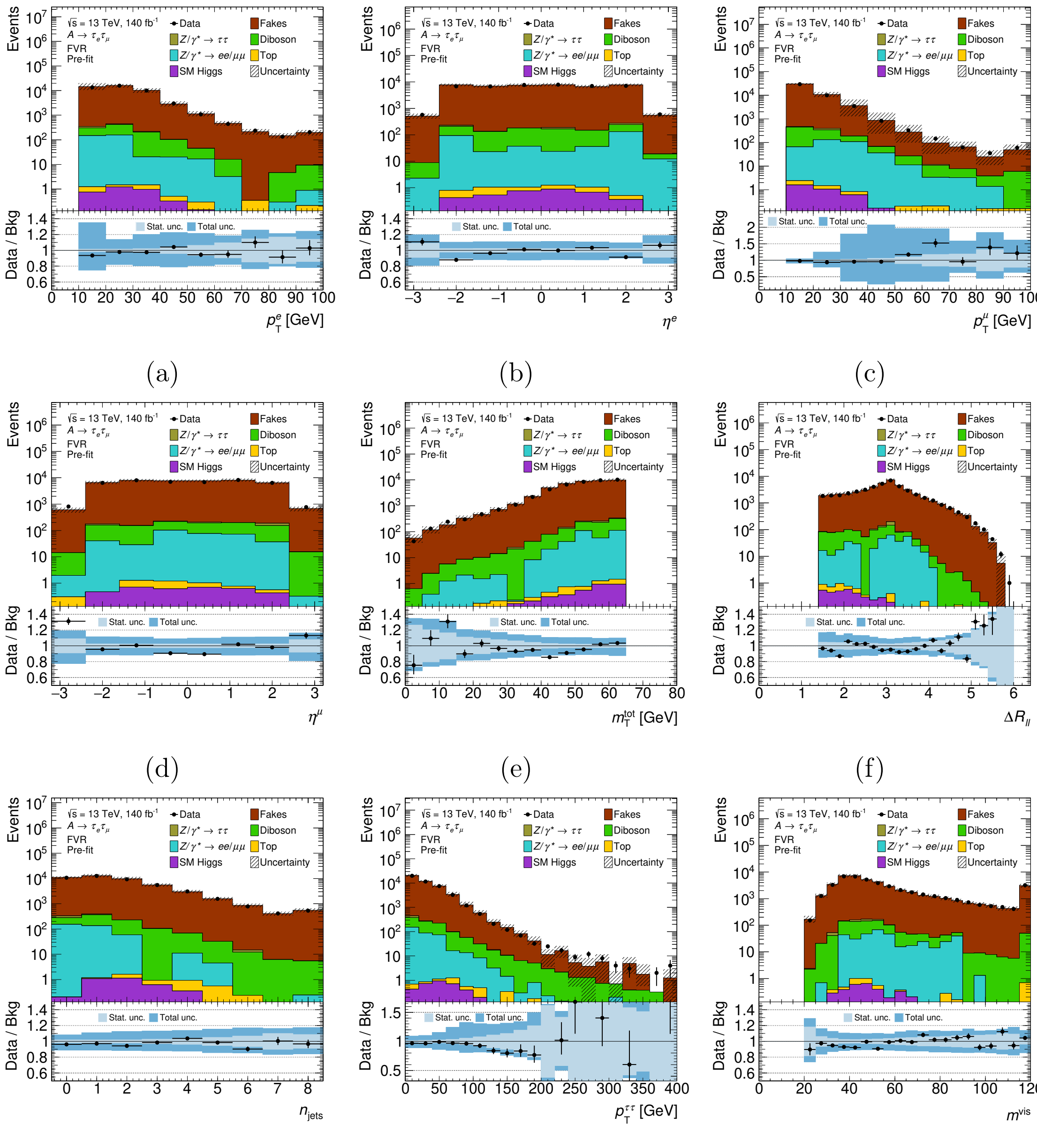

Figure B.15: Variable distributions in the FVR after complete selection criteria: (a) electron p_T, (b) electron η, (c) muon p_T, (d) muon η (e) m_T^{tot}, (f) $\Delta R_{\ell\ell}$, (g) number of jets, (h) p_T of the di-tau system and (g) m^{vis}.

Low-mass same-sign validation region

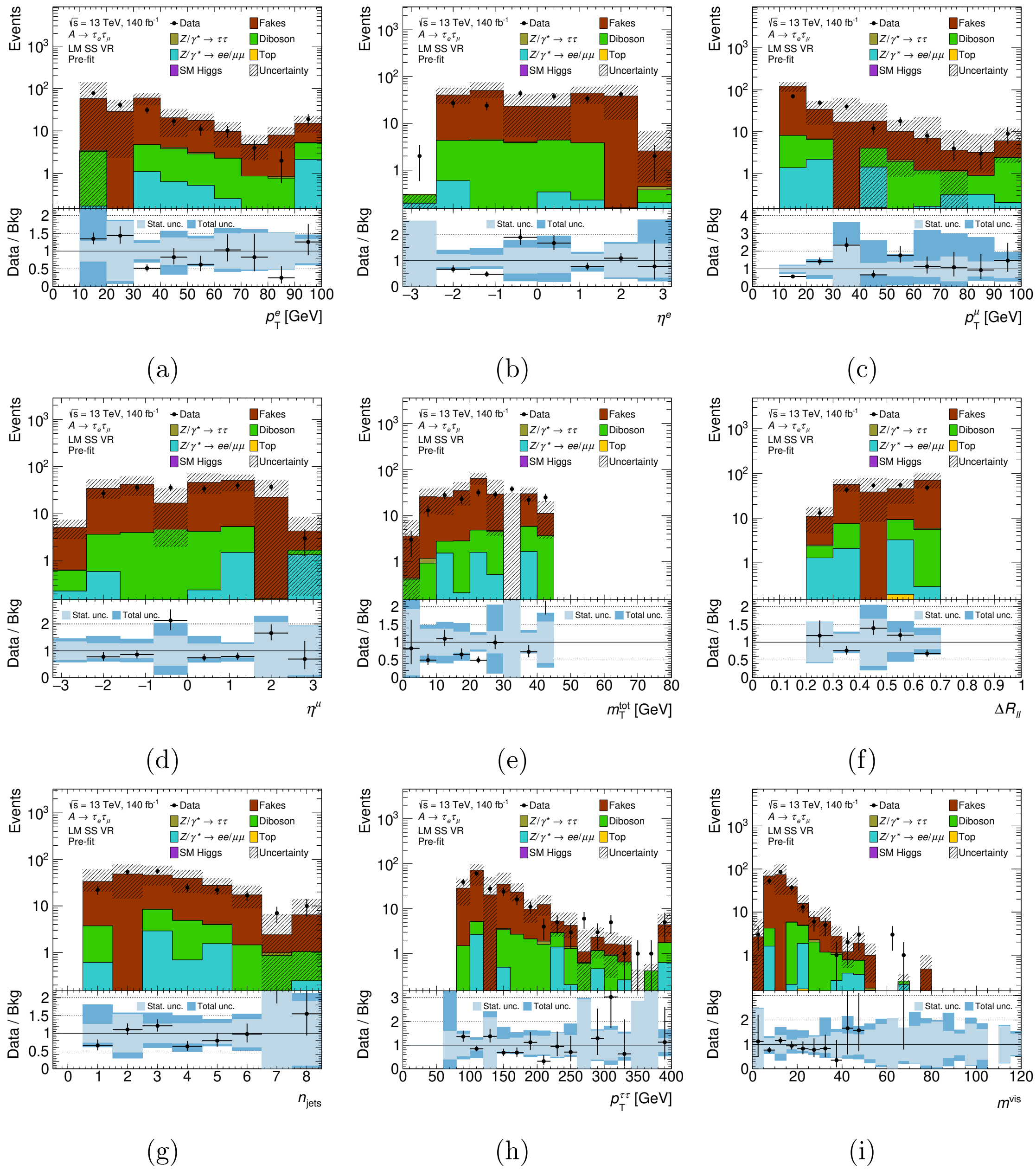

Figure B.16: Variable distributions in the LMSSVR after complete selection criteria: (a) electron p_{T}, (b) electron η, (c) muon p_{T}, (d) muon η (e) $m_{\mathrm{T}}^{\mathrm{tot}}$, (f) $\Delta R_{\ell\ell}$, (g) number of jets, (h) p_{T} of the di-tau system and (g) m^{vis}.

High-mass same-sign validation region

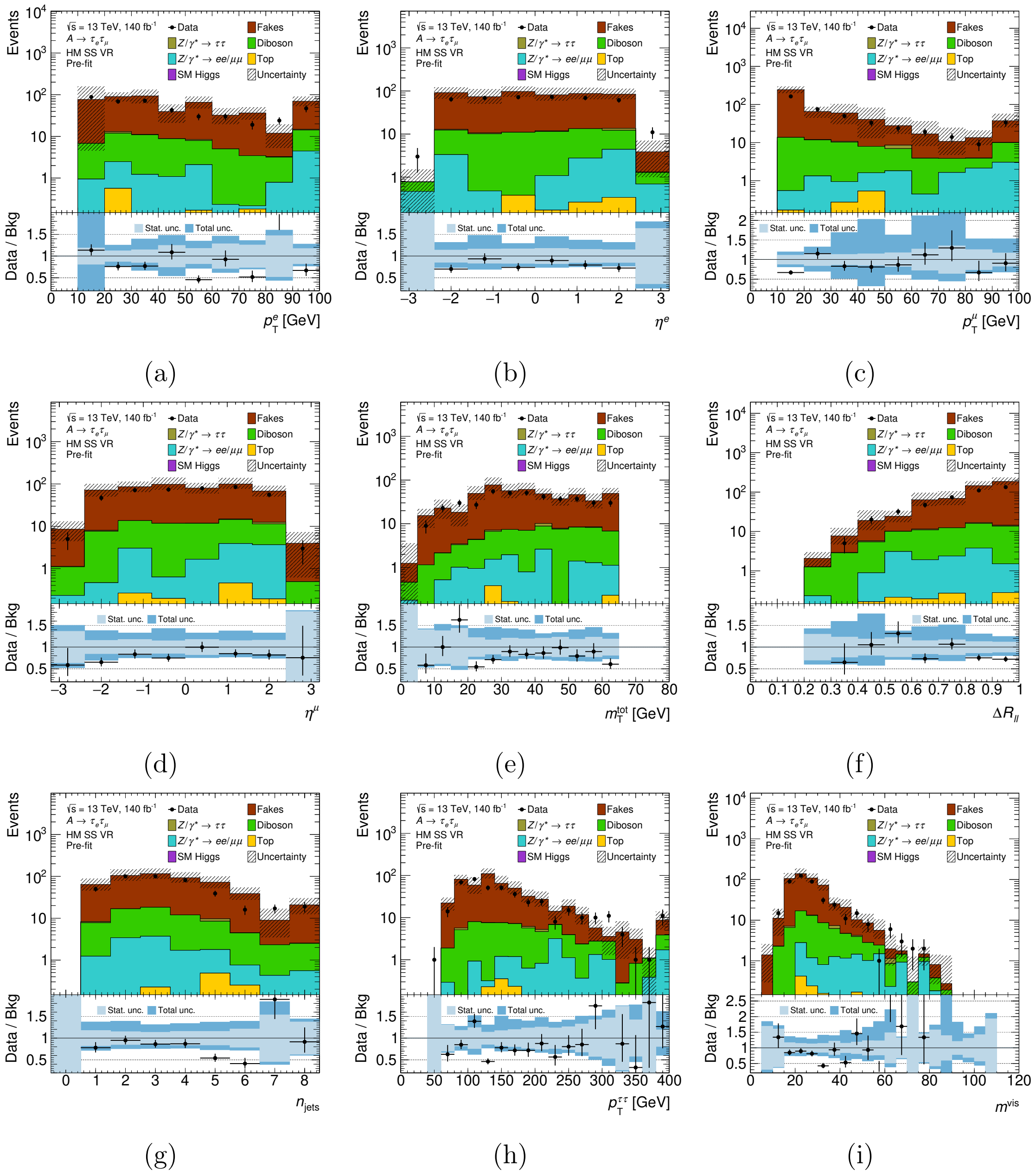

Figure B.17: Variable distributions in the HMSSVR after complete selection criteria: (a) electron p_{T}, (b) electron η, (c) muon p_{T}, (d) muon η (e) $m_{\mathrm{T}}^{\mathrm{tot}}$, (f) $\Delta R_{\ell\ell}$, (g) number of jets, (h) p_{T} of the di-tau system and (g) m^{vis}.

B.5 Study of single-lepton triggers

A study has been done[1], if the sensitivity of the analysis can be increased by adding single-lepton triggers to the electron–muon triggers used in this analysis. The following triggers are available for the full Run 2 period and have been studied: `HLT_e26_lhtight_nod0_ivarloose` and `HLT_mu26_ivarmedium`, which both have the transverse momentum thresholds $p_{\mathrm{T}}^{\ell} > 26\,\mathrm{GeV}$. A comparison of these triggers with the electron–muon triggers is illustrated in Figure B.18.

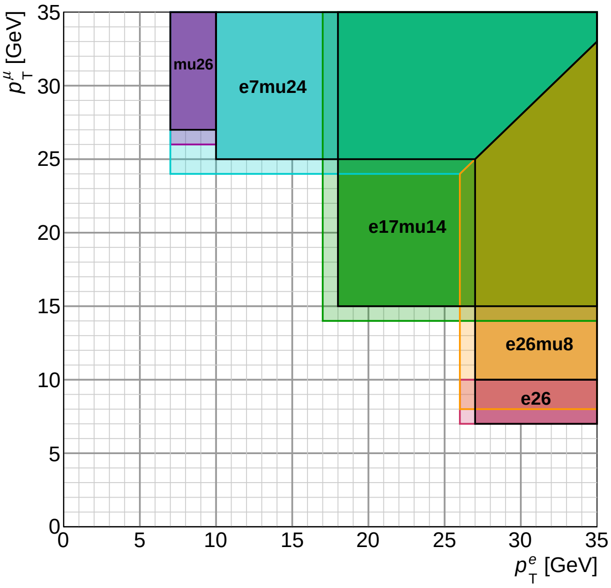

Figure B.18: Visualization of the available electron–muon triggers and single-lepton triggers. The single-lepton triggers in purple and pink colors could only add a small p_{T} band on either side, the rest is already covered by the electron–muon triggers.

A comparison of the distribution of m_{MMC} for using electron–muon and single-lepton triggers respectively is shown for the LMSR in Figure B.19 and for the HMSR in Figure B.20. For both regions the additional background has a significantly different constitution, being dominated by fake leptons now (denoted as 'Multijet' there) and having a much higher fraction of $W \to l\nu$ events. A comparison of the STAT-only limit is shown in Figure B.21.

[1] Note, that the study was carried out in an early stage of the analysis when the setup was not final yet. The SRs were still blinded, the fake-lepton background estimation was done by combining fake leptons from MC simulation (e.g. from the $W \to \ell\nu$ process) with a data-driven fake factor method, and the luminosity used was $139\,\mathrm{fb}^{-1}$.

In the LMSR adding the single-lepton triggers would add $+31\,\%$ background while the signals would gain $+25\,\%$ for A_{20}, $+9\,\%$ for A_{40} and $+2\,\%$ for A_{70}. In the HMSR, adding the single-lepton triggers would add $+32\,\%$ background while the signals would gain $+5\,\%$ for A_{80}, $+5\,\%$ for A_{100} and $+3\,\%$ for A_{110}. From these numbers and the limit it is concluded that the analysis does not profit from including the single-lepton triggers. For a future improvement of this analysis one could think of using single-lepton triggers to specifically enhance the sensitivity at $m_A = 20\,\mathrm{GeV}$, but this would need an extensive optimization study. By simply adding the triggers, the sensitivity is not improved. Another possible use case of single-lepton triggers would be to increase the available statistics for the efficiency determination for the MM. It would need to be studied, if a possible reduction in the statistical and systematic uncertainties of the fake-lepton background would be more beneficial than the general increase of the fake-lepton background with its large uncertainties in the SRs.

If the goal is to include hadronic τ-leptons into the analysis, then single-lepton triggers are needed without question.

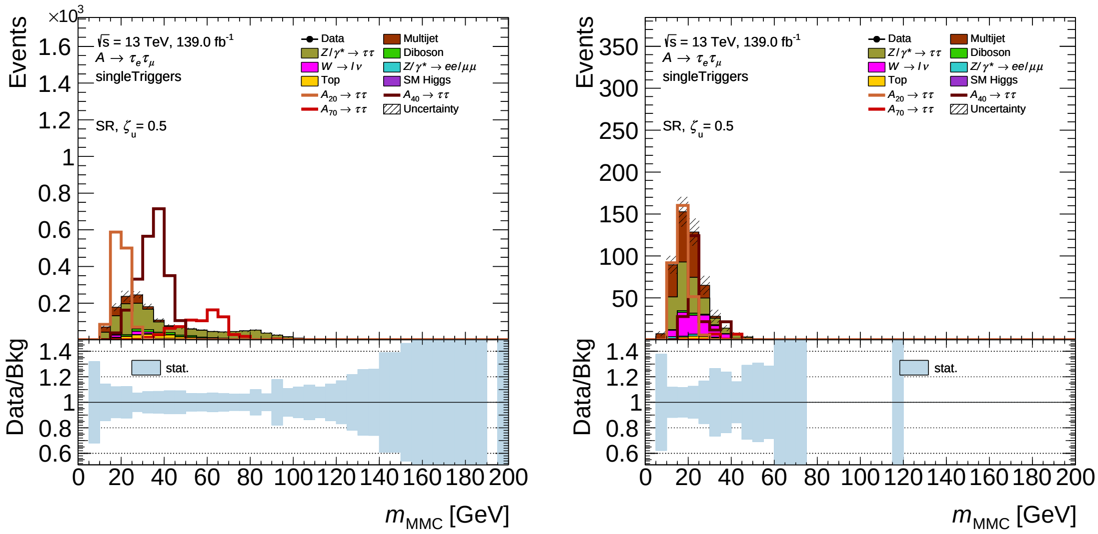

(a) (b)

Figure B.19: Comparison of m_{MMC} for (a) electron–muon and (b) single-lepton triggers in the LMSR. Note, that the study was carried out in an early stage of the analysis when the setup was not final yet. The SRs were still blinded, the fake-lepton background (denoted here as 'Multijet') estimation was done by combining fake leptons from MC simulation (e.g. from the $W \to \ell\nu$ process) with a data-driven fake factor method, and the luminosity used was $139\,\mathrm{fb}^{-1}$.

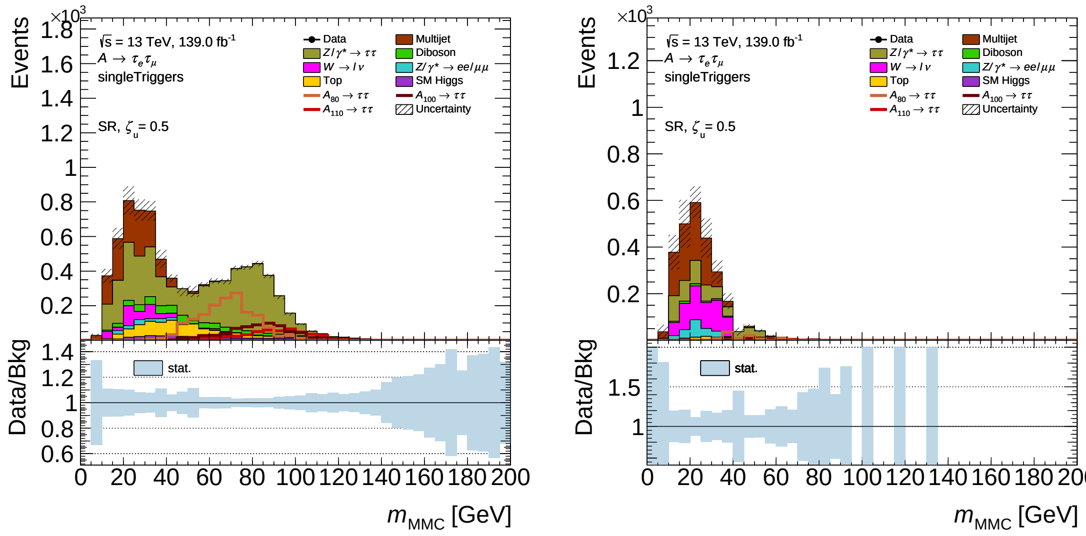

(a) (b)

Figure B.20: Comparison of m_{MMC} for (a) electron–muon and (b) single-lepton triggers in the HMSR. Note, that the study was carried out in an early stage of the analysis when the setup was not final yet. The SRs were still blinded, the fake-lepton background (denoted here as 'Multijet') estimation was done by combining fake leptons from MC simulation (e.g. from the $W \to \ell\nu$ process) with a data-driven fake factor method, and the luminosity used was $139\,\mathrm{fb}^{-1}$.

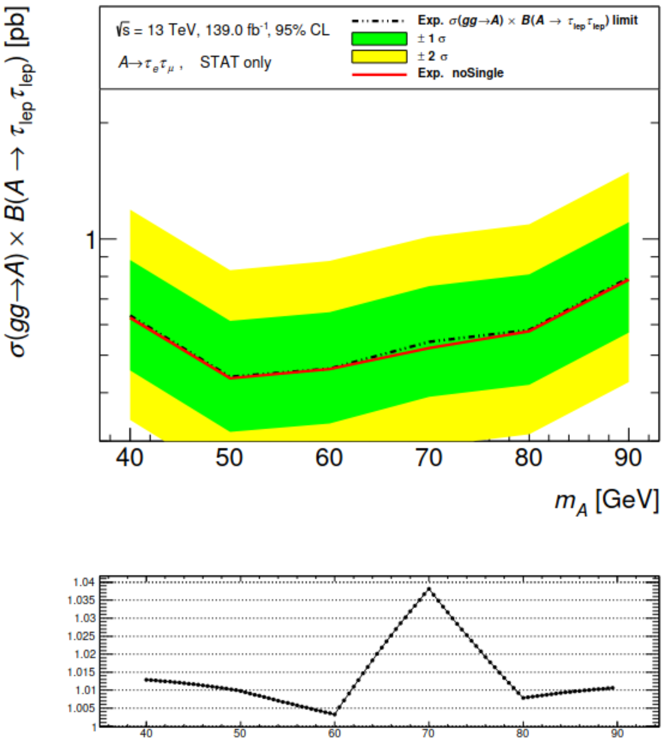

Figure B.21: Expected STAT-only limits on the production cross-section times the branching ratio of the observed signal process for A boson masses $40\,\mathrm{GeV} \leq m_A \leq 90\,\mathrm{GeV}$ with added single-lepton triggers. The dashed line show the limit including the single-lepton triggers while the limit with using only electron–muon triggers is shown in red. The limit gets slightly worse when adding the additional events from the single-lepton triggers.
Note: at the time this study was done, the signal mass points 20, 30, 100 and 110 GeV were not produced yet.

B.6 Investigation of $Z \to \tau\tau$ mismodeling

It is visible in Figure 6.7, that the $E_{\mathrm{T}}^{\mathrm{miss}}$ distribution in the ZCR is mismodeled in the region between 30 and 100 GeV. This area makes up a big portion of the SRs and, with $Z \to \tau\tau$ being the largest background in the SRs, could have a significant influence on the results.
Different approaches have been checked to pin down the problem without reaching a satisfying conclusion. A switch to the newer `Sherpa 2.2.11` Z+Jets samples does not bring any improvements as shown in Figure B.22. The shape of the $E_{\mathrm{T}}^{\mathrm{miss}}$ distribution is similar for data taken in different years (see Figure B.23) or with different triggers (see Figure B.24.) Tightening the lepton identification (ID) requirements makes the disagreement worse as shown in Figure B.25.
Changing the lepton pre-selection cuts for the $E_{\mathrm{T}}^{\mathrm{miss}}$ calculation from 7 GeV to 10 GeV does not bring any significant differences as shown in Figure B.26. Without finding the cause of the mismodeling, it was decided to reweight the $Z \to \tau\tau$ MC using the n_{jets} distribution, as jet variables are independent of all the other variables used in this analysis. This procedure is explained in Section 6.3.5.

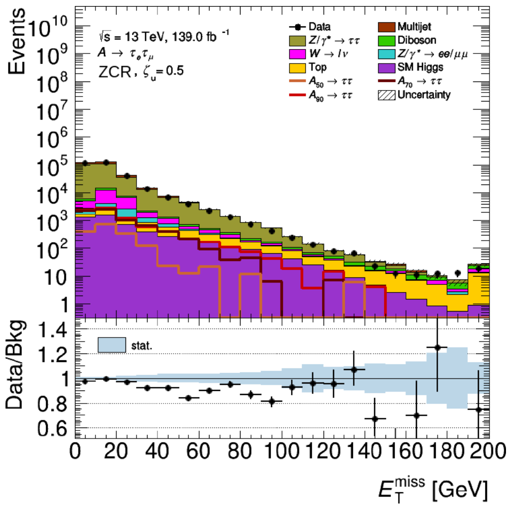

(a)

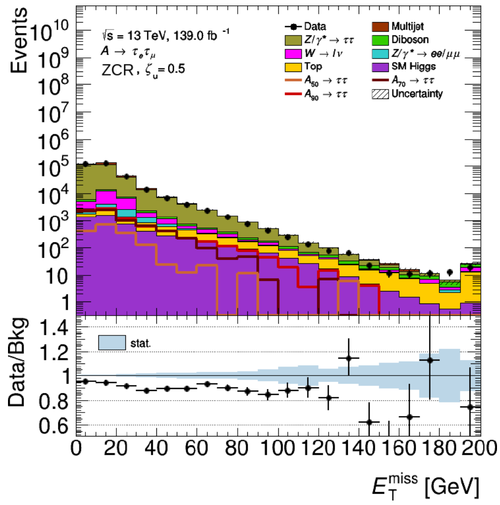

(b)

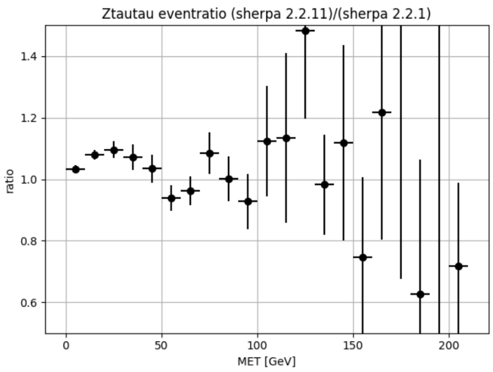

(c)

Figure B.22: $E_{\mathrm{T}}^{\mathrm{miss}}$ distribution in the ZCR for $Z \to \tau\tau$ modeled by the (a) SHERPA 2.2.1 samples (for this analysis nominal) and (b) SHERPA 2.2.11 samples. (c) shows the bin-wise ratio comparing the two sets of $Z \to \tau\tau$ samples. No significant improvement can be seen with the newer version samples.
Note, that the study was carried out in an early stage of the analysis when the setup was not final yet. The fake-lepton background (denoted here as 'Multijet') estimation was done by combining fake leptons from MC simulation (e.g. from the $W \to \ell\nu$ process) with a data-driven fake factor method.

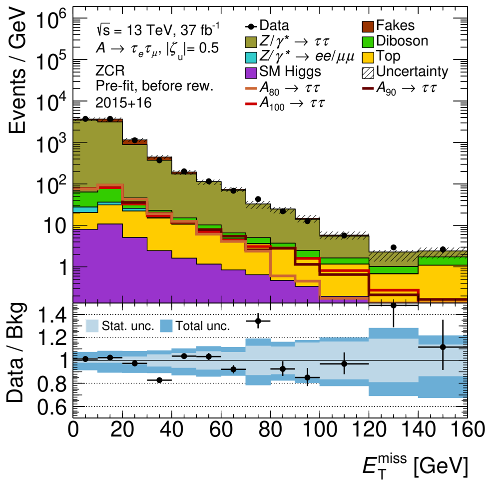

(a)

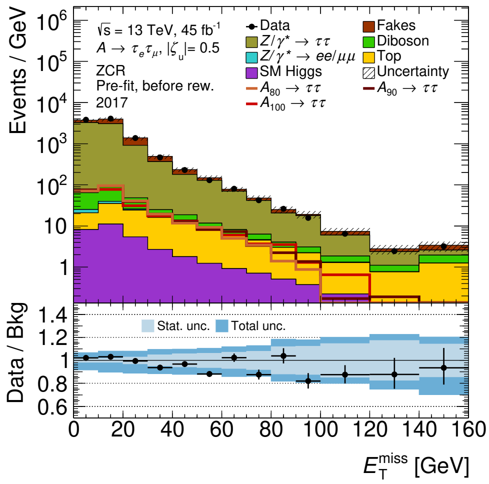

(b)

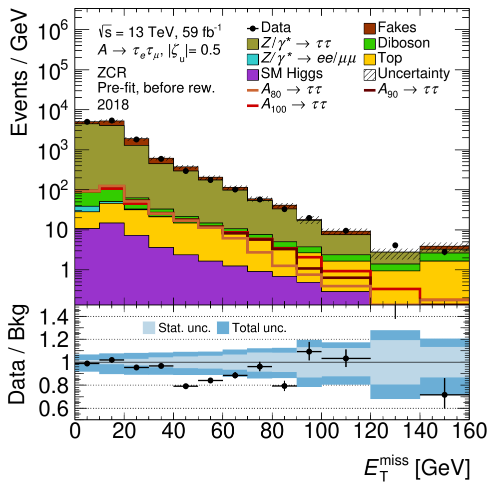

(c)

Figure B.23: $E_{\mathrm{T}}^{\mathrm{miss}}$ distribution in the ZCR for data taken in the years (a) 2015 and 2016, (b) 2017, and (c) 2018. No significant difference can be seen between the years.

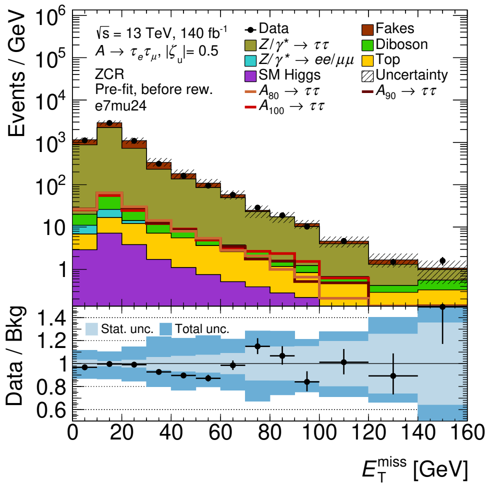

(a)

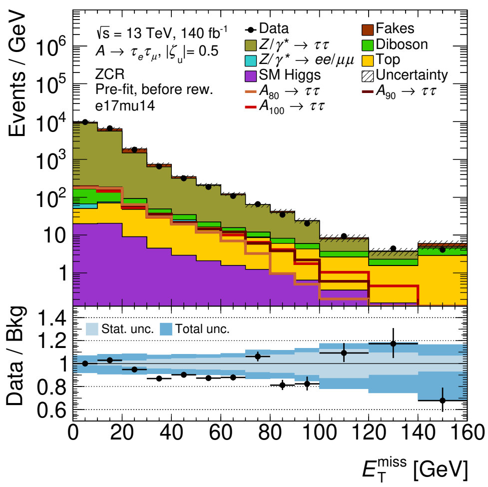

(b)

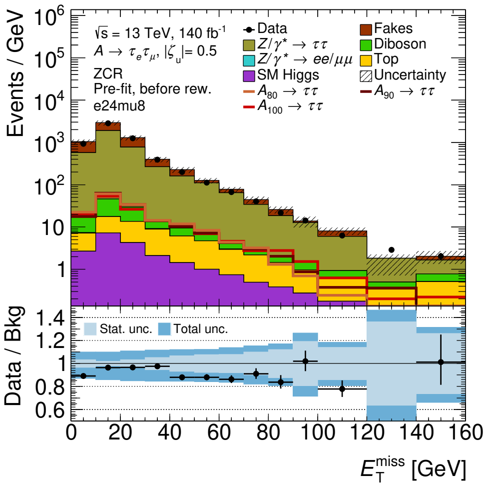

(c)

Figure B.24: $E_{\mathrm{T}}^{\mathrm{miss}}$ distribution in the ZCR for events triggered with the trigger (a) `e7mu24`, (b) `e17mu14` or (c) `e24mu8`. The exact trigger descriptions are given in Table 6.4. All three distributions show the mismodeling with no significant difference between the triggers.

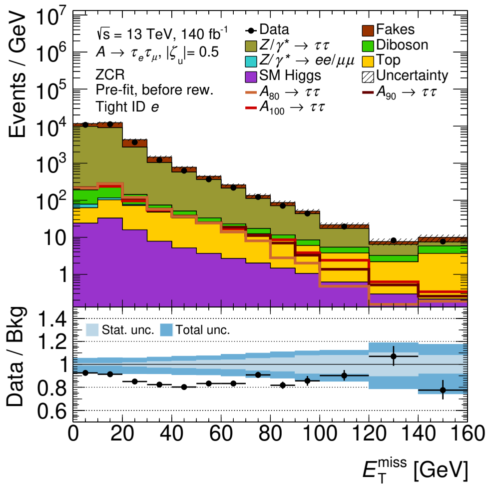

(a)

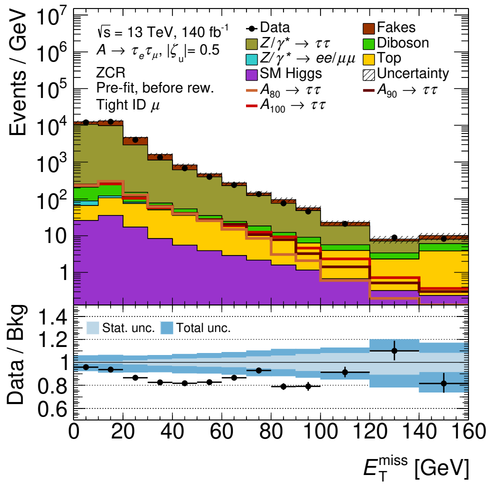

(b)

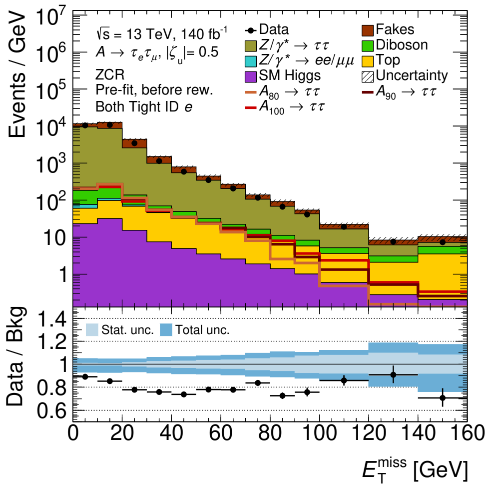

(c)

Figure B.25: E_T^{miss} distribution in the ZCR when raising the ID requirement to *Tight* for (a) the electron, (b) the muon, and (c) both leptons simultaneously. The discrepancy between data and MC grows slightly.

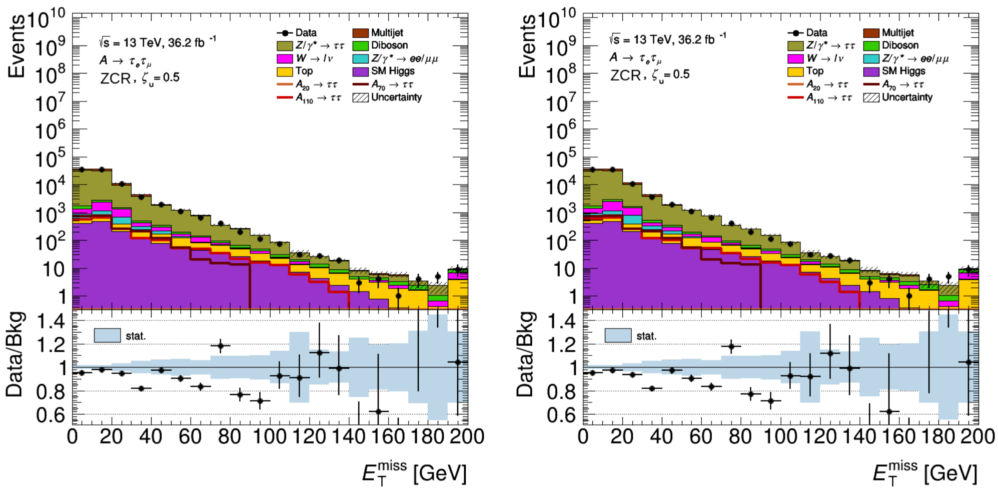

(a) (b)

Figure B.26: $E_{\mathrm{T}}^{\mathrm{miss}}$ distribution in the ZCR for data from 2015 and 2016. (a) shows the plot with the nominal pre-selection cuts ($p_{\mathrm{T}}^{\ell} > 7\,\mathrm{GeV}$ for $E_{\mathrm{T}}^{\mathrm{miss}}$ calculation) while in (b) the pre-selection p_{T} cut for leptons has been raised to be 10 GeV. Both distribution have a very similar shape with the $Z \to \tau\tau$ contribution agreeing within 0.5 % precision. Hence, the mismodeling cannot be accounted by the pre-selection cuts for leptons entering the $E_{\mathrm{T}}^{\mathrm{miss}}$ calculation. This was checked because 10 GeV is the standard cut used by the 'JetEtmiss' group.
Note, that the study was carried out in an early stage of the analysis when the setup was not final yet. The fake-lepton background (denoted here as 'Multijet') estimation was done by combining fake leptons from MC simulation (e.g. from the $W \to \ell\nu$ process) with a data-driven fake factor method.

B.7 $\Delta R_{\ell\ell}$ differences between signal and background

The angular separation between the two leptons in the final state is quantified by the observable $\Delta R_{\ell\ell}$. One can see in Figure B.27 that $\Delta R_{\ell\ell}$ is an excellent variable to separate the signal from the most prominent background: $Z \to \tau\tau$. Even though the 90 GeVsignal mass hypothesis and the Z boson have almost the identical mass, there is a visibly different shape in the $\Delta R_{\ell\ell}$ distributions. In particular the signal-to-background ratio gets much better for low $\Delta R_{\ell\ell}$ values. This motivates to introduce an upper cut on $\Delta R_{\ell\ell}$. For the lower mass points, the separation is even better because the mass difference leads to a tendency towards even lower $\Delta R_{\ell\ell}$ values.

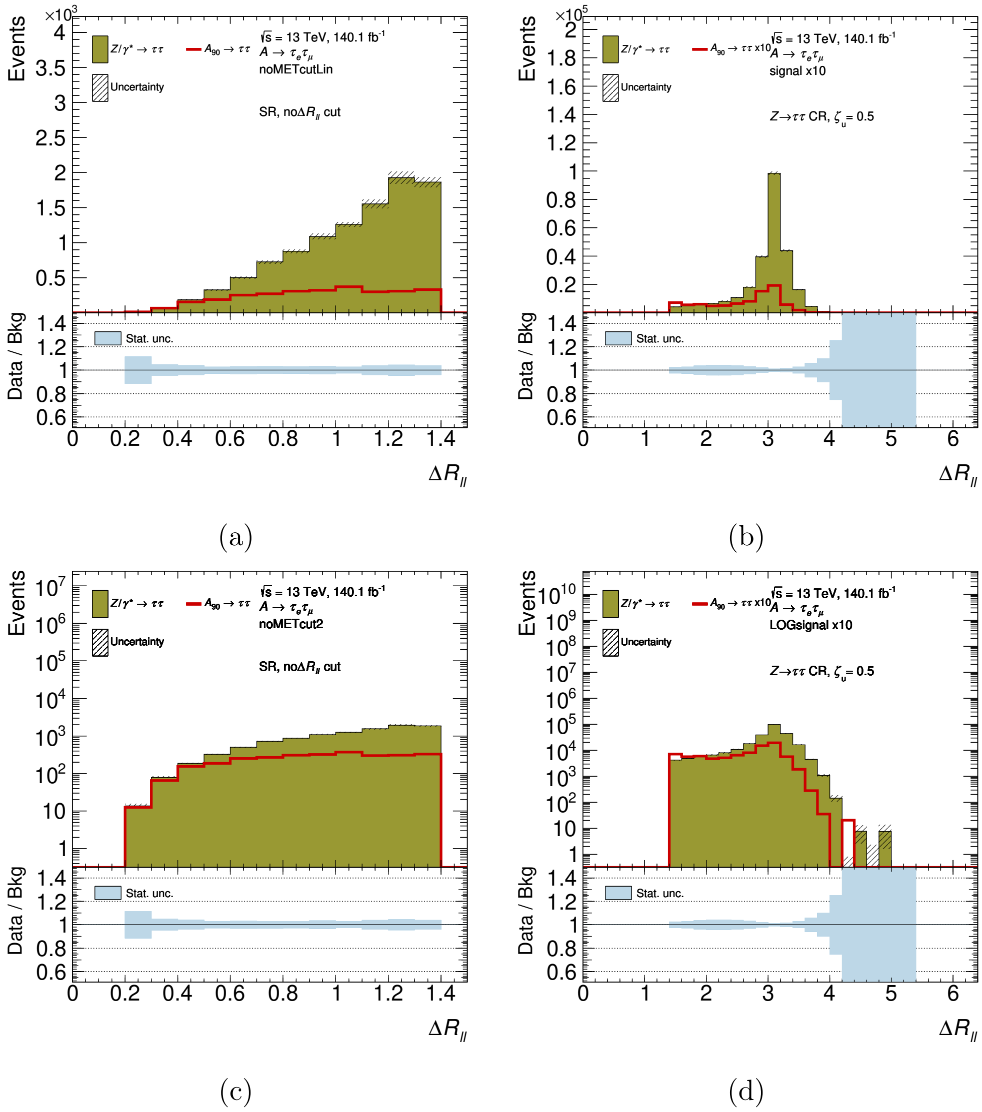

Figure B.27: Differences in $\Delta R_{\ell\ell}$ between the expected signal for $m_A = 90\,\text{GeV}$ and the $Z \to \tau\tau$ background. The distributions are compared in (a) a modified version of the HMSR and (b) the ZCR. These plots have a linear y-axis, while the same plots are shown in (c) and (d) with a logarithmic y-axis for better visualization. The HMSR has been altered by dropping the $E_{\mathrm{T}}^{\mathrm{miss}}$ cut and extending the $\Delta R_{\ell\ell}$ range to $\{0.0, 1.4\}$ to match the setup as closely as possible with the ZCR. In the ZCR, the signal has been scaled up by factor 10 to improve its visibility.

C Further material on the systematic uncertainties

C.1 List of systematic uncertainties

Signal cross-section

`ATLAS_xsec_SigAXXX`[1]

Signal modeling

`ATLAS_AXXX_AlphaS`[1]
`ATLAS_AXXX_MuRF`[1]
`ATLAS_AXXX_A14`[1]
`ATLAS_AXXX_PDF`[1]

Luminosity (LUMI)

`ATLAS_LUMI`

Muon calibration (MUON)

`ATLAS_MUON_CB`
`ATLAS_MUON_SAGITTA_DATASTAT`
`ATLAS_MUON_SAGITTA_RESBIAS`
`ATLAS_MUON_SCALE`

Muon efficiencies (MUON_EFF)

`ATLAS_MUON_EFF_ISO_STAT`
`ATLAS_MUON_EFF_ISO_SYS`
`ATLAS_MUON_EFF_RECO_STAT`

[1]The 'XXX' stands for the mass hypothesis of the respective signal.

```
ATLAS_MUON_EFF_RECO_STAT_LOWPT
ATLAS_MUON_EFF_RECO_SYS
ATLAS_MUON_EFF_RECO_SYS_LOWPT
ATLAS_MUON_EFF_TrigStatUncertainty_e17mu14
ATLAS_MUON_EFF_TrigStatUncertainty_e24mu8
ATLAS_MUON_EFF_TrigStatUncertainty_e7mu24
```

Electron calibration (EG)

```
ATLAS_EG_RESOLUTION_ALL
ATLAS_EG_SCALE_AF2
ATLAS_EG_SCALE_ALL
```

Electron efficiencies (EL_EFF)

```
ATLAS_EL_EFF_ID_CorrUncertaintyNP0-NP15
ATLAS_EL_EFF_ID_SIMPLIFIED_UncorrUncertaintyNP0-NP17
ATLAS_EL_EFF_Iso_CorrUncertaintyNP0-NP10
ATLAS_EL_EFF_Iso_SIMPLIFIED_UncorrUncertaintyNP0-NP17
ATLAS_EL_EFF_Reco_CorrUncertaintyNP0-NP7
ATLAS_EL_EFF_Reco_SIMPLIFIED_UncorrUncertaintyNP0-NP17
ATLAS_EL_EFF_Trigger_e17mu14_CorrUncertaintyNP0-NP10
ATLAS_EL_EFF_Trigger_e17mu14_SIMPLIFIED_UncorrUncertaintyNP0-NP17
ATLAS_EL_EFF_Trigger_e24mu8_CorrUncertaintyNP0-NP10
ATLAS_EL_EFF_Trigger_e24mu8_SIMPLIFIED_UncorrUncertaintyNP0-NP17
ATLAS_EL_EFF_Trigger_e7mu24_CorrUncertaintyNP0-NP10
ATLAS_EL_EFF_Trigger_e7mu24_SIMPLIFIED_UncorrUncertaintyNP0-NP17
```

Missing transverse momentum (MET)

```
ATLAS_MET_SoftTrk_ResoPara
ATLAS_MET_SoftTrk_ResoPerp
ATLAS_MET_SoftTrk_Scale
```

Jet calibration (JET)

```
ATLAS_JET_EtaIntercalibration_NonClosure_2018data
ATLAS_JET_EtaIntercalibration_NonClosure_highE
ATLAS_JET_EtaIntercalibration_NonClosure_negEta
ATLAS_JET_EtaIntercalibration_NonClosure_posEta
```

ATLAS_JET_Flavor_Response
ATLAS_JET_GroupedNP_1-NP_3
ATLAS_JET_JER_DataVsMC_MC16
ATLAS_JET_JER_EffectiveNP_1-NP_6
ATLAS_JET_JER_EffectiveNP_7restTerm
ATLAS_JET_JER_SINGLE_NP

Jet efficiencies (JET_EFF)

ATLAS_JET_fJvteff
ATLAS_jet_jvteff

Flavor-tagging efficiencies (FT_EFF)

ATLAS_btag_b_0-1
ATLAS_btag_c_0-2
ATLAS_btag_extrapolation
ATLAS_btag_extrapolation_from_charm
ATLAS_btag_light_0-3

Pile-up reweighting (PRW)

ATLAS_pu_prw

$Z \to \tau\tau$ modeling (Ztautau_MCGenSys)

ATLAS_Ztautau_alphaS
ATLAS_Ztautau_CKKW
ATLAS_Ztautau_MuRF
ATLAS_Ztautau_PDF
ATLAS_Ztautau_QSF

$Z \to \tau\tau$ n_{jets} reweighting (Ztautau_NJetWt)

Ztautau_NJetWt_DATA
Ztautau_NJetWt_MC
Ztautau_NJetWt_SYS

Diboson modeling (Diboson_MCGenSys)

```
ATLAS_Diboson_alphaS
ATLAS_Diboson_MuRF
ATLAS_Diboson_PDF
```

Background cross-sections

```
xsec_Ztautau
xsec_Diboson
xsec_Top
```

$t\bar{t}$ modeling (TTBar)

```
ATLAS_TTBar_FSR
ATLAS_TTBar_ISR
ATLAS_TTBar_ME
ATLAS_TTBar_PS
ATLAS_TTBar_V3C
```

Fake-lepton background (FAKEBKG)

```
FAKEBKG_STAT_ele_fake_NT_bin1-bin9
FAKEBKG_STAT_ele_fake_T_bin1-bin9
FAKEBKG_STAT_ele_real_NT_bin1-bin7
FAKEBKG_STAT_ele_real_T_bin1-bin7
FAKEBKG_STAT_muon_fake_NT_bin1-bin9
FAKEBKG_STAT_muon_fake_T_bin1-bin9
FAKEBKG_STAT_muon_real_NT_bin1-bin7
FAKEBKG_STAT_muon_real_T_bin1-bin7
FAKEBKG_SYST_Composition
FAKEBKG_SYST_metParameterization
FAKEBKG_SYST_etaParameterization
FAKEBKG_SYST_nJetsParameterization
```

C.2 Additional plots for systematic uncertainties on the fake-lepton background

Section 6.4.5 explained the different sources of systematic uncertainties in the MM. The individual contributions to the overall uncertainty are displayed here. The uncertainty from statistical sources in the efficiency measurement is shown in Figure C.1; the uncertainties from the parametrization of the efficiencies in η^{ℓ}, n_{jets} and $E_{\mathrm{T}}^{\mathrm{miss}}$ are visualized in Figure C.2, Figure C.3 and Figure C.4, respectively; and the uncertainty from the different composition of the regions is displayed in Figure C.5.

In the FVR, the main contribution to the total uncertainty comes from the composition uncertainty. In the low end of the m_{MMC} spectrum, the parametrizations in η^{ℓ} and n_{jets} also give significant contributions. The statistical component in the efficiency calculation is mostly negligible.

The LMSR shows much larger uncertainties on the fake-lepton background compared to the FVR. This is partially due to the much lower statistics and partially due to the fact that the LMSR is kinematically further away from the regions where the efficiencies were calculated. In the low-mass area, the contributions from the $E_{\mathrm{T}}^{\mathrm{miss}}$ parametrization and the composition are dominant, while for the high-mass domaine, the parametrizations of n_{jets} and η^{ℓ} become dominant. Same as for the FVR, the statistical component in the efficiency calculation is negligible compared to the other sources.

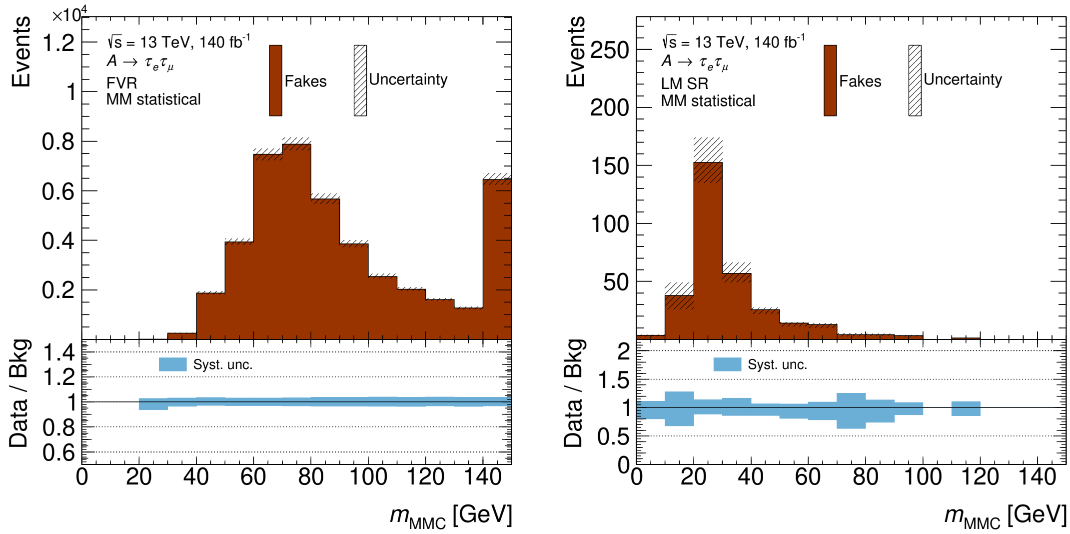

(a) (b)

Figure C.1: Distribution of m_{MMC} for the fake-lepton background estimated with the MM in (a) the FVR and (b) the LMSR. The uncertainty band shows the systematic uncertainty that arises from the statistical uncertainties in the efficiency measurements.

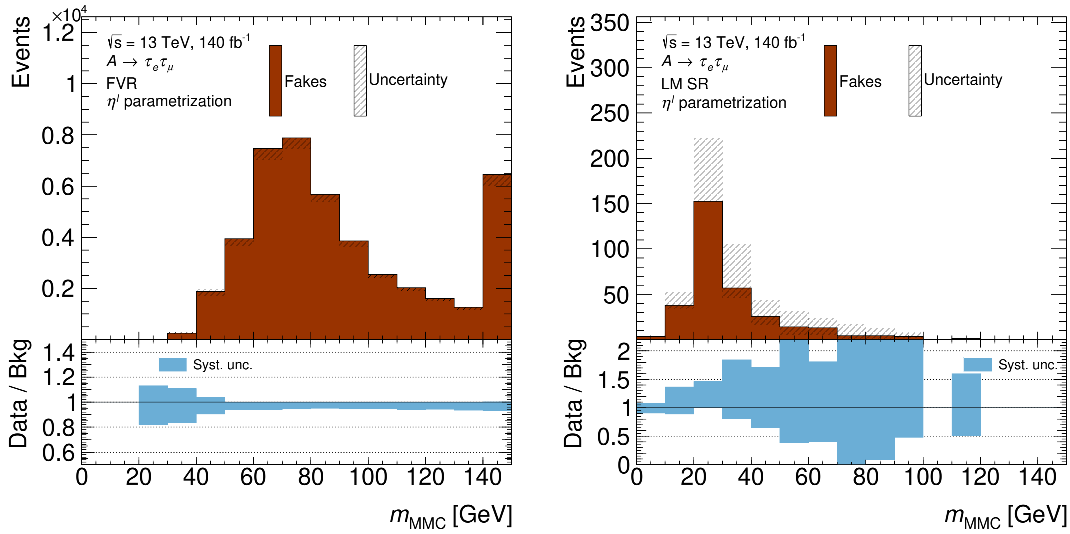

(a) (b)

Figure C.2: Distribution of m_{MMC} for the fake-lepton background estimated with the MM in (a) the FVR and (b) the LMSR. The uncertainty band shows the systematic uncertainty from the η^{ℓ} parametrization.

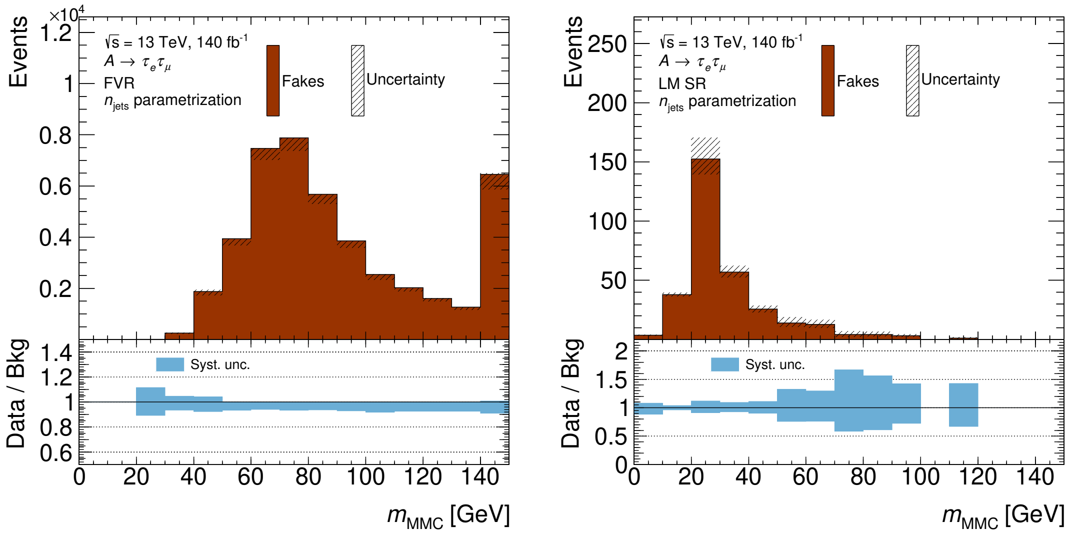

(a) (b)

Figure C.3: Distribution of m_{MMC} for the fake-lepton background estimated with the MM in (a) the FVR and (b) the LMSR. The uncertainty band shows the systematic uncertainty from the n_{jets} parametrization.

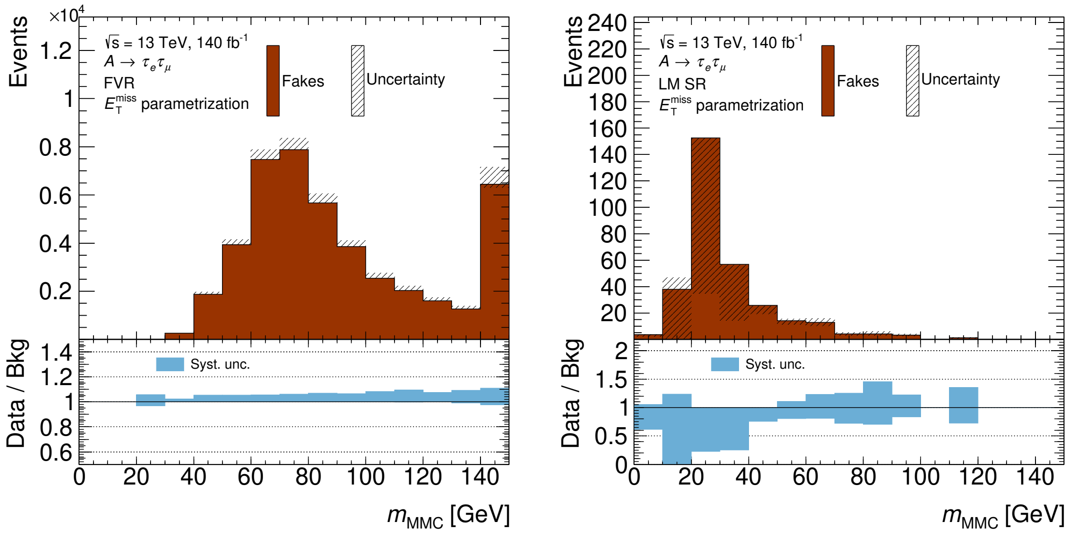

(a) (b)

Figure C.4: Distribution of m_{MMC} for the fake-lepton background estimated with the MM in (a) the FVR and (b) the LMSR. The uncertainty band shows the systematic uncertainty from the $E_{\mathrm{T}}^{\mathrm{miss}}$ parametrization.

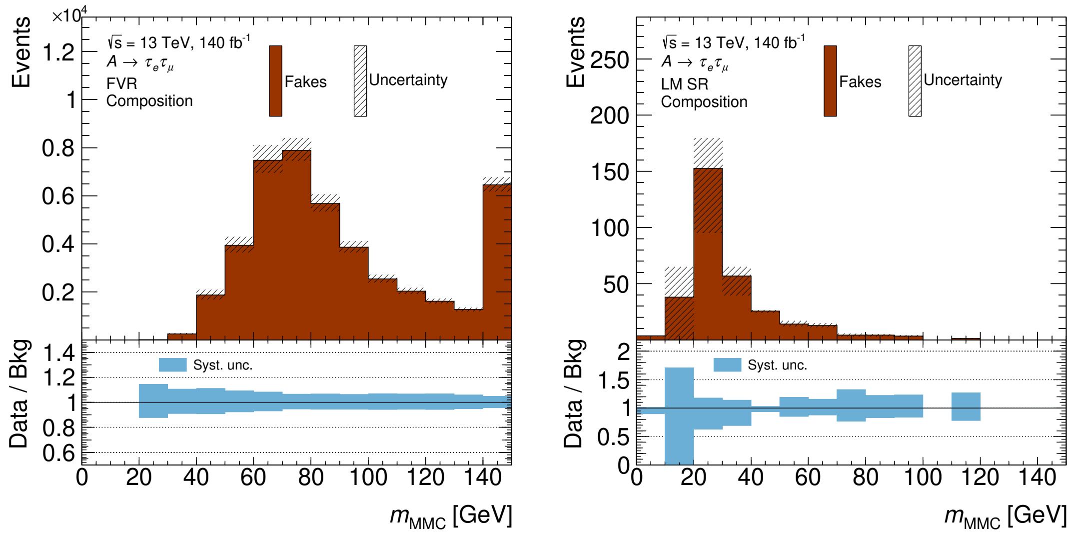

(a) (b)

Figure C.5: Distribution of m_{MMC} for the fake-lepton background estimated with the MM in (a) the FVR and (b) the LMSR. The uncertainty band shows the systematic uncertainty from the different fake-lepton background composition in the different regions.

C.3 Investigations on behavior of QSF and CKKW systematics on the $Z \to \tau\tau$ background

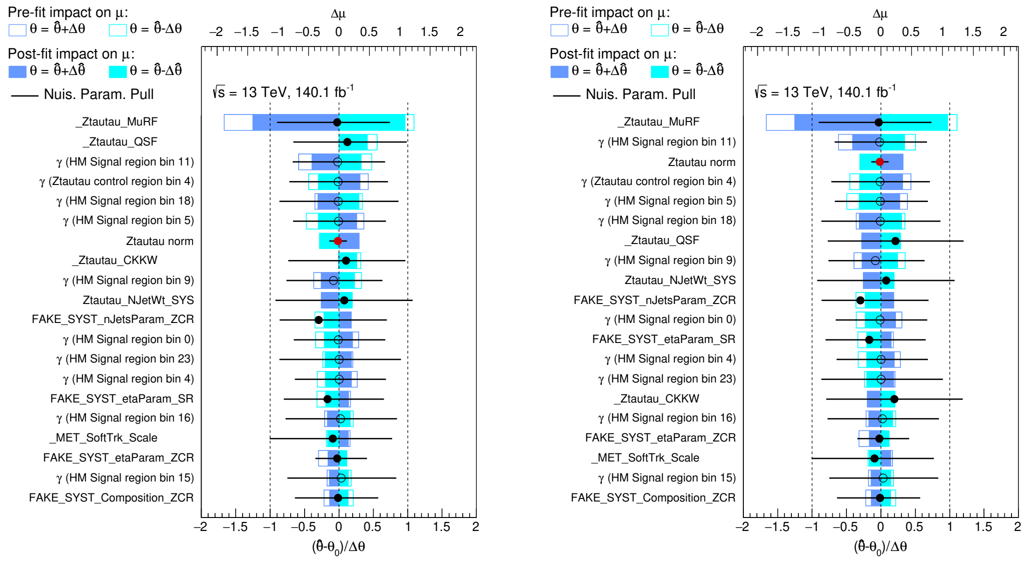

(a) (b)

Figure C.6: Ranking of systematic uncertainties due to post-fit impact on μ for the 20 NPs with the highest impact. The rankings are displayed for the signal mass $m_A = 90\,\text{GeV}$ with (a) the nominal setup and (b) symmetrized `ATLAS_Ztautau_QSF` and `ATLAS_Ztautau_CKKW` systematics.

As can be seen in Figure C.6(a), the NPs `ATLAS_Ztautau_QSF` and `ATLAS_Ztautau_CKKW` are ranked quite highly for the 90 GeV mass point (similar for the other signal masses in the HMSR) and show a one-sided behavior, meaning both the up and the down variation influence the point of interest (POI) μ in the same direction. This is usually not expected and will be investigated in this section.
These systematics are generator systematics for the $Z \to \tau\tau$ process and their estimation is described in Section 6.4.4. The resulting size of the systematics is displayed in Figure 6.10. It can already be seen there that the shape of both systematics is asymmetric. Taking a closer look at the exact input values for the variations of these two systematics to the fit in Figure C.7 and Figure C.9, one can see that this asymmetry is propagated correctly. For testing purposes, both systematics were symmetrized at the fit input to check the changes that come arise from this. The symmetrized inputs to the fit are shown in Figure C.8 and Figure C.10. The impact of this change on the rankings is displayed in Figure C.6(b).

The asymmetric impact on the POI disappears for both NPs and they drop a bit in the importance of all NPs. It can be concluded from this study that the one-sided behavior of both NPs in the nominal ranking plot is a direct consequence from the asymmetry of the NPs in the input stage. However, since this is a real effect from the systematics evaluation, it has been decided to leave the NPs as they are because symmetrizing them would change their nature quite drastically.

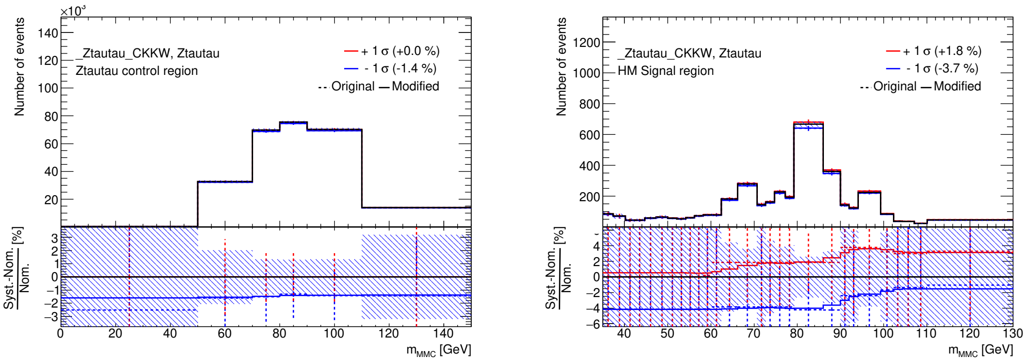

(a) (b)

Figure C.7: Input histogram for the systematic NP `ATLAS_Ztautau_CKKW` to the fit in (a) the ZCR and (b) the HMSR for the nominal case. The input values from the systematics calculation (dashed lines) are smoothed. The resulting values (solid lines) are used as fit inputs.

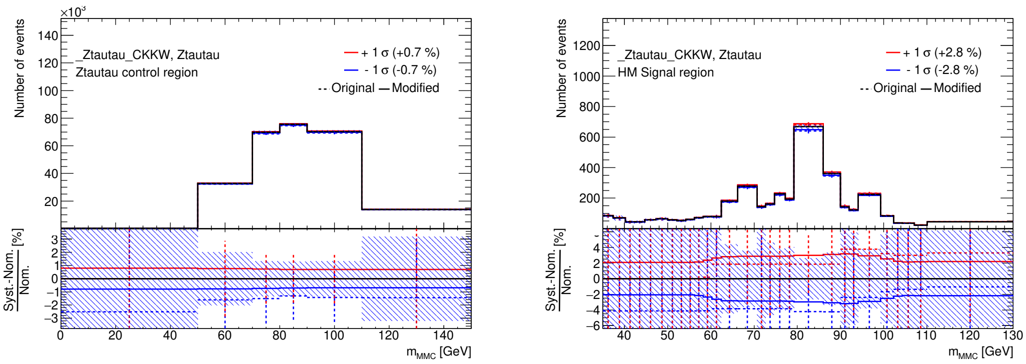

(a) (b)

Figure C.8: Input histogram for the systematic NP `ATLAS_Ztautau_CKKW` to the fit in (a) the ZCR and (b) the HMSR for the symmetrized case. The input values from the systematics calculation (dashed lines) are smoothed and symmetrized. The resulting values (solid lines) are used as fit inputs.

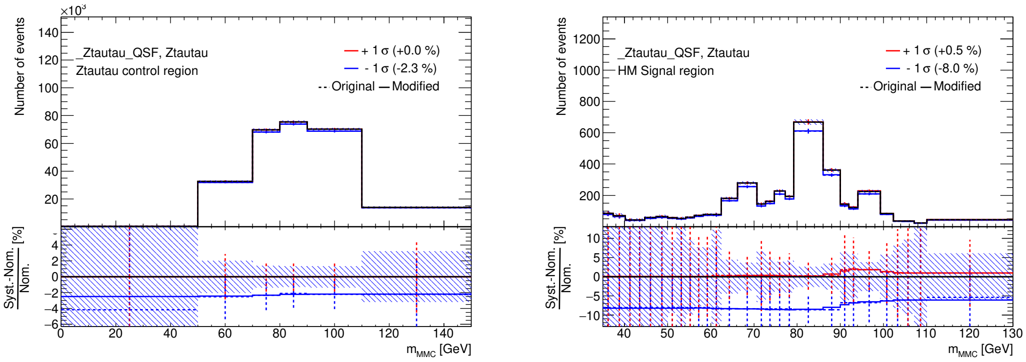

(a) (b)

Figure C.9: Input histogram for the systematic NP `ATLAS_Ztautau_QSF` to the fit in (a) the ZCR and (b) the HMSR for the nominal case. The input values from the systematics calculation (dashed lines) are smoothed. The resulting values (solid lines) are used as fit inputs.

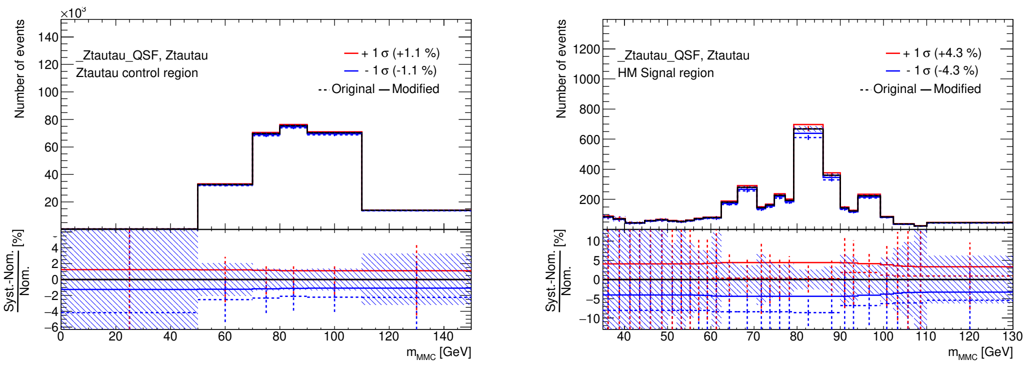

(a) (b)

Figure C.10: Input histogram for the systematic NP `ATLAS_Ztautau_QSF` to the fit in (a) the ZCR and (b) the HMSR for the symmetrized case. The input values from the systematics calculation (dashed lines) are smoothed and symmetrized. The resulting values (solid lines) are used as fit inputs.

D Auxiliary material on the statistical analysis

D.1 Details on p_0-values

Table D.1: Detailed p_0-values and significances Z_0 for all mass points in the LMSR. The same results were obtained for the cross-section and $|\zeta_u|$ fits up to the fourth digit.

	20	25	30	40	50	60	70	75
p_0-value	0.037	0.318	0.959	0.798	0.739	0.872	0.601	0.426
Z_0	1.787	0.473	-1.738	-0.836	-0.642	-1.136	-0.255	0.187

Table D.2: Detailed p_0-values and significances Z_0 for all mass points in the HMSR. The same results were obtained for the cross-section and $|\zeta_u|$ fits up to the fourth digit.

	75	80	85	90	95	100	105	110
p_0-value	0.389	0.224	0.103	0.23	0.817	0.917	0.981	0.986
Z_0	0.282	0.76	1.263	0.74	-0.905	-1.387	-2.069	-2.191

D.2 Limit tables

Table D.3: Expected and observed upper 95 % CL limits on cross-section times branching ratio with ±1 and ±2 σ uncertainty bands for A boson production via gluon–gluon fusion.

m_A [GeV]	Expected [pb]	$+2\,\sigma$ [pb]	$+1\,\sigma$ [pb]	$-1\,\sigma$ [pb]	$-2\,\sigma$ [pb]	Observed [pb]
20	42.324	32.082	14.689	10.926	18.383	67.482
25	23.718	16.199	7.448	5.645	9.601	26.121
30	11.376	8.657	3.947	2.926	4.909	6.971
40	5.118	4.307	1.948	1.403	2.336	3.911
50	3.930	3.407	1.529	1.092	1.812	3.205
60	4.283	3.842	1.705	1.203	1.991	2.999
70	5.494	4.940	2.207	1.551	2.563	5.174
75 (LMSR)	7.712	6.690	3.014	2.152	3.562	8.417
75	6.935	5.761	2.463	1.961	3.246	7.528
80	9.339	8.506	3.801	2.439	4.235	12.234
85	14.456	13.008	6.001	4.022	6.715	21.540
90	30.560	25.374	11.728	8.425	13.92	42.914
95	21.577	19.473	8.577	5.993	9.925	16.927
100	11.063	9.979	4.434	3.107	5.137	7.320
105	6.664	6.089	2.706	1.883	3.111	3.587
110	4.608	4.302	1.891	1.316	2.166	2.381

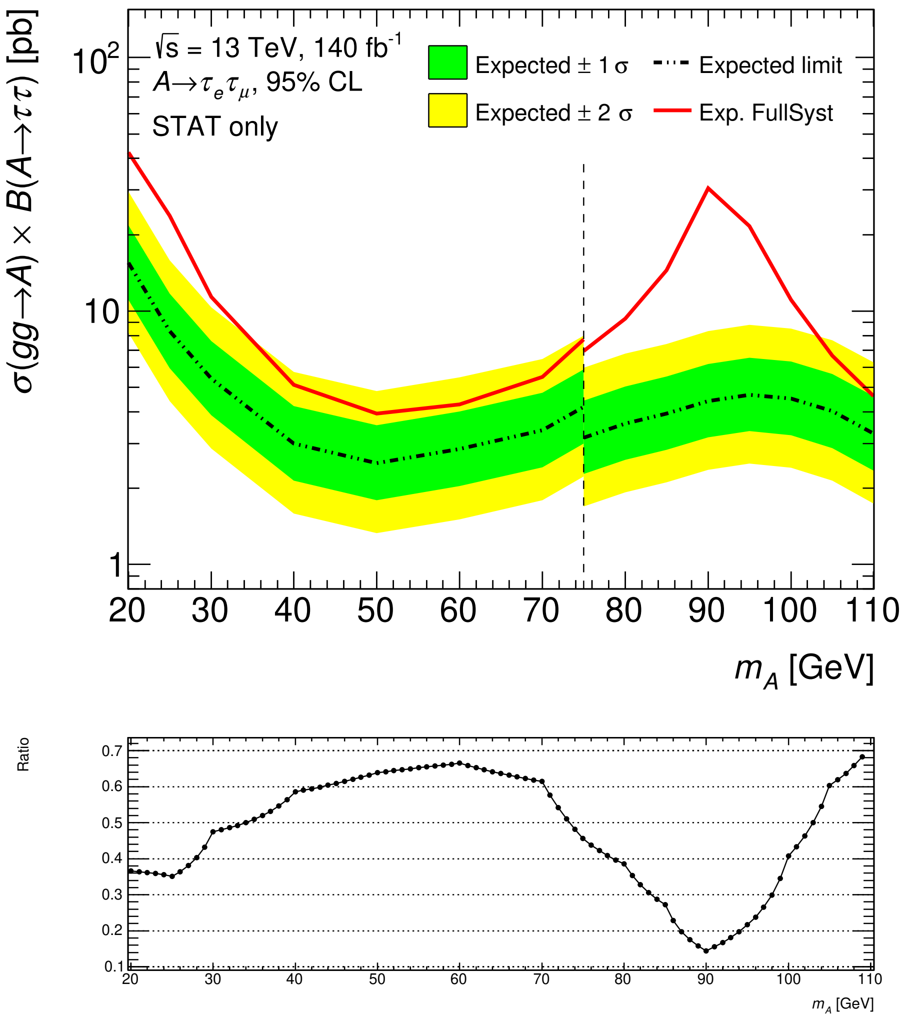

Figure D.1: Expected STAT-only limit on the production cross-section for $gg \to A$ times the branching ratio for A decaying into two τ-leptons for A boson masses from 20 to 110 GeV. The dash-dotted line shows the limit set by analyzing the shape of the m_{MMC} distribution with its $1\,\sigma$ and $2\,\sigma$ uncertainty bands in green and yellow, respectively. The solid red line shows the limit with all systematics included. The vertical dashed line visualizes the split into two SRs, the mass points on the left side are analyzed within the LMSR and the ones on the right side in the HMSR. The ratio plot shows the STAT-only limit divided by the obtained limit with all systematics.

Table D.4: Expected upper STAT-only 95 % CL limits on cross-section times branching ratio with ±1 and ±2 σ uncertainty bands for A boson production via gluon–gluon fusion.

m_A [GeV]	Exp. STAT-only [pb]	$+2\,\sigma$ [pb]	$+1\,\sigma$ [pb]	$-1\,\sigma$ [pb]	$-2\,\sigma$ [pb]
20	15.476	14.157	6.319	4.417	7.284
25	8.321	7.529	3.369	2.367	3.907
30	5.399	4.918	2.204	1.532	2.532
40	2.997	2.748	1.222	0.856	1.411
50	2.511	2.310	1.030	0.719	1.184
60	2.848	2.618	1.165	0.815	1.343
70	3.377	3.094	1.382	0.964	1.590
75 (LMSR)	4.182	3.806	1.703	1.189	1.963
75	3.162	2.806	1.263	0.891	1.474
80	3.599	3.188	1.435	1.013	1.676
85	3.934	3.480	1.568	1.106	1.831
90	4.413	3.904	1.761	1.239	2.053
95	4.673	4.143	1.870	1.313	2.175
100	4.505	4.023	1.811	1.270	2.101
105	4.018	3.634	1.628	1.140	1.882
110	3.277	3.001	1.336	0.936	1.542

Table D.5: Expected and observed upper 95 % CL limits on $|\zeta_u|$ with ± 1 and $\pm 2\,\sigma$ uncertainty bands.

m_A [GeV]	Expected $|\zeta_u|$ limit	$+2\,\sigma$	$+1\,\sigma$	$-1\,\sigma$	$-2\,\sigma$	Observed $|\zeta_u|$ limit
20	0.153	0.057	0.027	0.022	0.039	0.195
25	0.132	0.044	0.021	0.017	0.031	0.139
30	0.103	0.037	0.018	0.015	0.026	0.081
40	0.085	0.033	0.016	0.013	0.023	0.074
50	0.088	0.034	0.016	0.013	0.024	0.079
60	0.106	0.042	0.020	0.016	0.029	0.089
70	0.136	0.054	0.026	0.021	0.037	0.132
75 (LMSR)	0.171	0.066	0.032	0.026	0.046	0.179
75	0.162	0.060	0.028	0.025	0.044	0.169
80	0.199	0.079	0.038	0.028	0.052	0.228
85	0.260	0.103	0.051	0.040	0.070	0.319
90	0.398	0.148	0.072	0.060	0.105	0.472
95	0.350	0.138	0.065	0.053	0.094	0.310
100	0.262	0.103	0.049	0.040	0.071	0.213
105	0.212	0.084	0.040	0.033	0.058	0.156
110	0.184	0.074	0.035	0.029	0.050	0.132

D.3 Fit results for additional mass points

D.3.1 Post-fit plots for additional mass points

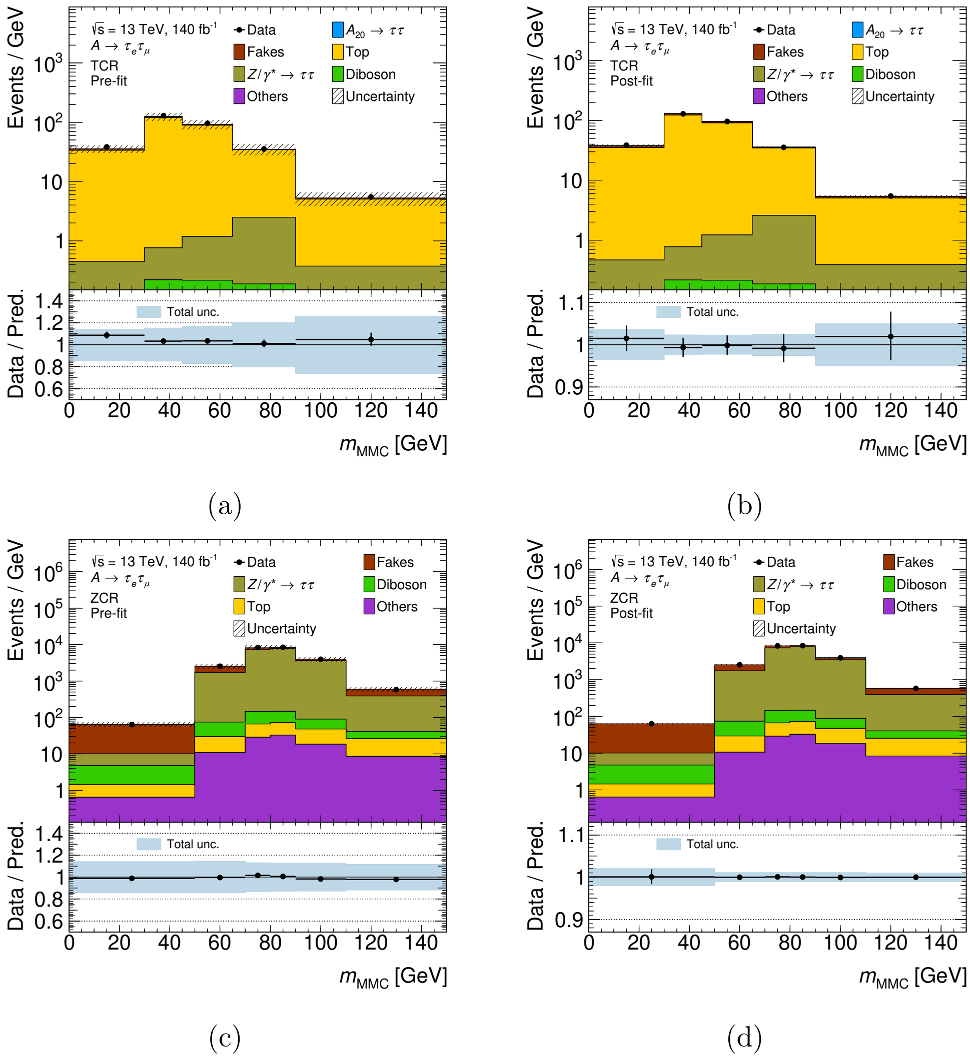

Figure D.2: Comparison of the pre-fit and the post-fit m_{MMC} distributions in the CRs for the $m_{\mathrm{A}} = 20\,\mathrm{GeV}$ signal mass. Shown are (a) the pre-fit distribution in the TCR, (b) the post-fit distribution in the TCR, (c) the pre-fit distribution in the ZCR and (d) the post-fit distribution in the ZCR. The pre-fit signal cross-section is defined to be 1 pb, while the fit result is used for the post-fit distributions. The processes $Z/\gamma^* \to \ell^+\ell^-$ and SM Higgs production are summarized to the 'Others' background. Events with values beyond the x-axis range are shown in the last bin of each distribution. The blue band in the ratio plot shows the total uncertainty of the background estimate.

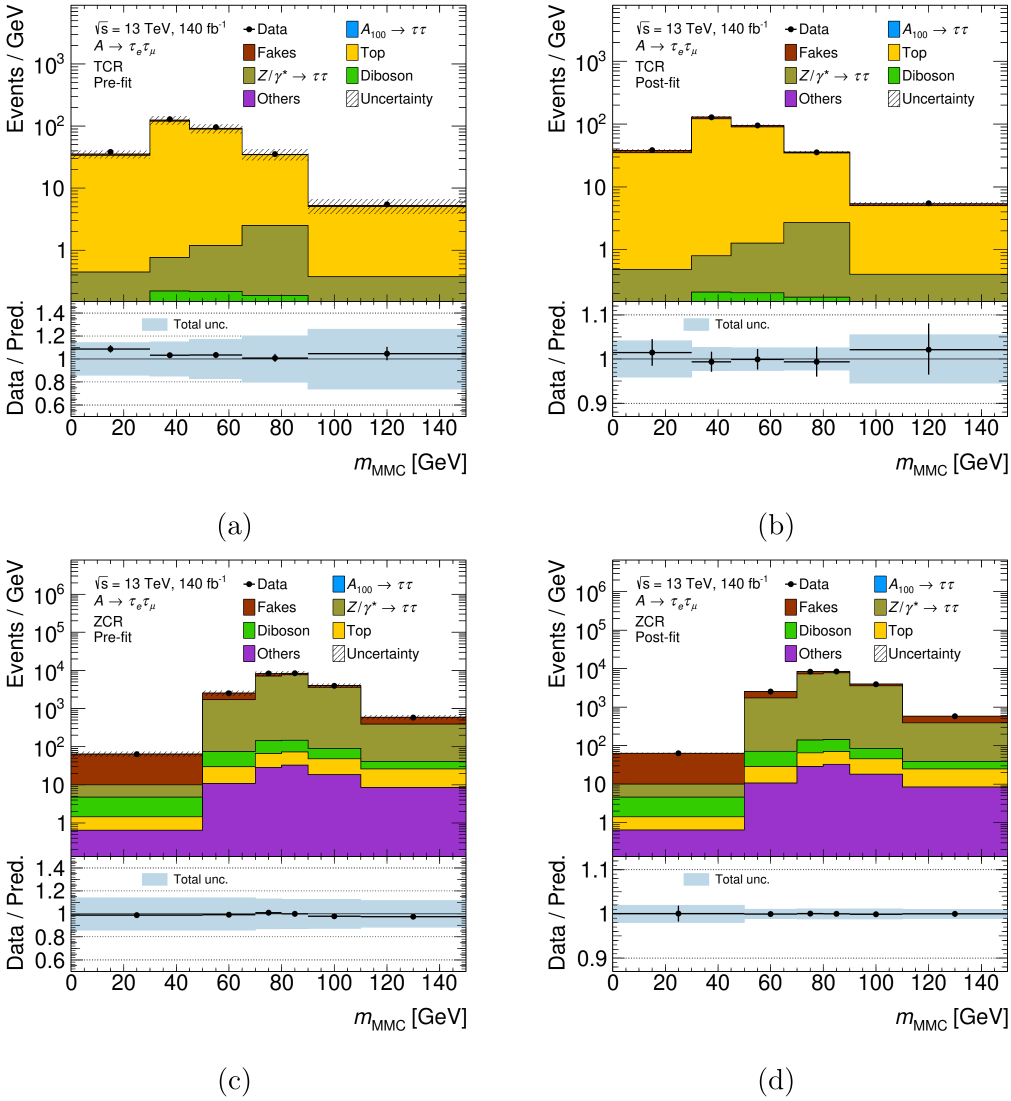

Figure D.3: Comparison of the pre-fit and the post-fit m_{MMC} distributions in the CRs for the $m_{\mathrm{A}} = 100\,\mathrm{GeV}$ signal mass. Shown are (a) the pre-fit distribution in the TCR, (b) the post-fit distribution in the TCR, (c) the pre-fit distribution in the ZCR and (d) the post-fit distribution in the ZCR. The pre-fit signal cross-section is defined to be 1 pb, while the fit result is used for the post-fit distributions. The processes $Z/\gamma^* \to \ell^+\ell^-$ and SM Higgs production are summarized to the 'Others' background. Events with values beyond the x-axis range are shown in the last bin of each distribution. The blue band in the ratio plot shows the total uncertainty of the background estimate.

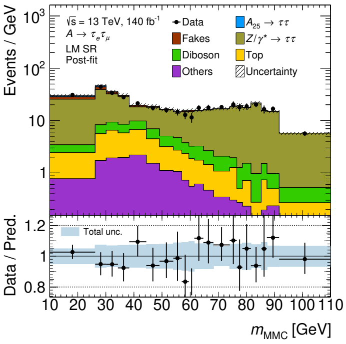

(a)

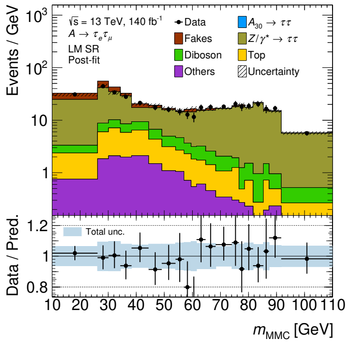

(b)

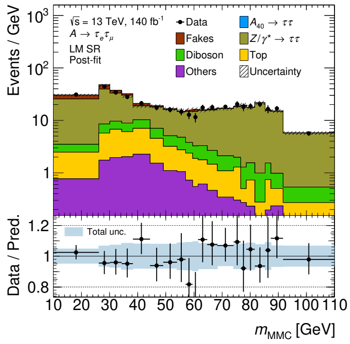

(c)

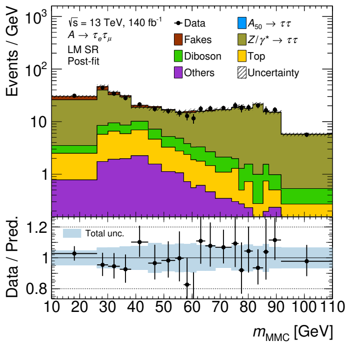

(d)

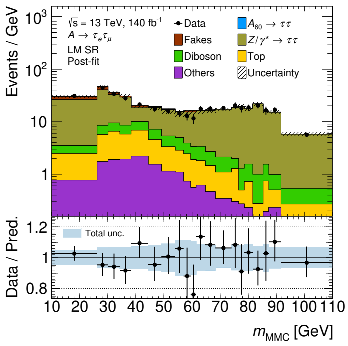

(e)

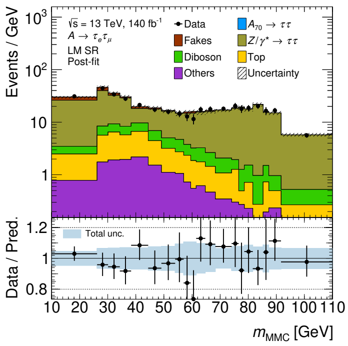

(f)

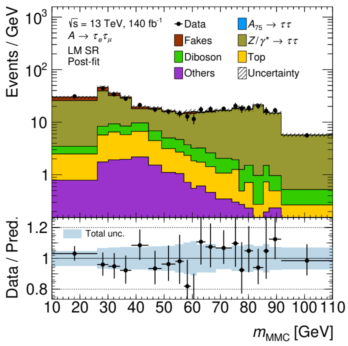

(g)

Figure D.4: Post-fit m_{MMC} distributions in the LMSR for the signal masses (a) $m_A = 25\,\mathrm{GeV}$, (b) $m_A = 30\,\mathrm{GeV}$, (c) $m_A = 40\,\mathrm{GeV}$, (d) $m_A = 50\,\mathrm{GeV}$, (e) $m_A = 60\,\mathrm{GeV}$, (f) $m_A = 70\,\mathrm{GeV}$ and (g) $m_A = 75\,\mathrm{GeV}$. The signal-plus-background hypothesis is used for the fits with the respective m_A. The processes $Z/\gamma^* \to \ell^+\ell^-$ and SM Higgs production are summarized to the 'Others' background. Events with values beyond the x-axis range are shown in the last bin of each distribution. The blue band in the ratio plot shows the total uncertainty of the background estimate.

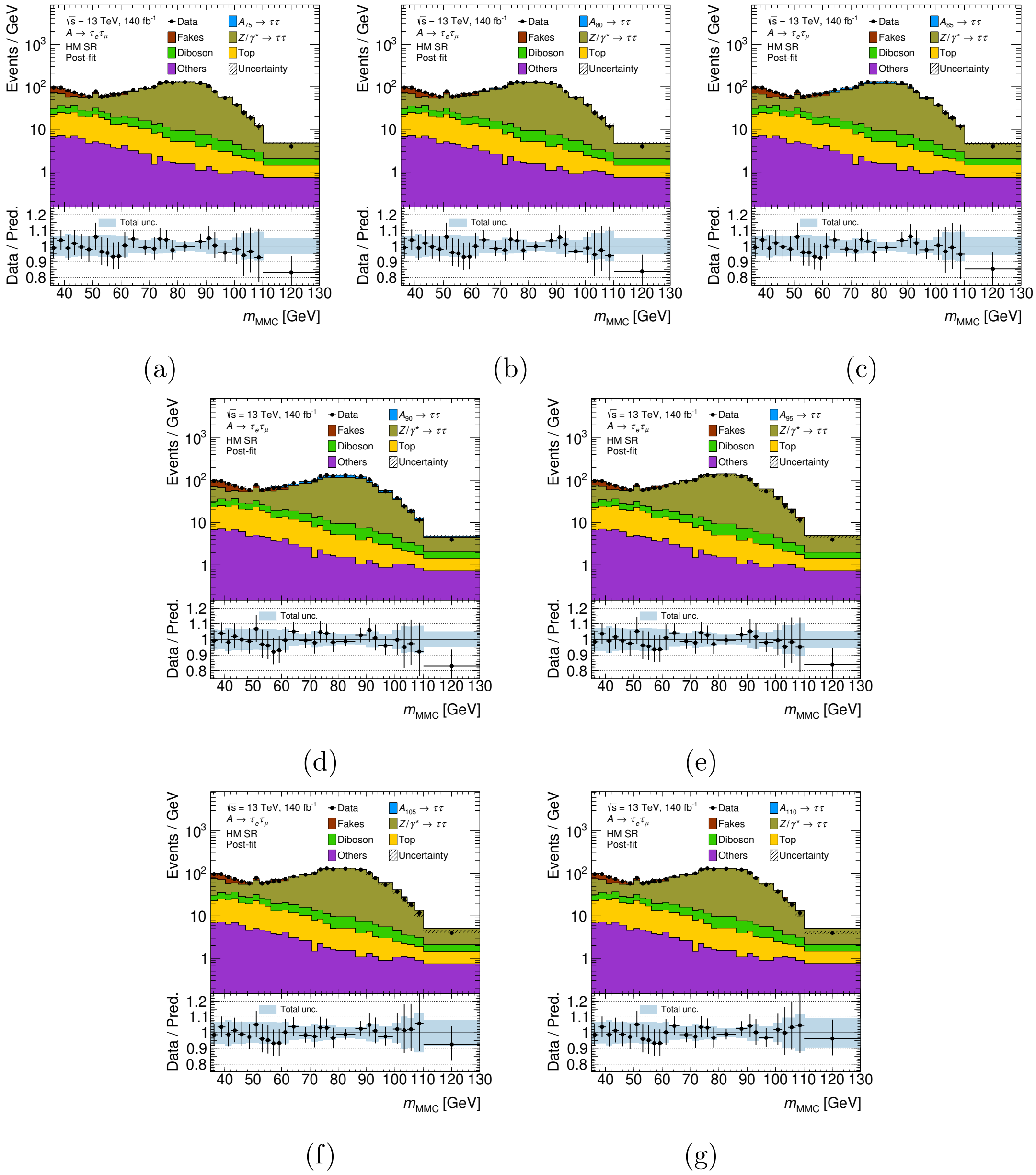

Figure D.5: Post-fit m_{MMC} distributions in the HMSR for the signal masses (a) $m_A = 75\,\mathrm{GeV}$, (b) $m_A = 80\,\mathrm{GeV}$, (c) $m_A = 85\,\mathrm{GeV}$, (d) $m_A = 90\,\mathrm{GeV}$, (e) $m_A = 95\,\mathrm{GeV}$, (f) $m_A = 105\,\mathrm{GeV}$ and (g) $m_A = 110\,\mathrm{GeV}$. The signal-plus-background hypothesis is used for the fits with the respective m_A. The processes $Z/\gamma^* \to \ell^+\ell^-$ and SM Higgs production are summarized to the 'Others' background. Events with values beyond the x-axis range are shown in the last bin of each distribution. The blue band in the ratio plot shows the total uncertainty of the background estimate.

D.3.2 Relative impact of systematics

Table D.6: Relative contributions to the uncertainty of the extracted signal strength μ from the likelihood fit to the data for the hypothesis $m_A = 25\,\text{GeV}$ and $m_A = 30\,\text{GeV}$. The contributions are calculated by fixing the relevant NPs to their post-fit values in the likelihood fit. The relative impact is obtained as the square-root of the difference of the squares of the nominal uncertainty and the obtained uncertainty, then dividing by the nominal uncertainty. The total uncertainty differs from the sum of all squared individual uncertainties due to correlations between uncertainties. The impact of data statistical uncertainties is determined by fitting with all NPs fixed to their post-fit values. The background statistical uncertainty includes the uncertainties from background MC statistics as well as the statistical uncertainty from the fake-lepton background determination. NP groups are only listed if they have a relative impact larger than 5%.

$m_A = 25\,\text{GeV}$		$m_A = 30\,\text{GeV}$	
Category	Relative contribution to $\Delta\mu$	Category	Relative contribution to $\Delta\mu$
Data statistical	33%	**Data statistical**	34%
Systematic	94%	**Systematic**	94%
Background statistical	71%	Background statistical	80%
Fake-lepton statistical	53%	*Fake-lepton statistical*	64%
$Z \to \tau\tau$ *statistical*	47%	$Z \to \tau\tau$ *statistical*	47%
Other background stat.	6%	*Other background stat.*	7%
Fake-lepton systematic	67%	Fake-lepton systematic	69%
Diboson modeling	10%	Signal modeling	6%
$Z \to \tau\tau$ modeling	9%		
Flavor tagging	8%		
$E_{\mathrm{T}}^{\mathrm{miss}}$	7%		
Muon efficiencies	6%		

Table D.7: Relative contributions to the uncertainty of the extracted signal strength μ from the likelihood fit to the data for the hypothesis $m_A = 40\,\mathrm{GeV}$ and $m_A = 50\,\mathrm{GeV}$. The contributions are calculated by fixing the relevant NPs to their post-fit values in the likelihood fit. The relative impact is obtained as the square-root of the difference of the squares of the nominal uncertainty and the obtained uncertainty, then dividing by the nominal uncertainty. The total uncertainty differs from the sum of all squared individual uncertainties due to correlations between uncertainties. The impact of data statistical uncertainties is determined by fitting with all NPs fixed to their post-fit values. The background statistical uncertainty includes the uncertainties from background MC statistics as well as the statistical uncertainty from the fake-lepton background determination. NP groups are only listed if they have a relative impact larger than 5%.

$m_A = 40\,\mathrm{GeV}$		$m_A = 50\,\mathrm{GeV}$	
Category	Relative contribution to $\Delta\mu$	Category	Relative contribution to $\Delta\mu$
Data statistical	51%	**Data statistical**	58%
Systematic	86%	**Systematic**	81%
Background statistical	76%	Background statistical	69%
$Z \to \tau\tau$ statistical	56%	*$Z \to \tau\tau$ statistical*	55%
Fake-lepton statistical	51%	*Fake-lepton statistical*	39%
Other background stat.	9%	*Other background stat.*	13%
Fake-lepton systematic	40%	Diboson modeling	23%
Flavor tagging	19%	Flavor tagging	22%
Diboson modeling	16%	Fake-lepton systematic	17%
$Z \to \tau\tau$ and $t\bar{t}$ norm.	9%	$Z \to \tau\tau$ and $t\bar{t}$ norm.	10%
Signal statistical	7%	$E_{\mathrm{T}}^{\mathrm{miss}}$	9%
Diboson cross-section	6%	$Z \to \tau\tau$ modeling	9%
$Z \to \tau\tau$ modeling	6%	Diboson cross-section	8%
		Signal statistical	7%

Table D.8: Relative contributions to the uncertainty of the extracted signal strength μ from the likelihood fit to the data for the hypothesis $m_A = 60\,\mathrm{GeV}$ and $m_A = 70\,\mathrm{GeV}$. The contributions are calculated by fixing the relevant NPs to their post-fit values in the likelihood fit. The relative impact is obtained as the square-root of the difference of the squares of the nominal uncertainty and the obtained uncertainty, then dividing by the nominal uncertainty. The total uncertainty differs from the sum of all squared individual uncertainties due to correlations between uncertainties. The impact of data statistical uncertainties is determined by fitting with all NPs fixed to their post-fit values. The background statistical uncertainty includes the uncertainties from background MC statistics as well as the statistical uncertainty from the fake-lepton background determination. NP groups are only listed if they have a relative impact larger than 5%.

$m_A = 60\,\mathrm{GeV}$		$m_A = 70\,\mathrm{GeV}$	
Category	Relative contribution to $\Delta\mu$	Category	Relative contribution to $\Delta\mu$
Data statistical	62%	**Data statistical**	57%
Systematic	79%	**Systematic**	82%
Background statistical	60%	Background statistical	56%
$Z \to \tau\tau$ statistical	48%	*$Z \to \tau\tau$ statistical*	44%
Fake-lepton statistical	33%	*Fake-lepton statistical*	33%
Other background stat.	13%	*Other background stat.*	10%
Diboson modeling	21%	$E_{\mathrm{T}}^{\mathrm{miss}}$	25%
$E_{\mathrm{T}}^{\mathrm{miss}}$	16%	Fake-lepton systematic	23%
Flavor tagging	16%	$Z \to \tau\tau$ modeling	16%
$Z \to \tau\tau$ modeling	13%	Signal statistical	16%
Signal statistical	11%	Diboson modeling	12%
Fake-lepton systematic	9%	$Z \to \tau\tau$ reweighting	11%
Diboson cross-section	8%	Flavor tagging	8%
$Z \to \tau\tau$ and $t\bar{t}$ norm.	7%	Electron calibration	6%
Pile-up	5%	$Z \to \tau\tau$ and $t\bar{t}$ norm.	6%
$Z \to \tau\tau$ reweighting	5%		

Table D.9: Relative contributions to the uncertainty of the extracted signal strength μ from the likelihood fit to the data for the hypothesis $m_A = 75\,\text{GeV}$ (LMSR) and $m_A = 75\,\text{GeV}$ (HMSR). The contributions are calculated by fixing the relevant NPs to their post-fit values in the likelihood fit. The relative impact is obtained as the square-root of the difference of the squares of the nominal uncertainty and the obtained uncertainty, then dividing by the nominal uncertainty. The total uncertainty differs from the sum of all squared individual uncertainties due to correlations between uncertainties. The impact of data statistical uncertainties is determined by fitting with all NPs fixed to their post-fit values. The background statistical uncertainty includes the uncertainties from background MC statistics as well as the statistical uncertainty from the fake-lepton background determination. NP groups are only listed if they have a relative impact larger than 5%.

$m_A = 75\,\text{GeV}$ (LMSR)		$m_A = 75\,\text{GeV}$ (HMSR)	
Category	Relative contribution to $\Delta\mu$	Category	Relative contribution to $\Delta\mu$
Data statistical	47%	**Data statistical**	44%
Systematic	88%	**Systematic**	90%
Background statistical	56%	Background statistical	66%
$Z \to \tau\tau$ statistical	43%	*Fake-lepton statistical*	50%
Fake-lepton statistical	35%	*$Z \to \tau\tau$ statistical*	42%
Other background stat.	8%	*Other background stat.*	8%
Fake-lepton systematic	34%	Flavor tagging	16%
$E_{\text{T}}^{\text{miss}}$	28%	$Z \to \tau\tau$ modeling	15%
$Z \to \tau\tau$ modeling	21%	Muon efficiencies	14%
$Z \to \tau\tau$ reweighting	17%	Fake-lepton systematic	11%
Signal statistical	16%	Diboson modeling	10%
Diboson modeling	10%	Signal statistical	8%
$Z \to \tau\tau$ and $t\bar{t}$ norm.	8%	Muon calibration	7%
Flavor tagging	6%	$Z \to \tau\tau$ reweighting	6%
Electron calibration	6%		

Table D.10: Relative contributions to the uncertainty of the extracted signal strength μ from the likelihood fit to the data for the hypothesis $m_A = 80\,\text{GeV}$ and $m_A = 85\,\text{GeV}$. The contributions are calculated by fixing the relevant NPs to their post-fit values in the likelihood fit. The relative impact is obtained as the square-root of the difference of the squares of the nominal uncertainty and the obtained uncertainty, then dividing by the nominal uncertainty. The total uncertainty differs from the sum of all squared individual uncertainties due to correlations between uncertainties. The impact of data statistical uncertainties is determined by fitting with all NPs fixed to their post-fit values. The background statistical uncertainty includes the uncertainties from background MC statistics as well as the statistical uncertainty from the fake-lepton background determination. NP groups are only listed if they have a relative impact larger than 5%.

$m_A = 80\,\text{GeV}$		$m_A = 85\,\text{GeV}$	
Category	Relative contribution to $\Delta\mu$	Category	Relative contribution to $\Delta\mu$
Data statistical	35%	**Data statistical**	24%
Systematic	94%	**Systematic**	97%
Background statistical	63%	Background statistical	58%
Fake-lepton statistical	46%	*Fake-lepton statistical*	42%
$Z \to \tau\tau$ *statistical*	42%	$Z \to \tau\tau$ *statistical*	39%
Other background stat.	7%	*Other background stat.*	7%
$Z \to \tau\tau$ modeling	20%	$Z \to \tau\tau$ reweighting	28%
Fake-lepton systematic	15%	$Z \to \tau\tau$ modeling	27%
Signal statistical	14%	Fake-lepton systematic	25%
Muon efficiencies	14%	Signal statistical	19%
$Z \to \tau\tau$ reweighting	13%	Muon calibration	12%
Flavor tagging	12%	Muon efficiencies	11%
Muon calibration	8%	$Z \to \tau\tau$ and $t\bar{t}$ norm.	11%
Electron calibration	8%	Electron calibration	10%
$E_{\mathrm{T}}^{\mathrm{miss}}$	7%	$t\bar{t}$ modeling	6%
Diboson modeling	6%	$E_{\mathrm{T}}^{\mathrm{miss}}$	5%

Table D.11: Relative contributions to the uncertainty of the extracted signal strength μ from the likelihood fit to the data for the hypothesis $m_A = 90\,\text{GeV}$ and $m_A = 95\,\text{GeV}$. The contributions are calculated by fixing the relevant NPs to their post-fit values in the likelihood fit. The relative impact is obtained as the square-root of the difference of the squares of the nominal uncertainty and the obtained uncertainty, then dividing by the nominal uncertainty. The total uncertainty differs from the sum of all squared individual uncertainties due to correlations between uncertainties. The impact of data statistical uncertainties is determined by fitting with all NPs fixed to their post-fit values. The background statistical uncertainty includes the uncertainties from background MC statistics as well as the statistical uncertainty from the fake-lepton background determination. NP groups are only listed if they have a relative impact larger than 5%.

$m_A = 90\,\text{GeV}$		$m_A = 95\,\text{GeV}$	
Category	Relative contribution to $\Delta\mu$	Category	Relative contribution to $\Delta\mu$
Data statistical	10%	**Data statistical**	21%
Systematic	99%	**Systematic**	99%
Background statistical	67%	Background statistical	61%
$Z \to \tau\tau$ statistical	48%	*Fake-lepton statistical*	43%
Fake-lepton statistical	47%	*$Z \to \tau\tau$ statistical*	43%
Other background stat.	8%	*Other background stat.*	6%
$Z \to \tau\tau$ reweighting	55%	Fake-lepton systematic	39%
Signal statistical	51%	$Z \to \tau\tau$ modeling	39%
Fake-lepton systematic	47%	$Z \to \tau\tau$ reweighting	32%
$Z \to \tau\tau$ modeling	45%	Signal statistical	29%
$Z \to \tau\tau$ and $t\bar{t}$ norm.	33%	$Z \to \tau\tau$ and $t\bar{t}$ norm.	26%
$t\bar{t}$ modeling	14%	Muon calibration	16%
Flavor tagging	14%	Flavor tagging	14%
Muon calibration	13%	Muon efficiencies	14%
$E_{\mathrm{T}}^{\mathrm{miss}}$	9%	Electron calibration	12%
Diboson modeling	6%	$t\bar{t}$ modeling	7%
Electron calibration	6%	Pile-up	7%

Table D.12: Relative contributions to the uncertainty of the extracted signal strength μ from the likelihood fit to the data for the hypothesis $m_A = 105\,\text{GeV}$ and $m_A = 110\,\text{GeV}$. The contributions are calculated by fixing the relevant NPs to their post-fit values in the likelihood fit. The relative impact is obtained as the square-root of the difference of the squares of the nominal uncertainty and the obtained uncertainty, then dividing by the nominal uncertainty. The total uncertainty differs from the sum of all squared individual uncertainties due to correlations between uncertainties. The impact of data statistical uncertainties is determined by fitting with all NPs fixed to their post-fit values. The background statistical uncertainty includes the uncertainties from background MC statistics as well as the statistical uncertainty from the fake-lepton background determination. NP groups are only listed if they have a relative impact larger than 5%.

$m_A = 105\,\text{GeV}$		$m_A = 110\,\text{GeV}$	
Category	Relative contribution to $\Delta\mu$	Category	Relative contribution to $\Delta\mu$
Data statistical	44%	**Data statistical**	57%
Systematic	90%	**Systematic**	82%
Background statistical	55%	Background statistical	53%
$Z \to \tau\tau$ statistical	44%	*$Z \to \tau\tau$ statistical*	43%
Fake-lepton statistical	31%	*Fake-lepton statistical*	29%
Other background stat.	10%	*Other background stat.*	12%
$Z \to \tau\tau$ modeling	30%	$Z \to \tau\tau$ modeling	20%
Muon calibration	20%	Muon calibration	18%
Fake-lepton systematic	14%	Diboson modeling	14%
Signal statistical	14%	Fake-lepton systematic	14%
Diboson modeling	10%	Signal statistical	13%
Muon efficiencies	8%	Signal modeling	8%
Electron calibration	7%	$t\bar{t}$ modeling	7%
$t\bar{t}$ modeling	6%	Muon efficiencies	7%
Signal modeling	5%	Flavor tagging	5%

D.3.3 Ranking of systematics for additional mass points

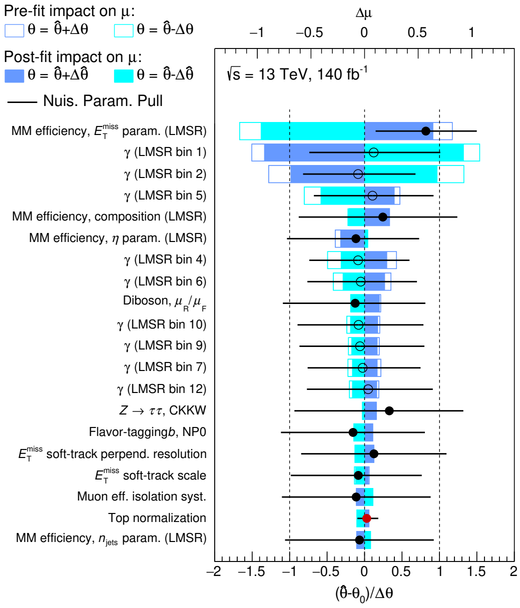

(a)

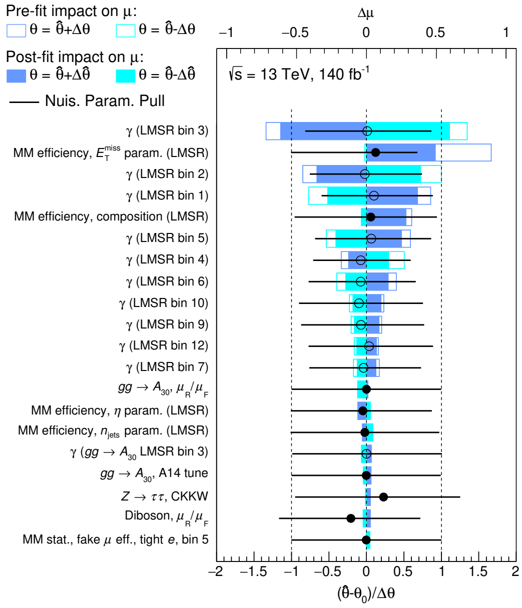

(b)

Figure D.6: Ranking of systematic uncertainties based on their post-fit impact on the signal strength μ in the model-independent fit. The 20 NPs with the highest impact are displayed in the LMSR for (a) the $m_A = 25\,\text{GeV}$ signal and (b) the $m_A = 30\,\text{GeV}$ signal. The top axis measures the pre- and post-fit impact $\Delta\mu$ of each NP, while the bottom axis parametrizes the NP pulls and constraints of each NP in standard deviations $\Delta\theta$ of its pre-fit value θ_0. The pre-fit (post-fit) impact of a NP is determined as the difference between the fitted μ value in the nominal fit and a fit when fixing the NP to $\hat{\theta} \pm \Delta\theta$ ($\hat{\theta} \pm \Delta\hat{\theta}$), with $\hat{\theta}$ being the best-fit value of the NP and $\Delta\theta$ ($\Delta\hat{\theta}$) representing its pre-fit (post-fit) uncertainty.

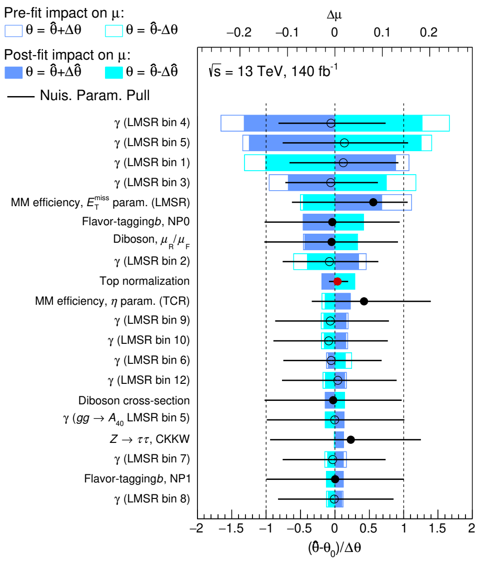

(a)

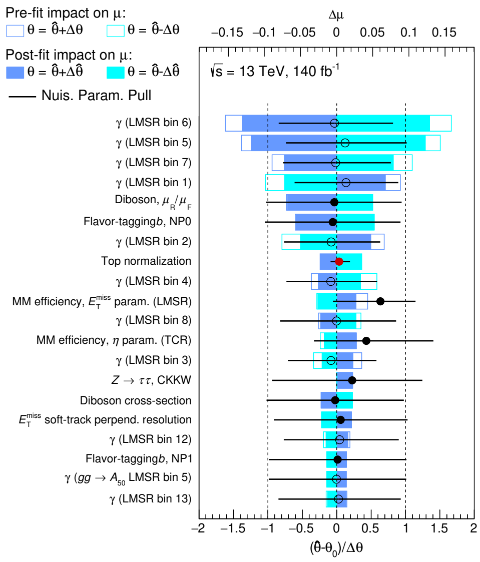

(b)

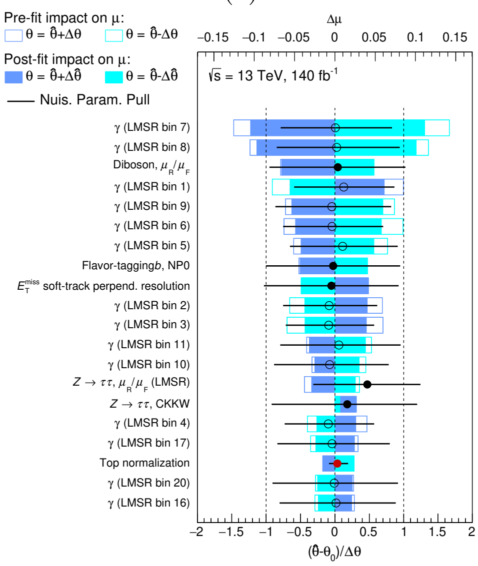

(c)

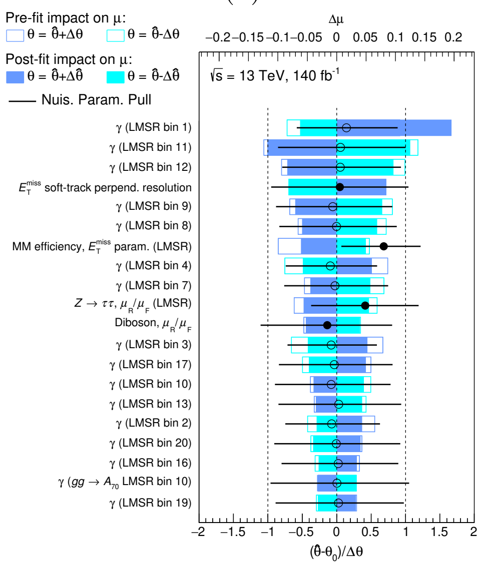

(d)

Figure D.7: Ranking of systematic uncertainties based on their post-fit impact on the signal strength μ in the model-independent fit. The 20 NPs with the highest impact are displayed in the LMSR for (a) the $m_A = 40\,\text{GeV}$ signal, (b) the $m_A = 50\,\text{GeV}$ signal, (c) the $m_A = 60\,\text{GeV}$ signal and (d) the $m_A = 70\,\text{GeV}$ signal. The top axis measures the pre- and post-fit impact $\Delta\mu$ of each NP, while the bottom axis parametrizes the NP pulls and constraints of each NP in standard deviations $\Delta\theta$ of its pre-fit value θ_0. The pre-fit (post-fit) impact of a NP is determined as the difference between the fitted μ value in the nominal fit and a fit when fixing the NP to $\hat{\theta} \pm \Delta\theta$ ($\hat{\theta} \pm \Delta\hat{\theta}$), with $\hat{\theta}$ being the best-fit value of the NP and $\Delta\theta$ ($\Delta\hat{\theta}$) representing its pre-fit (post-fit) uncertainty.

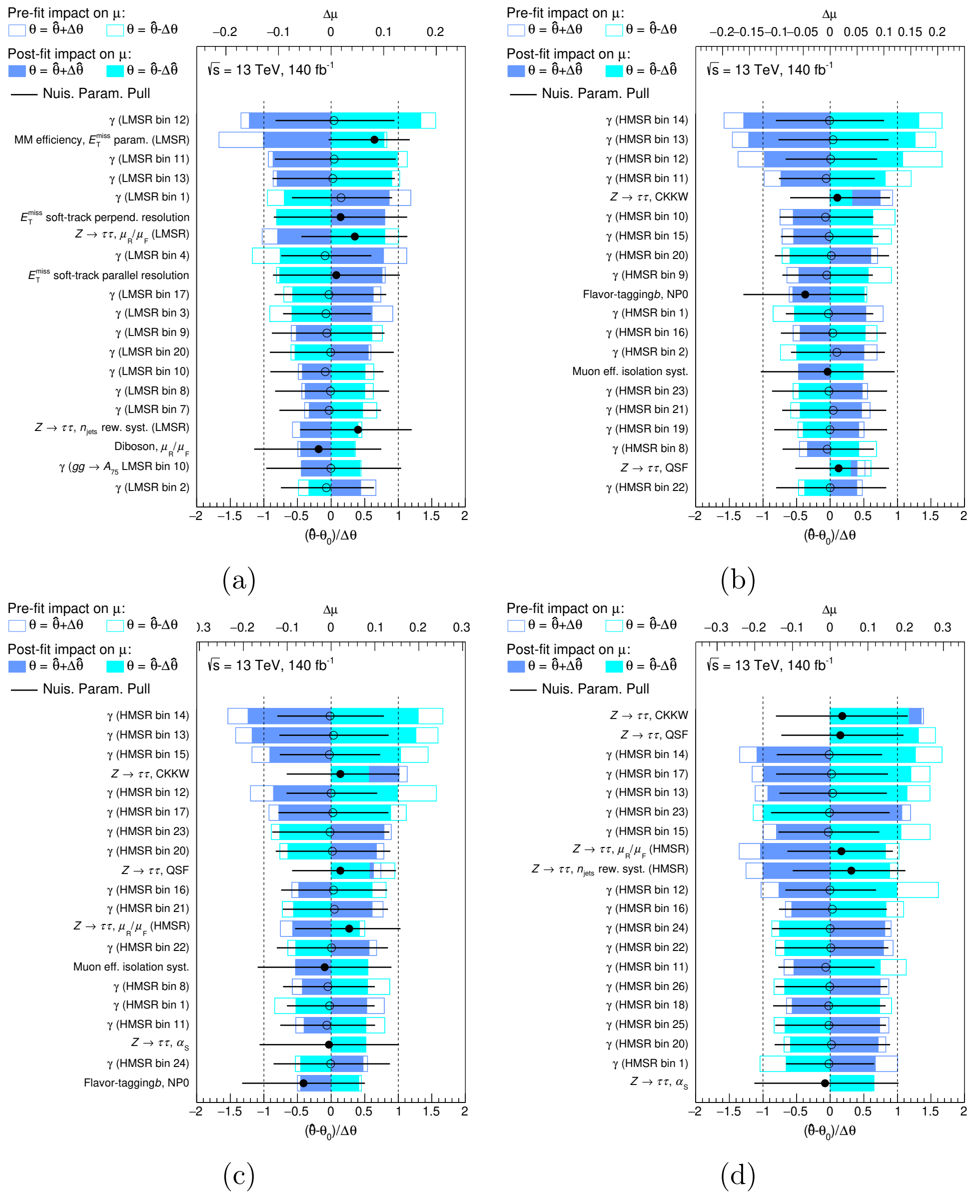

Figure D.8: Ranking of systematic uncertainties based on their post-fit impact on the signal strength μ in the model-independent fit. The 20 NPs with the highest impact are displayed in (a) the LMSR for the $m_A = 75\,\text{GeV}$ signal, and in the HMSR for (b) the $m_A = 75\,\text{GeV}$ signal, (c) the $m_A = 80\,\text{GeV}$ signal and (d) the $m_A = 85\,\text{GeV}$ signal. The top axis measures the pre- and post-fit impact $\Delta\mu$ of each NP, while the bottom axis parametrizes the NP pulls and constraints of each NP in standard deviations $\Delta\theta$ of its pre-fit value θ_0. The pre-fit (post-fit) impact of a NP is determined as the difference between the fitted μ value in the nominal fit and a fit when fixing the NP to $\hat{\theta} \pm \Delta\theta$ ($\hat{\theta} \pm \Delta\hat{\theta}$), with $\hat{\theta}$ being the best-fit value of the NP and $\Delta\theta$ ($\Delta\hat{\theta}$) representing its pre-fit (post-fit) uncertainty.

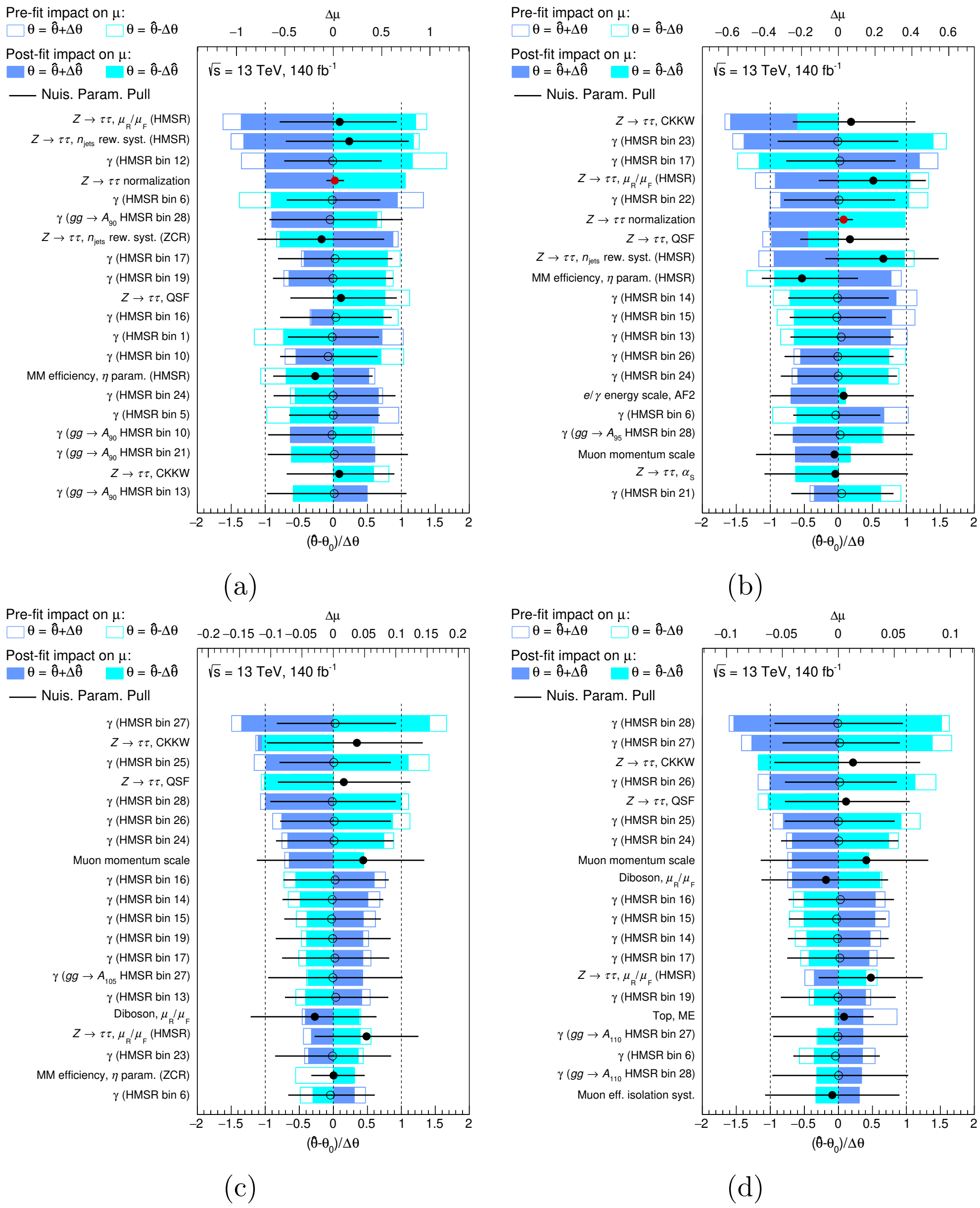

Figure D.9: Ranking of systematic uncertainties based on their post-fit impact on the signal strength μ in the model-independent fit. The 20 NPs with the highest impact are displayed in the HMSR for (a) the $m_A = 90\,\text{GeV}$ signal (b) the $m_A = 95\,\text{GeV}$ signal, (c) the $m_A = 105\,\text{GeV}$ signal and (d) the $m_A = 110\,\text{GeV}$ signal. The top axis measures the pre- and post-fit impact $\Delta\mu$ of each NP, while the bottom axis parametrizes the NP pulls and constraints of each NP in standard deviations $\Delta\theta$ of its pre-fit value θ_0. The pre-fit (post-fit) impact of a NP is determined as the difference between the fitted μ value in the nominal fit and a fit when fixing the NP to $\hat{\theta} \pm \Delta\theta$ ($\hat{\theta} \pm \Delta\hat{\theta}$), with $\hat{\theta}$ being the best-fit value of the NP and $\Delta\theta$ ($\Delta\hat{\theta}$) representing its pre-fit (post-fit) uncertainty.

D.3.4 Ranking of systematics for additional mass points in the model-dependent fit

The ranking plots for the model-dependent fit are very similar to the ones from the model-independent fit in Section D.3.3. Here are only the mass points listed, for which the additional signal cross-section NP appears under the top 20: $m_A =$ 25 and 30 GeV in Figure D.10 and $m_A = 40, 50, 60$ and 105 GeV in Figure D.11. For the mass points $m_A = 70, 75, 80, 85, 90$ and 95 GeV, the top 20 of the NP ranking is identical with the rankings of the model-independent fit in Section D.3.3.

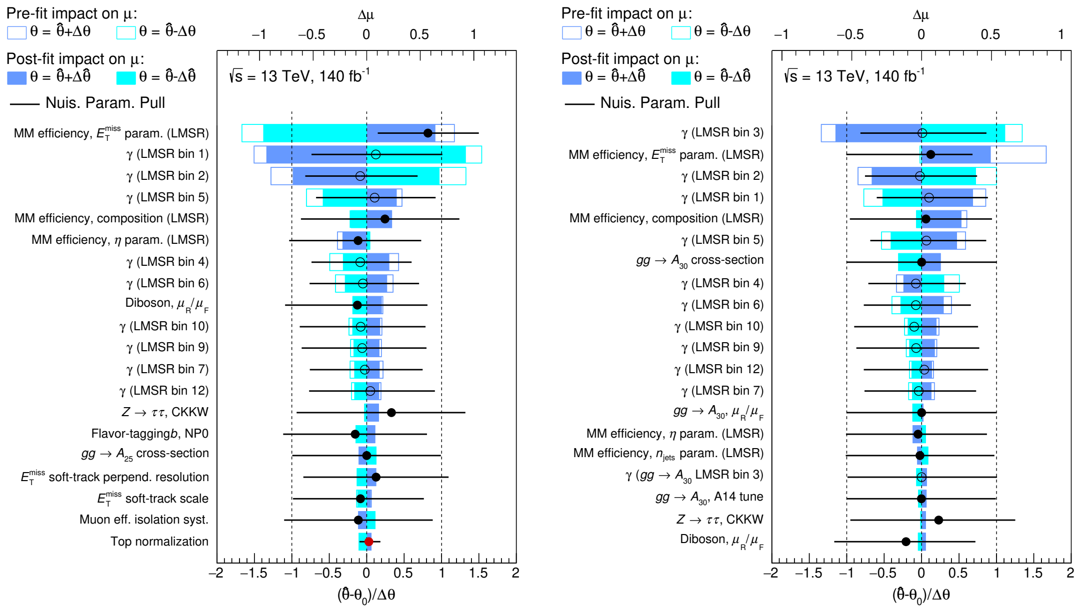

(a) (b)

Figure D.10: Ranking of systematic uncertainties based on their post-fit impact on the signal strength μ in the model-dependent fit. The 20 NPs with the highest impact are displayed in the LMSR for (a) the $m_A = 25$ GeV signal and (b) the $m_A = 30$ GeV signal. The top axis measures the pre- and post-fit impact $\Delta\mu$ of each NP, while the bottom axis parametrizes the NP pulls and constraints of each NP in standard deviations $\Delta\theta$ of its pre-fit value θ_0. The pre-fit (post-fit) impact of a NP is determined as the difference between the fitted μ value in the nominal fit and a fit when fixing the NP to $\hat{\theta} \pm \Delta\theta$ ($\hat{\theta} \pm \Delta\hat{\theta}$), with $\hat{\theta}$ being the best-fit value of the NP and $\Delta\theta$ ($\Delta\hat{\theta}$) representing its pre-fit (post-fit) uncertainty.

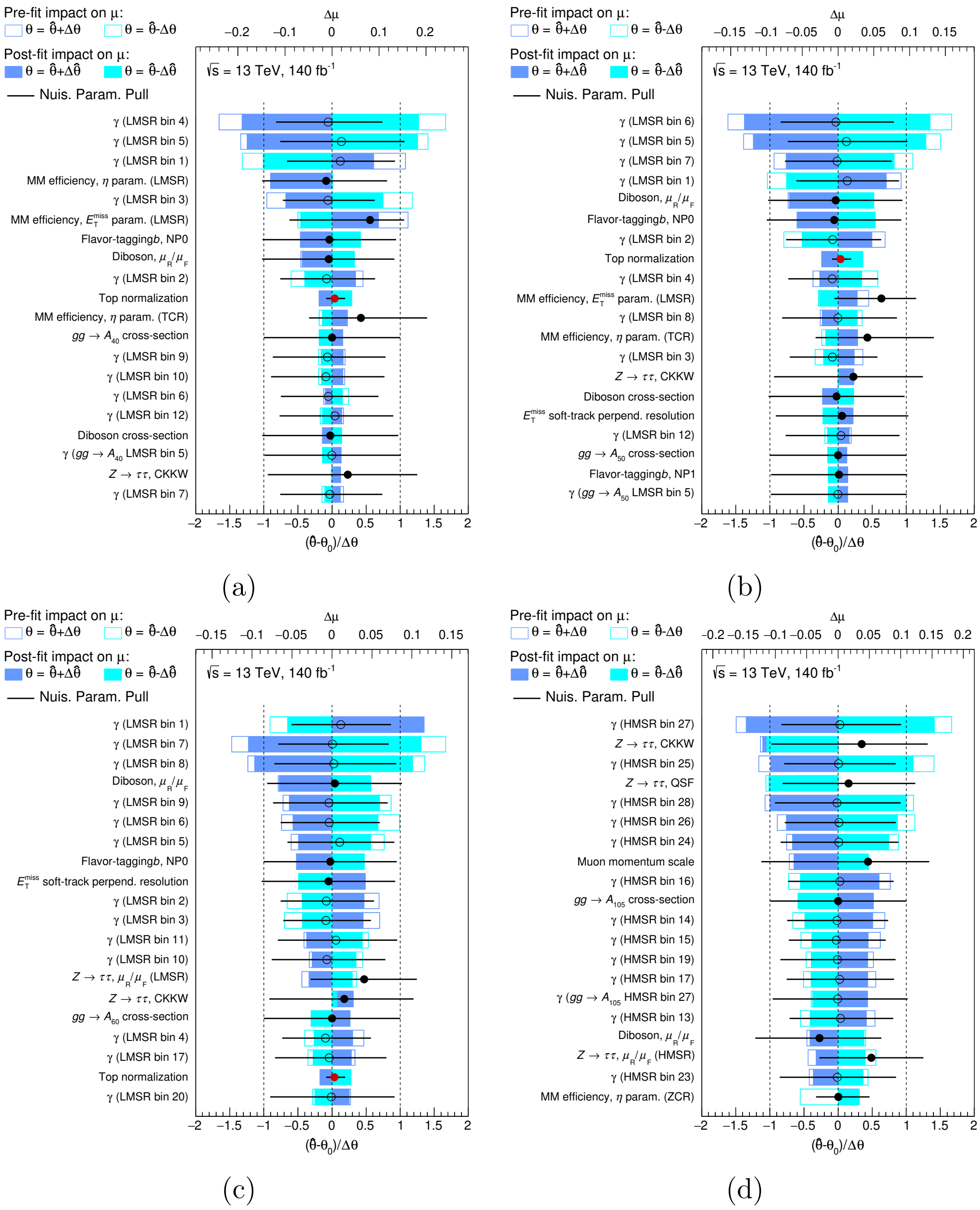

Figure D.11: Ranking of systematic uncertainties based on their post-fit impact on the signal strength μ in the model-independent fit. The 20 NPs with the highest impact are displayed in the LMSR for (a) the $m_A = 40\,\text{GeV}$ signal, (b) the $m_A = 50\,\text{GeV}$ signal and (c) the $m_A = 60\,\text{GeV}$ signal, and (d) in the HMSR for the $m_A = 105\,\text{GeV}$ signal. The top axis measures the pre- and post-fit impact $\Delta\mu$ of each NP, while the bottom axis parametrizes the NP pulls and constraints of each NP in standard deviations $\Delta\theta$ of its pre-fit value θ_0. The pre-fit (post-fit) impact of a NP is determined as the difference between the fitted μ value in the nominal fit and a fit when fixing the NP to $\hat{\theta} \pm \Delta\theta$ ($\hat{\theta} \pm \Delta\hat{\theta}$), with $\hat{\theta}$ being the best-fit value of the NP and $\Delta\theta$ ($\Delta\hat{\theta}$) representing its pre-fit (post-fit) uncertainty.

D.3.5 Correlation matrices for additional mass points

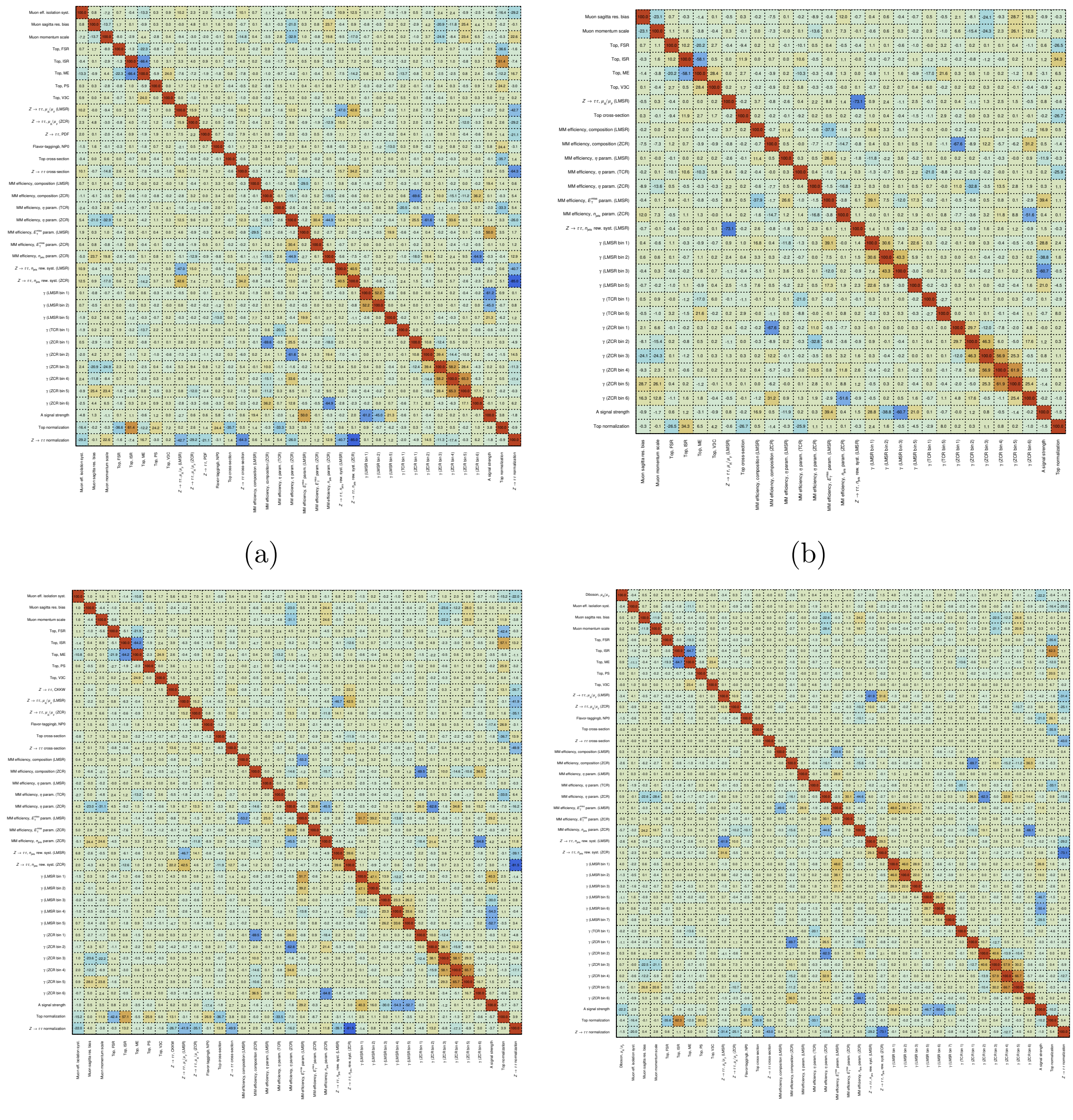

(a) (b) (c) (d)

Figure D.12: Correlation matrix for all NPs with a correlation > 20% of the fit to data. The considered signals from the LMSR are (a) $m_A = 25\,\text{GeV}$, (b) $m_A = 30\,\text{GeV}$, (c) $m_A = 40\,\text{GeV}$ and (d) $m_A = 50\,\text{GeV}$.

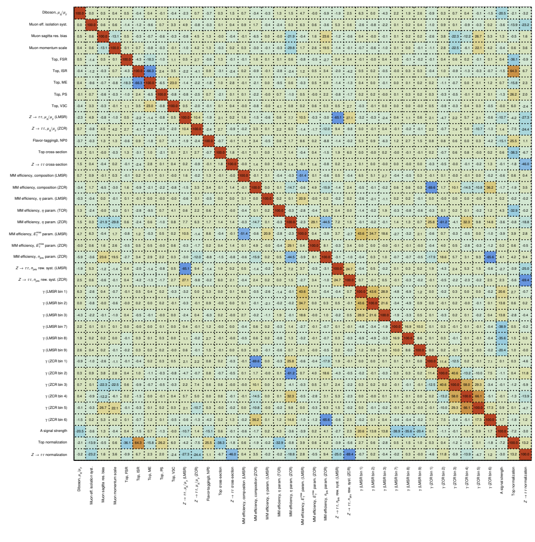

(a)

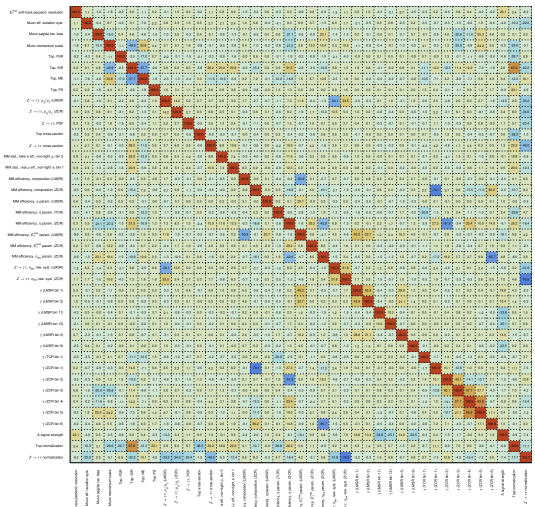

(b)

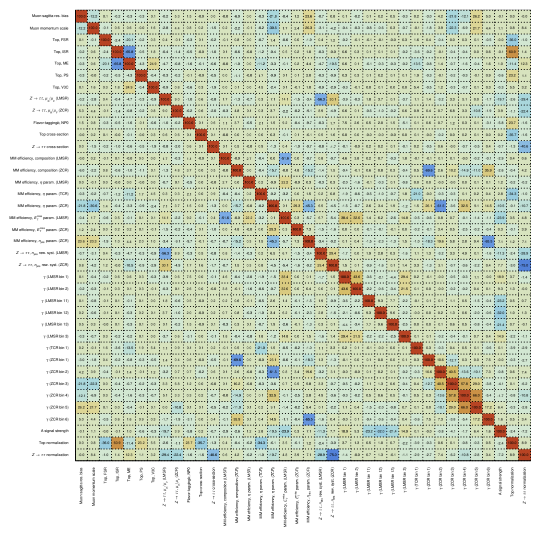

(c)

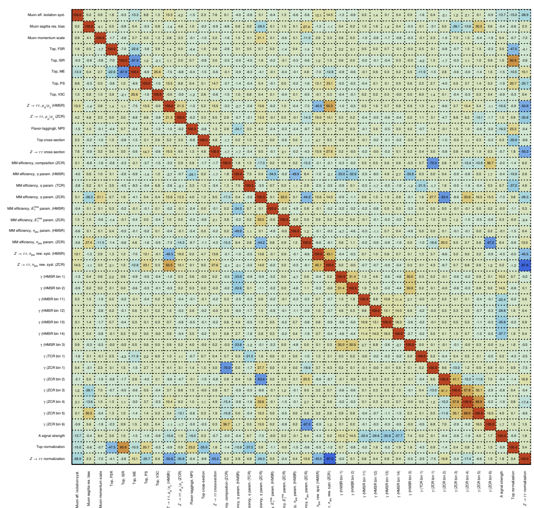

(d)

Figure D.13: Correlation matrix for all NPs with a correlation $> 20\%$ of the fit to data. The considered signals from the LMSR are (a) $m_A = 60\,\mathrm{GeV}$, (b) $m_A = 70\,\mathrm{GeV}$ and (c) $m_A = 75\,\mathrm{GeV}$, and from the HMSR (d) $m_A = 75\,\mathrm{GeV}$.

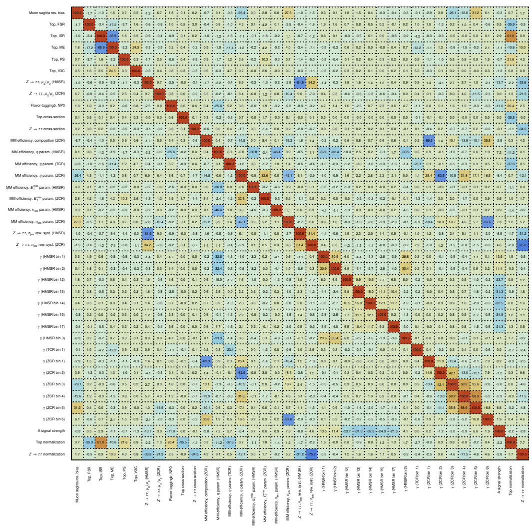

(a)

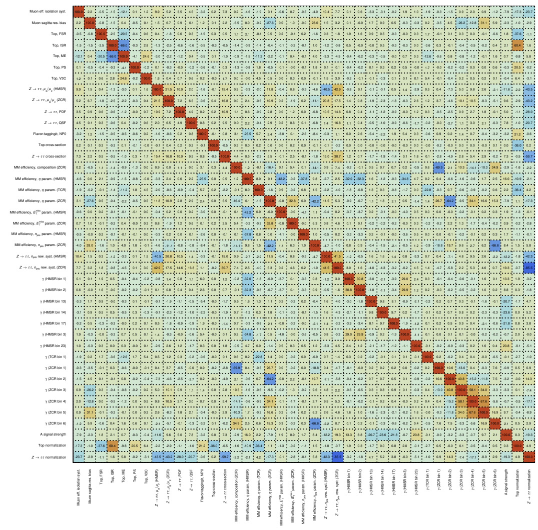

(b)

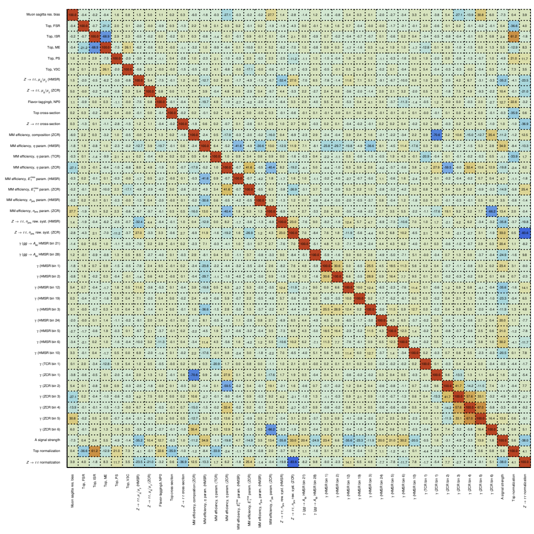

(c)

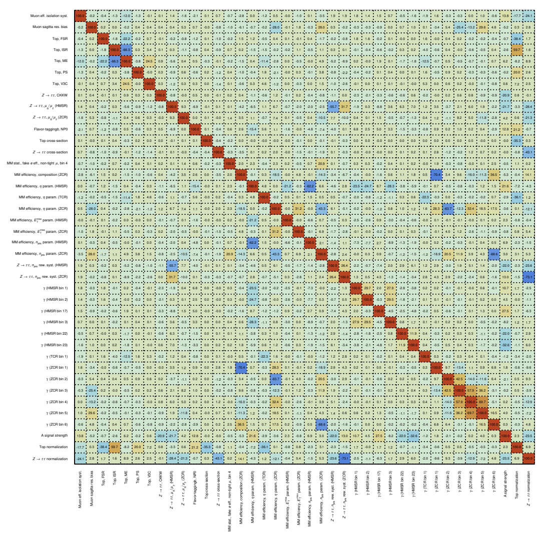

(d)

Figure D.14: Correlation matrix for all NPs with a correlation > 20% of the fit to data. The considered signals from the HMSR are (a) $m_A = 80\,\mathrm{GeV}$, (b) $m_A = 85\,\mathrm{GeV}$, (c) $m_A = 90\,\mathrm{GeV}$ and (d) $m_A = 95\,\mathrm{GeV}$.

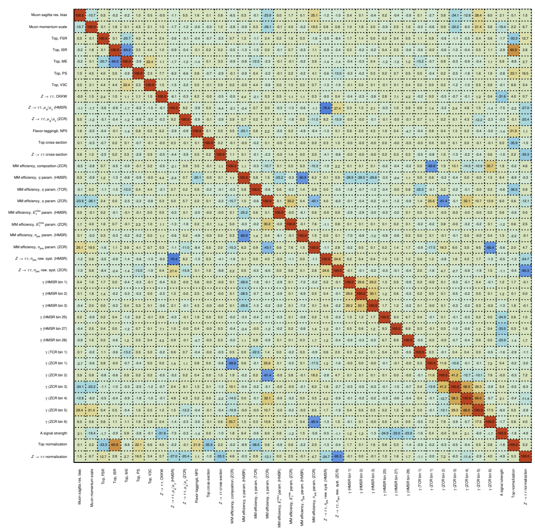

(a)

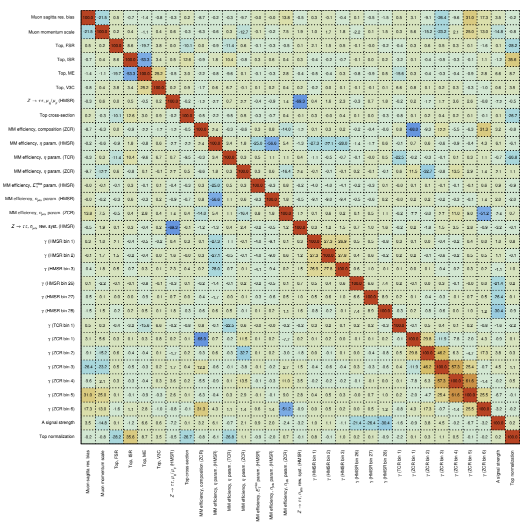

(b)

Figure D.15: Correlation matrix for all NPs with a correlation > 20% of the fit to data. The considered signals from the HMSR are (a) $m_A = 105\,\mathrm{GeV}$ and (b) $m_A = 110\,\mathrm{GeV}$.

List of Figures

List of Tables

Glossary

Notation	Description	Page List
2HDM	Two-Higgs-doublet model	1–3, 13–19, 73, 134, 140, 143, 231
AF2	ATLAS fast simulation II	149
AFP	ATLAS Forward Proton detector	35, 36
ALFA	Absolute Luminosity For ATLAS	35, 36
ALICE	A Large Ion Collider Experiment	24
ALTI	ATLAS Local Trigger Interface	2, 43–52, 144, 241
A-side	A-side of the ATLAS Detector, along the positive z-axis and in the direction of the airport	46, 47, 52
ATLAS	ATLAS detector at the LHC	1, 23, 25–27, 34–36, 38, 39
BC	Bunch crossing	45, 48, 49
BCR	Bunch counter reset	45
BNL	Brookhaven National Laboratory	17
BOOSTER	Proton Synchrotron Booster	23, 24
BUSY	Signal generated when the subdetector readout buffers are full	45, 49, 50
CALREQ	Signal issued by the subdetector to request generation of a calibration trigger	45
CB	Combined muon	56, 57
CDI	Calibration data interface	150
CERN	European Organisation for Nuclear Research	23, 24
CKKW	CKKW matrix element matching method developed by S. Catani, F. Krauss, R. Kuhn and B.R. Webber in Ref. [168]	8, 93, 94, 129, 195, 197

Notation	**Description**	**Page List**
CKM	Cabbibo–Kobayashi–Maskawa matrix	15
CL	Confidence level	90, 93, 120, 121, 132, 142, 200, 202, 203, 232
CMS	Compact Muon Solenoid	1, 20, 23
CP	Charge and Parity symmetry	12, 14, 17, 22
CPT	Charge, Parity and Time symmetry	12
CPU	Central Processing Unit	44
CR	Control region	67, 73, 85, 101, 102, 104, 122–126, 141, 142, 205, 206
CSC	Cathode Strip Chambers	35
C-side	C-side of the ATLAS Detector, along the negative z-axis and in the direction of Charly's Pub	46, 47, 52
CT	Calorimeter-tagged muon	57
CTP	Central Trigger Processor	2, 37, 43–45, 50, 144
DELPHI	Detector with Lepton, Photon and Hadron Identification	19
DSID	Dataset identifier	42
DT	Digital Trigger	43, 48, 50, 52, 144
DTA	Digital Trigger A-side	47
DTC	Digital Trigger C-side	47
ECAL	Electromagnetic calorimeter	29, 55, 56
ECR	Event counter reset	45
EM	Electromagnetic	29–31, 51, 52
EMB	Electromagnetic Barrel Calorimeter	30, 47
EMBA	Electromagnetic Barrel Calorimeter A-Side	47
EMBC	Electromagnetic Barrel Calorimeter C-Side	47
EMEC	Electromagnetic End-Cap Calorimeters	30, 48
EMECA	Electromagnetic End-Cap Calorimeters A-side	47
EMECC	Electromagnetic End-Cap Calorimeters C-side	47

Notation	**Description**	**Page List**
EMF	Electronics Maintenance Facility, test setup for the LAr detector	51, 241
EW	Electroweak	76, 77
FCal	Forward Calorimeter	29, 31, 48
FCNC	Flavor-changing neutral current	14, 15
FE	Front-end	37, 43–45
FEB	Front-end board	32, 50
FELIX	Front-End Link eXchange	44
FJVT	Forward-jet vertex tagger	58, 149
FPGA	Field programmable gate array	44
FSR	Final state radiation	40, 95–97
FVR	Fake-lepton validation region	67, 74, 81, 85, 93, 98–100, 103–106, 109, 122, 159–162, 165, 171, 191–194, 228, 229
GRL	Good Runs List	39, 67, 152
HCAL	Hadronic Calorimeter	29
HEC	Hadronic end-cap calorimeter	31, 48
HL-LHC	High-Luminosity LHC	144
HLT	High Level Trigger	37, 38, 69, 70
HMSR	High-mass signal region	61, 67, 71–74, 77, 81–83, 93, 94, 96, 99, 100, 106, 112, 115, 121, 123–126, 128, 130–132, 134–136, 138, 139, 143, 159–161, 164, 168, 174–176, 185, 195–197, 199, 201, 208, 212, 218, 219, 221, 223–225, 228, 229, 232

Notation	Description	Page List
HMSSVR	High-mass same-sign validation region	67, 74, 99, 100, 102–106, 111, 122, 161, 165, 173, 228, 229
IBL	Insertable B-Layer	28
ID	Inner Detector	27–29, 41, 53–57, 59, 87, 182
ID	Identification	178
IO	Inside-out combined muon	56, 57
IP	LHC interaction point	23–28, 35, 36, 56
ISR	Initial state radiation	40, 95–97, 129
JER	Jet energy resolution	57
JES	Jet energy scale	57
JVT	Jet vertex tagger	58, 149
L1	Level-1 trigger	36–38, 52, 70
L1A	Level-1 accept signal	48, 49
L1Calo	Level-1 Calorimeter trigger (Run 2 & 3)	37, 46, 47, 49–52
L1Muon	Level-1 Muon trigger (Run 2 & 3)	37
L1Topo	Level-1 Topological Processor	37
LAr	Liquid argon	1, 2, 29–33, 43, 46–52, 144, 241
LB	Luminosity block	38, 39, 67, 152
LEP	Large Electron–Position Collider	18, 19, 23
LH	Likelihood	56
LHC	Large Hadron Collider	1, 2, 17, 19, 20, 22–26, 34, 36, 38, 39, 43, 45, 48, 50–53, 56, 141–143
LHCb	Large Hadron Collider Beauty	24
LINAC2	Linear accelerator at CERN for LHC *pp* runs until 2018	23, 24
LINAC4	Linear accelerator at CERN for LHC *pp* runs from 2020	23, 24
LMSR	Low-mass signal region	61, 67, 71–74, 77, 81–83, 96, 98–100, 106, 112, 114, 121, 123–126, 128–132, 134–136, 138, 139, 167, 174, 175, 191–194, 199–203, 207, 212, 216–218, 220–223, 228, 229, 232

Notation	Description	Page List
LMSSVR	Low-mass same-sign validation region	67, 74, 102–106, 110, 122, 172, 228, 229
LO	Leading order	64, 66, 75, 76
LS2	Long Shutdown 2	2, 28, 43, 46, 47, 51, 144
LTP	ATLAS Local Trigger Processor	43, 45–47, 51
LTPi	ATLAS Local Trigger Processor Interface	43, 46, 47
LUCID-2	LUminosity Cherenkov Integrating Detector	35, 38
MC	Monte Carlo simulation	23, 39–42, 55, 57, 58, 63, 64, 67, 73, 75–79, 81, 82, 84, 85, 88, 89, 92, 99–101, 117, 118, 122, 126–129, 141, 143, 144, 149, 159, 174–176, 178, 179, 182, 183, 209–215, 228, 241
MC16a	MC16a simulation campaign corresponding to the data-taking years 2015-16	41
MC16d	MC16d simulation campaign corresponding to the data-taking year 2017	41
MC16e	MC16e simulation campaign corresponding to the data-taking year 2018	42
MDT	Monitored Drift Tubes	35
ME	Matrix element	39, 40, 64, 66, 75, 76, 94, 95, 129
ME	Spectrometer extrapolated muon	56, 57
MHO	Missing higher orders	89–91, 96, 97
MLE	Maximum-likelihood estimator	117, 118, 121
MM	Matrix Method	97, 98, 100, 104, 113, 129, 160, 162, 164, 175, 191–194, 231
MMC	Missing Mass Calculator	59, 71, 99–101, 116, 142
MPI	Multi parton interaction	40, 96, 97
MS	Muon Spectrometer	29, 34, 36, 41, 53, 56, 57, 87

Notation	Description	Page List
MVA	Multivariate algorithm	56
N^3LO	Next-to-next-to-next-to-leading order	64, 65, 76, 90, 91, 103, 135, 152, 231
NLO	Next-to-leading order	75–77, 95
NN	Neural network	58
NNLO	Next-to-next-to-leading order	75–77, 89
NP	Nuisance parameter	85–89, 92, 98–101, 105, 116–119, 122, 125–130, 133, 134, 195–197, 209–225, 231
OFC	Optimal filtering coefficient	32
pdf	Probability density function	56, 60, 118–120
PDF	Parton density function	40, 41, 64, 75, 76, 89–97
Phase-1	Phase-1 Upgrade of the LAr Detector installed during LS2	43, 52
PMT	Photomultiplier tube	34, 36
POI	Point of interest	195, 196
PRW	Pile-up reweighting	151
PS	Proton Synchrotron	23, 24
PS	Parton shower	39–41, 75, 76, 94–96
PS	Presampler	30
QCD	Quantum Chromodynamics	6, 40, 57, 75–77, 89, 93
QFT	Quantum Field Theory	3
QSF	Resummation scale for soft-gluon emission	8, 93, 94, 129, 195, 197
RMS	Root mean square	162
ROD	Readout Driver	37
RoI	Region of interest	37
ROS	Readout System	37
RPC	Resistive-Plate Chambers	35, 36
Run 1	Run 1 of the LHC from 2009-2013	29, 122, 142
Run 2	Run 2 of the LHC from 2015-2018	2, 23–25, 37–39, 41, 43, 46, 47, 137, 141, 144, 174, 227

Notation	Description	Page List
Run 3	Run 3 of the LHC that started in 2022	5, 23, 24, 43, 44, 46, 48, 49, 51, 52, 143, 144
SBC	Single board computer	44
SCT	Semiconductor Tracker	27, 28, 53
SF	Scale factor	149
SM	Standard Model of particle physics	1, 3–9, 11–14, 16–18, 20, 25, 59, 61, 63, 67, 72, 74–77, 102, 119, 140–142, 227
SNO	Sudbury Neutrino Observatory	4
SPS	Super Proton Synchrotron	23, 24
SR	Signal region	67, 71–73, 75, 81, 82, 84, 85, 93, 99–102, 113, 121–123, 125, 126, 130–132, 135, 136, 138, 139, 141–144, 161, 174–176, 178, 201, 228
SS	Same-sign, referring to the lepton charges	102, 161
ST	Segment-tagged muon	57
TCR	Top control region	67, 74, 77, 78, 95, 102, 104, 105, 108, 121, 123–126, 141, 170, 205, 206, 228, 229
TGC	Thin-Gap Chambers	35, 36
Tile	Tile calorimeter of the ATLAS detector	32, 34, 46, 47
TR	Transition radiation	29
TRT	Transition Radiation Tracker	27–29, 53
TTC	Trigger, timing and control signals	43–52
TTCex	TTC encoder/transmitter	43, 47
TTCvi	TTC VMEbus interface	43, 47
VEV	Vacuum expectation value	9, 10, 14
VME	Versa Module Eurocard	44, 47
VME64x	Versa Module Eurocard with support for 64-bit data transfers	44

Notation	Description	Page List
VR	Validation Region	67, 73, 85, 102, 104
WP	Working point	148
ZCR	$Z \to \tau\tau$ control region	61, 67, 73, 74, 81–85, 93, 94, 99–102, 104, 105, 107, 121, 123–126, 141, 161, 164, 169, 178–183, 185, 196, 197, 205, 206, 228, 229
ZDC	Zero Degree Calorimeters	35, 36, 46

Bibliography

[1] ATLAS Collaboration, *Observation of a new particle in the search for the Standard Model Higgs boson with the ATLAS detector at the LHC*, Phys. Lett. B **716** (2012) 1, arXiv: `1207.7214 [hep-ex]`.

[2] CMS Collaboration, *Observation of a new boson at a mass of 125 GeV with the CMS experiment at the LHC*, Phys. Lett. B **716** (2012) 30, arXiv: `1207.7235 [hep-ex]`.

[3] ATLAS Collaboration, *The ATLAS Experiment at the CERN Large Hadron Collider*, JINST **3** (2008) S08003.

[4] CMS Collaboration, *The CMS Experiment at the CERN LHC*, JINST **3** (2008) S08004.

[5] L. Evans and P. Bryant, *LHC Machine*, JINST **3** (2008) S08001.

[6] ATLAS Collaboration, *A detailed map of Higgs boson interactions by the ATLAS experiment ten years after the discovery*, Nature **607** (2022) 52, arXiv: `2207.00092 [hep-ex]`, Erratum: Nature **612** (2022) E24.

[7] CMS Collaboration, *A portrait of the Higgs boson by the CMS experiment ten years after the discovery*, Nature **607** (2022) 60, arXiv: `2207.00043 [hep-ex]`, Erratum: Nature **623** (2023) E4.

[8] P. W. Higgs, *Broken Symmetries and the Masses of Gauge Bosons*, Phys. Rev. Lett. **13** (1964) 508.

[9] D. P. Aguillard et al., *Measurement of the Positive Muon Anomalous Magnetic Moment to 0.20 ppm*, Phys. Rev. Lett. **131** (2023) 161802, arXiv: `2308.06230 [hep-ex]`.

[10] A. Pich and P. Tuzon, *Yukawa Alignment in the Two-Higgs-Doublet Model*, Phys. Rev. D **80** (2009) 091702, arXiv: `0908.1554 [hep-ph]`.

[11] A. Djouadi, *The Anatomy of electro-weak symmetry breaking. II. The Higgs bosons in the minimal supersymmetric model*, Phys. Rept. **459** (2008) 1, arXiv: `hep-ph/0503173 [hep-ph]`.

[12] G. Branco et al., *Theory and phenomenology of two-Higgs-doublet models*, Phys. Rept. **516** (2012) 1, arXiv: `1106.0034 [hep-ph]`.

[13] ATLAS Collaboration,
Search for neutral MSSM Higgs bosons decaying to $\tau^+\tau^-$ pairs in proton–proton collisions at $\sqrt{s} = 7$ TeV with the ATLAS detector,
Phys. Lett. B **705** (2011) 174, arXiv: `1107.5003 [hep-ex]`.

[14] ATLAS Collaboration,
Search for neutral Higgs bosons of the minimal supersymmetric standard model in pp collisions at $\sqrt{s} = 8$ TeV with the ATLAS detector,
JHEP **11** (2014) 056, arXiv: `1409.6064 [hep-ex]`.

[15] ATLAS Collaboration, *Search for Heavy Higgs Bosons Decaying into Two Tau Leptons with the ATLAS Detector Using pp Collisions at $\sqrt{s} = 13$ TeV*, Phys. Rev. Lett. **125** (2020) 051801, arXiv: `2002.12223 [hep-ex]`.

[16] CMS Collaboration, *Search for additional neutral MSSM Higgs bosons in the $\tau\tau$ final state in proton–proton collisions at $\sqrt{s} = 13$ TeV*,
JHEP **09** (2018) 007, arXiv: `1803.06553 [hep-ex]`.

[17] CMS Collaboration, *Searches for additional Higgs bosons and for vector leptoquarks in $\tau\tau$ final states in proton–proton collisions at $\sqrt{s} = 13$ TeV*,
JHEP **07** (2023) 073, arXiv: `2208.02717 [hep-ex]`.

[18] P. Athron et al., *New physics explanations of a_μ in light of the FNAL muon $g-2$ measurement*, JHEP **09** (2021) 080, arXiv: `2104.03691 [hep-ph]`.

[19] ATLAS Collaboration,
Search for a light CP-odd Higgs boson decaying into a pair of τ-leptons in proton-proton collisions at $\sqrt{s} = 13$ TeV with the ATLAS detector,
JHEP **12** (2024) 126, arXiv: `2409.20381 [hep-ex]`.

[20] S. Tomonaga, *On a relativistically invariant formulation of the quantum theory of wave fields*, Prog. Theor. Phys. **1** (1946) 27.

[21] J. Schwinger, *Quantum Electrodynamics. I. A Covariant Formulation*, Phys. Rev. **74** (10 1948) 1439.

[22] R. P. Feynman, *Mathematical Formulation of the Quantum Theory of Electromagnetic Interaction*, Phys. Rev. **80** (3 1950) 440.

[23] S. L. Glashow, *Partial-symmetries of weak interactions*,
Nuclear Physics **22** (1961) 579, ISSN: 0029-5582.

[24] A. Salam, *Weak and Electromagnetic Interactions*,
Conf. Proc. C **680519** (1968) 367.

[25] S. Weinberg, *A model of leptons*, Physical review letters **19** (1967) 1264.

[26] H. Fritzsch, M. Gell-Mann, and H. Leutwyler,
Advantages of the color octet gluon picture,
Physics Letters B **47** (1973) 365, ISSN: 0370-2693.

[27] P. Higgs, *Broken symmetries, massless particles and gauge fields*, Physics Letters **12** (1964) 132, ISSN: 0031-9163.

[28] F. Englert and R. Brout, *Broken Symmetry and the Mass of Gauge Vector Mesons*, Phys. Rev. Lett. **13** (1964) 321.

[29] G. S. Guralnik, C. R. Hagen, and T. W. B. Kibble, *Global Conservation Laws and Massless Particles*, Phys. Rev. Lett. **13** (1964) 585.

[30] P. W. Higgs, *Spontaneous Symmetry Breakdown without Massless Bosons*, Phys. Rev. **145** (1966) 1156.

[31] Wikimedia Commons, *Standard Model of Elementary Particles*, [Accessed: 16 January 2025].

[32] Q. R. Ahmad et al., *Measurement of the Rate of $\nu_e + d \rightarrow p + p + e^-$ Interactions Produced by ^8B Solar Neutrinos at the Sudbury Neutrino Observatory*, Phys. Rev. Lett. **87** (7 2001) 071301.

[33] P. A. Dirac, *The quantum theory of the electron*, Proc. Roy. Soc. Lond. A **A117** (1928) 610.

[34] K. G. Wilson, *Confinement of Quarks*, Phys. Rev. D **10** (1974) 2445, ed. by J. C. Taylor.

[35] H. Yukawa, *On the Interaction of Elementary Particles I*, Proc. Phys. Math. Soc. Jap. **17** (1935) 48.

[36] P. Langacker, "Introduction to the Standard Model and Electroweak Physics", *Theoretical Advanced Study Institute in Elementary Particle Physics: The Dawn of the LHC Era*, 2010, arXiv: `0901.0241 [hep-ph]`.

[37] J. Ellis, "Higgs Physics", *2013 European School of High-Energy Physics*, 2015, arXiv: `1312.5672 [hep-ph]`.

[38] Y. Nambu and G. Jona-Lasinio, *Dynamical Model of Elementary Particles Based on an Analogy with Superconductivity. 1.*, Phys. Rev. **122** (1961) 345, ed. by T. Eguchi.

[39] J. Goldstone, A. Salam, and S. Weinberg, *Broken Symmetries*, Phys. Rev. **127** (1962) 965.

[40] S. Navas et al., *Review of particle physics*, Phys. Rev. D **110** (2024) 030001.

[41] D. Griffiths, *Introduction to elementary particles*, 1987 122, ISBN: 978-3-527-40601-2.

[42] C. S. Wu, E. Ambler, R. W. Hayward, D. D. Hoppes, and R. P. Hudson, *Experimental Test of Parity Conservation in Beta Decay*, Phys. Rev. **105** (4 1957) 1413.

[43] ATLAS Collaboration, *Determination of spin and parity of the Higgs boson in the $WW^* \to e\nu\mu\nu$ decay channel with the ATLAS detector*, Eur. Phys. J. C **75** (2015) 231, arXiv: `1503.03643 [hep-ex]`.

[44] J. Christenson, J. Cronin, V. Fitch, and R. Turlay, *Evidence for the 2π Decay of the K_2^0 Meson*, Phys. Rev. Lett. **13** (1964) 138.

[45] G. Luders, *Proof of the TCP theorem*, Annals Phys. **2** (1957) 1.

[46] E. Corbelli and P. Salucci, *The Extended Rotation Curve and the Dark Matter Halo of M33*, Mon. Not. Roy. Astron. Soc. **311** (2000) 441, arXiv: `astro-ph/9909252`.

[47] D. Clowe et al., *A Direct Empirical Proof of the Existence of Dark Matter*, The Astrophysical Journal **648** (2006) L109.

[48] T. Aoyama et al., *The anomalous magnetic moment of the muon in the Standard Model*, Phys. Rept. **887** (2020) 1, arXiv: `2006.04822 [hep-ph]`.

[49] G. Colangelo et al., *Prospects for precise predictions of a_μ in the Standard Model*, (2022), arXiv: `2203.15810 [hep-ph]`.

[50] S. Borsanyi et al., *Leading hadronic contribution to the muon magnetic moment from lattice QCD*, Nature **593** (2021) 51.

[51] A. Boccaletti et al., *High precision calculation of the hadronic vacuum polarisation contribution to the muon anomaly*, (2024), arXiv: `2407.10913 [hep-lat]`.

[52] CMD-3 Collaboration, *Measurement of the $e^+e^- \to \pi^+\pi^-$ cross section from threshold to 1.2 GeV with the CMD-3 detector*, Phys. Rev. D **109** (2024) 112002, arXiv: `2302.08834 [hep-ex]`.

[53] T. D. Lee, *A Theory of Spontaneous T Violation*, Phys. Rev. D **8** (1973) 1226, ed. by G. Feinberg.

[54] J. F. Gunion and H. E. Haber, *CP-conserving two-Higgs-doublet model: The approach to the decoupling limit*, Phys. Rev. D **67** (7 2003) 075019.

[55] S. L. Glashow and S. Weinberg, *Natural conservation laws for neutral currents*, Phys. Rev. D **15** (7 1977) 1958.

[56] E. A. Paschos, *Diagonal neutral currents*, Phys. Rev. D **15** (7 1977) 1966.

[57] I. Chakraborty and A. Kundu, *Two-Higgs doublet models confront the naturalness problem*, Phys. Rev. D **90** (2014) 115017, arXiv: `1404.3038 [hep-ph]`.

[58] A. Cherchiglia, D. Stöckinger, and H. Stöckinger-Kim, *Muon $g-2$ in the 2HDM: Maximum results and detailed phenomenology*, Phys. Rev. D **98** (2018) 035001, arXiv: `1711.11567 [hep-ph]`.

[59] M. Misiak and M. Steinhauser, *Weak radiative decays of the B meson and bounds on $M_{H^{\pm}}$ in the Two-Higgs-Doublet Model*, Eur. Phys. J. C **77** (2017) 201, arXiv: `1702.04571 [hep-ph]`.

[60] G. W. Bennett et al., *Final Report of the Muon E821 Anomalous Magnetic Moment Measurement at BNL*, Phys. Rev. D **73** (2006) 072003, arXiv: `hep-ex/0602035`.

[61] B. Abi et al., *Measurement of the Positive Muon Anomalous Magnetic Moment to 0.46 ppm*, Phys. Rev. Lett. **126** (14 2021) 141801.

[62] V. Ilisie, *New Barr-Zee contributions to $(g-2)_\mu$ in two-Higgs-doublet models*, JHEP **04** (2015) 077, arXiv: `1502.04199 [hep-ph]`.

[63] S. M. Barr and A. Zee, *Electric Dipole Moment of the Electron and of the Neutron*, Phys. Rev. Lett. **65** (1990) 21, Erratum: Phys. Rev. Lett. **65** (1990) 2920.

[64] D. Chang, W.-F. Chang, C.-H. Chou, and W.-Y. Keung, *Large two loop contributions to $g-2$ from a generic pseudoscalar boson*, Phys. Rev. D **63** (2001) 091301, arXiv: `hep-ph/0009292`.

[65] K.-m. Cheung, C.-H. Chou, and O. C. W. Kong, *Muon anomalous magnetic moment, two Higgs doublet model, and supersymmetry*, Phys. Rev. D **64** (2001) 111301, arXiv: `hep-ph/0103183`.

[66] Y.-L. Wu and Y.-F. Zhou, *Muon anomalous magnetic moment in the standard model with two Higgs doublets*, Phys. Rev. D **64** (2001) 115018, arXiv: `hep-ph/0104056`.

[67] M. Krawczyk, *Precision muon $g-2$ results and light Higgs bosons in the 2HDM(II)*, Acta Phys. Polon. B **33** (2002) 2621, arXiv: `hep-ph/0208076`.

[68] J. Abdallah et al., *Searches for neutral higgs bosons in extended models*, Eur. Phys. J. C **38** (2004) 1, arXiv: `hep-ex/0410017`.

[69] S. Chatrchyan et al., *Search for neutral Higgs bosons decaying to tau pairs in pp collisions at s=7 TeV*, Physics Letters B **713** (2012) 68.

[70] CERN, *LEP design report*, CERN-LEP-84-01, CERN, 1984.

[71] ALICE Collaboration, *The ALICE experiment at the CERN LHC*, Journal of Instrumentation **3** (2008) S08002.

[72] LHCb Collaboration, *The LHCb Detector at the LHC*, Journal of Instrumentation **3** (2008) S08005.

[73] E. Lopienska, *The CERN accelerator complex, layout in 2022. Complexe des accélérateurs du CERN en janvier 2022*, ().

[74] B. Salvachua, *Overview of Proton-Proton Physics during Run 2*, 9th LHC Operations Evian Workshop (2019) 7.

[75] ATLAS Collaboration, *Track Reconstruction Performance of the ATLAS Inner Detector at* $\sqrt{s} = 13$ *TeV*, ATL-PHYS-PUB-2015-018, 2015.

[76] ATLAS Collaboration, *ATLAS Inner Detector: Technical Design Report, Volume 1*, ATLAS-TDR-4; CERN-LHCC-97-016, 1997.

[77] ATLAS Collaboration, *ATLAS Inner Detector: Technical Design Report, Volume 2*, ATLAS-TDR-5, CERN-LHCC-97-017, 1997.

[78] ATLAS Collaboration, *ATLAS pixel detector electronics and sensors*, JINST **3** (2008) P07007.

[79] ATLAS Collaboration, *The Pixel Detector of the ATLAS experiment for Run 2 of the Large Hadron Collider*, JINST **9** (2014) C12034.

[80] ATLAS Collaboration, *ATLAS Insertable B-Layer: Technical Design Report*, ATLAS-TDR-19; CERN-LHCC-2010-013, 2010, Addendum: ATLAS-TDR-19-ADD-1; CERN-LHCC-2012-009, 2012.

[81] ATLAS Collaboration, *Operation and performance of the ATLAS semiconductor tracker*, JINST **9** (2014) P08009, arXiv: `1404.7473 [hep-ex]`.

[82] A. Ahmad et al., *The Silicon microstrip sensors of the ATLAS semiconductor tracker*, Nucl. Instrum. Meth. A **578** (2007) 98.

[83] ATLAS TRT Collaboration, *The ATLAS Transition Radiation Tracker (TRT) proportional drift tube: Design and performance*, JINST **3** (2008) P02013.

[84] ATLAS Collaboration, *Performance of the ATLAS Transition Radiation Tracker in Run 1 of the LHC: tracker properties*, JINST **12** (2017) P05002, arXiv: `1702.06473 [hep-ex]`.

[85] ATLAS Collaboration,
ATLAS Liquid Argon Calorimeter: Technical Design Report,
ATLAS-TDR-2; CERN-LHCC-96-041, 1996.

[86] M. Aharrouche et al.,
Response uniformity of the ATLAS liquid argon electromagnetic calorimeter,
Nuclear Instruments and Methods in Physics Research Section A:
Accelerators, Spectrometers, Detectors and Associated Equipment **582**
(2007) 429.

[87] ATLAS Collaboration, *ATLAS Tile Calorimeter: Technical Design Report*,
ATLAS-TDR-3; CERN-LHCC-96-042, 1996.

[88] ATLAS Collaboration,
ATLAS Muon Spectrometer: Technical Design Report,
ATLAS-TDR-10; CERN-LHCC-97-022, CERN, 1997.

[89] M. Maerker, *Search for heavy neutral Higgs bosons decaying into the fully hadronic di-tau final state with ATLAS*, CERN-THESIS-2021-270,
Dresden, 2021.

[90] L. Adamczyk et al.,
Technical Design Report for the ATLAS Forward Proton Detector,
CERN-LHCC-2015-009, ATLAS-TDR-024, 2015.

[91] G. Avoni et al., *The new LUCID-2 detector for luminosity measurement and monitoring in ATLAS*, JINST **13** (2018) P07017.

[92] ATLAS Collaboration, *Zero Degree Calorimeters for ATLAS*,
CERN-LHCC-2007-001, LHCC-I-016, 2007.

[93] S. Abdel Khalek et al., *The ALFA Roman Pot Detectors of ATLAS*,
JINST **11** (2016) P11013, arXiv: `1609.00249 [physics.ins-det]`.

[94] Yu Nakahama on behalf of the ATLAS Collaboration,
The ATLAS Trigger System: Ready for Run-2,
Journal of Physics: Conference Series **664** (2015) 082037.

[95] ATLAS Collaboration, *Operation of the ATLAS trigger system in Run 2*,
JINST **15** (2020) P10004, arXiv: `2007.12539 [physics.ins-det]`.

[96] ATLAS collaboration,
Public ATLAS Luminosity Results for Run-2 of the LHC,
[Accessed: 16 May 2024].

[97] ATLAS Collaboration, *Luminosity determination in pp collisions at* $\sqrt{s} = 13$ *TeV using the ATLAS detector at the LHC*,
Eur. Phys. J. C **83** (2023) 982, arXiv: `2212.09379 [hep-ex]`.

[98] T. Golling, H. S. Hayward, P. U. E. Onyisi, H. J. Stelzer, and P. Waller, *The ATLAS Data Quality Defect Database System*, Eur. Phys. J. C **72** (2012) 1960, arXiv: `1110.6119 [physics.ins-det]`.

[99] P. Laycock et al., *ATLAS data preparation in run 2*, Journal of Physics: Conference Series **898** (2017) 042050.

[100] T. Gleisberg et al., *Event generation with SHERPA 1.1*, JHEP **02** (2009) 007, arXiv: `0811.4622 [hep-ph]`.

[101] ATLAS Collaboration, *ATLAS Computing: Technical Design Report*, ATLAS-TDR-17; CERN-LHCC-2005-022, 2005.

[102] ATLAS Collaboration, *Athena*, version 21.0.127, 2021.

[103] ATLAS Collaboration, *The ATLAS Simulation Infrastructure*, Eur. Phys. J. C **70** (2010) 823, arXiv: `1005.4568 [physics.ins-det]`.

[104] T. Sjöstrand et al., *An introduction to PYTHIA 8.2*, Comput. Phys. Commun. **191** (2015) 159, arXiv: `1410.3012 [hep-ph]`.

[105] E. Bothmann et al., *Event generation with Sherpa 2.2*, SciPost Phys. **7** (2019) 034, arXiv: `1905.09127 [hep-ph]`.

[106] S. Alioli, P. Nason, C. Oleari, and E. Re, *A general framework for implementing NLO calculations in shower Monte Carlo programs: the POWHEG BOX*, JHEP **06** (2010) 043, arXiv: `1002.2581 [hep-ph]`.

[107] ATLAS Collaboration, *ATLAS Pythia 8 tunes to* 7 *TeV data*, ATL-PHYS-PUB-2014-021, 2014.

[108] S. Agostinelli et al., GEANT4 – *a simulation toolkit*, Nucl. Instrum. Meth. A **506** (2003) 250.

[109] ATLAS Collaboration, *The simulation principle and performance of the ATLAS fast calorimeter simulation FastCaloSim*, ATL-PHYS-PUB-2010-013, 2010.

[110] ATLAS Collaboration, *The Pythia 8 A3 tune description of ATLAS minimum bias and inelastic measurements incorporating the Donnachie–Landshoff diffractive model*, ATL-PHYS-PUB-2016-017, 2016.

[111] ATLAS Collaboration, *Emulating the impact of additional proton–proton interactions in the ATLAS simulation by presampling sets of inelastic Monte Carlo events*, Comput. Softw. Big Sci. **6** (2022) 3, arXiv: `2102.09495 [hep-ex]`.

[112] P. Kuzmanovic, *Development and Testing of the ALTI Module for Timing and Synchronization in the ATLAS experiment at CERN*, CERN-THESIS-2018-335, Belgrade, 2018.

[113] G. Aad et al., *The Phase-I trigger readout electronics upgrade of the ATLAS Liquid Argon calorimeters*, JINST **17** (2022) P05024, arXiv: `2202.07384 [physics.ins-det]`.

[114] CERN EDMS, *ALTI - Atlas LTrg Interface*, EDA-03627, CERN, 2023.

[115] CERN EDMS, *ALTI - Atlas LTrg Interface - Mezzanine*, EDA-03628, CERN, 2018.

[116] Clement Camincher, Huacheng Cai, private communication.

[117] N. P. Konstantinidis et al., *The Atlantis event visualisation program for the ATLAS experiment*, 2005.

[118] ATLAS collaboration, *Public ATLAS Luminosity Results for Run-3 of the LHC*, [Accessed: 28 November 2024].

[119] ATLAS collaboration, *Level-1 Calorimeter Trigger Public Results*, [Accessed: 28 November 2024].

[120] ATLAS Collaboration, *Performance of the ATLAS track reconstruction algorithms in dense environments in LHC Run 2*, Eur. Phys. J. C **77** (2017) 673, arXiv: `1704.07983 [hep-ex]`.

[121] R. Fruhwirth, *Application of Kalman filtering to track and vertex fitting*, Nucl. Instrum. Meth. A **262** (1987) 444.

[122] ATLAS Collaboration, *Reconstruction of primary vertices at the ATLAS experiment in Run 1 proton–proton collisions at the LHC*, Eur. Phys. J. C **77** (2017) 332, arXiv: `1611.10235 [hep-ex]`.

[123] ATLAS Collaboration, *Topological cell clustering in the ATLAS calorimeters and its performance in LHC Run 1*, Eur. Phys. J. C **77** (2017) 490, arXiv: `1603.02934 [hep-ex]`.

[124] ATLAS Collaboration, *Electron and photon performance measurements with the ATLAS detector using the 2015–2017 LHC proton–proton collision data*, JINST **14** (2019) P12006, arXiv: `1908.00005 [hep-ex]`.

[125] ATLAS Collaboration, *Muon reconstruction and identification efficiency in ATLAS using the full Run 2 pp collision data set at $\sqrt{s} = 13$ TeV*, Eur. Phys. J. C **81** (2021) 578, arXiv: `2012.00578 [hep-ex]`.

[126] ATLAS Collaboration, *Jet reconstruction and performance using particle flow with the ATLAS Detector*, Eur. Phys. J. C **77** (2017) 466, arXiv: `1703.10485 [hep-ex]`.

[127] M. Cacciari, G. P. Salam, and G. Soyez, *The anti-k_t jet clustering algorithm*, JHEP **04** (2008) 063, arXiv: `0802.1189 [hep-ph]`.

[128] ATLAS Collaboration, *Jet energy scale and resolution measured in proton–proton collisions at $\sqrt{s} = 13$ TeV with the ATLAS detector*, Eur. Phys. J. C **81** (2021) 689, arXiv: `2007.02645 [hep-ex]`.

[129] ATLAS Collaboration, *Selection of jets produced in 13 TeV proton–proton collisions with the ATLAS detector*, ATLAS-CONF-2015-029, 2015.

[130] ATLAS Collaboration, *Performance of pile-up mitigation techniques for jets in pp collisions at $\sqrt{s} = 8$ TeV using the ATLAS detector*, Eur. Phys. J. C **76** (2016) 581, arXiv: `1510.03823 [hep-ex]`.

[131] ATLAS Collaboration, *Identification and rejection of pile-up jets at high pseudorapidity with the ATLAS detector*, Eur. Phys. J. C **77** (2017) 580, arXiv: `1705.02211 [hep-ex]`, Erratum: Eur. Phys. J. C **77** (2017) 712.

[132] ATLAS Collaboration, *ATLAS flavour-tagging algorithms for the LHC Run 2 pp collision dataset*, Eur. Phys. J. C **83** (2023) 681, arXiv: `2211.16345 [physics.data-an]`.

[133] ATLAS Collaboration, *Performance of electron and photon triggers in ATLAS during LHC Run 2*, Eur. Phys. J. C **80** (2020) 47, arXiv: `1909.00761 [hep-ex]`.

[134] ATLAS Collaboration, *Performance of the ATLAS muon triggers in Run 2*, JINST **15** (2020) P09015, arXiv: `2004.13447 [physics.ins-det]`.

[135] ATLAS Collaboration, *Tagging and suppression of pileup jets with the ATLAS detector*, ATLAS-CONF-2014-018, 2014.

[136] ATLAS Collaboration, *ATLAS b-jet identification performance and efficiency measurement with $t\bar{t}$ events in pp collisions at $\sqrt{s} = 13$ TeV*, Eur. Phys. J. C **79** (2019) 970, arXiv: `1907.05120 [hep-ex]`.

[137] ATLAS Collaboration, *The performance of missing transverse momentum reconstruction and its significance with the ATLAS detector using 140 fb^{-1} of $\sqrt{s} = 13$ TeV pp collisions*, (2024), arXiv: `2402.05858 [hep-ex]`.

[138] A. Elagin, P. Murat, A. Pranko, and A. Safonov, *A New Mass Reconstruction Technique for Resonances Decaying to di-tau*, Nucl. Instrum. Meth. A **654** (2011) 481, arXiv: `1012.4686 [hep-ex]`.

[139] ATLAS Collaboration,
Measurements of Higgs boson production cross-sections in the $H \to \tau^+\tau^-$ decay channel in pp collisions at $\sqrt{s} = 13$ TeV with the ATLAS detector,
JHEP **08** (2022) 175, arXiv: `2201.08269 [hep-ex]`.

[140] M. Melcher, *Untersuchung der Lepton-Isolation für die Suche nach $A \to \tau\tau \to e2\nu\mu2\nu$ Zerfällen*, BA thesis: TU Dresden, Germany, 2022.

[141] V. Rothert, *Optimierung der Suche nach CP-ungeraden Higgs-Bosonen im Zerfall zu Tau-Lepton-Paaren bei ATLAS*,
BA thesis: TU Dresden, Germany, 2023.

[142] P. Moder, *Search for a light CP-odd Higgs boson decaying into a $\tau\tau$ pair*,
MA thesis: TU Dresden, Germany, 2018.

[143] T. Kreße, *Search for a light CP-odd Higgs boson decaying into a pair of τ-leptons with the ATLAS detector*,
MA thesis: TU Dresden, Germany, 2020.

[144] X.-M. Sonntag, *Optimized search for a light CP-odd Higgs boson decaying into two τ-leptons using the ATLAS detector*,
MA thesis: TU Dresden, Germany, 2021.

[145] J. Friese,
Search for a light CP-odd Higgs boson decaying into a pair of tau-leptons,
MA thesis: TU Dresden, Germany, 2022.

[146] C. R. Schmidt,
Top quark background uncertainty and fake lepton background estimation in the search for a light CP-odd Higgs boson using the ATLAS detector,
MA thesis: TU Dresden, Germany, 2023.

[147] H. Jacobi, *Improvements of the search for a light CP-odd Higgs boson decaying to a pair of tau leptons using artificial neural networks*,
MA thesis: TU Dresden, Germany, 2023.

[148] R. Barlow, *Practical statistics for particle physics*, en,
CERN Yellow Reports: School Proceedings **Vol. 5** (2020 2020) 12.

[149] R. D. Ball, M. Bonvini, S. Forte, S. Marzani, and G. Ridolfi,
Higgs production in gluon fusion beyond NNLO,
Nucl. Phys. B **874** (2013) 746, arXiv: `1303.3590 [hep-ph]`.

[150] M. Bonvini, R. D. Ball, S. Forte, S. Marzani, and G. Ridolfi,
Updated Higgs cross section at approximate N^3LO,
J. Phys. G **41** (2014) 095002, arXiv: `1404.3204 [hep-ph]`.

[151] M. Bonvini, S. Marzani, C. Muselli, and L. Rottoli, *On the Higgs cross section at N^3LO+N^3LL and its uncertainty*, JHEP **08** (2016) 105, arXiv: `1603.08000 [hep-ph]`.

[152] T. Ahmed et al., *Pseudo-scalar Higgs boson production at $N^3LO_A+N^3LL$*, Eur. Phys. J. C **76** (2016) 663, arXiv: `1606.00837 [hep-ph]`.

[153] M. Bonvini and S. Marzani, *Double resummation for Higgs production*, Phys. Rev. Lett. **120** (2018) 202003, arXiv: `1802.07758 [hep-ph]`.

[154] M. Bonvini, *An approximate N^3LO cross section for Higgs production in gluon fusion*, EPJ Web Conf. **60** (2013) 12008, ed. by M. Bosman, A. Juste, M. Mart ınez, and V. Sorin, arXiv: `1306.6633 [hep-ph]`.

[155] R. V. Harlander and W. B. Kilgore, *Next-to-next-to-leading order Higgs production at hadron colliders*, Phys. Rev. Lett. **88** (2002) 201801, arXiv: `hep-ph/0201206`.

[156] R. V. Harlander and K. J. Ozeren, *Finite top mass effects for hadronic Higgs production at next-to-next-to-leading order*, JHEP **11** (2009) 088, arXiv: `0909.3420 [hep-ph]`.

[157] R. V. Harlander, H. Mantler, S. Marzani, and K. J. Ozeren, *Higgs production in gluon fusion at next-to-next-to-leading order QCD for finite top mass*, Eur. Phys. J. C **66** (2010) 359, arXiv: `0912.2104 [hep-ph]`.

[158] C. Anastasiou et al., *Higgs boson gluon-fusion production beyond threshold in N^3LO QCD*, JHEP **03** (2015) 091, arXiv: `1411.3584 [hep-ph]`.

[159] C. Anastasiou et al., *High precision determination of the gluon fusion Higgs boson cross-section at the LHC*, JHEP **05** (2016) 058, arXiv: `1602.00695 [hep-ph]`.

[160] B. Mistlberger, *Higgs boson production at hadron colliders at N^3LO in QCD*, JHEP **05** (2018) 028, arXiv: `1802.00833 [hep-ph]`.

[161] F. Buccioni et al., *OpenLoops 2*, Eur. Phys. J. C **79** (2019) 866, arXiv: `1907.13071 [hep-ph]`.

[162] F. Cascioli, P. Maierhöfer, and S. Pozzorini, *Scattering Amplitudes with Open Loops*, Phys. Rev. Lett. **108** (2012) 111601, arXiv: `1111.5206 [hep-ph]`.

[163] A. Denner, S. Dittmaier, and L. Hofer, COLLIER*: A fortran-based complex one-loop library in extended regularizations*, Comput. Phys. Commun. **212** (2017) 220, arXiv: `1604.06792 [hep-ph]`.

[164] T. Gleisberg and S. Höche, *Comix, a new matrix element generator*, JHEP **12** (2008) 039, arXiv: `0808.3674 [hep-ph]`.

[165] S. Schumann and F. Krauss, *A parton shower algorithm based on Catani–Seymour dipole factorisation*, JHEP **03** (2008) 038, arXiv: `0709.1027 [hep-ph]`.

[166] S. Höche, F. Krauss, M. Schönherr, and F. Siegert, *A critical appraisal of NLO+PS matching methods*, JHEP **09** (2012) 049, arXiv: `1111.1220 [hep-ph]`.

[167] S. Höche, F. Krauss, M. Schönherr, and F. Siegert, *QCD matrix elements + parton showers. The NLO case*, JHEP **04** (2013) 027, arXiv: `1207.5030 [hep-ph]`.

[168] S. Catani, F. Krauss, B. R. Webber, and R. Kuhn, *QCD Matrix Elements + Parton Showers*, JHEP **11** (2001) 063, arXiv: `hep-ph/0109231`.

[169] S. Höche, F. Krauss, S. Schumann, and F. Siegert, *QCD matrix elements and truncated showers*, JHEP **05** (2009) 053, arXiv: `0903.1219 [hep-ph]`.

[170] NNPDF Collaboration, R. D. Ball, et al., *Parton distributions for the LHC run II*, JHEP **04** (2015) 040, arXiv: `1410.8849 [hep-ph]`.

[171] C. Anastasiou, L. Dixon, K. Melnikov, and F. Petriello, *High-precision QCD at hadron colliders: Electroweak gauge boson rapidity distributions at next-to-next-to leading order*, Phys. Rev. D **69** (2004) 094008, arXiv: `hep-ph/0312266`.

[172] S. Frixione, G. Ridolfi, and P. Nason, *A positive-weight next-to-leading-order Monte Carlo for heavy flavour hadroproduction*, JHEP **09** (2007) 126, arXiv: `0707.3088 [hep-ph]`.

[173] P. Nason, *A new method for combining NLO QCD with shower Monte Carlo algorithms*, JHEP **11** (2004) 040, arXiv: `hep-ph/0409146`.

[174] S. Frixione, P. Nason, and C. Oleari, *Matching NLO QCD computations with parton shower simulations: the POWHEG method*, JHEP **11** (2007) 070, arXiv: `0709.2092 [hep-ph]`.

[175] S. Alioli, P. Nason, C. Oleari, and E. Re,
A general framework for implementing NLO calculations in shower Monte Carlo programs: the POWHEG BOX, JHEP **06** (2010) 043,
arXiv: `1002.2581 [hep-ph]`.

[176] ATLAS Collaboration,
Studies on top-quark Monte Carlo modelling for Top2016,
ATL-PHYS-PUB-2016-020, 2016.

[177] S. Frixione, E. Laenen, P. Motylinski, C. White, and B. R. Webber,
Single-top hadroproduction in association with a W boson,
JHEP **07** (2008) 029, arXiv: `0805.3067 [hep-ph]`.

[178] NNPDF Collaboration, R. D. Ball, et al.,
Parton distributions with LHC data, Nucl. Phys. B **867** (2013) 244,
arXiv: `1207.1303 [hep-ph]`.

[179] D. J. Lange, *The EvtGen particle decay simulation package*,
Nucl. Instrum. Meth. A **462** (2001) 152.

[180] K. Hamilton, P. Nason, E. Re, and G. Zanderighi,
NNLOPS simulation of Higgs boson production, JHEP **10** (2013) 222,
arXiv: `1309.0017 [hep-ph]`.

[181] K. Hamilton, P. Nason, and G. Zanderighi, *Finite quark-mass effects in the NNLOPS POWHEG+MiNLO Higgs generator*, JHEP **05** (2015) 140,
arXiv: `1501.04637 [hep-ph]`.

[182] J. Butterworth et al., *PDF4LHC recommendations for LHC Run II*,
J. Phys. G **43** (2016) 023001, arXiv: `1510.03865 [hep-ph]`.

[183] ATLAS Collaboration,
Measurement of the Z/γ^* boson transverse momentum distribution in pp collisions at $\sqrt{s} = 7$ TeV with the ATLAS detector, JHEP **09** (2014) 145,
arXiv: `1406.3660 [hep-ex]`.

[184] A. Djouadi, J. Kalinowski, and M. Spira, *HDECAY: a program for Higgs boson decays in the Standard Model and its supersymmetric extension*,
Comput. Phys. Commun. **108** (1998) 56, arXiv: `hep-ph/9704448`.

[185] M. Spira, *QCD Effects in Higgs Physics*, Fortsch. Phys. **46** (1998) 203,
arXiv: `hep-ph/9705337`.

[186] A. Djouadi, M. M. Mühlleitner, and M. Spira, *Decays of Supersymmetric Particles: the Program SUSY-HIT (SUspect-SdecaY-Hdecay-InTerface)*,
Acta Phys. Polon. B **38** (2007) 635, arXiv: `hep-ph/0609292`.

[187] A. Bredenstein, A. Denner, S. Dittmaier, and M. M. Weber, *Radiative corrections to the semileptonic and hadronic Higgs-boson decays $H \to WW/ZZ \to 4$ fermions*, JHEP **02** (2007) 080, arXiv: `hep-ph/0611234`.

[188] A. Bredenstein, A. Denner, S. Dittmaier, and M. M. Weber, *Precise predictions for the Higgs-boson decay $H \to WW/ZZ \to 4$ leptons*, Phys. Rev. D **74** (2006) 013004, arXiv: `hep-ph/0604011 [hep-ph]`.

[189] A. Bredenstein, A. Denner, S. Dittmaier, and M. M. Weber, *Precision calculations for the Higgs decays $H \to ZZ/WW \to 4$ leptons*, Nucl. Phys. B Proc. Suppl. **160** (2006) 131, arXiv: `hep-ph/0607060 [hep-ph]`.

[190] D. de Florian et al., *Handbook of LHC Higgs Cross Sections: 4. Deciphering the Nature of the Higgs Sector*, (2017), arXiv: `1610.07922 [hep-ph]`.

[191] C. Anastasiou, C. Duhr, F. Dulat, F. Herzog, and B. Mistlberger, *Higgs Boson Gluon-Fusion Production in QCD at Three Loops*, Phys. Rev. Lett. **114** (2015) 212001, arXiv: `1503.06056 [hep-ph]`.

[192] F. Dulat, A. Lazopoulos, and B. Mistlberger, *iHixs 2 – Inclusive Higgs cross sections*, Comput. Phys. Commun. **233** (2018) 243, arXiv: `1802.00827 [hep-ph]`.

[193] R. V. Harlander and K. J. Ozeren, *Top mass effects in Higgs production at next-to-next-to-leading order QCD: Virtual corrections*, Phys. Lett. B **679** (2009) 467, arXiv: `0907.2997 [hep-ph]`.

[194] A. Pak, M. Rogal, and M. Steinhauser, *Finite top quark mass effects in NNLO Higgs boson production at LHC*, JHEP **02** (2010) 025, arXiv: `0911.4662 [hep-ph]`.

[195] S. Actis, G. Passarino, C. Sturm, and S. Uccirati, *NLO electroweak corrections to Higgs boson production at hadron colliders*, Phys. Lett. B **670** (2008) 12, arXiv: `0809.1301 [hep-ph]`.

[196] S. Actis, G. Passarino, C. Sturm, and S. Uccirati, *NNLO computational techniques: The cases $H \to \gamma\gamma$ and $H \to gg$*, Nucl. Phys. B **811** (2009) 182, arXiv: `0809.3667 [hep-ph]`.

[197] M. Bonetti, K. Melnikov, and L. Tancredi, *Higher order corrections to mixed QCD-EW contributions to Higgs boson production in gluon fusion*, Phys. Rev. D **97** (2018) 056017, arXiv: `1801.10403 [hep-ph]`, Erratum: Phys. Rev. D **97** (2018) 099906(E).

[198] M. Ciccolini, A. Denner, and S. Dittmaier,
Strong and Electroweak Corrections to the Production of a Higgs Boson + 2 Jets via Weak Interactions at the Large Hadron Collider,
Phys. Rev. Lett. **99** (2007) 161803, arXiv: `0707.0381 [hep-ph]`.

[199] M. Ciccolini, A. Denner, and S. Dittmaier, *Electroweak and QCD corrections to Higgs production via vector-boson fusion at the CERN LHC*,
Phys. Rev. D **77** (2008) 013002, arXiv: `0710.4749 [hep-ph]`.

[200] P. Bolzoni, F. Maltoni, S.-O. Moch, and M. Zaro, *Higgs Boson Production via Vector-Boson Fusion at Next-to-Next-to-Leading Order in QCD*,
Phys. Rev. Lett. **105** (2010) 011801, arXiv: `1003.4451 [hep-ph]`.

[201] M. L. Ciccolini, S. Dittmaier, and M. Krämer, *Electroweak radiative corrections to associated WH and ZH production at hadron colliders*,
Phys. Rev. D **68** (2003) 073003, arXiv: `hep-ph/0306234 [hep-ph]`.

[202] O. Brein, A. Djouadi, and R. Harlander,
NNLO QCD corrections to the Higgs-strahlung processes at hadron colliders,
Phys. Lett. B **579** (2004) 149, arXiv: `hep-ph/0307206`.

[203] O. Brein, R. V. Harlander, M. Wiesemann, and T. Zirke,
Top-quark mediated effects in hadronic Higgs-Strahlung,
Eur. Phys. J. C **72** (2012) 1868, arXiv: `1111.0761 [hep-ph]`.

[204] L. Altenkamp, S. Dittmaier, R. V. Harlander, H. Rzehak, and T. J. E. Zirke,
Gluon-induced Higgs-strahlung at next-to-leading order QCD,
JHEP **02** (2013) 078, arXiv: `1211.5015 [hep-ph]`.

[205] A. Denner, S. Dittmaier, S. Kallweit, and A. Mück,
HAWK 2.0: A Monte Carlo program for Higgs production in vector-boson fusion and Higgs strahlung at hadron colliders,
Comput. Phys. Commun. **195** (2015) 161, arXiv: `1412.5390 [hep-ph]`.

[206] O. Brein, R. V. Harlander, and T. J. E. Zirke,
vh@nnlo – Higgs Strahlung at hadron colliders,
Comput. Phys. Commun. **184** (2013) 998, arXiv: `1210.5347 [hep-ph]`.

[207] R. V. Harlander, A. Kulesza, V. Theeuwes, and T. Zirke,
Soft gluon resummation for gluon-induced Higgs Strahlung,
JHEP **11** (2014) 082, arXiv: `1410.0217 [hep-ph]`.

[208] ATLAS Collaboration,
Measurements of top-quark pair differential cross-sections in the lepton+jets channel in pp collisions at $\sqrt{s} = 8$ TeV using the ATLAS detector,
Eur. Phys. J. C **76** (2016) 538, arXiv: `1511.04716 [hep-ex]`.

[209] M. Czakon et al.,
Top-pair production at the LHC through NNLO QCD and NLO EW,
Journal of High Energy Physics **2017** (2017).

[210] ATLAS Collaboration, *Tools for estimating fake/non-prompt lepton backgrounds with the ATLAS detector at the LHC*,
JINST **18** (2023) T11004, arXiv: `2211.16178 [hep-ex]`.

[211] ATLAS Collaboration,
Study of $Z \to ll\gamma$ decays at $\sqrt{s} = 8$ TeV with the ATLAS detector,
Eur. Phys. J. C **84** (2023) 195, arXiv: `2310.11574 [hep-ex]`.

[212] ATLAS Collaboration, *Electron and photon energy calibration with the ATLAS detector using LHC Run 2 data*, JINST **19** (2023) P02009,
arXiv: `2309.05471 [hep-ex]`.

[213] ATLAS Collaboration, *Studies of the muon momentum calibration and performance of the ATLAS detector with pp collisions at $\sqrt{s} = 13$ TeV*,
Eur. Phys. J. C **83** (2023) 686, arXiv: `2212.07338 [hep-ex]`.

[214] ATLAS Collaboration, *Measurement of $W^{\pm}$ and Z-boson production cross sections in pp collisions at $\sqrt{s} = 13$ TeV with the ATLAS detector*,
Phys. Lett. B **759** (2016) 601, arXiv: `1603.09222 [hep-ex]`.

[215] M. Czakon and A. Mitov, *Top++: A program for the calculation of the top-pair cross-section at hadron colliders*,
Comput. Phys. Commun. **185** (2014) 2930, arXiv: `1112.5675 [hep-ph]`.

[216] M. Botje et al., *The PDF4LHC Working Group Interim Recommendations*,
(2011), arXiv: `1101.0538 [hep-ph]`.

[217] A. D. Martin, W. J. Stirling, R. S. Thorne, and G. Watt,
Uncertainties on α_S in global PDF analyses and implications for predicted hadronic cross sections, Eur. Phys. J. C **64** (2009) 653,
arXiv: `0905.3531 [hep-ph]`.

[218] J. Gao et al., *CT10 next-to-next-to-leading order global analysis of QCD*,
Phys. Rev. D **89** (2014) 033009, arXiv: `1302.6246 [hep-ph]`.

[219] ATLAS Collaboration, *Measurement of fiducial and differential W^+W^- production cross-sections at $\sqrt{s} = 13$ TeV with the ATLAS detector*,
Eur. Phys. J. C **79** (2019) 884, arXiv: `1905.04242 [hep-ex]`.

[220] ATLAS Collaboration,
Measurement of $W^{\pm}Z$ production cross sections and gauge boson polarisation in pp collisions at $\sqrt{s} = 13$ TeV with the ATLAS detector,
Eur. Phys. J. C **79** (2019) 535, arXiv: `1902.05759 [hep-ex]`.

[221] ATLAS Collaboration, *Measurement of ZZ production in the $\ell\ell\nu\nu$ final state with the ATLAS detector in pp collisions at $\sqrt{s} = 13$ TeV*, JHEP **10** (2019) 127, arXiv: `1905.07163 [hep-ex]`.

[222] ATLAS Collaboration, *Measurement of the four-lepton invariant mass spectrum in 13 TeV proton–proton collisions with the ATLAS detector*, JHEP **04** (2019) 048, arXiv: `1902.05892 [hep-ex]`.

[223] S. Catani and M. Grazzini, *Next-to-Next-to-Leading-Order Subtraction Formalism in Hadron Collisions and its Application to Higgs-Boson Production at the Large Hadron Collider*, Phys. Rev. Lett. **98** (2007) 222002, arXiv: `hep-ph/0703012 [hep-ph]`.

[224] S. Dulat et al., *New parton distribution functions from a global analysis of quantum chromodynamics*, Phys. Rev. D **93** (2016) 033006, arXiv: `1506.07443 [hep-ph]`.

[225] L. A. Harland-Lang, A. D. Martin, P. Motylinski, and R. S. Thorne, *Parton distributions in the LHC era: MMHT 2014 PDFs*, Eur. Phys. J. C **75** (2015) 204, arXiv: `1412.3989 [hep-ph]`.

[226] M. Bähr et al., *Herwig++ physics and manual*, Eur. Phys. J. C **58** (2008) 639, arXiv: `0803.0883 [hep-ph]`.

[227] J. Bellm et al., *Herwig 7.0/Herwig++ 3.0 release note*, Eur. Phys. J. C **76** (2016) 196, arXiv: `1512.01178 [hep-ph]`.

[228] J. Alwall et al., *The automated computation of tree-level and next-to-leading order differential cross sections, and their matching to parton shower simulations*, JHEP **07** (2014) 079, arXiv: `1405.0301 [hep-ph]`.

[229] J. R. Klein and A. Roodman, *Blind analysis in nuclear and particle physics*, Ann. Rev. Nucl. Part. Sci. **55** (2005) 141.

[230] G. Cowan, K. Cranmer, E. Gross, and O. Vitells, *Asymptotic formulae for likelihood-based tests of new physics*, Eur. Phys. J. C **71** (2011) 1554, arXiv: `1007.1727 [physics.data-an]`, Erratum: Eur. Phys. J. C **73** (2013) 2501.

[231] R. Barlow and C. Beeston, *Fitting using finite Monte Carlo samples*, Comput. Phys. Commun. **77** (1993) 219.

[232] S. S. Wilks, *The Large-Sample Distribution of the Likelihood Ratio for Testing Composite Hypotheses*, Ann. Math. Statist. **9** (1938) 60.

[233] A. Wald, *Tests of Statistical Hypotheses Concerning Several Parameters When the Number of Observations is Large*, *Transactions of the American Mathematical Society* **54** no. 3, (1943) 426-482.

[234] A. L. Read, *Presentation of search results: the CL_S technique*, J. Phys. G **28** (2002) 2693.

[235] ATLAS Collaboration, *Search for the $b\bar{b}$ decay of the Standard Model Higgs boson in associated $(W/Z)H$ production with the ATLAS detector*, JHEP **01** (2015) 069, arXiv: `1409.6212 [hep-ex]`.

[236] *Proceedings of the 1974 CERN School of Computing: Godøysund, Norway 11 - 24 Aug 1974. 3rd CERN School of Computing*, CERN-74-23, CERN, 1974.

[237] I. Zurbano Fernandez et al., *High-Luminosity Large Hadron Collider (HL-LHC): Technical design report*, **10/2020** (2020), ed. by I. Béjar Alonso et al.

Own Contributions

Particle physics is a highly complex field that required thousands of people to work closely together. Therefore, the contribution of a single member of a collaboration has to be put into context of the whole collaboration, since it relies on previous work of many other people. Here, my own contributions to the different topics covered within this thesis are summarized.

For the ALTI integration described in Chapter 4, I was one member in the three person LAr ALTI team. I contributed notably to the physical integration and cabling of the boards and had significant contributions to the software integration into the LAr system. I was the sole responsible for setting up the pattern generator and the standalone pulsing scripts. Furthermore, I had major contributions to the online monitoring panel and the ALTI integration at the EMF.

In the analysis described in Chapter 6, which lead to the ATLAS publication [19], we were a team of two PhD students, four master's students, one postdoctoral researcher and our academic supervisor. I was the sole responsible for the MC sample selection, the signal MC production, and the signal cross-section uncertainty determination. Furthermore, I had major contributions to the MC sample derivations, the analysis region definitions, the experimental uncertainty determination, the n-tuple production, the statistical analysis, and the interpretation of the obtained results. Aside from that, I contributed significantly to the trigger strategy, the event selection, the plotting framework, the efficiency calculation and efficiency studies for the matrix method, and the $Z \rightarrow \tau\tau$ reweighting with its accompanying uncertainties. In addition, I made notable contributions to the matrix method implementation and the determination of the matrix method uncertainties.

Danksagung

Ich möchte mich bei allen bedanken, die mich durch meine Promotion begleitet haben. Mein Dank geht zuerst an Prof. Arno Straessner für die sehr gute Betreuung und die Möglichkeit, meine Arbeit in so einem interessanten Forschungsgebiet anzufertigen. Weiterhin möchte ich allen Mitarbeitern des IKTP für das schöne Arbeitsklima und die Möglichkeit, stets nach Rat fragen zu können, danken. Hervorzuheben ist hier zum einen Prof. Dominik Stöckinger, welcher immer für Fragen zum theoretischen Hintergrund zur Verfügung stand. Zum anderen geht ein besonderer Dank an die weiteren Mitglieder der Arbeitsgruppe an der TU Dresden, Max, David, Xynia, Jannik, Marius, Manuel, Christian, Hannah, Valentin und Asma, für Hilfe bei technischen Fragen, ausgedehnte Diskussionen über physikalische Themen, das Korrekturlesen dieser Arbeit und natürlich auch interessante nicht-physikalische Gespräche in der Mittagspause.
Nach meinem Umzug zum CERN nach Genf habe ich auch dort schnell Anschluss an die LAr-Arbeitsgruppe gefunden und möchte mich bei allen Mitarbeitern für die gemeinsame Zeit und Unterstützung bedanken.
Für den nötigen Ausgleich neben der Promotion möchte ich mich außerdem bei all meinen Freunden für viele schöne Momente, gelegentlich geschmückt mit der einen oder anderen roten Hopfenkaltschale, bedanken. Danke für all die gemeinsamen Urlaube, Festivals, Konzerte, bestiegenen Berge, Klettertouren, Skitage, Spieleabende, Radtouren und sonstige Unternehmungen. Außerdem möchte ich mich bei meiner Freundin für viele schöne gemeinsame Momente und ihre Unterstützung bedanken. Zuletzt geht mein Dank an meine Familie, die mich über meine gesamte Promotionszeit hinweg unterstützt hat und mir immer in Rat und Tat zur Seite stand.

Versicherung

Hiermit versichere ich, dass ich die vorliegende Arbeit ohne unzulässige Hilfe Dritter und ohne Benutzung anderer als der angegebenen Hilfsmittel angefertigt habe; die aus fremden Quellen direkt oder indirekt übernommenen Gedanken sind als solche kenntlich gemacht. Die Arbeit wurde bisher weder im Inland noch im Ausland in gleicher oder ähnlicher Form einer anderen Prüfungsbehörde vorgelegt.
Die vorliegende Dissertation wurde am Institut für Kern- und Teilchenphysik der Technischen Universität Dresden unter wissenschaftlicher Betreuung von Prof. Dr. Arno Straessner angefertigt.
Es haben keine früheren erfolglosen Promotionsverfahren stattgefunden.
Ich erkenne die Promotionsordnung des Bereichs Mathematik und Naturwissenschaften der Technischen Universität Dresden vom 23.02.2011 in der Fassung vom 23.05.2018 an.

Dresden, den 04.03.2025

Tom Kreße